Investigating biomineralization and other geobiological challenges

A dissertation presented to
the faculty of the School of Engineering and Applied Sciences
University of Virginia

In partial fulfillment of the requirements for the degree

Doctor of Philosophy

By

Toriana Vigil

August 2024

Abstract

Biomineralization is a natural process that transforms inorganic precursors to mineralized products. With applications to materials synthesis and mineral extraction, biomineralization is a green alternative to traditional wet chemistry and hydrometallurgical techniques. In these traditional approaches, organic solvents, high temperatures, and hazardous wastes are ubiquitous, but via biomineralization the same results can be achieved at room temperature in aqueous conditions. In this work, I probe the structure and function of precision biomineralization protein silicatein for applications in inorganic oxide nanoparticle synthesis. While silicatein produces monodisperse, crystalline particles, the rate of production is not competitive with current wet chemistry techniques. Therefore, enzyme solubility and kinetics are targeted via the addition of fusion tags, directed evolution, and rationale-based design.

Further, I examine the robust biomineralization protein smCSE as a tool for rare earth element (REE) extraction. Crystallography of smCSE with metal precursor reveals a probable metal-interaction site, which I probe via site-directed mutagenesis, followed by evaluation of biomineralization with REEs and targeted end use with simulated waste streams.

While biomineralization is promising for materials synthesis applications, it may also be a valuable tool for critical mineral extraction. Accordingly, I consider the harsh conditions associated with mining REEs in order to identify promising new biomineralization actors. Collection and culture of microbial species identified from mines in southwestern Virginia, followed by screening for tolerance and degradation of bituminous compounds and metals reveals *Lysinibacillus sphaericus.* In regards to bitumen degradation, *L. sphaericus* degrades polycyclic aromatic hydrocarbons anthracene and naphthalene in minimal media. Moreover, *L. sphaericus* also shows biomineralization of saline lithium chloride to lithium hydroxide nanoparticles, which may be promising as a critical mineral extraction technique.

Finally, in collaboration with researchers at the United States Air Force Academy, this work implements silicatein in cyanobacteria for a carbon-negative biomanufacturing approach and applies silicatein biosilicification for biocementation in austere environments. These applications highlight the versatility and wide applicability of biomineralization.

Overall, this work highlights structure and function of biomineralization proteins with applications in materials synthesis and mineral extraction.

Acknowledgements

I would like to thank my advisor, Dr. Bryan Berger, for his guidance and mentorship. Your enthusiasm and ideas have been a source of inspiration to me throughout my time at UVa. Through your mentorship I have also learned many valuable skills for teaching students, networking, addressing reviewers, and grant writing. Thank you to my committee members: Dr. Rachel Letteri, Dr. Christopher Paolucci, Dr. Marcos Pires, and Dr. Leah Spangler. A special thank you to Dr. Leah Spangler for allowing me to contribute to her biomineralization review. I would also like to thank Dr. Jordan Steel at USAFA for coordinating and supporting my time with the iGEM team and LSRC, but especially for being a thoughtful mentor and scientist.

Thank you to my lab-mates: Dr. Madison Mann, Samantha Felton, Bill Fahy, Mack Kinkeade, and Kevin Lynn for invaluable discussion and insight in the lab and with experiments. A special thank you to Dr. Madison Mann for sharing her expertise with Graphpad Prism, Snapgene, and Biorender. Thank you to my talented undergraduates: M.J. Rowson, Abigail Frost, and Abigail Janiga for their dedication, enthusiasm, and hard work.

This work was funded via NSF grants 172-7166 and 182-1389 (I helped write this one!) as well as the UVa Dean's Fellowship.

Lastly, I would like to thank my family and friends for their support, and Bandit and Smokey for listening to all my practice presentations.

Figures and Tables *(in order of appearance)*	
Figure 1.	**Comparing current nanoceria production with silicatein production in two cases.** Estimates made for theoretical bioreactor size, TF-silicatein concentration, and V_{max} and K_{cat} for TF-silicatein with ceria. Notably, to produce 2,000 L of 2 µM TF-silicatein as proposed in this scenario, 500,000 L of recombinant *E. coli* cell culture would be necessary (calculation based on current experimental silicatein production). Cerion Nanomaterials and Toyota information from cerionnano.com and autodealertodaymagazine.com. Figure made with Biorender.
Figure 2.	**Biomineralization with silicatein.** Enzymatic biomineralization with silicatein transforms an inorganic salt to an inorganic oxide. In the case of native substrate, a silica salt species is transformed to silica oxide. Figure utilizes PDB structure 6ZQ3.
Figure 3.	**E-waste recycling** includes physical/mechanical pre-treatment then traditional manufacturing techniques utilize pyro and hydrometallurgy to recover metal mixtures. In the future, biometallurgy techniques are promising for isolating concentrated and purified metal mixtures. Figure made with Biorender.
Figure 4.	**A comparison of MICP with *S. pasteurii* and the proposed mechanism for biocementation via biosilicification with *E. coli* INP-silicatein.** Soil particles are initially unbound and

	have minimal compressive strength. A) MICP with the addition of *S. pasteurii,* urea, ammonium chloride, and calcium chloride leads to calcium carbonate precipitation, cementing particles together. Additional treatments lead to additional particle "growth." B) Addition of *E. coli* INP-silicatein leads to the polymerization of silica species, forming bridges between particles and "growing" aggregate size. Further treatments strengthen these connections by inducing further polymerization. Figure made with Biorender.
Figure 1A-1.	SDS-PAGE for purified silicatein fusions.
Figure 1A-2.	Silver-stained Native PAGE gel shows *in vitro* protein interactions.
Figure 1A-3.	Biomineralization of silica and ceria with silicatein fusions
Figure 1B-1.	BL21 *E coli* survival following ceria exposure.
Figure 1B-2.	GFP fluorescence for library screening.
Figure 1B-3.	Establishing toxic concentration of ceria ammonium nitrate.
Figure 1B-4.	Expected and alternative outcomes of the experimental procedure surrounding directed evolution with recombinant silicatein.
Figure 1B-5.	Sequence alignment for WT compared to >80% consensus sequences for 2.6, 2.7, and 2.8.
Figure 1B-6.	A) Ceria mineralization of wild-type and mutant TF-silicateins in whole cell lysates, normalized to the production of WT.

	B) Specialized Native PAGE of wild-type and mutants 2.6, 2.7, 2.8. correlating protein size with biomineralization activity.
Figure 1B-7.	A) SDS PAGE with whole cell lysates. B) Immunoblot with whole cell lysates.
Figure 1B-8.	Sequences for mutant family 2.6. Earliest truncation is at AA 128.
Figure 1B-9.	Silicatein structure (PDB 6ZQ3) with A) truncated tail of mutant family 2.6 consensus highlighted in orange. B) shows the truncated consensus protein of mutant family 2.6.
Figure 1B-10.	A) Ceria mineralization for purified TF-silicatein and catalytic triad mutants.
Fig 1C-1.	Silicatein enzyme kinetics as measured with precursor ceria ammonium nitrate resulting in ceric oxide formation. A Michaelis-Menten curve fit was applied to calculate v_{max} = 8.1 x 10^{-8}, 2.7 x 10^{-8}, and 8.3 x 10^{-9} moles/hr for TF-sil, GFP-sil, and CAN only, respectively. The calculated Km values were 14.6, 4.7, and 1.3 mM respectively. N = 30
Figure 1C-2.	IUPRED disorder predictions for the proposed mutants. Left, IUPRED predicts decreasing disorder as the polyS region is mutated to A. On the right, each mutation to proline results in increased intrinsic disorder. (Note, pictured is IUPRED prediction which is less specific than the postulated amyloid aggregation.)

Fig. 1C-3.	Silicatein crystal structure 6ZQ3 with polyS region highlighted in red and predicted amyloid-like region in blue.
Figure 1C-4.	PEP-FOLD predictions with YPFVGK (magenta). Row 1 shows P61-K97 or PYGNHGCHGGNMYDAFLYVIANEGVDQDSAYPFVGK. Row 2 shows F76-M112 or FLYVIANEGVDQDSAYPFVGKQSSCNYNSKYKGTSM and H64-C100 or HGCHGGNMYDAFLYVIANEGVDQDSAYPFVGKQSSC. Row 3 shows nonapeptides S74-Q83 or SAYPFVGKQ and mutant SAPPFVGKQ.
Figure 1C-5.	SDS-PAGE gels for polyS purifications. Red arrows indicate bands of interest at 75 and 26 kDa.
Figure 1C-6.	Ceria biomineralization yields of polyS mutants relative to WT TF-silicatein. Error bars represent SEM. One-way ANOVA shows no significant difference between ceria biomineralization yields of any of the mutants and WT TF-silicatein.
Figure 1C-7.	SDS-PAGE for H64A and H67A immobilized metal affinity chromatography purifications showing flow through (FT), 10, 25, 50, and 500 mM elutions.
Figure 1C-8.	Ceria biomineralization yields of histidine mutants relative to WT TF-silicatein. Error bars represent SEM. One-way ANOVA shows no significant difference between ceria biomineralization yields of any of the mutants and WT TF-silicatein.

Figure 2A-1.	A) Coordination of cadmium ion between H49, E53, H351. Imidazole rings from histidine side chains form imidazole "trap." Adapted from unpublished work by P. Mahanta, R. Acharya, B. W. Berger. B) H49 and H351 (without Cd exposure) and associated proline brackets (P46 & P60, P346 & P355)
Figure 2A-2.	SDS-PAGE for WT smCSE and histidine mutants. The purified fraction is shown at 1M imidazole elution, then the column flow through (FT).
Figure 2A-3.	Fluorescence over time shows cadmium sulfide quantum dot formation (exc. 360, em. 520 nm) of WT smCSE and mutant H49A.
Figure 2A-4.	**A)** Hydrogen sulfide generation for WT smCSE, H49A, and H351A mutants. The "enzyme only" (negative control) and + L-cysteine conditions are shown as well as L-cysteine without added enzyme. **B)** Native PAGE for smCSE H351A. Band is above 242 kDa, anticipated tetramer molecular weight would be approximately 192 kDa.
Table 2B-1.	Rare earth element sulfides and their colors.
Figure 2B-1.	smCSE biomineralization of CAN. Sample 1 is smCSE only, without precursors. Sample 2 is smCSE with CAN and L-cysteine. Sample 3 is CAN and L-cysteine.
Figure 2B-2.	Preliminary biomineralization with smCSE and REEs. Sample 1) smCSE only, 2) smCSE + ceria ammonium nitrate + L-cysteine, 3) ceria ammonium nitrate + L-cysteine, 4) smCSE + lanthanum (III) nitrate + L-cysteine, 5) lanthanum

	(III) nitrate + L-cysteine, 6) smCSE + neodymium (III) nitrate + L-cysteine, and 7) neodymium (III) nitrate + L-cysteine. Precipitates evident in samples 2, 3, 4, and 6.
Figure 2B-3.	X-ray diffraction spectra for REE sulfide compounds formed via reaction with smCSE.
Figure 2B-4.	XRD spectra comparing REE sulfide samples made via enzymatic biomineralization with smCSE and known REE sulfide compounds (left). The closest matches are shown on the right.
Figure 2B-5.	smCSE biomineralization with cadmium and cerium precursors evaluated via fluorescence (exc 360 nm, em 520 nm) over 36 hours. Fluorescence is indicative of CdS quantum dot formation. CeS quantum dots do not fluoresce with this excitation and emission. Area under the curve is 376 and 373 for smCSE + CdAc + Cys and smCSE + CdAc + CAN + Cys respectively, illustrating no significant difference (two-tailed unpaired t-test, $p = 0.9951$).
Figure 2C-1.	Proposed column biological soil crust formation for smCSE and waste mixtures. In step 1, the protein is affixed to the column. In step 2, the waste mixture is poured over the column. In step 3, the REE "chunks" are visible and available for collection. Figure made with Biorender.
Figure 2C-2.	Small batch reaction of smCSE, cadmium acetate, and L-cysteine as compared to cadmium acetate and L-cysteine (no enzyme) conditions over a time-course of several days. At 24 hours of incubation, there is no detectable difference in

	fluorescence between the precursor only condition and the smCSE + precursor condition. Additional precursors were added to each. After 96 hours, there is notable difference in fluorescence between the two cases (fluorescence manifests as darkness with this imager).
Table 3A-1	Bacteria identified from western Virginia coal samples.
Figure 3A-1	Growth of *Lysinibacillus*, *Pseudomonas*, and *Bacillus Aryabhattai* with hydrocarbons over 16 hours.
Figure 3A-2.	**Figure 3A-2**. *Lysinibacillus sphaericus* growth with polycyclic aromatic hydrocarbons as sole carbon source (left) and LB as a carbon source (right) over a period of 18 hours. For PAHs, blue shows growth with anthracene while pink represents growth with naphthalene.
Figure 3A-3.	*Lysinibacillus sphaericus* growth with and degradation of naphthalene. Time-course for *L. sphaericus* growth in minimal media with naphthalene (OD600, left y axis) compared to fluorescence intensity (arbitrary units, right y axis).
Figure 3B-1.	Coal friends survival and tolerance to ceria ammonium nitrate.
Figure 3B-2.	Coal friends screening with ceria ammonium nitrate, lanthanum nitrate, neodymium nitrate, and lithium chloride in liquid culture.
Figure 3B-3.	**A)** Lithium recovery following incubation with *Lysinibacillus sphaericus* cells as measured by HPBO fluorescent assay. "Li" is the LiCl only condition, normalized to 1. *L. sphaericus*

	coincubated with LiCl is "LysB + Li". A two-tailed un-paired t-test df = 17 results in p = 0.0011. **B)** Comparing lithium and sodium precipitation by *L. sphaericus,* as measured by HPBO and CoroNa green fluorescent assays. HPBO for lithium species, and CoroNa green for sodium species. "LysB + Li" and "LysB + Li + Na" show that lithium species are precipitated with LysB significantly more than in the "Li + Na only" condition. Further, "LysB + Li + Na" shows that lithium species are in much greater abundance than sodium species.
Figure 3B-4.	Fourier transform infrared spectra for precipitated lithium.
Figure 3B-5.	Transmission electron microscopy imaging for lithium hydroxide nanoparticles.
Figure 3B-6.	SDS-PAGE for concentrated LiOH nanoparticles. 80, 45, and 10 kDa bands were taken for analysis via mass spectrometry.
Table 3B-1.	Biomolecules associated with LiOH nanoparticles as identified by ESI-LC-MS/MS.
Figure 3B-7.	SDS-PAGE gel for ghost extraction. MW of ghost proteins is anticipated at approximately 125 kDa. Band highlighted by red arrow is at approximately 125 kDa.
Table 3B-2.	Normalizing *L. sphaericus* cells and ghosts via OD600 for biomineralization experiments.
Table 3C-1.	LigFa concentrations for various samples.
Figure 3C-1.	**A)** Western blot for purified recombinant LigFa. The full-length protein has an anticipated MW of 77 kDa. Amersham rainbow ladder shows 76 kDa in yellow and 52 kDa in purple. **B)** Absorbance at 564 nm shows LigFa has significantly

	greater absorbance than a buffer-only blank as analyzed with an unpaired t test, $p<0.01$.
Figure 3C-2.	Absorbance of LigFa compared to a buffer only solution. LigFa curve is comparable to what has been previously reported by Ferrer, et al.
Table 3M-1.	Annotated results for *L. sphaericus* 16s rRNA sequencing from Azenta.
Table 4-1.	Selected CyanoGate parts
Figure 4-1.	Colony PCR for CG1, CG2, and CG3.
Figure 4-2.	Colony PCR for pAM1954-eGFP-sil.
Figure 4-3.	Growing cyanobacteria transformed with CGF or pAM-eGFP-sil in 6-well plates.
Figure 5-1.	His-tag purification for recombinant INP-silicatein.
Figure 5-2.	*In vivo* biomineralization with INP-silicatein-a. Silica mineralization can be visualized as precipitate after sample ultra-centrifugation. 1) Precipitate from *E. coli* INP-silicatein-a and sodium orthosilicate after 24 hour incubation, 2) precipitate from WT BL21 *E. coli* and sodium orthosilicate after 24 hour incubation, 3) precipitate from sodium orthosilicate alone after 24 hour incubation. B) Comparison of precipitated silica (ng) as quantified via silicomolybdate assay. Two-tailed unpaired t-test ($p<0.05$).
Figure 5-3.	Immunocytochemistry of WT BL21 *E. coli* and *E. coli* INP-silicatein-a. Green fluorescence shows AlexaFluor 488 conjugated to anti-silicatein-a. Blue fluorescence shows DAPI

	staining of nucleic acids, highlighting the interior of bacterial cells. Overlay shows co-localization of INP-silicatein-a on the exterior of DAPI-stained cells for *E. coli* INP-silicatein-a, but not on WT BL21 *E. coli.*
Figure 5-4.	Unconfined compressive strengths for *S. pasteurii* and *E. coli* INP-silicatein-a bricks. *S. pasteurii* bricks show an average tolerance to 229 kPa (S.E.M. 36 kPa). *E. coli* INP-silicatein-a bricks show an average tolerance of 197 kPa (S.E.M. 34 kPa). A two-tailed unpaired t-test shows no significant difference between the two (p=0.597).
Table 5-1.	Unconfined compressive strengths for bricks made with fine-grain sand.
Figure 5-5.	Unconfined compressive strengths for *S. pasteurii* and *E. coli* INP-silicatein-a martian regolith simulant bricks. *S. pasteurii* bricks show an average tolerance to 31.4 kPa (S.E.M. 27.2 kPa). *E. coli* NP-silicatein-a bricks show an average tolerance of 87.9 kPa (S.E.M. 14.8 kPa). A two-tailed unpaired t-test shows no significant difference between the two (p=0.2098).
Figure 5-6.	INP-silicatein biomineralization with ceria ammonium nitrate. 1) Supernatant from INP-silicatein with ceria ultracentrifuged at 50,000 x g, showing rust-colored precipitate. 2) Supernatant from ceria ammonium nitrate only condition, ultracentrifuged at 50,000 x g, showing no precipitate.

Figure 5-7.	Cylindrical 3D-printed mold for biocementation bricks.

Introduction

Modern technology utilizes a wide range of inorganic materials, from a nanoscopic to macroscopic scale, for gas sensors, batteries, solar cells, and more.[1] Some of these materials can be chemically synthesized from readily available materials, but others require raw materials that must be extracted from the earth via mining. In both cases there is increased demand for safer, greener ways to utilize natural resources. Synthetic biology takes inspiration from natural systems to implement bio-based solutions for diverse applications in agriculture, medicine, and the environment.[2] Household examples of synthetic biology include "green" enzyme-based cleaning products that have risen in popularity as alternatives to more commonly used cleaners that utilize bleach, sodium hydroxide, ammonia, and other chemicals. Products such as these are often derived from naturally occurring proteins engineered to more effectively address specific applications. Similarly, synthetic biology techniques will aid in the development of greener methods for materials synthesis and resource extraction.

Nature's synthesis of inorganic materials is often mediated by biomineralization proteins. Via protein engineering, naturally occurring proteins can be adapted for use in industrial settings.[3] Engineering biomineralization proteins is a promising path to transform the current chemically-intensive and dangerous approaches to materials synthesis and resource extraction. This work will discuss protein-based approaches to these challenges in the following chapters: 1) ***Biomineralization with silicatein: A route for materials synthesis,*** 2) ***Biomineralization with smCSE: Rare earth element extraction and reclamation,*** 3) ***Identifying microbes and proteins compatible with the harsh conditions associated with rare earth elements,*** 4) ***Silicatein expression in cyanobacteria,*** and 5) ***Biocementation with silicatein.***

Biomineralization Background

Biomineralization is a natural process where metal precursors are transformed to mineralized products, such as carbonates, oxides, or sulfides.[4–6] The mild temperatures and aqueous conditions for biomineralization

are in stark contrast with the extremely high temperatures, highly reactive chemicals, and hazardous waste products associated with chemical synthesis techniques.[1] Additionally, biomineralization also offers significant control over a reaction, generating size-controlled nanoparticles.[4]

One example of biomineralization is bone, where-in the protein osteocalcin mediates the formation of hydroxyapatite ($Ca_5(PO_4)_3$).[7] Other examples of biomineralization products are teeth and shells (sea shells and egg shells), as well as more complex structures including tortoise carapaces and rhinoceros' horns.[8–11] Overall biomineralization is a wide umbrella that encompasses many unique interactions and mechanisms that generate a variety of minerals with diverse material properties. Accordingly, fundamental understanding of these processes can aid in the development and applications of greener and safer technologies. This work will focus on protein-mediated biomineralization, which is often subdivided into two categories: *biologically-induced* and *biologically-controlled* mineralization.[6]

In biologically-induced biomineralization, the protein enables biomineralization by modulating the availability of a key precursor compound.[6,12] One example would be a membrane protein that pumps necessary precursor into the reaction space; another would be a protein that generates precursor necessary for the biomineralization reaction to occur.[8] In general, biomineralization processes fall under the classic nucleation and growth model, as described by LaMer and Dinegar.[13] Mineral formation via biologically-induced biomineralization can be described by the microkinetic and inhibition growth model.[14] Two basic assumptions underlie this model: 1) "Kink" nucleation – which we might simplistically think of as imperfection nucleation, or phase- boundary nucleation, and 2) equivalent stoichiometry.[15–17] Here, biomineralization is kicked off by solution supersaturation and therefore modulated by saturation index.[15] When the system is sufficiently oversaturated, crystals form, resulting in overall decreased interfacial energy.[18] Therefore, with the two examples introduced previously (membrane protein that pumps necessary precursor into the reaction space; a protein that generates precursor), these proteins effectively modulate the precursor concentration.

In biologically-controlled mineralization, the protein acts as a catalyst: effectively increasing the rate of mineralization by decreasing the activation energy of the reaction.[6,12] The physics of particle nucleation and growth here are described by Gebauer and Colfen with the formation of a "pre-nucleation cluster" and a notable structural or conformational change.[19] The direct role of the protein in guiding structure and controlling this biomineralization process tends to lead to relatively uniform particle production. Therefore, biologically-controlled mineralization is also characterized by patterning or templating behavior.[6,12] Templated products may have regular, ordered structures that exhibit controlled crystallinity and size, but can also form superstructures that extend beyond these fundamental patterns.[20–23] For example, the beautiful and delicate skeletons of glass sponges are superstructures of crystalline silica, produced by silicateins in an interplay with sillafins, silintaphins, and others. Cnidaria, porifera, and diatoms also frequently display these intricate structures.[7,23,24]

Biomineralization with silicatein: A route for materials synthesis

Common nanoparticle synthesis techniques require toxic reactants and high temperatures while also producing toxic byproducts.[25,26] These processes require highly trained workers, and are dangerous and costly. Synthetic biology presents a greener, safer alternative for nanoparticle synthesis via genetic and protein engineering. Silicatein, named for "***sili****ca* pro***tein***"[24] is a protein native to marine sponges that transforms ambient silica salts to silica oxide.[27] Previous work shows that silicatein retains biomineralization activity as a single enzyme,[28] making it a promising candidate for the production of nanoparticles with a simple reactor-based system, with basics as shown in Figure 1. Current colloidal-batch synthesis of monodisperse particles via a reactor- based system presents several heat and mass transfer limitations associated with crystal nucleation and growth.[29] However, this continues to be an industrially-relevant goal, for which the precision of protein- mediated biomineralization is promising.[5]

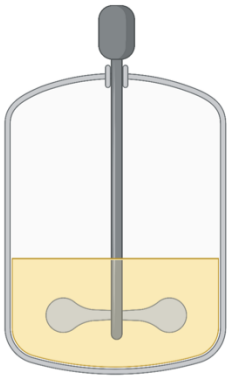

Case 1

Cerion Nanomaterials makes 150 metric tons of nanoceria per year
150 metric tons is 150 million grams, or 870,000 moles

A 2,000 L bioreactor of 2uM TFsilicatein can produce 0.95 moles / min nanoceria
To make 870,000 moles, it will take 920,000 min, 15,333 min, or 639 days

To make an 150 metric tons of nanoceria with silicatein, it would take 1.75 years

Case 2

One catalytic converter contains 0.58 moles of CeO2

A 2,000 L bioreactor of 2uM TFsilicatein can produce 0.95 moles / min nanoceria
This produces an equivalent of 2,400 catalytic converters / day

Toyota makes 24,000 cars per day, presumably 24,000 catalytic converters
This is 10x the amount silicatein can produce

Figure 1. Comparing current nanoceria production with silicatein production in two cases. Estimates made for theoretical bioreactor size, TF-silicatein concentration, and V_{max} and K_{cat} for TF-silicatein with ceria. Notably, to produce 2,000 L of 2 uM TF-silicatein as proposed in this scenario, 500,000 L of recombinant *E. coli* cell culture would be necessary (calculation based on current experimental silicatein production). Cerion Nanomaterials and Toyota information from cerionnano.com and autodealertodaymagazine.com. Figure made with Biorender.

As noted above, silicatein is a biomineralization protein originally found in marine sponges. In the native sponge, silicatein mineralizes ambient silica species to form ordered silicon oxide nanoparticles, which ultimately make up the spicules and exoskeleton of the sponge.[27] Here, biomineralization involves several proteins and molecules, and also occurs on a relatively long time-scale. With consideration to the slow growth of marine sponges, for which average growth rates of 0.1 mm^2 per day are typical,[30] slow enzyme kinetics are biologically sufficient. In order to harness and optimize the biomineralization activity of silicatein for applications such as nanoparticle synthesis, it is paramount to understand enzyme kinetics and function. An understanding of silicatein's biomineralization mechanism will allow for optimization of enzyme activity.

Previous work with silicatein shows several players involved in the biomineralization process, including silintaphins,[31] silaffins,[32] and silicatein which is then further subdivided into alpha, beta, and gamma

subunits.[33] While other macromolecules do play a role in biomineralization in the native marine sponge, *in vitro* studies show that silicatein-alpha (henceforth referred to as silicatein, unless otherwise specified) is capable of mineralizing silica without other helper molecules (Figure 2). Work by Curran, *et al.*, terms this activity as direct biomineralization – encompassing both the catalytic and bio-templating steps.[28]

While the exact mechanism is still largely not understood, the leading theory for silicatein biomineralization stems from high sequence homology with enzyme Cathepsin L, a catalytic protease which has a unique catalytic triad motif. An analogous catalytic triad (S26, H165, N185) has been identified in silicatein as a probable mechanism.[27,33–35] Several mutagenesis studies observe that mutation of the catalytic triad results in less biomineralization activity,[33,35,36] however there is disagreement as to whether biomineralization is completely abolished.[34,37] A confounding factor in these studies is the autohydrolysis of common precursor tetra-ethyl-orthosilicate (TEOS). TEOS can spontaneously transform to silicon oxide in the presence of water – therefore some background levels of product are formed regardless of enzyme biomineralization activity. Silica biomineralization measurements are convoluted further due to the innate low solubility and propensity for aggregation of silicatein.[38,39] Furthermore, Cathepsin L produces similar amorphous particles to silicatein – and abolition of the catalytic triad residues still resulted in particle formation with either enzyme.[34] An alternative mode of action based on surface-templated biosilification is suggested by Povarova, *et al.* and reasons that silicatein may direct structure of particle formation for a pre-hydrolyzed precursor compound.[34] This hypothesis is supported by non-catalytic amorphous particle formation with collagen or glassin in marine sponges,[20,40] as well as silica formation associated with short peptides.[41] In the specific case of glassin, a distinct histidine, aspartic acid, and threonine peptide motif was identified as most impactful for silica formation – this corresponds with hypotheses that intrinsic disorder plays a key role to enable particle formation.[40,42] An important distinction between the catalytic triad and intrinsic disorder theories may be the crystallinity of particles formed, i.e. does one mechanism primarily produce ordered nanocrystals as opposed to amorphous ones? Gebauer and Colfen suggest that protein-mediated biomineralization is distinctly a two-step process, where-in nucleation results in an amorphous particle

aggregate that secondarily undergoes a transition from amorphous to crystalline.[19] According to this rationale, particles that stay amorphous are those that underwent quick solution supersaturation and particle precipitation[19] – suggesting that the amorphous to crystalline transition depends on controlled reaction kinetics. Although elucidation of silicatein's biomineralization mechanism may be key to harnessing silicatein biomineralization for nanoparticle production, studies are limited in scope due to the enzyme's poor solubility and propensity for aggregation.

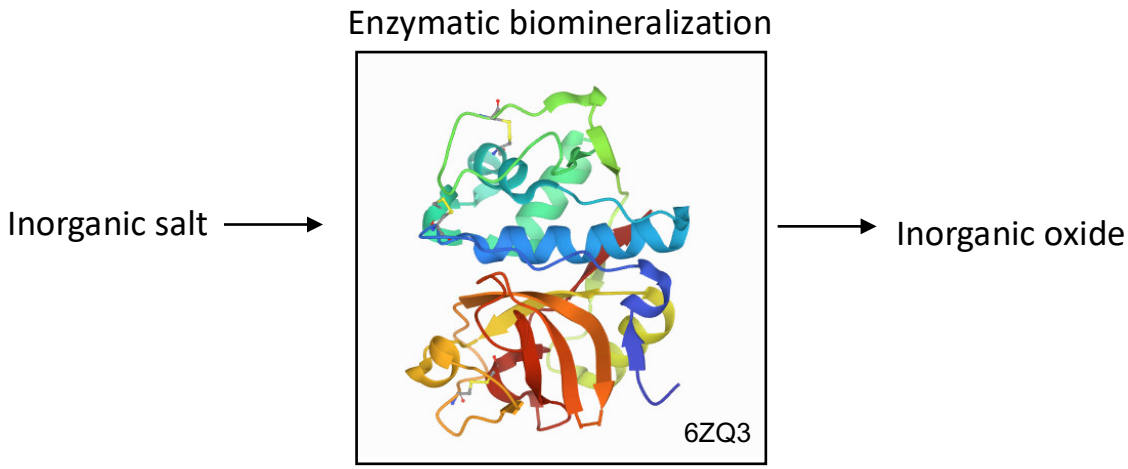

Figure 2. Biomineralization with silicatein. Enzymatic biomineralization with silicatein transforms an inorganic salt to an inorganic oxide. In the case of native substrate, a silica salt species is transformed to silica oxide. Figure utilizes PDB structure 6ZQ3.

A 2012 study strived to circumvent the solubility problem by cell-free recombinant protein expression directly onto a solid microbead surface.[43] After library generation via DNA shuffling (shuffling partners silicatein-alpha and silicatein-beta), each microbead was effectively associated with an isogenic silicatein mutant. The functional silicatein mutants identified in this work conserved the putative catalytic triad residues, and researchers noted a high number of non-functional truncated mutants.[43] Additionally, other researchers report mineralization with silicatein fixed to a solid surface, producing particles of 200-300 nm in the span of an hour.[44] Interestingly, 200-300 nm particles are 100x larger than the 2 nm particles produced

by silicatein in solution. Thus far, the mechanism of silicatein remains unclear, and the general consensus within the field looks to increasing protein solubility and stability in an effort to clarify mechanistic studies.

A popular approach to improve silicatein solubility includes the addition of a fusion protein. Solubility fusion proteins are proteins that are physically linked to the protein of interest to increase stability and/or solubility.[45,46] In 2017, Dakhili et al. made silicatein fusions with glutathione-S-transferase, thioredoxin, small ubiquitin-like modifier, maltose binding protein, and trigger factor. The trigger factor fusion was identified as highest expressing and most soluble, the other fusions were discarded.[37] Sparkes, *et al.* 2020 explored trigger factor silicatein further to establish optimal buffer conditions and purification (yields umol/L), followed by tertiary structure and activity.[47] Although TF-silicatein has been the gold-standard within the silicatein realm, there is still considerable room for improvement, as often the protein aggregates to form insoluble bodies within several hours.[39,47,48]

Green fluorescent protein (GFP) is another common protein fusion partner, often improving solubility of the protein of interest,[45] however few studies have made a GFP-silicatein fusion. Oguri et al., confirmed functionality of GFP-silicatein for silica formation, and utilized fluorescence microscopy to examine association of the protein and particles. The particles formed were approximately 100 μm aggregates, with detectable levels of GFP fluorescence within, which researchers concluded indicates incorporation of the protein within the mineralized structure.[48]

While the current state-of-the-field includes a widespread understanding of silicatein's tendency for aggregation, there is still no clear solution. As described above, mechanistic and kinetic studies are controversial and limited. An understanding of silicatein aggregation as related to biomineralization activity is fundamentally necessary to move forward to mechanistic and kinetic studies. In Aim I, I address silicatein insolubility and aggregation and show the relationship with biomineralization activity, then probe enzyme mechanism and kinetics.

Rare Earth Element Background

Elements in the Lanthanides group, such as ceria, lanthanum, and neodymium are considered rare earth elements (REEs) and are found in low concentrations throughout the earth's crust. When identified, the secondary challenges become separation from contaminants, and finally separation from each other.

REEs are valuable for their optical, electronic, and magnetic properties. They are ubiquitous in our everyday lives; commonly found in lenses, batteries, magnets, and computer disks; fundamental to the function of our phones and cars, as well as commonly used in petroleum refinement.[49] According to a U.S. 2022 Minerals Commodities Report, $160 million of REEs were imported to the U.S. in 2021, more than a $100 million increase from 2020.[50]

Although REEs are of increasing demand, China controls between 60 to 95% of in-ground, available REE deposits.[49,51,52] This is in part due to the economic feasibility of extracting REEs in China, where they occur as "ion-adsorption clay deposits." These clay deposits form following years of rainfall, leaching, and accumulation and are easy to reclaim with relatively neutral treatments and low-cost labor.[49] Carbonatites and alkaline igneous rocks are other sources with relatively high levels of REEs. In short, carbonatites are carbonate-based rock formations and alkaline igneous rocks feature an overabundance of alkaline elements, such as sodium and potassium.[51] REEs are soluble at extremely high temperatures in the mantle, forming insoluble precipitates as temperature and pressure drop. Furthermore, REE enrichments are localized to carbonatites and alkaline igneous rocks likely due to ionic interactions and instability, although this has not been proven.[51] Regardless, REEs are difficult to isolate from carbonatites and alkaline igneous rocks, with the current state-of-the-art techniques including acid/base solvent extraction and various hydrometallurgy techniques.[53] Although mining is traditionally used to source metals, the increasing use and subsequent disposal of these metals is leading to great accumulation in waste streams.

Waste streams such as acid-mine drainage or e-waste can be a secondary source of REEs with selective extraction techniques. The conventional approach to REE recovery from waste streams looks to leaching with strong acids or bases, with microbial bio-leaching emerging as a potential alternative.[54] The synthetic biology toolkit has been expanded to include microbial consortia and bio-degradation approaches.[55] Although this is an area of active study, there remains an immediate need for green, cost- effective REE extraction and separation techniques.[54]

Biomineralization with smCSE: rare earth element reclamation from complex waste streams

smCSE (*Stenotrophomonas maltophilia* cystathionine gamma lyase) is a biomineralization enzyme identified from soil samples.[56] Since 2017, homologous proteins have been identified in *pedobacter,*[57] *raoultella,*[58] *pseudomonas,*[59] *treponema,*[60] and *acidithiobacillus.*[61] Previous work shows smCSE mineralization activity produces cadmium sulfide quantum dots, as well as zinc and lead sulfide, with particle formation induced by H_2S generation.[62,63] Interestingly, smCSE also produces CdSe, likely through H_2Se production, in an analogous mechanism with H_2S generation.[64]

Unlike silicatein, smCSE is easy to produce via recombinant protein production in *E. coli* and thus has been characterized more thoroughly. Wang, et al. 2021 show smCSE is functional as a tetramer modulated by interactions between extended loop domains and suggest that smCSE structure directly impacts biomineralization.[63] Human cystathionine gamma lyase (hCSE) and smCSE share 90% sequence identity, both producing H_2S, however hCSE does not show quantum dot generation activity.[63] Although hCSE does not produce quantum dots, it is known to be crucial in biomineralization of bone, with diseases like osteoporosis correlating to reduced expression of hCSE.[65] The quantum dot generation function of smCSE suggests that smCSE has unique features and that H_2S production alone does not result in biomineralization. Wang et al. 2021 identified four non-conserved surface regions in smCSE, thought to be involved in substrate binding.[63] With point mutations to the innocuous side-chain alanine, absorbance spectra showed

little to no CdS production, from which researchers concluded that these four regions are necessary for substrate binding and quantum dot production.[63]

Pyridoxyl 5' phosphate (PLP) is a necessary cofactor for cystathionine gamma lyases – and has been shown to also be necessary for quantum dot production with smCSE. Without PLP, H_2S production stops, and biomineralization does not occur.[66] Analysis of smCSE crystal structures in the PLP-bound and unbound states, reveal there is no corresponding conformational change associated with PLP binding.[63,66] In contrast, unpublished work (Mahanta, Acharya, Berger) investigates possible conformational changes associated with exposure to the cadmium precursor to interrogate smCSE interaction with the metal biomineralization substrate. With this approach, Mahanta, Acharya, Berger identify histidine at positions 49 and 351 (H49, H351) as directly involved with cadmium ion binding. In Aim 2, I examine the role of H49 and H351 in substrate binding via a directed mutagenesis approach followed by subsequent biomineralization activity assessment. These experiments will inform the use of smCSE as a potential mineralizer of REEs, and subsequent applications in REE extraction.

Identifying microbes and proteins compatible with the harsh conditions associated with rare earth elements.

Rare earth elements (REEs) are in 0.0017% relative abundance to other elements within the earth's crust,[51] which can be considered analogous to salt and pepper on a salad. Thus, recovering REEs can be likened to picking individual grains of salt and pepper from the salad. REEs are both difficult to identify and extract, and precision and selectivity are key. To identify sources of REEs, a field sampling must be collected, then sent for analysis with inductively coupled plasma mass spectroscopy (ICP-MS), or inductively coupled plasma optical emission spectroscopy (ICP-OES) which are techniques that are expensive, destructive, and require user expertise. If REEs are identified in viable amounts, then extraction and recovery requires harsh solvents, is time-intensive, and yields very little. Overall, current REE identification and extraction methods are costly, time-intensive, and inefficient.

One complicating factor in the identification of REEs is encapsulation in bitumen. Bitumen is an oily, tarry, substance found with coal made up of mostly polycyclic aromatic hydrocarbons (PAHs) and short chain hydrocarbons.[67] In the salad analogy, bitumen can be represented by salad dressing. REEs encapsulated in bitumen are like salt particles covered in a glob of dressing – difficult to identify and extract. Acid digestion has been used to treat bitumen and collect samples for ICP-MS, yielding some levels of cerium, lanthanum, and neodymium.[68] However, acid digestion is both hazardous and environmentally harmful, and ICP-MS remains expensive and destructive. For Aim 3a, I explore a biological approach to bitumen degradation based on selective identification of microbes from bituminous conditions. I then evaluate these microbes for biomineralization activity (Aim 3b), with the rationale that bitumen and metal species are both prevalent in the native environments of these species, and therefore both bitumen-degradation and biomineralization behavior would confer greater species survival. Combined bitumen degradation and biomineralization qualities are promising for future e-waste recovery utilizing biometallurgy techniques (Fig. 3).

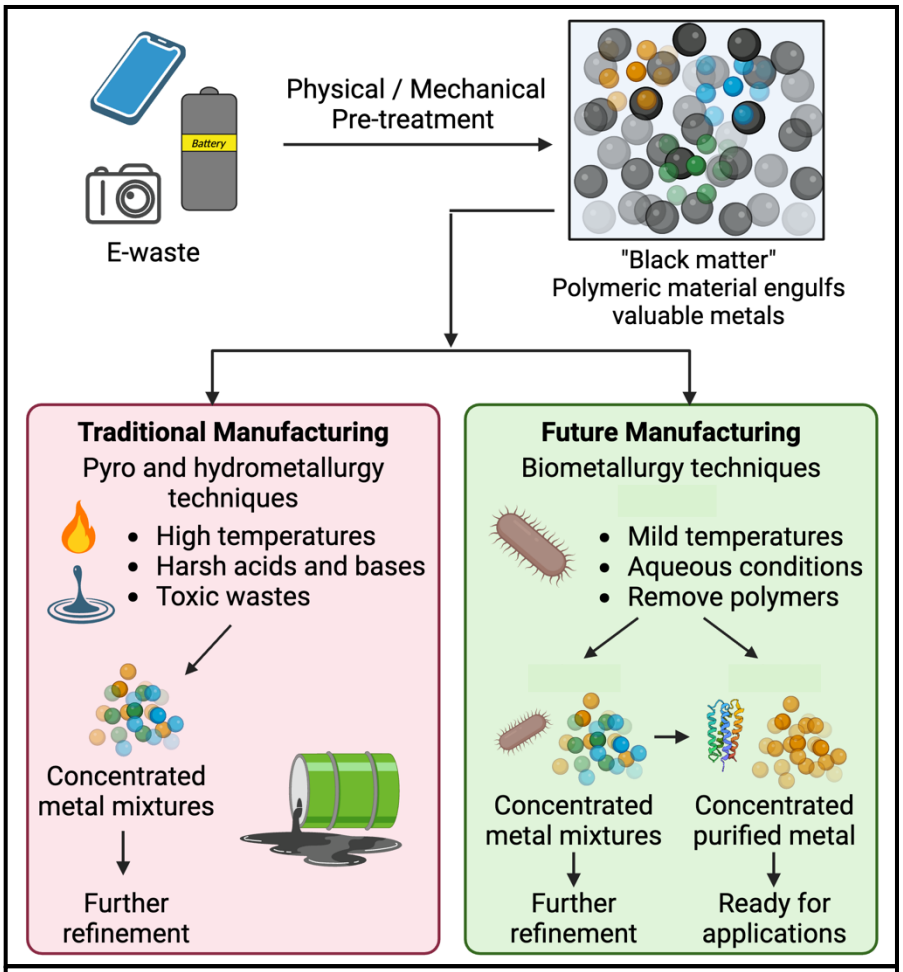

Figure 3. E-waste recycling includes physical/mechanical pre-treatment then traditional manufacturing techniques utilize pyro and hydrometallurgy to recover metal mixtures. In the future, biometallurgy techniques are promising for isolating concentrated and purified metal mixtures. Figure made with Biorender.

Via techniques similar to those discussed in 3a and 3b, researchers in Spain identified a purple acidophilic protein, LigFa.[69] For Aim 3c, I plan to investigate iron-binding LigFa as an optical indicator for REE detection. An ideal REE field-use biosensor will be sensitive (able to detect low levels of REEs), specific (able to discriminate REEs vs. non-REEs), and functional in acidic conditions (as in acid mine drainage). Lanmodulin, a metal-binding protein from methylotrophic bacteria, has been pioneered by the Cotruvo group at Pennsylvania State University as an REE biosensor.[70,71] Lanmodulin has specificity for REEs and

picomolar binding affinity. However, lanmodulin conjugation to a FRET-sensitive group, forming the biosensor LaMP1, is limited to neutral pH conditions and is susceptible to non-specific binding.[70] (Note: another Lamp1 protein for biomineralization of lanthanides has been identified, with similar drawbacks.)[72] With consideration to LaMP1, Featherston *et al.* speculate that stability in acidic conditions is crucial for the success of an REE biosensor, and therefore seek to add optical properties to lanmodulin to contribute synergistically with REE intrinsic luminescence.[70] While the works with lanmodulin are promising, it is not being widely used as a biosensor. Accordingly, I examine LigFa as an alternative biosensor, with the foundation that the protein is tolerant to acidic conditions.

Harnessing photosynthetic cyanobacteria for a carbon-negative biomanufacturing approach

Biomanufacturing with silicatein is a promising pathway for enzyme-mediated nanoparticle production as well as rare earth element recovery. While an enzyme-mediated approach is more environmentally friendly than current nanoparticle production techniques, recombinant production of silicatein in *E. coli* is imperfect. Yeast and cyanobacteria are well-established chassis in biotechnology for genetic and protein engineering.[73–75] Both yeast and cyanobacterial systems are capable of implementing post-translational modifications,[76] which can aid in the solubility and stability of the target protein. Furthermore, cyanobacteria perform photosynthesis as part of their endogenous metabolic processes, which makes them attractive from a resources standpoint – less carbon needs to be added as sugar since cyanobacteria utilize CO_2 for their carbon source.[77] As cyanobacteria consume CO_2 via photosynthesis, they produce oxygen. The consumption of greenhouse gas and production of oxygen is an attractive bonus for implementing recombinant protein in cyanobacteria. In this way, biomanufacturing can be made to be carbon-negative.[73]

Another attractive quality of cyanobacteria is the diversity of strains and environmental adaptations.[73,74] There are thousands of cyanobacterial strains that have unique adaptations for austere environments, which may be promising for applications to waste streams such as acid mine drainage and e-waste. While acid mine drainage and e-waste are two examples of austere conditions for biological applications on earth,

cyanobacteria have also shown promising survival in outer space.[78–81] The value of cyanobacteria in biotechnology increases significantly with possibilities for application in outer space, as yeast and *E. coli* do not seem to be good candidates for the associated austere conditions. Here, our primary goal is to translate silicatein recombinant expression to cyanobacteria for a carbon-negative biomanufacturing approach with the added benefit that implementing a cyanobacterial expression system has far-reaching potential. All cyanobacteria work described here was done at the Life Sciences Research Center of the United States Air Force Academy.

Engineering biosilicification for biocementation applications

In majority of this work, silicatein engineering is targeted towards REEs for materials manufacturing and critical mineral extraction applications, however, silicatein biomineralization with native substrate silica may be promising to address another geobiological challenge. Both erosion and increasing levels of greenhouse gases can be tackled with biocementation. Biocementation is the biomanufacturing of cement which is most commonly achieved via microbially induced calcite precipitation (MICP). MICP harnesses the ureolytic properties of select microbes to break down urea for the production of ammonium and carbonate ions (in stable forms: ammonia and carbonic acid). In soil, carbonate ions then react with calcium cations yielding a solid calcium carbonate precipitate. Calcium carbonate precipitate functions to "cement" soil or sand particles together.

MICP with ureolytic *S. pasteurii* has been extensively studied for erosion mitigation, historical preservation, building, and construction applications.[82–87] A major drawback to MICP is the production of ammonium and carbonate ions and their longevity in the environment. Excessive ammonia can cause environmental harms such soil toxicity and eutrophication.[88,89] Thus, in an effort to mitigate erosion, MICP inadvertently contributes to pollution. Another drawback to MICP is the significant amount of added calcium required – with some studies reporting up to 28 w/v% added calcium necessary.[90–92]

For field applications spray, trench, and wicking techniques are used.[93] To achieve sufficient coverage with spray solutions, all vegetation is cleared from the treatment area prior to MICP application.[93] The challenges associated with this are two-fold: first, vegetation plays a key role in mitigating erosion, therefore if vegetation needs to be removed to apply erosion control via MICP the benefits are accompanied by significant costs, and second, if vegetation is left intact, the high levels of ammonia and carbonic acid produced via MICP may negatively impact plant health. Following several successive treatments the laboratory-scale challenge of column "clogging" manifests as the formation of surface crusts.[93]

Overall, although biocementation via MICP has been the subject of many studies, there are several areas for improvement. Here we propose a biocementation pathway via biosilicification, where-in surface-displayed silicatein biomineralizes the naturally abundant silica species in soil or sand (Fig. 4).[94–96] With this strategy, the need to add significant amounts of substrate is eliminated. Furthermore, biosilicification with silicatein does not produce ammonia and carbonic acid by-products, eliminating further environmental pollution as a byproduct of the process.

In our collaboration with the United States Air Force Academy, biocementation via biosilicification is further motivated by the possibility of applications in space. Space exploration and colonization is currently limited by transportation costs, with simplified estimates from NASA concluding that each added kilogram of cargo launched into low earth orbit has a cost of $4,990.[97,98] With this in mind, we can estimate the cost of sending 20,000 kg of concrete (enough for a 1,000 sq ft building) into space as $100 million. The calcium chloride required to perform MICP for 20,000 kg of Martian soil substrate is roughly 5,600 kg resulting in a cost of $28 million. These estimates are low – as the cost of launching cargo to Mars will be greater than the cost to launch into low earth orbit – and simplified, as additional materials are required to activate concrete and additional materials (bacterial cultures, urea, etc.) are required for MICP. Nonetheless, these estimates provide some perspective on the extreme costs of building in space and motivate the need for less expensive alternatives. *In situ* resource utilization (ISRU) describes the practice of using resources that

are naturally occurring at a given site for the desired applications.[99] In the case of Mars, martian regolith is the naturally abundant "sand" covering the surface of the planet and is composed of approximately 60% silica species.[100] Applying a biocementation via biosilicification strategy here, with ISRU principles of martian regolith as silica source has the potential to enable building in space.

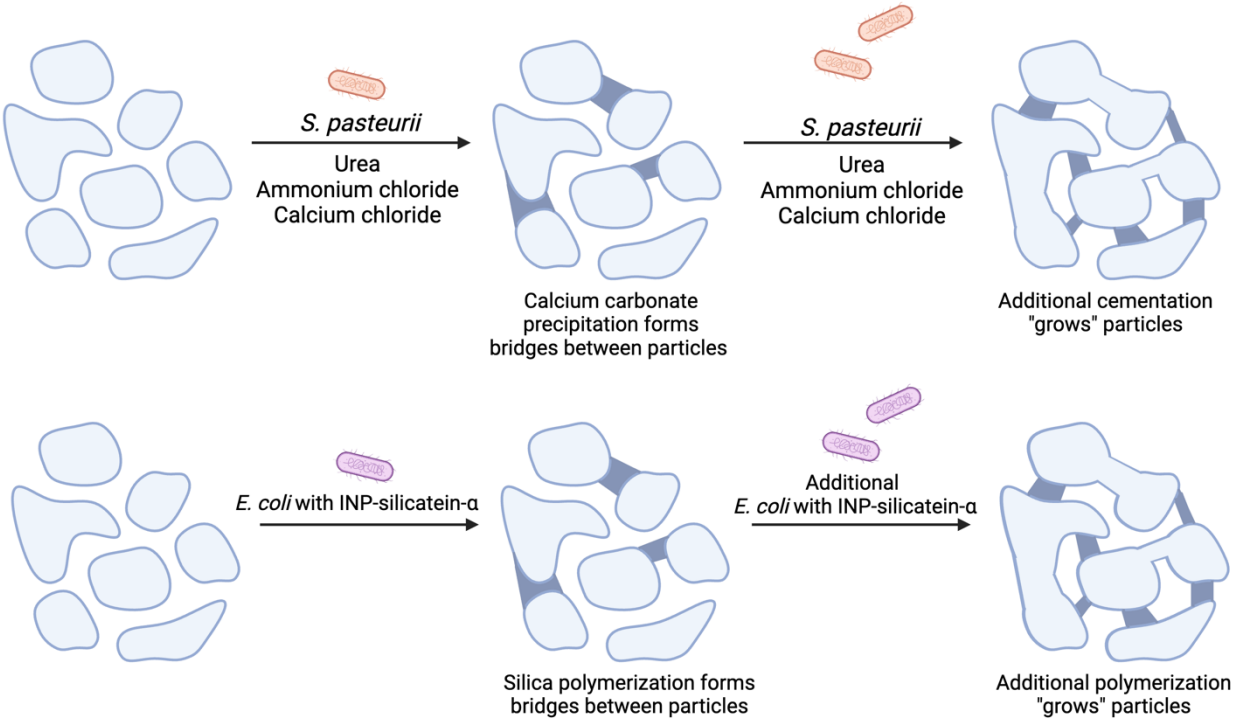

Figure 4. A comparison of MICP with *S. pasteurii* and the proposed mechanism for biocementation via biosilicification with *E. coli* INP-silicatein. Soil particles are initially unbound and have minimal compressive strength. A) MICP with the addition of *S. pasteurii,* urea, ammonium chloride, and calcium chloride leads to calcium carbonate precipitation, cementing particles together. Additional treatments lead to additional particle "growth." B) Addition of *E. coli* INP-silicatein leads to the polymerization of silica species, forming bridges between particles and "growing" aggregate size. Further treatments strengthen these connections by inducing further polymerization. Figure made with Biorender.

Chapter 1: Understanding the biomineralization mechanism and kinetics of silicatein

**Portions of this work are described in manuscript "Understanding the relationships between solubility, stability, and activity of silicatein" and "Directed evolution of silicatein reveals biomineralization synergism between protein sequences"*

Key Findings

- Silicatein biomineralization activity is not impacted by fusion partner
- Directed evolution with survival-based selection for silicatein leads to genetic mosaicism
- Truncated silicatein mutants retain biomineralization activity
- Silicatein tolerates a multitude of sequence changes yet retains biomineralization activity
- Low-complexity intrinsic disorder within the polyS region is not the sole mechanism for biomineralization activity
- Most single site-directed mutagenesis does not result in significant changes to ceria biomineralization activity

Silicatein may be a valuable biosynthetic tool for nanoparticles at an industrial scale, but thus far has been hindered by solubility and kinetics. In order to address silicatein solubility and activity, I aim to ***1a)*** improve silicatein solubility via addition of eGFP-fusion tag, ***1b)*** perform directed evolution of silicatein to highlight important domains/motifs for biomineralization while creating a more efficient enzyme, and ***1c)*** manipulate intrinsically disordered regions in silicatein to promote biomineralization.

Aim 1a

Hypothesis: Improved silicatein solubility via addition of an eGFP fusion tag will lead to increased biomineralization yields.

Approach: Silicatein solubility has been a challenge throughout the field since the enzyme's discovery in marine sponges in 1999.[27] A variety of silicatein fusion proteins have been produced, although the most soluble to date is Trigger Factor silicatein (TF-silicatein), which can be produced in micromolar quantities.[47]

In order to further study the mechanism and kinetics of silicatein, a variant with improved solubility and stability would be ideal. I hypothesized that increased enzyme solubility is crucial to improve overall reaction kinetics, thus resulting in greater biomineralization. Improving enzyme solubility is a common first approach in protein engineering for increasing enzyme activity. In a scenario where substrate concentration is in great excess, enzyme solubility is a target property for optimization. With greater enzyme solubility, the overall yield of a target compound will also increase.[101,102] Here I selected eGFP as a fusion tag to improve solubility and stability, as well as confer a visible signal indicative of protein stability, as previously illustrated by Waldo, *et al.*[45] With an eGFP solubility tag, fluorescence would be indicative of proper silicatein folding and would therefore suggest available enzyme activity.[45]

Strategies and Results:

TF-silicatein and eGFP-silicatein were produced side-by-side via recombinant protein expression in *E coli* and purified via immobilized metal affinity chromatography. For eGFP-silicatein, fluorescence intensity was noted from production within the cell to purification, with varying and limited results.

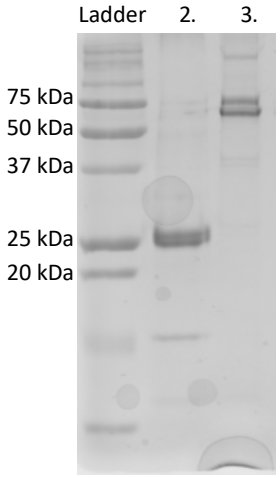

Figure 1A-1. SDS-PAGE for purified silicatein fusions. 2. eGFP-silicatein (52 kDa) and 3. TF-silicatein (75 kDa). GFP-silicatein sample exhibits a prominent band at approximately 25 kDa, identified by mass spectrometry as chaperone DnaK binding domain.

Following purification, I characterized TF-siliicatein and eGFP-silicatein with SDS-PAGE, Native PAGE, and biomineralization activity assays. For TF-silicatein, SDS-PAGE results were consistent with previous works, with a

prominent band at 75 kDa (Fig. 1A-1). As shown in Figure 1A-1, eGFP-silicatein does not appear at the expected MW of 52 kDa but does show a prominent secondary protein at ~26 kDa. Mass spectrometry was used to identify this protein as *E coli* chaperone DnaK, whose binding domain is 26 kDa. The over-production of DnaK suggests that eGFP-silicatein is very difficult to fold and therefore requires extra help from chaperones.[103] Although eGFP fluorescence was intended to serve as an optical indicator of eGFP-silicatein, purified eGFP-silicatein does not exhibit notable fluorescence. However, while no fluorescence was evident, biomineralization activity was intact. Work by Martinez-Alonso *et al.* notes that GFP quenching occurs in the presence of high levels of DnaK.[104] Since eGFP was selected as a fusion partner in part for fluorescence to serve as a signal of protein folding, this is a significant event to note.

eGFP-silicatein quaternary structure was analyzed via native PAGE, which shows the full size of the folded protein structure. Purified eGFP-silicatein was seen at ~150 kDa (Fig. 1A-2), which points to oligomerization of the eGFP-silicatein monomer. TF-silicatein appears at approximately 75 kDa, which is true-to-size for the monomer. A special monomeric GFP variant (msGFP2) was introduced to examine if oligomerization is silicatein-driven or eGFP-driven. msGFP2-silicatein appeared at ~150 kDa like eGFP-silicatein, suggesting that oligomerization is silicatein-driven. Disulfide bonds were reduced and blocked to highlight their contributions to oligomerization activity: eGFP-silicatein increased in size from 150 kDa to 250 kDa, msGFP2-silicatein decreased from 150 kDa to 100 kDa, and TF-silicatein increased in size to approximately 150 kDa. When disulfide bonds are disrupted, silicatein oligomerization is influenced more significantly by hydrophobic properties and fusion partner.

Furthermore, the biomineralization activity of the eGFP-silicatein oligomer was confirmed via a specially designed native page assay, wherein the gel is incubated in ceria ammonium nitrate precursor compound and then imaged to view ceria conglomeration corresponding with the eGFP-silicatein oligomer band (Supplemental Fig. 1).

In order to compare activity between silicatein fusions, biomineralization assays for TF-silicatein and eGFP-silicatein with commonly used precursor tetra-ethyl orthosilicate (TEOS) were conducted side by side. TEOS is a popular precursor compound because it reflects activity with native silicon-containing substrates, effectively reproducing biosilification with marine sponges. Via quantification with a colorimetric silicomolybdate assay, TF-silicatein and eGFP-silicatein produced comparable levels of silica to each other. It should also be noted that biomineralization yields for TF-silicatein here are comparable to those reported in other works, but nanosilica production it still very small (<0.04%).[47,47,48] Although these experiments with TEOS biomineralization reflect literature results, biomineralization with TEOS is convoluted by TEOS autohydrolysis and overall low biomineralization yields. Analyzing improvements and changes to biomineralization yields this low would thus require very precise and specific experimentation. However, Curran, *et al*. show silicatein biomineralization with ceria ammonium nitrate as precursor.[28] Ceria ammonium nitrate is highly water soluble, has limited auto-hydrolysis, and biomineralization to ceric oxide produces an insoluble precipitate.[105] Furthermore, biomineralization with

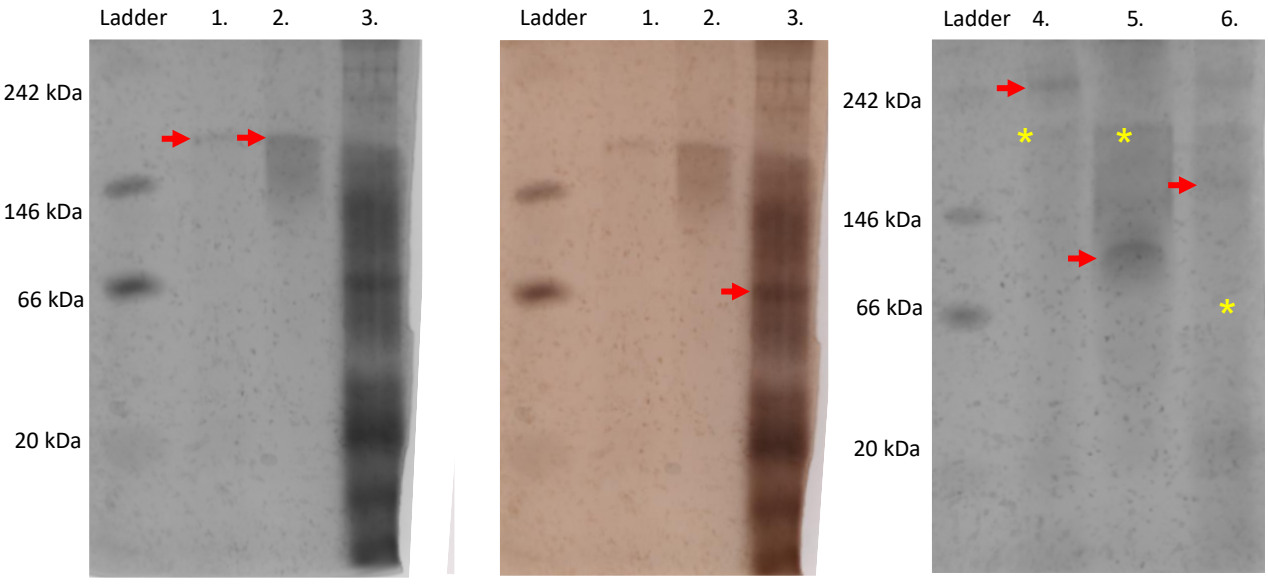

Figure 1A-2. Silver-stained Native PAGE gel shows *in vitro* protein interactions. 1) eGFP-silicatein, 2) msGFP2-silicatein, and 3) TF-silicatein under native conditions. The same gel is shown in color to allow for easier viewing of the TF-silicatein band. 4) eGFP-silicatein reduced with BME and thiol-blocked, 5) msGFP2-silicatein reduced with BME and thiol-blocked, 6) TF-silicatein reduced with BME and thiol-blocked. Yellow asterisks highlight the approximate locations of non-reduced protein bands, for easy reference.

ceria shows much greater yields than biomineralization with silica, and therefore presents as a more favorable platform for comparing biomineralization efficiencies between fusion proteins. A comparison of silica and ceria mineralization is shown in Fig. 1A-3, each measured via colorimetric assay.

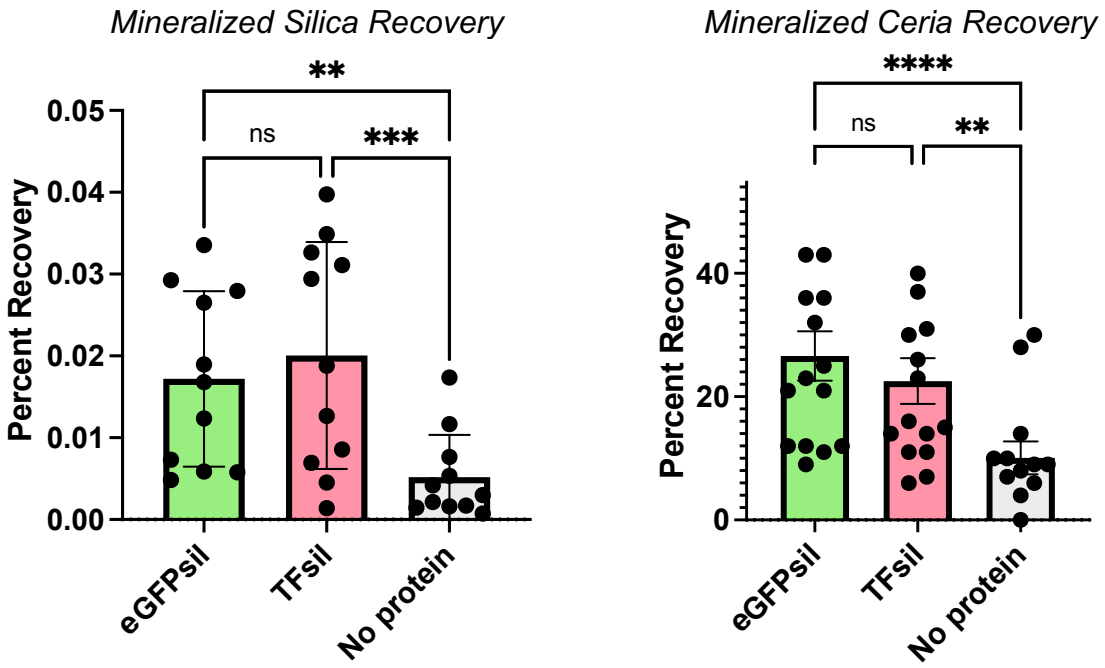

Figure 1A-3. Biomineralization of silica and ceria with silicatein fusions. Silica recovered following biomineralization with eGFP-silicatien and TF-silicatein was quantified between 0.005 and 0.04%. Biomineralization with ceria allows for much greater percent recovery, in the 20-40% range. Two-way ANOVA, p values **<0.001,***<0.0002, ****<0.0001

Biomineralization of ceria ammonium nitrate to nanoceria was characterized with x-ray diffraction with no obvious differences in crystallinity of nanoceria produced by the different silicatein fusions (Supplemental Fig. 2). Furthermore, with quaternary structure of silicatein fusions disrupted and blocked (disulfide bridges, as in Fig. 1A-2), no changes were observed in nanoceria produced.

Summary

The addition of an eGFP fusion tag to silicatein did not improve enzyme solubility or biomineralization yields. However, via a specialized native PAGE analysis, I identified an eGFP-silicatein oligomer at 150 kDa that interacted with ceria, from which I postulate that this interaction is representative of biomineralization activity. Silicatein oligomerization is mediated in part by intra- and intermolecular disulfide bridges, with fusion proteins contributing a limited role.

Traditional biomineralization assays with TEOS highlighted constant biomineralization activity, even though the fusion did not improve stability or solubility. Although silica is the native substrate/product of silicatein biomineralization, analysis with silica experiments is limited due to poor solubility and autohydrolysis. Here, I measured biomineralization activity with ceria, followed by quantification with an arsenazo-III colorimetric assay. Experimentation with ceria instead of silica allows us to evaluate changes at a larger scale, requiring less precise quantitation for analysis (*i.e.* the difference between 10 and 20% is easier to observe than the difference between 0.01 and 0.04%).

From this work with silicatein fusion tags, I conclude that any desired improvements to biomineralization need to be accomplished via intrinsic manipulation of the enzymes – understanding enzyme mechanism, kinetics, role of domains / motifs. Intrinsic manipulation of silicatein is described in Aim 1b and 1c.

Publication: Vigil, T. N.; Rowson, M.-J. C.; Frost, A. J.; Berger, B. W. Understanding the Relationships between Solubility, Stability, and Activity of Silicatein. *Mater Adv* **2023**, *4* (2), 662–668. https://doi.org/10.1039/D2MA00938B.

Aim 1b

Hypothesis: Directed evolution to form a silicatein mutant library, screened for survival to ceria will highlight important roles of domains/motifs for biomineralization activity.

Approach: Little is understood about how silicatein's structure and sequence impact enzyme function, severely limiting rationale-based protein modifications. Accordingly, a random mutagenesis approach was chosen for directed evolution. I generated a silicatein library via error-prone PCR with dNTP analogues, followed by survival screening in BL21 *E. coli* exposed to toxic levels of ceria. Error-prone PCR with dNTP analogues can have a rate of up to 20% mutagenicity,[106] which is favorable since I want to generate a huge variety of random mutants. The screen is based on survival to toxic levels of ceria ammonium nitrate (CAN), a precursor compound for silicatein biomineralization. Survival to high concentrations of CAN is indicative of protein function: biomineralization of toxic ceria to insoluble and non-toxic nanoceria will save the cells, therefore I selected mutants that conferred survival to otherwise toxic levels of ceria. The selected mutants were then sequenced and characterized.

Strategies/Techniques:

Design of screen

The library screen was designed with rationale that CAN is toxic to *E. coli*, however, when biomineralized via silicatein the non-toxic nanoceria product will result in *E. coli* survival. This screen was first designed with the eGFP-silicatein fusion protein, with rationale that GFP would serve as a fluorescent indicator of silicatein presence and efficacy. I established critical concentrations of CAN toxic to BL21 *E. coli* for two cases: pet28 vector only, and pet28 vector with eGFP-silicatein. BL21 *E.* coli with pet28 plasmid vector allows for T7 transcription of the protein and subsequent high production,[107] so the pet28 eGFP-silicatein condition will have high levels of protein. With the zero CAN dose, the vector only and silicatein conditions had the same CFU. At low CAN (0.6 mM), the vector only cells had higher survival than cells with

silicatein. This finding is consistent with previous reports that low levels of rare earth elements actually confer greater survival to cells by disrupting the membrane sufficiently to allow additional nutrient uptake.[108] However at high CAN (1.25 mM and above), pet28 eGFP-silicatein conferred greater survival than the pet28 vector only condition, as exhibited with 2x CFU (Fig. 1B-1). Here, 1.25 mM is the critical concentration for which silicatein confers greater survival, and therefore the threshold for success in our survival assay. There are reports of CeO_2 toxicity to E coli,[109] however, nanoceria toxicity via our survival screen protocol was examined, with CFU not impacted by nanoceria (Supplemental Fig. 3). These results support our hypothesis that *E coli* survival will be indicative of silicatein biomineralization.

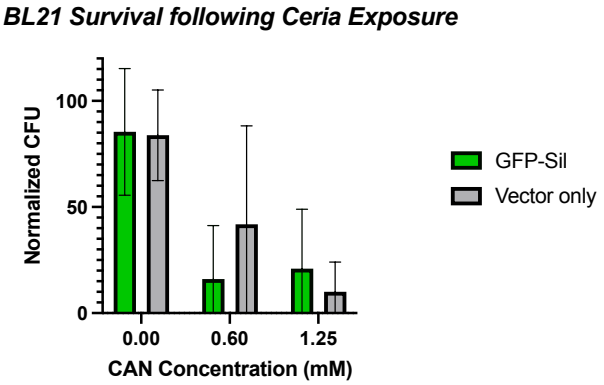

Figure 1B-1. BL21 *E coli* survival following ceria exposure. Conditions are with eGFP-silicatein, and without.

Although the eGFP-silicatein fusion protein did not exhibit improved solubility, I hypothesized that the eGFP-silicatein fusion protein would allow for quick screening of our library mutants via GFP fluorescence, with the rationale being that GFP fluorescence is indicative of increased mutant stability. Noting that DnaK quenches GFP fluorescence, this rationale can be extended to increased GFP fluorescence indicative of less DnaK overexpression, and therefore an easier to fold protein. As a preliminary sweep, library mutants that survived the high CAN condition were grown in autoinduction media overnight, then read for fluorescence (Fig. 1B-2). Sequencing of these mutants revealed that high GFP performance is not indicative of greater mutant stability, in fact high GFP fluorescence was often associated with no silicatein presence. High GFP fluorescence in the absence of silicatein is consistent with overexpression of DnaK (due to silicatein folding) resulting in fluorescence quenching. Therefore, the absence of silicatein results in the absence of DnaK and then high GFP fluorescence. These findings show that there are no fluorescence associated

benefits to using eGFP-silicatein as opposed to TF-silicatein for library generation and screening. Therefore, GFP fluorescence will not be used as an additional selection mechanism for our screen.

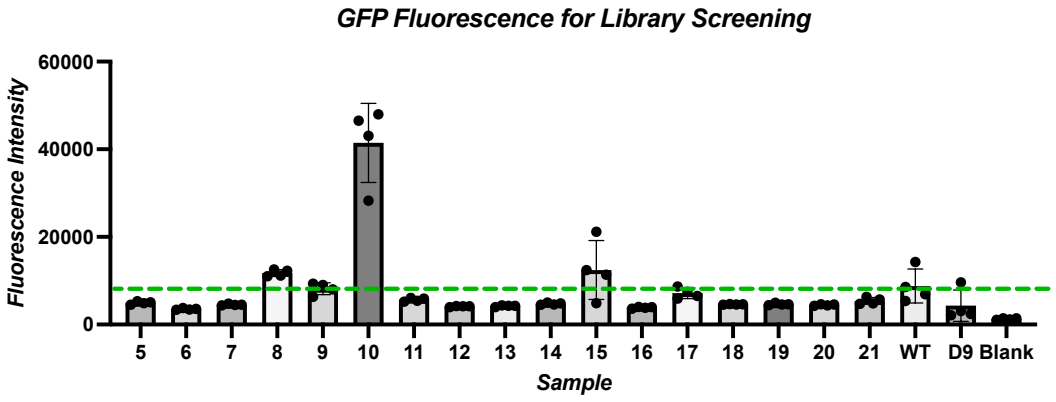

Figure 1B-2. GFP fluorescence for library screening. Samples with greater fluorescence than the WT were hypothesized to be eGFP-silicatein mutants with greater solubility and stability. D9 was a previously identified eGFP-silicatein mutant. Sequencing showed #10 and #15 were GFP *without* silicatein, and #5 as an eGFP-silicatein mutant.

Instead, moving forward, TF-silicatein is used as the template for library generation in combination with a CAN toxicity/survival-based screen. TF-silicatein confers greater survival to *E coli* than a vector only control, with TF-silicatein mutants showing additional increased survival (Fig 1B-3).

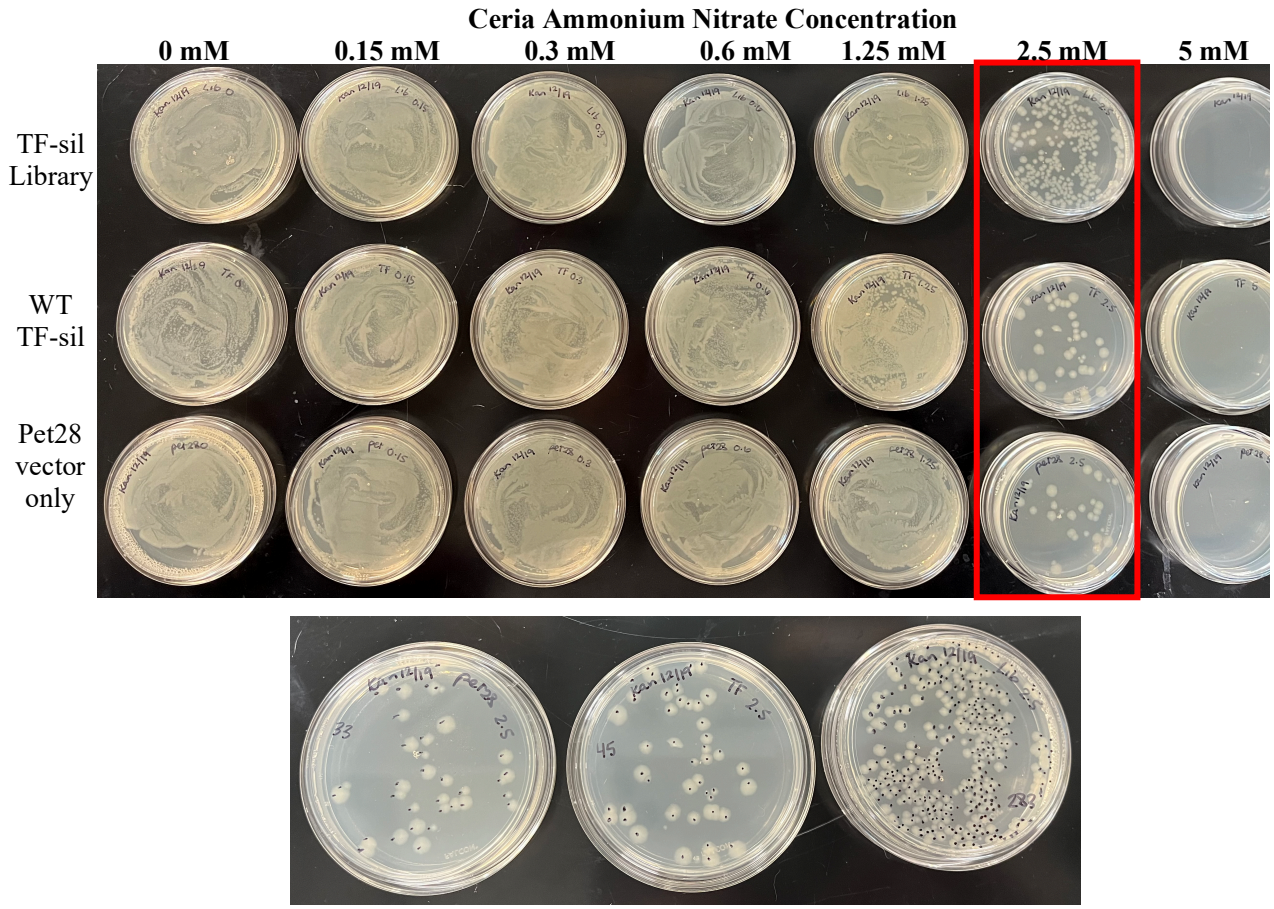

Figure 1B-3. Establishing toxic concentration of ceria ammonium nitrate. *E. coli* with pet28 vector only, WT TF-silicatein, and TF-silicatein library. Notable differences in *E. coli* survival occur at 2.5 mM ceria ammonium nitrate, boxed in red. A closer view of 2.5 mM ceria ammonium nitrate is shown, with 33, 45, and 288 colonies at pet28 vector only, WT TF-sil, and TF-sil library respectively.

Library generation

Previous work by Bawazer, et al. (2012) implements directed evolution via DNA shuffling of silicatein alpha and silicatein beta.[43] In the aforementioned work, only two full-length mutants were identified and in each the catalytic triad residues were conserved. Many truncated silicatein mutants were also observed. Due to the inconclusive results surrounding the catalytic triad hypothesis, and with limited structure and function understanding surrounding silicatein, this work utilizes a random mutagenesis approach to directed evolution. Directed evolution via random mutagenesis is an established approach to probe protein structure and function, with the ultimate goal of improving protein function.[106] Error-prone PCR with dNTP analogues has up to 20% mutagenicity, which is significantly greater than other random mutagenesis

techniques.[106] Basic PCR amplification mathematics, accounting for error-prone conditions, estimates a total library of $1x10^6$, with $9.85x10^5$ full length mutants and a mean number of amino acid changes of 3 per mutant.[110]

Sequencing and characterization

Common wisdom in microbiology suggests that each colony will be isogenic, however, recent studies have shown that co-transformation events, where-in multiple different plasmids co-exist within the same colony are more common than previously supposed. Works by Goldsmith, et al. and Tomoaiga et al. highlight the little known prevalence of multiple transformation events, contrary to the widespread myth that a single bacterial colony is isogenic.[111,112] These works note that up to 11 different plasmids may be expressed within a single colony, and suggest two different approaches to mitigate these occurrences: 1) transform very small amounts of DNA (ng), and 2) iterative clone isolation.[111,112] Goldsmith, et. al report that with 50 ng of DNA there is less than 0.1% occurrence of double or multiple transformations.[111] In this work, a maximum of 12.5 ng were transformed each time, so the probability of double transformations randomly occurring is less than 0.1%. If a preventative approach to avoid

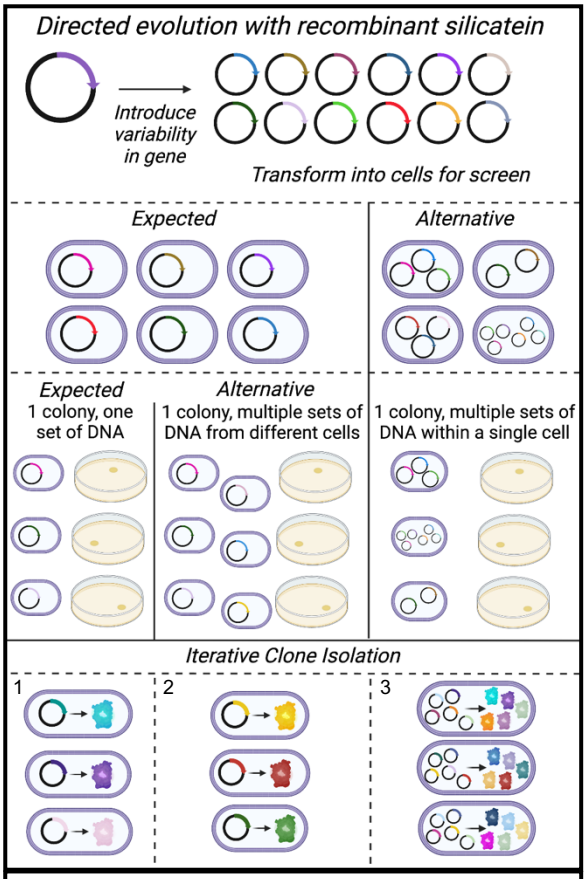

Figure 1B-4. Expected and alternative outcomes of the experimental procedure surrounding directed evolution with recombinant silicatein are shown. The expected outcomes are consistent with traditional microbiology wisdom. Alternative scenarios have been documented in literature, however, remain rare. The three potential outcomes following interative clone isolation are shown, with 1 and 2 being one set of DNA associated with each colony, and 3 showing multiple sets of DNA coinciding. Figure made with Biorender.

multiple transformations is not effective, iterative clone isolation can be used to disentangle the many plasmids present.

The different scenarios for co-transformation are shown in Figure 1B-4. In one scenario, cells within a colony contain different DNA, however each singular cell contains only one set of DNA. In this case, DNA can be isolated via iterative clone isolation. In another scenario, each cell within a colony contains multiple sets of DNA. Here iterative clone isolation will not enable the separation or isolation of a single set of DNA. For practical purposes, this means that with DNA isolation there will be multiple plasmid sequences and therefore Sanger sequencing will generate multiple results. The abundance of results makes a singular sequence difficult to identify, and with repeated sequencing attempts, multiple sequences will result.

In most libraries, after selection and sequencing, sequence alignments can be interpreted looking for common trends within the library associated with specific outcomes. However, the multiple sequences that result with each mutant makes this difficult to do, with the potential to confound results. With consideration to our library generation and screening procedures, I proceeded with iterative clone isolation. In cases where multiple transformations result due to the conglomeration of multiple cells with a unique plasmid into a single colony (*i.e.* two cells each with a unique plasmid join to form one colony) iterative clone isolation will function to isolate a single unique plasmid (as shown in case 2, Fig. 1B-4).

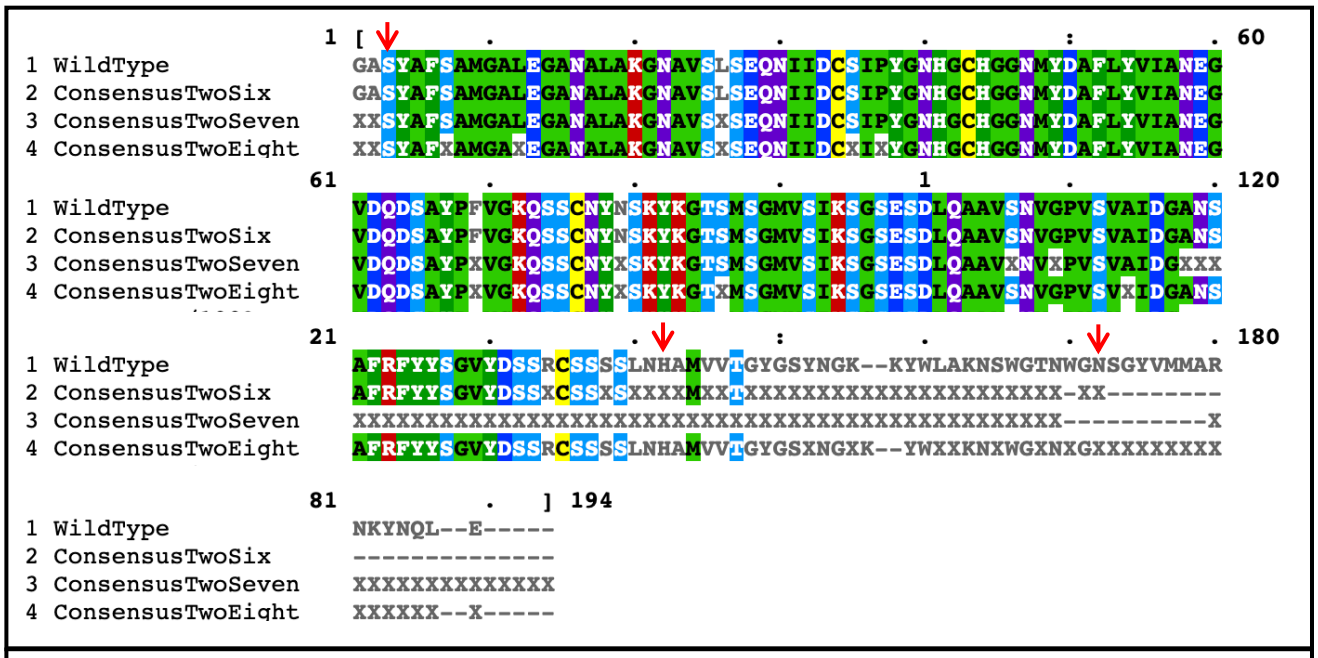

Figure 1B-5. Sequence alignment for WT compared to >80% consensus sequences for 2.6, 2.7, and 2.8. Deviations from WT sequence are not colored. Consensus with WT are colored according to ClustalX amino acid properties. "X" refers to non-specific amino acid. Catalytic triad residues are indicated with red arrows. Sequence alignments prepared with EMBL-EBI 2022.

With up to eight repeated rounds of iterative clone isolation, no singular plasmid was able to be isolated (all Supplemental Figures S.2B). An 80% consensus is necessary to compare mutant families overall with WT TF-silicatein (Fig. 1B-5). Failure of iterative clone isolation is consistent with case 3, where-in multiple plasmids were transformed into a singular cell resulting in the co-expression of multiple different proteins. In nature the co-expression of multiple versions of a single gene is known as genetic mosaicism. Interestingly, genetic mosaicism naturally results from somatic mutations – referring to cells in the reproductive system.[113] Therefore, our library has artificially induced genetic mosaicism as a survival response.

Studies of marine corals show genetic mosaicism as an adaptation to the changing environment associated with climate change.[114,115] Our survival assay is similar to the evolutionary pressure of climate change, in the sense that survival is predicated on adaptation. Some researchers postulate that this genetic variation is already present in some marine organisms, but does not become prominent without pressure.[115] This is

known as cryptic genetic variation, i.e. genetic variation is occurring in the background, preparing the organism for survival challenges but not apparent until those challenges occur.[115] The mutant families associated with our library is the co-expression of each genetic variant that helps *E. coli* survive the otherwise toxic concentrations of ceria ammonium nitrate.

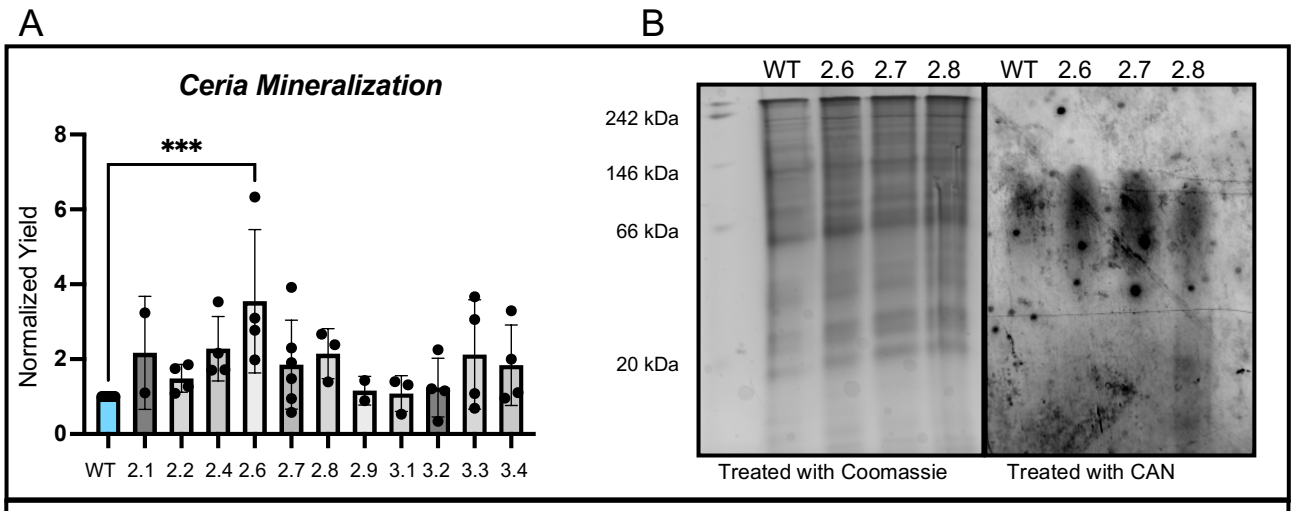

Figure 1B-6. A. Ceria mineralization of wild-type and mutant TF-silicateins in whole cell lysates, normalized to the production of WT. Each sample normalized by total protein concentration. Additional details in Materials and Methods. Two-way ANOVA, n > 2, *** P<0.001, **B.** Specialized Native PAGE of wild-type and mutants 2.6, 2.7, 2.8. correlating protein size with biomineralization activity. Specific details in Materials and Methods. In both panels, whole cell lysate samples were normalized by total protein concentrations as determined by standard Bradford assay.

It is also worthwhile to consider the variations of silicatein in nature amongst difference genus and species of sponges. Supplemental Fig. S.1B-5 shows sequence alignments for silicatein from *T. aurantia, H. okadai, L. baicalensis, P. ficiformis,* and *S. domuncula.* A direct comparison of protein sequences shows the lowest percent identity at 54% between *T. aurantia* and *P. ficiformis*, with a percent similarity of 71%. As silicatein from both *T. aurantia* and *P. ficiformis* are used for silica biomineralization *in vitro*, overall sequence flexibility is supported. Interestingly, the catalytic triad residues are mostly conserved amongst silicatein from different sponges, which contributes to the attractiveness of the catalytic triad theory. Catalytic triad residues are mostly conserved in the library as well, with the exception of truncated mutants (Fig. 1B-5).

Biomineralization of ceria with whole cell lysates reveals significantly higher nanoceria yields with mutant 2.6 relative to the WT TF-silicatein ($p<0.001$) (Fig. 1B-6). Native PAGE analysis qualitatively shows greater biomineralization activity associated with 2.6 and 2.7 than with WT (Fig 1B-6). Furthermore, Native PAGE reveals potential dimerization associated with the mutant, as biomineralization active proteins appear spanning between molecular weights of approximately 75 – 150 kDa. These data are consistent with the anticipated biomineralization associated with silicatein mutants and suggests that mutant 2.6 has intrinsic properties that increase biomineralization.

Mutants 2.6, 2.7, and 2.8 were examined further to compare overall protein expression to that of WT TF-silicatein. With an immunoblot targeting the hexa-histidine tag, cell lysates were normalized for total protein concentration via Bradford assay. The 1x total protein concentration of TF-silicatein shows abundant signal, with no comparable associated with the mutants. Two-fold serial dilutions of WT TF-silicaetin at 1/2x, 1/4x, and 1/8x also appear to show more protein than with mutants. The 1/16x dilution of total protein concentration in TF-silicatein appears to qualitatively match that of mutant 2.6, still exceeding 2.7 and 2.8 (Fig. 1B-7). This illustrates significantly less recombinant protein expression associated with the mutants per total protein in whole cell lysate. Combined with the cell lysate mineralization assays, this shows that greater mineralization is associated with less recombinant silicatein production, suggesting that the intrinsic biomineralization of silicatein mutants is fundamentally greater than that of the WT.

Importantly, the SDS PAGE also shows significant DnaK expression associated with mutant 2.7, which qualitatively appears greater than in WT TF-silicatein and other mutants (Fig. 1B-7). Increased DnaK expression suggests that there is additional difficulty associated with protein folding. In Aim 1a there was increased DnaK expression associated with eGFP-silicatein, however, despite the seemingly poor solubility and instability of the protein, biomineralization activity remained comparable to that of TF-silicatein as

shown in Figure 4. Therefore, the increased DnaK expression associated with mutant 2.7 should not be considered as necessarily detrimental to protein activity. In fact, the instability denoted by DnaK overexpression may contribute to biomineralization mechanisms stemming from alternative nucleation sites.

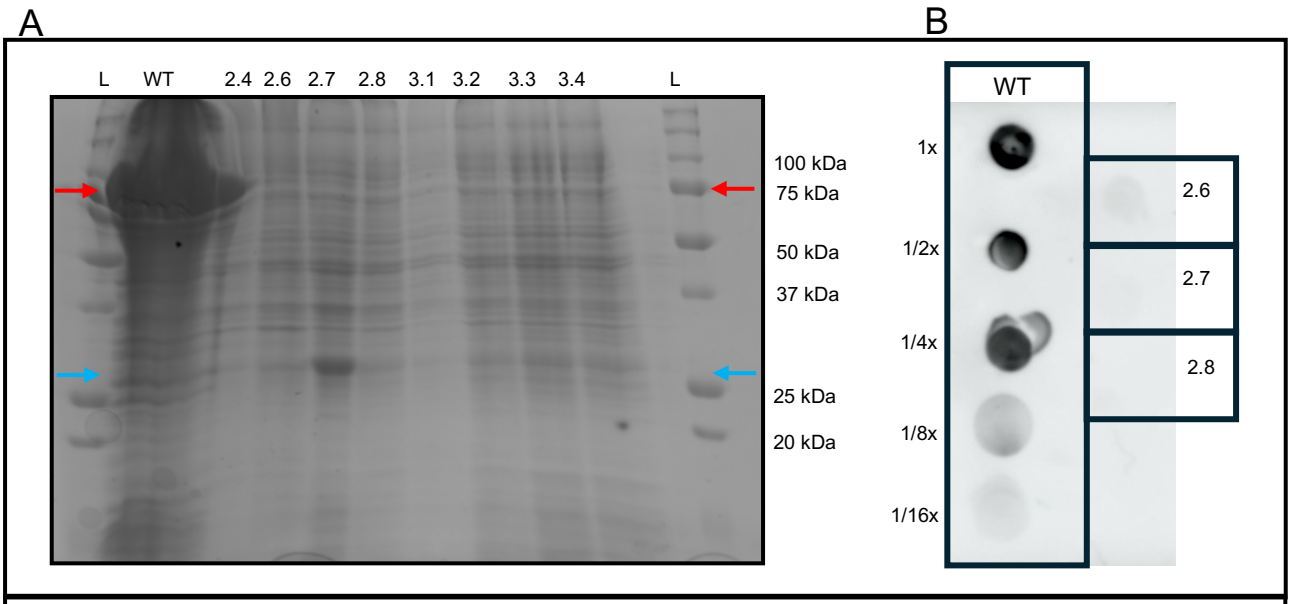

Figure 1B-7. A. SDS PAGE with whole cell lysates. Anticipated molecular weight of TF-silicatein and mutants is 75 kDa, indicated by red arrow. Anticipated molecular weight of DnaK chaperone protein is 26 kDa indicated by blue arrow. **B.** Immunoblot with whole cell lysates. WT TF-silicatein dilutions are shown compared to 1x of mutants 2.6, 2.7, and 2.8.

Taken together, the whole cell lysate biomineralization data (Fig. 1B-6 A) and relative protein expression shown with dot blot (Fig. 1B-7) suggest that the intrinsic biomineralization activity of mutant 2.6 is high despite relatively low expression. In other words, although mutant 2.6 is only made in small amounts, it has sufficient biomineralization activity to produce more nanoceria than the better expressing WT TF-silicatein. With this in mind, the whole cell lysate biomineralization data (Fig. 1B-6 A) and relative protein expression shown with dot blot (Fig. 1B-7) as applied to mutants 2.7 and 2.8 may also suggest high intrinsic activity associated with the mutants, in spite of low overall expression. One caveat, however, is that the dot blot targets the hexa-histidine tag of the protein – for WT TF-silicatein there is a hexa-histidine tag preceding TF then immediately following silicatein. For the truncated mutants this entails that the second hexa-histidine tag is not present and thus the mutant only has the hexa-histidine tag preceding the TF fusion

protein. Altogether, for a sample that has all post-silicatein hexa-histidine tags truncated we would anticipate only half the signal associated with WT TF-silicatein. So although the expression visualized in the dot blot may be slightly skewed for the truncated mutants, the expression remains very low. For

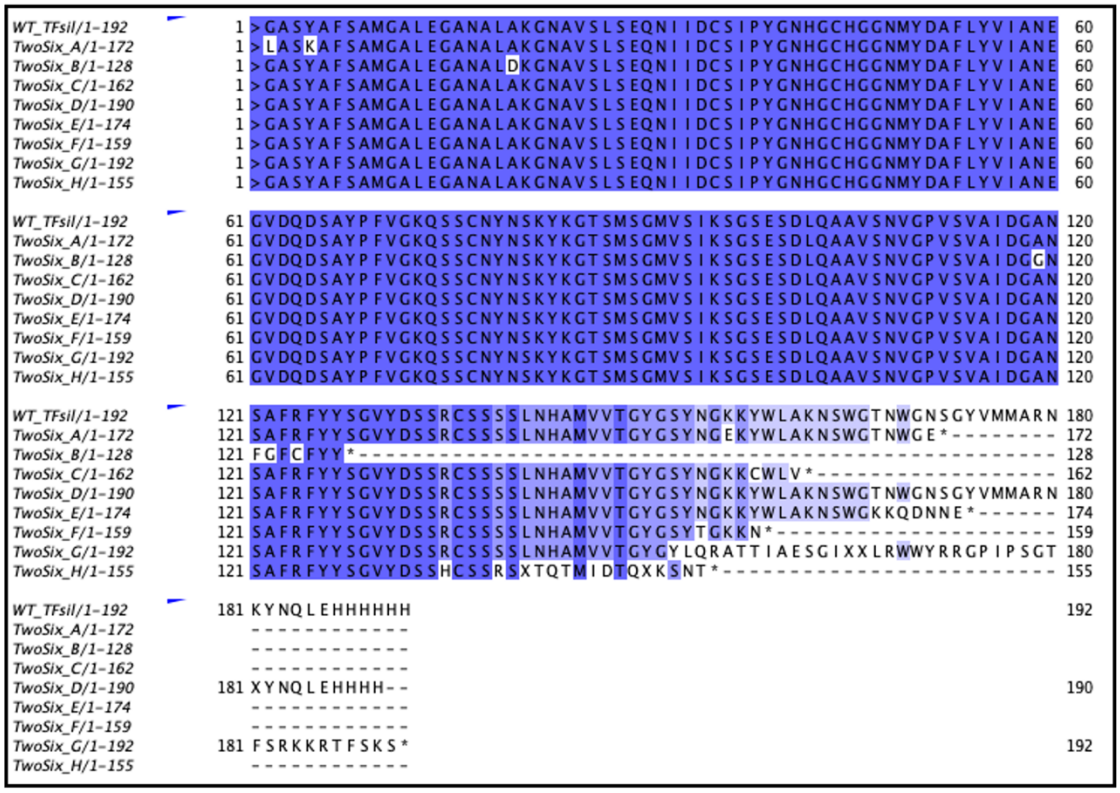

Figure 1B-8. Sequences for mutant family 2.6. Earliest truncation is at AA 128.

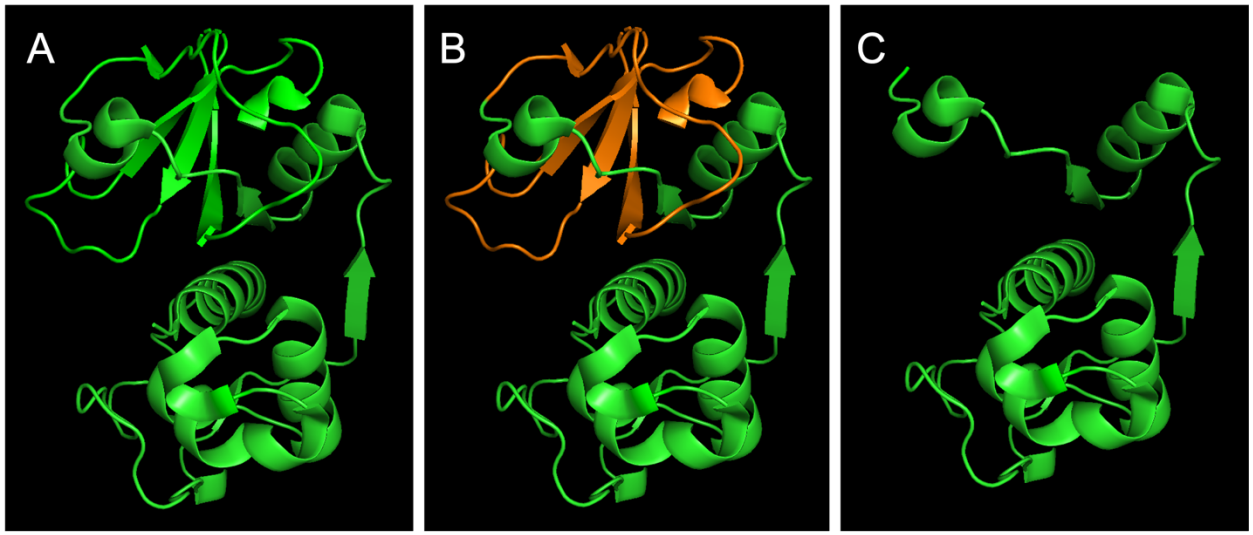

Figure 1B-9. Silicatein structure (PDB 6ZQ3) with A) full length silicatein, B) truncated tail (starting at AA 128) of mutant family 2.6 consensus highlighted in orange, C) truncated tail of mutant family 2.6 invisible.

example, if mutant 2.6 has all post-silicatein hexa-histidine tags truncated the 1/16x expression should be adjusted to 1/8x expression relative to WT.

These findings bring us back to the sequencing conundrum. Since there is not a singular sequence associated with the enhanced biomineralization of mutants, it is impossible to attribute enhanced biomineralization properties with specific amino acid changes. Instead, by setting an 80% consensus threshold, we can see that silicatein mutants are often shorter than the WT TF-silicatein (Fig. 1B-5). In simple cases, a premature stop codon resulting in a truncated silicatein mutant that conferred greater survival suggests the deleted tail was un-important or even detrimental to activity. In this work, however, since a premature stop codon and truncated sequence is not present in all versions of each mutant, we cannot definitively say that the N-terminal of silicatein is un-important.

An examination of mutant family 2.6 shows the earliest stop codon at amino acid 128 (Fig 1B-8). Utilizing the known crystal structure of silicatein (PDB 6ZQ3) we can visualize the early truncation (Fig 1B-9). With this early truncation, an alpha helix and three beta sheets are eliminated. Before attributing increased biomineralization to these changes, it is important to recall that the other proteins from mutant family 2.6 are being co-expressed. Assuming each mutant is co-expressed in equal amounts (which we do not know), then 1/8 the proteins present are truncated at amino acid 128. A more conservative consideration may take into account that only two proteins in mutant family 2.6 are full length, therefore six are truncated. The latest truncation takes place at amino acid 174, which similarly results in the elimination of an alpha helix and two beta sheets.

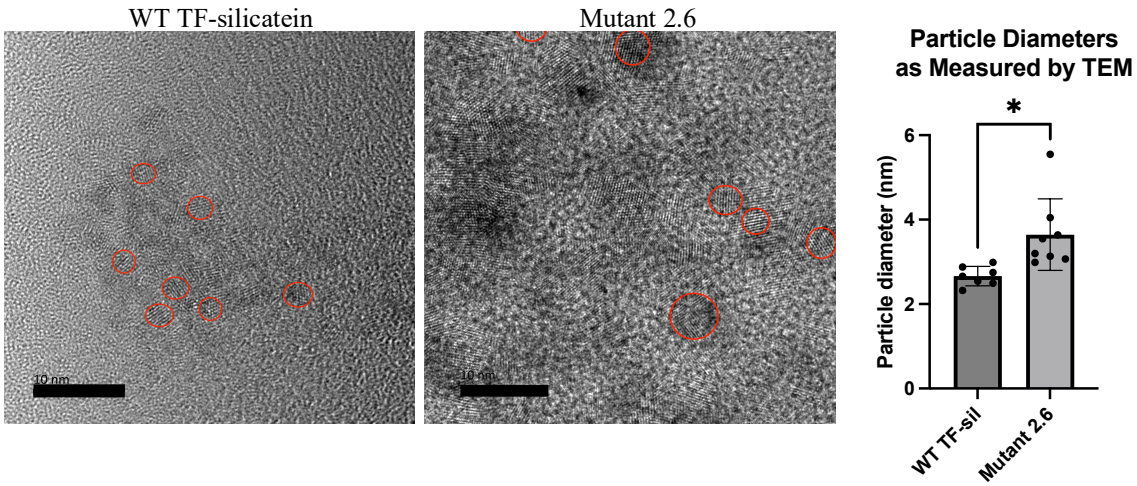

Figure 1B-10. Transmission electron microscopy for particles made with WT TF-silicatein (average diameter 2.5 nm) and mutant 2.6 (average diameter 3.6 nm). A two-tailed unpaired t-test shows that the average particle diameters are significantly different t = 4.202, df = 13, p = 0.01.

The nanoceria made with mutant 2.6 were significantly larger than particles made with WT TF-silicatein as compared with a two-tailed unpaired test (df = 13, p = 0.01) (Fig. 1B-10). Nanoceria mineralized by mutant 2.6 had an average diameter of 3.6 nm as compared to nanoceria made with WT TF-silicatein at 2.5 nm. Consideration of the mutant 2.6 consensus sequence may point to the truncated tail as a contributor to the change in particle size. Figure 1B-9 compares WT TF-silicatein (panel A) with the consensus for mutant 2.6 (panel C), and one can imagine that the openings created by the protein truncations may lead to larger particle growth, i.e. less physical constraint results in larger particles. This is a purely physical hypothesis, it is also possible that the amino acids in the truncated tail played a critical role in guiding particle growth in a more mechanistic manner.

Silicatein Library and the Catalytic Triad Hypothesis

Similar nuance must be observed with the interpretation of the controversial catalytic triad (S26, H165, N185). In the consensus sequences, S26 remains conserved while H165 and N185 tend to be more variable, especially with sequence truncations. Interestingly, amino acids adjacent to S26 are also changed in mutants 2.7 and 2.8 (Fig. 1B-5). This is consistent with previous work from Povarova, et al. 2018 which

suggests that mutations adjacent to S26 may be favorable to "open up" the space surrounding this residue.[34] For mutant 2.7, E, S, and C are found at A25. Contrary to creating space near S26, these charged amino acids may function to coordinate with precursor ions, potentially positioning them favorably for coordination with S26. A similar change from A25 to E is found in mutant 2.8.

The conservation of S26 within the library is consistent with the site-directed mutagenesis of the catalytic triad. Several studies have examined impacts of catalytic triad mutations with silica biomineralization, with controversial results.[34,116] In this work, the same catalytic triad mutations were performed, but testing ceria biomineralization as a measure of protein catalytic activity rather than silica biomineralization. By evaluating biomineralization activity with ceria, it is evident that H165A, and H265/S26A mutants do not have significantly impacted functionality (Fig 1B-11). The single mutation of S26A, however, does show significantly impaired biomineralization yields, with average activity only 84% of WT TF-silicatein ($p < 0.05$, $n = 6$).

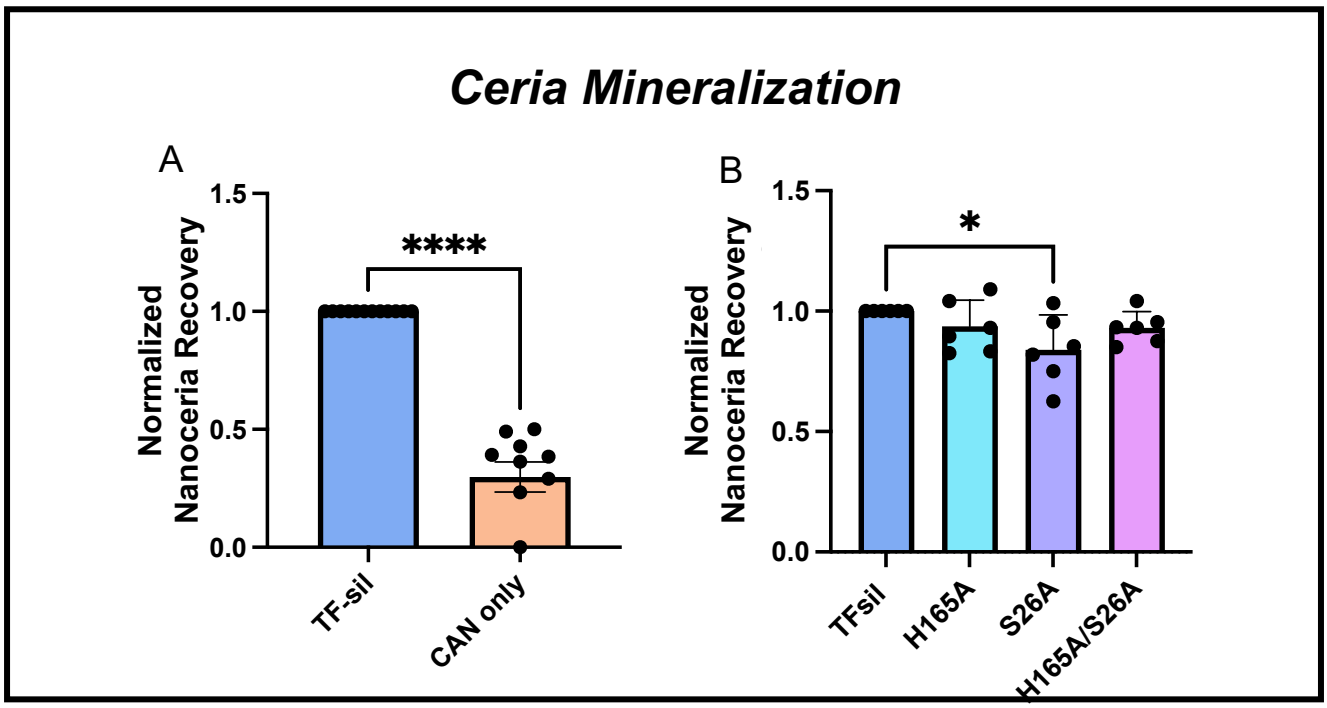

Figure 1B-11. A) Ceria mineralization for purified TF-silicatein in comparison to a ceria ammonium nitrate only, no protein control highlighting significantly greater nanoceria recovery with TF-silicatein than without. $p < 5x10^{-6}$, n = 10. B) Ceria mineralization for purified TF-silicatein and TF-silicatein mutants H165A, S26A, and H165/S26A, showing a significant difference between TF-sil and S26A nanoceria recovery, but no significant difference with H165A and H165/S26A. $p < 0.05$, n = 6. Data originally quantified by moles, then percent recovery, and finally normalized to TF-silicatein outputs following the methods of Povarova, *et al.* 2018.

Summary

Overall, a single mutant did not display improved activity due to the intertwined nature of multiple transformations. SDS-PAGE illustrates notable DnaK expression with mutant 2.7, however with the Western blot of WT TF-silicatein and mutant lysates (normalized by total protein concentration), mutant 2.7 is indistinguishable from mutants 2.6 and 2.8 (Fig. 1B-6). These results suggest that the mutants do not put significantly more or less stress on the cells, although it is notable that the protein produced per total protein in cell is much lower than the WT. In Native PAGE analysis, the mutants oligomerize similarly to the WT and show comparable biomineralization activity within the Native PAGE.

Future Work

This work shows genetic mosaicism associated with silicatein mutant library, suggesting that silicatein has significant sequence flexibility and that multiple versions of the protein contribute positively to biomineralization activity. In order to further examine individual sequences and therefore the impacts of specific amino acid changes, each mutant of interest will need to be transformed individually with the purified target DNA. While this may provide some insight into the mechanism of the enzyme, it will require serious time and resources and does not seem likely to yield a "super" enzyme.

An interesting perspective to consider is the possibility of *in vivo* biomineralization with silicatein mutant families for applications to austere environments such as acid mine drainage, e-waste streams, or extraterrestrial zones. In these cases, it may further benefit the organism to display genetic mosaicism and one could leverage the challenges of each austere environment to direct evolution of the protein. It is possible that each directed evolution in each austere environment may produce a unique family of mutant silicateins. For example, mutant silicatein produced via directed evolution in acid mine drainage may differ from mutant silicatein produced via directed evolution for extraterrestrial applications. With consideration to silicatein sequence flexibility, this could be a promising approach for a variety of challenges.

Publication: *Submitted, In Review:* Vigil, T.N., Rowson, M.J.C., Frost, A.J., Janiga, A.R., Berger, B.W. "Directed evolution of silicatein reveals biomineralization synergism between protein sequences" 2024.

Aim 1c

Hypothesis: Some biomineralization protein activity is mediated by intrinsic disorder within protein structure, therefore I hypothesize that intrinsic disorder within silicatein contributes to biomineralization.

Approach: Although silicatein biomineralization is reported to be catalytic, with the catalytic triad theory prevailing,[37,116] this theory is controversial. Silicatein biomineralization with ceria can be fit according to Michaelis-Menten kinetics (Fig 1C-1). Similarly, previous work by Dakhili, et al. shows Michaelis-Menten kinetics between silicatein and various silica precursors.[37] These results point to enzymatic activity, however, site-directed mutagenesis with the catalytic triad did not abolish biomineralization activity (Fig 1B-8). Therefore, the catalytic triad is not the active site, or is one of multiple active sites. The silicatein library and co-occurrence of multiple silicatein mutants seems to support the possibility that there are multiple routes of biomineralization associated with silicatein.

Biomineralization can also be mediated by intrinsic disorder.[117,118] Intrinsic disorder facilitates crystal nucleation via phase separation as a result of poor solubility.[117,118] One example is nacre-protein PFMG1, which has interactive regions of disorder that facilitate calcium carbonate biomineralization.[119,120] Other proteins co-localized with PFMG1 also display intrinsic disorder and contribute to biomineralization activity.[119,120] Here, I can draw a comparison with silicatein, which also has biomineralization activity and is co-located with several other potential biomineralization contributors.

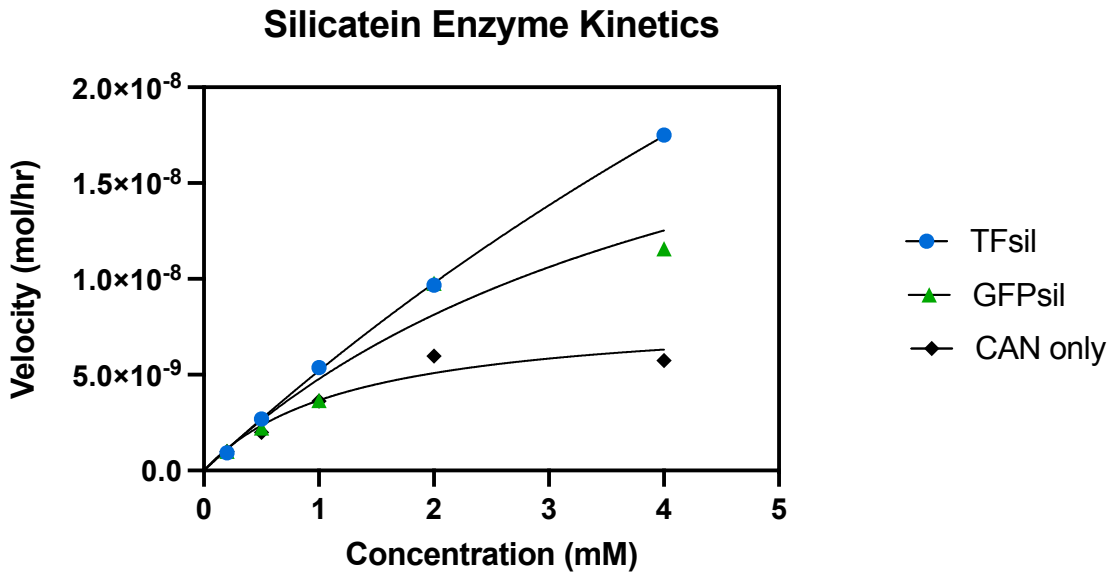

Figure 1C-1. Silicatein enzyme kinetics as measured with precursor ceria ammonium nitrate resulting in ceric oxide formation. A Michaelis-Menten curve fit was applied to calculate v_{max} = 8.1 x 10^{-8}, 2.7 x 10^{-8}, and 8.3 x 10^{-9} moles/hr for TF-sil, GFP-sil, and CAN only, respectively. The calculated Km values were 14.6, 4.7, and 1.3 mM respectively. N = 30

Many studies of intrinsic disorder note trends in hydrophobic, polar, and charged amino acids as well as low complexity repeat regions.[118,121,122] One subset of intrinsic disorder is amyloid-like aggregation, which describes a whole class of behavior distinguished by beta sheet folding and associated protein aggregates.[121] PFMG1 aggregation is likely mediated by this behavior, with base-line secondary structure of 35% beta sheets that reportedly increase with further aggregation and biomineralization activity.[120] In contrast, Dakhili et al. showed that silicatein has approximately 17% beta sheets by circular dichroism.[37] Furthermore, pi-pi stacking of aromatic amino that reportedly increase with further aggregation and biomineralization activity.[123] The Budapest Amyloid Predictor[124] flags one hexapeptide region within silicatein as amyloid-like, starting at tyrosine 76, followed by PFVGK (6/183 AA). For comparison, Budapest Amyloid Predictor identifies 4 hexapeptide regions in PFMG1 (24/136 AA).

Other intrinsic disorder predictors such as IUPRED3 and PrDOS predict regions of disorder by evaluating amino acid energy in context of neighboring amino acids, as well as similarity to model sequences.[41,125,126] Utilizing these methods, only final residues N and Q have greater than a 50% probability of disorder. Analysis with PSIPRED also identifies N182 and Q183 as disordered, along with K180 and Y181 (Fig. 8).[126] It is important to note that these residues appear at the end of the sequence – therefore do not have as many contacts as residues within the protein, and therefore more likely to be identified as disordered. This is an artifact of this predictive approach that must be considered. With this in mind, there are no residues predicted to be disordered in silicatein, but the same analysis with PFMG1 identifies 39 residues.[120]

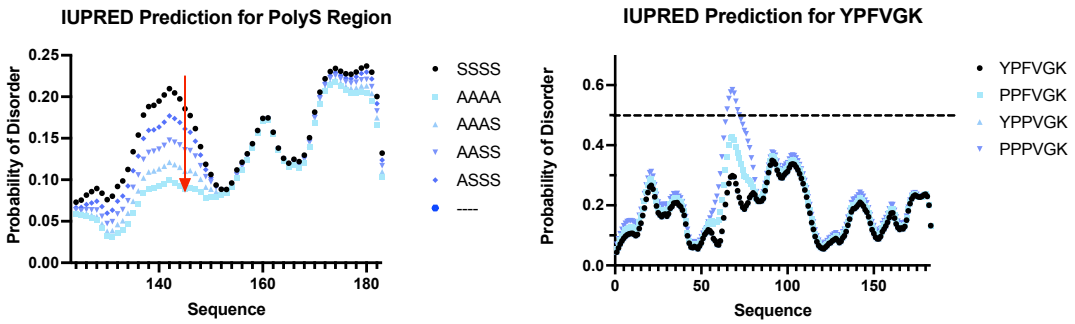

Figure 1C-2. IUPRED disorder predictions for the proposed mutants. Left, IUPRED predicts decreasing disorder as the polyS region is mutated to A. On the right, each mutation to proline results in increased intrinsic disorder. (Note, pictured is IUPRED prediction which is less specific than the postulated amyloid aggregation.)

Finally, I consider low sequence complexity as a measure of intrinsic disorder. Silicatein has four sequential serines starting at AA 159 (numbering according to H165), which shall henceforth be referred to as the polyS region. Repeats of polar amino acids are reported to cause phase separation behavior, which corresponds with the theory of crystal nucleation resulting from phase separation.[117,127] Additionally, longer repeats are associated with greater disorder.[118] With consideration to these changes, Table 2 relates protein properties to what we can experimentally measure, which may help with interpretation of results.

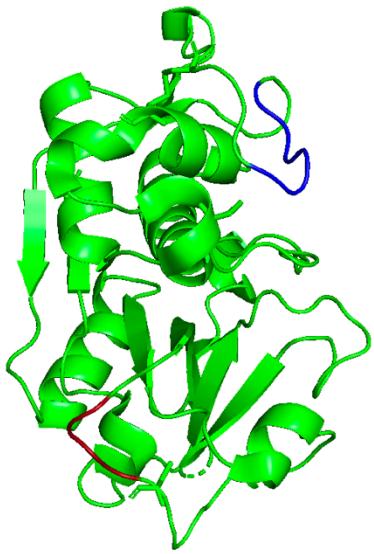

Figure 1C-3. Silicatein crystal structure 6ZQ3 with polyS region highlighted in red and predicted amyloid-like region in blue.

Table 2. Protein properties as related to experimental results.

Protein Property		**Measurables**			
Solubility	Activity	DnaK expression	Overall protein concentration	Mineralization Yields	Material properties
Increase	Increase	Decrease	Increase	Increase	?
Increase	Decrease	Decrease	Increase	?	?
Decrease	Increase	Increase	Decrease	?	?
Decrease	Decrease	Increase	Decrease	Decrease	?

Strategies and Results

For the YPFVGK region, the crystal structure 6ZQ3 shows random loops and coils rather than beta sheets. Using 3D-folding secondary structure prediction software, PEP-FOLD, the YPFVGK region was examined further for beta sheet formation. PEP-FOLD predicts 3D-folding based on amino acid identity and

proximity, generating approximately 100 models to account for the different conformational changes.[128,129] From these 100, the five most common are selected as representative of the 3D-folding of the peptide.

For the YPFVGK region, the 30 amino acids immediately preceding YPFVGK (i.e. P61-K97) were input to PEP-FOLD, generating a structure that closely resembles the known crystal structure of 6ZQ3, shown in Figure 1C-4. P61-K97 shows the same alpha helix preceding YPFVGK, and the YPFVGK region itself remains random loops and coils. As noted above, however, the end of an amino acid sequence may have higher propensity for disorder or randomness when evaluated via predictors due to the lack of neighboring amino acid residues, therefore F76-M112 and H64-C100 also examined. In each case, the alpha helix preceding YPFVGK and the random loops and coils of YPFVGK remained intact. Finally, short nonapeptide region S94-Q103 (eliminating the influence of neighboring peptides) showed random loop and coil structure with little change seen between SAYPFVGKQ and SAPPFVGKQ. Simulations at pH 5 and pH 8 also did not show any secondary structure changes for YPFVGK. Altogether, PEP-FOLD and IUPRED results did not support any amyloid aggregation resulting from the YPFVGK region, and YPFVGK mutants were not further explored.

Consideration of the library sequences from mutants 2.6, 2.7, and 2.8 show that the YPFVGK region was mostly conserved, with the only mutations occurring with F. For mutants 2.7D and 2.8A, F was substituted with L. For mutant 2.8F, F was substituted with V. Each case substitutes hydrophobic F with another hydrophobic amino acid. Although the hydrophobic nature of the side chain is conserved, L and V would not contribute to any pi-pi stacking with Y. In all sequences, YP and VGK remained unchanged, therefore this region underwent a single amino acid substitution for three of a total of 19 mutants. The single amino acid substitution preserved the hydrophobic character of original amino acid, F, but disrupts any pi-pi stacking with Y. Considering that mutants 2.6, 2.7, and 2.8 each had greater biomineralization yields than WT TF-sil and overall conserved the YPFVGK character may suggest that this region contributes positively

or negligibly to biomineralization, however, this region does not mediate biomineralization via amyloid aggregation.

Overall, the library findings concerning YPFVGK support a lack of amyloid folding, which is in agreement with a lack of amyloid folding in this region with crystal structure 6ZQ3 from Goerlich et al.[21] The proposed hypothesis, that the YPFVGK region contributes to amyloid aggregation, is therefore very unlikely. This further supports the decision not to pursue site-directed mutagenesis with YPFVGK.

Row 1

Row 2

Row 3

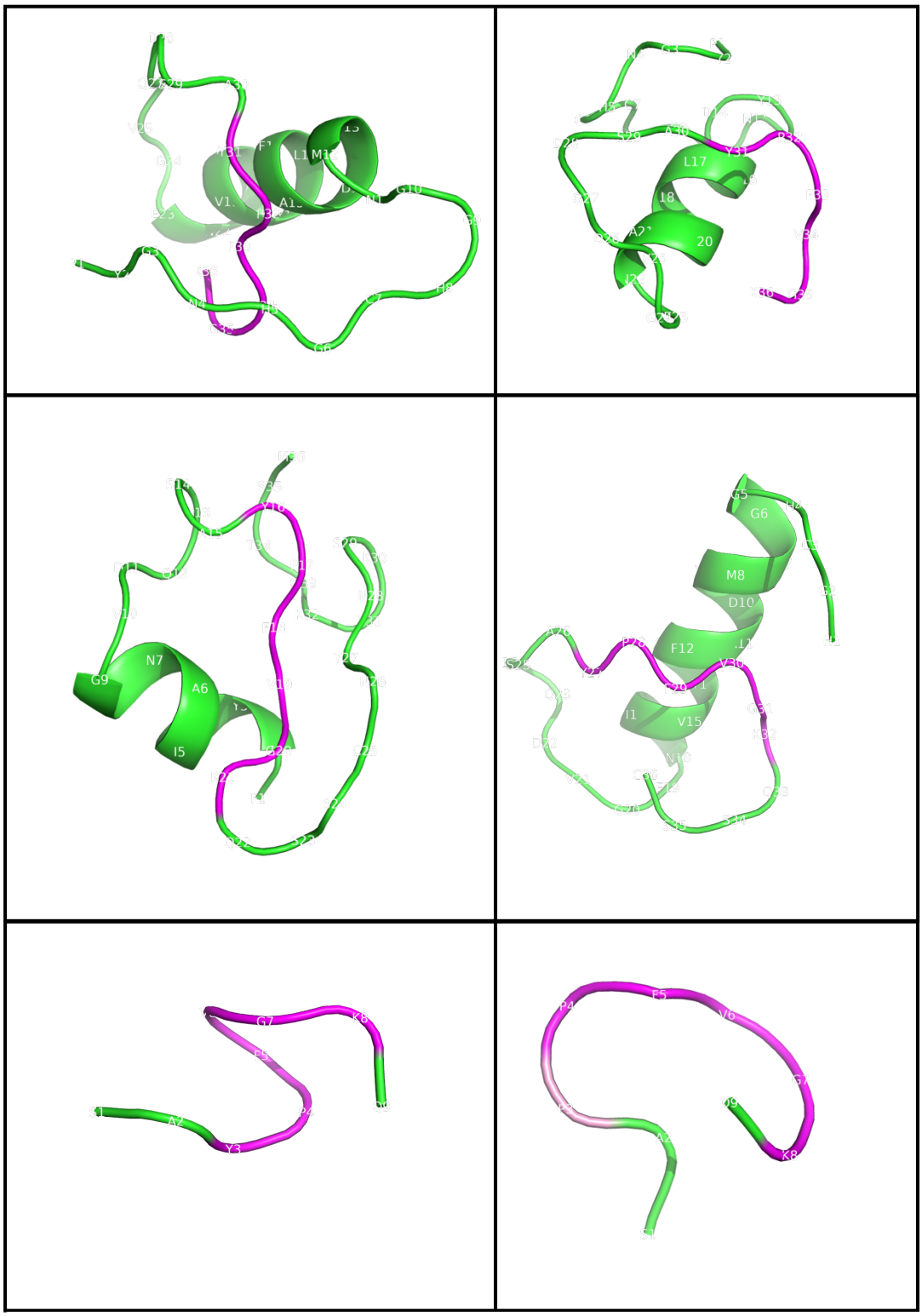

Figure 1C-4. PEP-FOLD predictions with YPFVGK (magenta). Row 1 shows P61-K97 or PYGNHGCHGGNMYDAFLYVIANEGVDQDSAYPFVGK. Row 2 shows F76-M112 or FLYVIANEGVDQDSAYPFVGKQSSCNYNSKYKGTSM and H64-C100 or HGCHGGNMYDAFLYVIANEGVDQDSAYPFVGKQSSC. Row 3 shows nonapeptides S74-Q83 or SAYPFVGKQ and mutant SAPPFVGKQ.

Low-complexity regions are a hallmark of intrinsic disorder,[122,130] which contributes to biomineralization in the case of PFMG1.[119,120] Low-complexity regions are also found in marine sponge glassin, although these have not been structurally confirmed as intrinsically disordered.[42] In silicatein, the polyS region may mediate biomineralization via intrinsic disorder due to low-complexity. In one study, Goncalves-Kulik et al. showed that S occurs as a low-complexity repeat in approximately 65% of intrinsically-disordered regions with a published PDB structure and is the fourth-most high occurring low-complexity region observed in the proteome.[131] Table 3 lists the mutations that will be made to the polyS region.

Table 3. Intrinsic disorder mutants

Original sequence	**Sequence made with site-directed mutagenesis**	**Mutant name**
159-SSSS	159-ASSS	polyS1
159-SSSS	159-AASS	polyS2
159-SSSS	159-AAAS	polyS3
159-SSSS	159-AAAA	polyS4

The polyS mutants were made and characterized for solubility and stability qualitatively by SDS-PAGE. In SDS-PAGE, the intensity of target band at 75 kDa, as well as DnaK band at 26 kDa were considered. In each of the polyS purifications, the TF-sil polySx band is evident at 75 kDa, although not overly intense (Fig. 1C-5). In each case, the 26 kDa DnaK band is equally or more prevalent than the target 75 kDa band. In contrast, WT TF-silicatein generally produces a large band without any at 26 kDa. This may suggest that the polyS mutants are less stable than WT TF-silicatein.

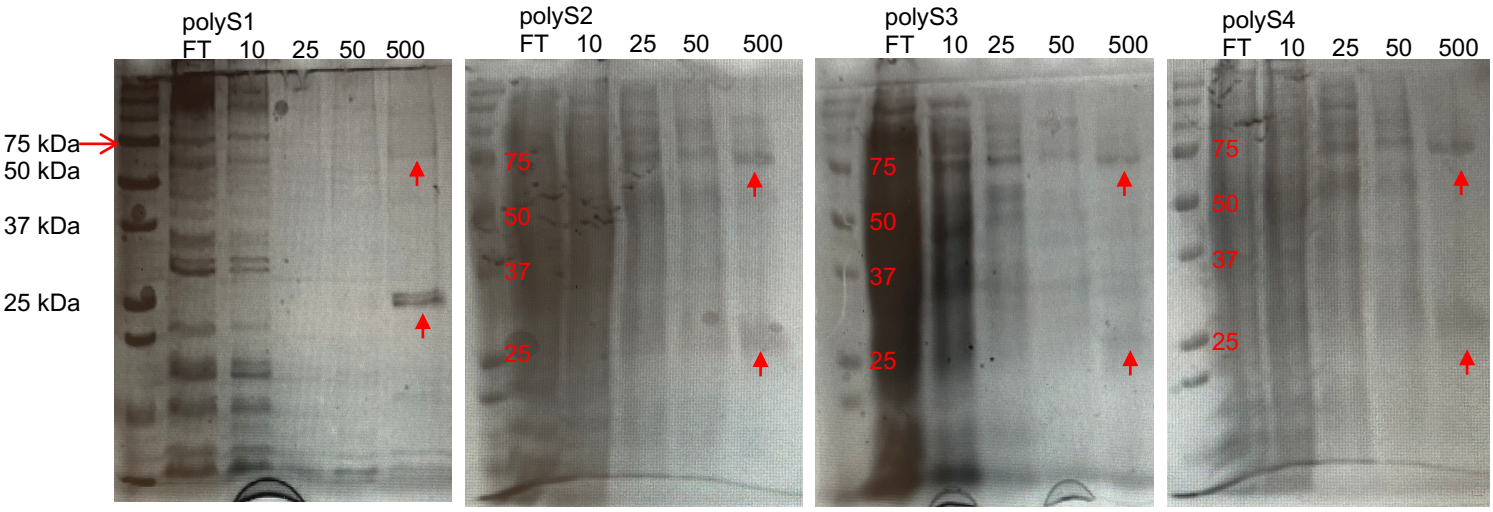

Figure 1C-5. SDS-PAGE gels for polyS purifications. Red arrows indicate bands of interest at 75 and 26 kDa.

As each polyS1 and polyS2 have smaller low complexity regions than WT TF-silicatein (ASSS, AASS has fewer amino acid repeats than SSSS) it might be anticipated that intrinsic disorder would be lower and that protein solubility and stability would be greater. If this were the case, we would anticipate less DnaK expression than with WT TF-silicatein, which is not shown in Fig. 1C-5. Mutants polyS3 and polyS4 (AAAS, AAAA) although different from the low complexity seen in the original SSSS, have low complexity with A repeats. Although the A repeats are low complexity, the trends in intrinsic disorder suggest that polar amino acids have a strong role, therefore AAAS and AAAA might be expected to have less intrinsic disorder than SSSS although they do have low complexity. While the precise details of which amino acids cause specific aspects of disorder within silicatein cannot be sorted out, there are no clear trends of increased or decreased solubility and stability associated with the polyS mutants.

With consideration to biomineralization yields, the polyS mutants also did not show any significant differences from those of WT TF-silicatein (Fig. 1C-6). While these results are anti-climactic, they do support the findings of Aim 1B which show that multiple mutants co-expressed increase biomineralization activity. Therefore, one could postulate that while none of these mutations alone result in any significant changes to biomineralization, it is possible that multiple mutants working together would.

Furthermore, the library mutant family 2.6 reveals that only 1 of 8 identified sequences is truncated prior to the polyS region, and only 1 of 8 identified sequences shows a mutation in the polyS region (SSRS). Library mutant family 2.7 shows 2 out of 5 identified sequences is truncated prior to the polyS region, and 1 of 5 identified sequences has a mutation in the polyS region (SSSY). Finally, the library mutant family 2.8 shows the polyS region as conserved for all six identified sequences. Taken together, these results support the notion that the polyS region does not solely define biomineralization activity but that it may play an assisting role.

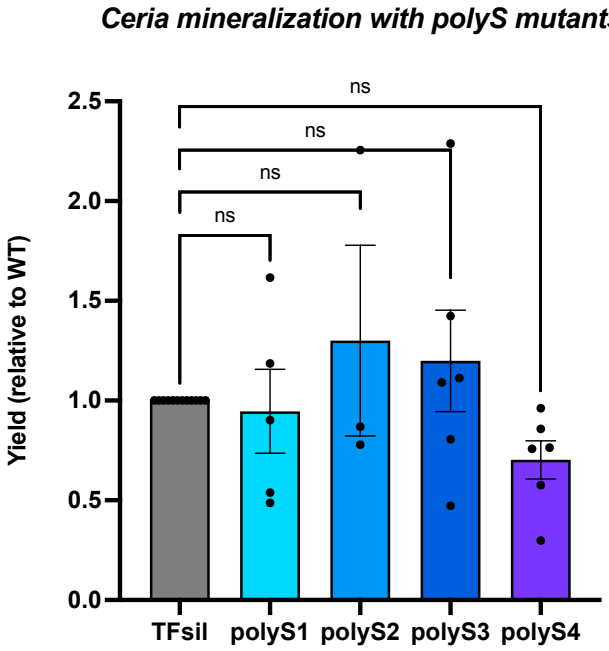

Figure 1C-6. Ceria biomineralization yields of polyS mutants relative to WT TF-silicatein. Error bars represent SEM. One-way ANOVA shows no significant difference between ceria biomineralization yields of any of the mutants and WT TF-silicatein.

Silicatein has many S residues (28/183), which are hypothesized to influence biomineralization through the hydroxy moiety.[27] In their examination of low-complexity regions, Lee et. al (2022) observe that clusters of amino acid repeats often interact with other clusters.[132] Figure 1C-3 shows the polyS region highlighted in red as an random loop. As there are no other amino acid repeats in silicatein, the polyS region random loop does not follow low-complexity cluster interaction behavior. Lee et al. (2022) also describe characteristic R and S-rich regions as low-complexity.[132] Prior to the polyS region in silicatein are amino acids S, S, R, and C. This perspective suggests two possibilities: 1) although the polyS region does not interact with another low complexity cluster within the protein monomer, it is may be possible the polyS regions between two protein monomers bridge in low-complexity cluster interaction behavior, 2) although the polyS region is separated from nearby S by R and C amino acids, it may be wise to consider these 8

amino acids together as a functional unit rather than polyS alone (S-S-R-C-S-S-S-S). These possibilities may be valuable considerations for future studies.

Di-histidine mutants

Two histidine mutants, H64A and H67A, were also evaluated here. Although histidine is not known to be a strong contributor of intrinsic disorder, the di-histidine motif has been implicated in biomineralization.[133,134] For magnetite formation in magnetotactic bacteria, Hershey et al. showed that a di-histidine motif plays a critical role.[133] Histidine is also widely considered a metal chelator, and thought to contribute to biomineralization in that way. H165 is a histidine in silicatein's putative catalytic triad, which we showed with ceria ammonium nitrate as precursor is not critical for biomineralization (Fig. 1B-11).

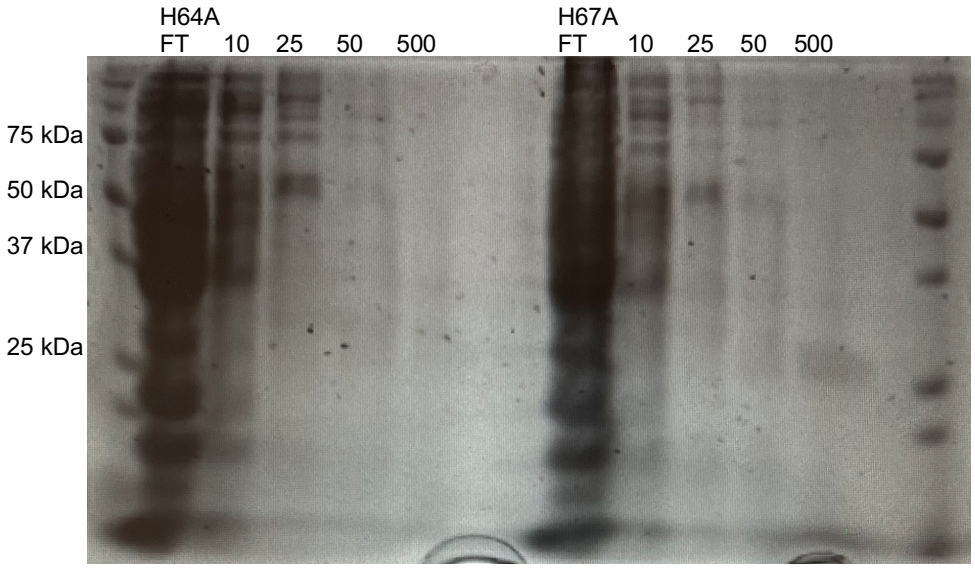

Figure 1C-7. SDS-PAGE for H64A and H67A immobilized metal affinity chromatography purifications showing flow through (FT), 10, 25, 50, and 500 mM elutions.

H64A and H67A mutants showed some diminished expression with notable DnaK expression for H67A in the 500 mM elution (Fig 1C-7). However, with consideration to eGFP-silicatein, the silicatein library mutants, and polyS mutants this change in expression seen with SDS-PAGE was not considered indicative

of protein activity, i.e. significant DnaK expression was seen with eGFP-silicatein, however eGFP-silicatein retained biomineralization activity. Ceria biomineralization with these mutants showed no significant changes to nanoceria yields (Fig. 1C-8). Interestingly, of all the mutants sequenced for the silicatein mutant library, each had H64 and H67 conserved. Similar to analysis of library results with the polyS region this may suggest that biomineralization activity is in part supported by H64 and H67, but that these amino acids are not solely responsible for activity.

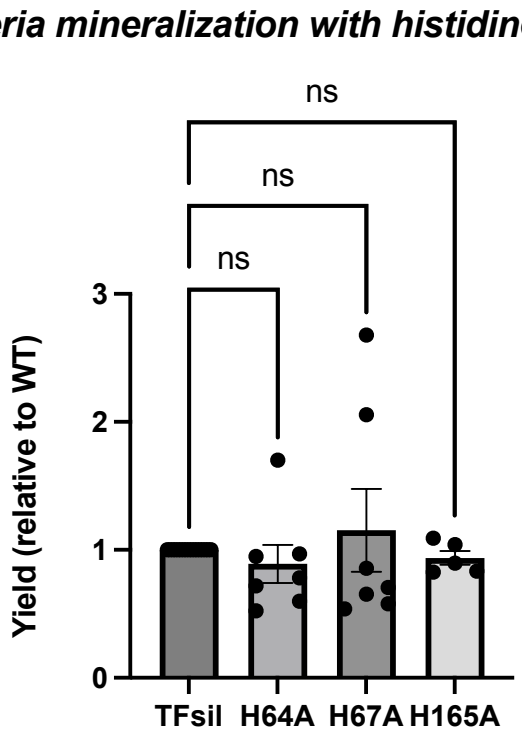

Figure 1C-8. Ceria biomineralization yields of histidine mutants relative to WT TF-silicatein. Error bars represent SEM. One-way ANOVA shows no significant difference between ceria biomineralization yields of any of the mutants and WT TF-silicatein.

Summary

Intrinsic disorder mediates biomineralization via liquid-liquid phase separation in some proteins, with PFMG1 being a notable example. In this work IUPRED did not predict a high probability of disorder for

any residues within silicatein. However, in an investigation of intrinsic disorder mediated by amyloid aggregation, the Budapest Amyloid Predictor[124] identified hexapeptide sequence YPFVGK. Thorough analysis with PEPFOLD illustrated no amyloid folding with YPFVGK, even with changes in pH. To investigate intrinsic disorder as a function of low-complexity regions, we examined the polyS region. Site-directed mutagenesis to change hydroxyl-functionalized S to A did not result in any significant changes in biomineralization yields (Fig. 1C-6). Finally, a di-histidine motif with H64 and H67 was examined via site-directed mutagenesis to A. The di-histidine motif has reportedly modulated metal cation binding for some biomineralization proteins,[133,134] however in this case there were no changes to biomineralization yields, suggesting that H64 and H67 do not play a critical role in biomineralization activity. The results here align with library results from Aim1b, suggesting that silicatein is permissive to a variety of sequence changes. Furthermore, these results indicate that silicatein biomineralization activity is not mediated by a single mechanism but is instead the result of complex interplay between multiple modes of activity.

Future Work

There is no single path forward with silicatein. As discussed with the polyS case, one possibility is evaluating S-S-R-C-S-S-S-S rather than S-S-S-S alone since S and R are known to have complex interactions within low-complexity regions. Another possibility is complete mutagenesis of all S present in silicatein (28/183) to A to evaluate complete abolition of the S hydroxyl moiety. This approach can be extended further to systematically evaluate the role of other amino acids such as C/H/M and W/R/K as these amino acids have been identified as critical for binding and reduction in various biomineralization studies.[4] To evaluate the implications of select mutations on the material properties of biomineralization product, analysis such as XRD and TEM should be considered.

Materials and Methods:

Molecular Biology

Standard molecular biology procedures were used for DNA maintenance and cloning using *E. coli* DH5α. For TF-silicatein, eGFP-silicatein, and library work, the Monarch PCR and DNA Clean-up Kit (NEB), and Monarch Gel Extraction Kit (NEB) were used according to manufacturer's instructions. All mini-and maxi-preps were performed according to established Berger lab protocols. pET-28a(+) TF-silicatein and pET-28a(+) eGFP-silicatein were legacy mini-preps from the work of Melissa Deschamps (UVa Master of Science 2019). Plasmids were confirmed via whole plasmid sequencing (Plasmidsaurus).

Frequently used primers

T7: 5' TAATACGACTCACTATAGGG 3'

Sil F: 5' tacatAAGCTTGGTGCGAGTTATGCTTTTTCTGC 3'

Sil R: 5' cccaccCTCGAGTTGATTGTATTTGTT 3'

T7term: 5' GCTAGTTATTGCTCAGCGG 3'

TF F: 5' ATGCAAGTTTCAGTTGAAACCACT 3'

Middle TF F: 5' ACCTTCCCGGAAGAATACCAC 3'

Protein production and purification

pet28a(+) eGFP-silicatein, TF-silicatein, and eGFP/TF-silicatein mutants were transformed into *E. coli* BL21. Single colonies were picked for starter cultures in LB, grown at 37 °C shaking overnight. Cultures were centrifuged at 3,000 x g for 10 minutes and supernatant discarded. Cell pellet was inoculated in TB with kanamycin (minimum 50 mL) and grown to OD600 of 0.6-0.8. At OD600 > 0.6, isopropyl β-D-1-thiogalactopyranoside (IPTG) was added to a final concentration of 0.1 mM and flasks moved to 20 °C shaking incubator overnight. Cells were harvested via centrifugation at 3,000 x g for 10 minutes and supernatant discarded. Pellet was resuspended in sonication lysis buffer (5% v/v glycerol (99+%), 36 mM

tris HCl, 20 mM tris base, 100 mM NaCl, and 5 mM imidazole) at 5 mL buffer / 1 g pellet. Lysis was performed via sonication at 20% amplitude, for 20 minutes in 20 second on/off pulses. Lysate was centrifuged at 10,000 x g for minimum of 10 minutes, supernatant was collected and filtered with 0.4 μm syringe filter then purified via his-tag affinity chromatography. Purification fractions were collected and analyzed via 8% SDS PAGE.

Following purification, 500 mM elution was transferred to dialysis in 0.1 M Tris buffer, pH 8 and dialyzed overnight (minimum 4 hrs) at room temperature. Protein concentration was then measured via A280. Dialyzed protein was stored at room temperature. Mass precipitation begins occurring after approximately 1 week.

SDS-PAGE

8% SDS-PAGE with Blue Precision Plus Protein ladder (BioRad) was loaded with denatured lysates and purified samples, run at 110 V for 10 minutes, then 150 V for 1 hour. For staining, gel was transferred to fixing solution with Coomassie blue for at least 30 minutes (0.025% w/v brilliant blue, 7.5% v/v acetic acid, 50% v/v ethanol (95%), and 42.5% v/v DI H_2O), then de-stained (7.5% v/v acetic acid, 10% v/v ethanol (95%), and 82.5% v/v DI H_2O) for 1 hour. Imaged with colorimetric transillumination on Amersham Imager 680.

Native PAGE

8% Native PAGE with Native Mark Unstained Protein Standard ladder (ThermoFisher) and protein samples (>50 mmol/L) was run at 110 V for 2 hours in 1.5x native PAGE buffer (192 mM glycine, 25 mM tris, pH 8.3). Gel was stained with FASTsilver (G Biosciences) or Coomassie staining solution. For biomineralization assay, gel was run normally then cut into three separate pieces and transferred to appropriate stains / buffers for 12 hours. The Coomassie blue stained gel was imaged with colorimetric

transillumination. Buffer control and 2 mM CAN gels were imaged at 460 nm excitation to detect nanoceria. Fluorescence gels were imaged using an Amersham Imager 680 with semi-automatic exposure.

Silver Stain

FASTsilver kit from EMD Millipore. All steps performed on an orbital mixer. Gel was incubated in fixative I (30% ethanol, 10% acetic acid) for at least 30 minutes, then washed twice for 10 minutes each in fixative II (10% ethanol). Next, gel was washed three times for 10 minutes in DI H_2O. Following water discard, gel was soaked in sensitizing solution (5 mL silver, 65 µL sensitizer I, 45 mL DI H_2O) for 30 minutes. For 10-20 seconds, gel was rinsed in DI H_2O then soaked in developer (2.5 g developer powder, 32.5 µL sensitizer I, 32.5 µL sensitizer II, 45 mL DI H_2O) until bands are visible. 5 mL stopper solution (22% acetic acid) was added and gel was left to rock on orbital mixer for 10 minutes.

Library generation

Silicatein mutants were generated via error-prone PCR with dNTP analogues, adapted from Chao, et al. 2006[135] and shown below.

EP-PCR Part 1

PCR Reaction Components	Final concentration
10 × Taq buffer	1 ×
50 mM $MgCl_2$	2 mM
10 µM Forward primer	0.5 µM
10 µM Reverse primer	0.5 µM
10 mM dNTPs	200 µM
Template DNA	100 ng
20 µM 8-oxo-dGTP	2 µM
20 µM dPTP	2 µM
Fill to desired volume with DI H_2O	
5 U/µl Taq DNA polymerase	0.05 U/µl

EP-PCR Part 2

PCR Reaction Components	Final concentration
10 × Taq buffer	1 ×
50 mM $MgCl_2$	2 mM
10 µM Forward primer	0.5 µM
10 µM Reverse primer	0.5 µM
10 mM dNTPs	200 µM
Extracted PCR product	Minimim 10 ng
Fill to desired volume with DI H_2O	
5 U/µl Taq DNA polymerase	0.05 U/µl

Cycling Conditions

Temperature (°C)	Time
94	3 min
94	30 sec
58	30 sec
58	1 min
Repeat 30 cycles	
58	10 min

Cycling Conditions

Temperature (°C)	Time
94	3 min
94	30 sec
60	30 sec
58	1 min
Repeat 30 cycles	
58	10 min

The forward primer for this random mutagenesis was: 5' TAC ATA AGC TTG GTG CGA GTT ATG CTT TTT CTG C 3' and the reverse primer was 5' CCC ACC CTC GAG TTG ATT GTA TTT GTT 3'. PCR product was then re-ligated into the pet28a(+) vector with Trigger Factor (Accession # WP_096260434.1) or eGFP (Accession # P42212) at HindIII and XhoI according to NEB T4 Ligation protocol. The ligation product was transformed directly into BL21 *E. coli*, then screened via survival assay (50 ng DNA in 20 µL total, so 2.5 ng/µL).

Survival assay

BL21 *E. coli* was transformed via electroporation with library DNA mixture (2.5 ng/µL) and quenched with LB. The transformation recovery culture was grown in 37 °C shaking incubator overnight. Cells were harvested via centrifugation at 3,000 x g for 10 minutes, then pellet was resuspended in Terrific Broth and grown to an OD600 of 0.6. At OD600 = 0.6, 0.1 mM IPTG was added, then culture was incubated at 20 °C shaking overnight. After induction, media was removed and cells were resuspended in water, then exposed to varying concentrations (2.5 mM to 0 mM) of ceria ammonium nitrate (CAN) grown overnight

at 37 °C shaking. Cultures were diluted 1/1000 then plated on LB agar according to CAN exposure concentration and grown at 37 °C for 18 hours. Colonies grown at or above critical concentration were selected for further screening.

Bradford assay

Total protein concentration was sometimes measured by Bradford assay with BioRad's Bradford reagent (catalogue #5000205). A standard curve was prepared in 96-well plate from 1,500 ng BSA followed by two-fold serial dilutions (150 µL BSA, 150 µL Bradford reagent). Sample triplicates were added to wells at 150 µL, followed by the addition of 150 µL Bradford reagent. Absorbance was read at 595 nm on BioTek Synergy Neo2 plate reader.

Silicomolybdate assay

Silica recovery was measured with the silicomolybdate assay adapted from Povarova, et al. 2018 with extinction coefficient as derived by Coradin, et al. 2004.[136] Biomineralization samples were centrifuged at 21,000 x g for 30 minutes. Supernatant was discarded, samples were dried and resuspended in 0.2 M NaOH. Samples were then titrated to pH 1.6-1.9 with 2 M HCl. After recording total sample volume, samples were transferred to 96-well plate in 200 µL increments. 15 µL of molybdate reagent was added to each well then incubated at RT for 15 minutes. Then 15 µL of 0.1% ascorbic acid and 15 µL of 0.1% oxalic acid were added to each well and incubated at RT for 2 hours. Absorbance was read at 820 nm on BioTek Synergy Neo2 plate reader.

Arsenazo III assay

A ceric ammonium nitrate standard curve in 10 mM citrate buffer pH 3 (high concentration 1.25×10^{-7} moles) was prepared fresh for each reading. Samples were dried and resuspended in citrate buffer. In 96-well plate, samples were further diluted 1/15 in 10 mM citrate buffer (pH 3), and a final concentration of 2 mM arsenazo III dye was added, adapted from Hogendoorn, et al. 2018.[137] Following 1 minute centrifugation

at 100 x g, absorbance at 650 nm was read on BioTek Synergy Neo2 plate reader. Based on best-fit line of standard curve concentrations and absorbances, sample concentrations were calculated, averaged, then transformed into percent yield (based on initial CAN availability of $1x10^{-7}$ moles in biomineralization assay).

X-ray diffraction

Samples were characterized with a Bruker ApexII Duo diffractometer with a Cu 1.54 angstrom source at room-temperature with expertise from Dr. Diane Dickey at the UVa XRD Core (instrument funding from NSF-MRI program (CHE-2018870)). Sample spectra were compared and matched to standards listed in the Inorganic Crystal Structure Database.

Transmission electron microscopy

Nanoceria samples were separated via centrifugation, then resuspended in 10 mM citrate buffer (pH 3.0). 100 μL samples were applied to TEM sample grid and let dry at room temperature. Samples were examined with FEI Titan 80-300 Transmission Electron Microscope. Image analysis and particle size measurement conducted with ImageJ. Utilization of the FEI Titan 80-300 Transmission Electron Microscope within UVa's Nanoscale Materials Characterization Facility was instrumental to this work. Dr. Grayson Johnson performed image acquisition and assistance with data analysis.

Chapter 2: Evaluating smCSE biomineralization and testing for applications to remediate acid mine drainage

**Portions of this work are described in manuscript "Structural basis for the CdS quantum dot (QDs) nanocrystals formation by cystathionine γ-lyase from Stenotrophomonas maltophilia strain (smCSE)"*

Key Findings

- H351 is crucial for smCSE quantum dot production
- smCSe can mineralize ceria ammonium nitrate, lanthanum (III) nitrate, and neodymium (III) nitrate to sulfides
- smCSE reaction time is a key consideration for rare earth element extraction – with WT smCSE, an *in vitro* reaction time greater than 24 hours will precipitate bulk minerals
- Applications for smCSE in REE extraction are likely not suitable for a flow-based reactor system, but a batch reactor simulation has shown promising results

Cystathionine gamma-lyase from *S. maltophilia* (smCSE) has been shown to produce CdS quantum dots when combined with appropriate cysteine- and cadmium-based precursors.[62–64,138] In this work I will evaluate smCSE biomineralization by ***2a)*** examining unique sequence features of smCSE that enable quantum dot production, ***2b)*** examining smCSE substrate flexibility with REEs for the production of REE sulfides, and ***2c)*** applying and evaluating smCSE as an agent in biological soil crusts for waste remediation.

Aim 2a

Hypothesis: Sequence and structural analysis show H49 as unique to smCSE, *i.e.* the 49th residue is not conserved with other non-biomineralizing CSEs, therefore I hypothesize that H49 is necessary for biomineralization activity.

Approach: Structural analysis of smCSE suggests that H49 and H351 (both conserved from human CSE, P32929),[139] both situated between proline brackets, coordinate with metal precursor via imidazolium side chains for biomineralization. Wang, et al.'s non-conserved surface regions (NSRm1: L11A/L13A, NSRm2: R119A/R120A/R121A/T122A, NSRm3: C324A/E325A/K326A/T327A/E328A, NSRm4: P355A/V356A/R358A) were identified via sequence comparisons with other, non-biomineralizing CSEs, whereas H49 and H351 were identified via protein crystal structure interaction with the cadmium ion.[63] Therefore, although the involvement of H49 is not supported by previous smCSE research findings, it is still worth exploring with some simple mutagenesis experiments. I will evaluate the involvement of H49 and H351 in biomineralization via site-directed mutagenesis to alanine, whose neutral, nonpolar sidechain will not coordinate with the metal substrate.

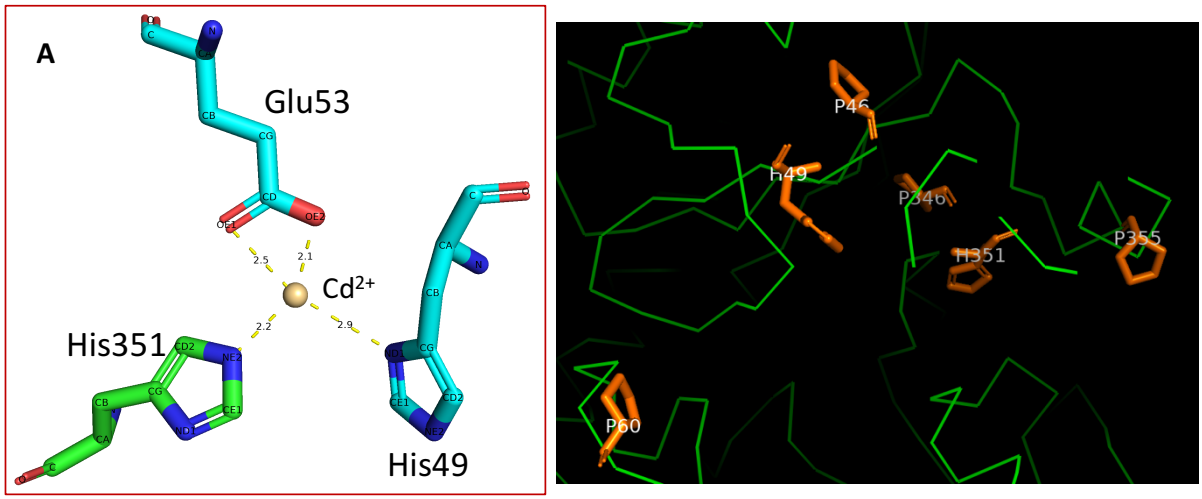

Figure 2A-1. A) Coordination of cadmium ion between H49, E53, H351. Imidazole rings from histidine side chains form imidazole "trap." Adapted from unpublished work by P. Mahanta, R. Acharya, B. W. Berger. B) H49 and H351 (without Cd exposure) and associated proline brackets (P46 & P60, P346 & P355)

Wang, et al. did evaluate E53 (conserved with human CSE),[139] the third amino acid implicated in cadmium cation binding by the cadmium-soaked crystal structure generated by P. Mahanta, R. Acharya, B.W. Berger. Interestingly, Wang et al. conclude that E53A results in enhanced quantum dot production as indicated by greater absorbance at 350 nm after 60 minutes than with WT smCSE.[63] This may suggest that E53A opens up the binding space but that cadmium ions still coordinate with H49 and H351 – deprotonated H49 and

H351 would each carry a negative charge. Similar sets of di-histidine pairs have been implicated in metal binding for other biomineralization proteins MamO and kallikrein.[134,140] In the case of MamO, the di-histidines coordinate the metal with three additional water molecules.[133] With kallikrein, the di-histidines coordinate the metal with an aspartic acid.[134] Given these precedents, it seems equally likely that H49 and H351 may or may not coordinate the metal ion in partnership with E53.

H49 and H351 are surrounded in 3D space by proline brackets P46, P60, P346, and P355 (Fig 2A-1 B). Each of these prolines is conserved with human CSE except P355 (in human CSE, L355).[139] The location of the proline brackets suggests a role possibly contributing to metal coordination and/or solvent accessibility. Of note, P355 was identified by Wang et al. in their NSRm4, along with decreased (slower) biomineralization activity.[63] NSRm1 and NSRm3 also exhibited decreased biomineralization activity, while NSRm2 biomineralization activity was completely abolished. NSRm2 also lost tetramerization, forming a dimer instead.[63]

Protein Expression

WT smCSE has a reputation for being relatively easy to express recombinantly in *E. coli*, often producing a very large band on SDS-PAGE gels for purified protein.[62,63] Although the mutants H49A and H351A are of interest for their potential impacts on biomineralization activity rather than hypothesized changes to protein stability, it is notable that SDS-PAGE expression for these purified proteins differs slightly in the case of H351A (Fig. 2A-2). Where purified H49A creates a large band comparable to WT smCSE, H351A creates a much smaller, diffuse band. This is especially evident in the purified fraction, however, comparison of the column flow through does not show significant differences between WT, H49A, and H351A. Dialysis of purified protein fractions, however, still leads to detectable levels of protein via A280, which are normalized for all biomineralization experiments. So although expression of H351A seems to be notably different, the amount of protein used for biomineralization experiments is consistent.

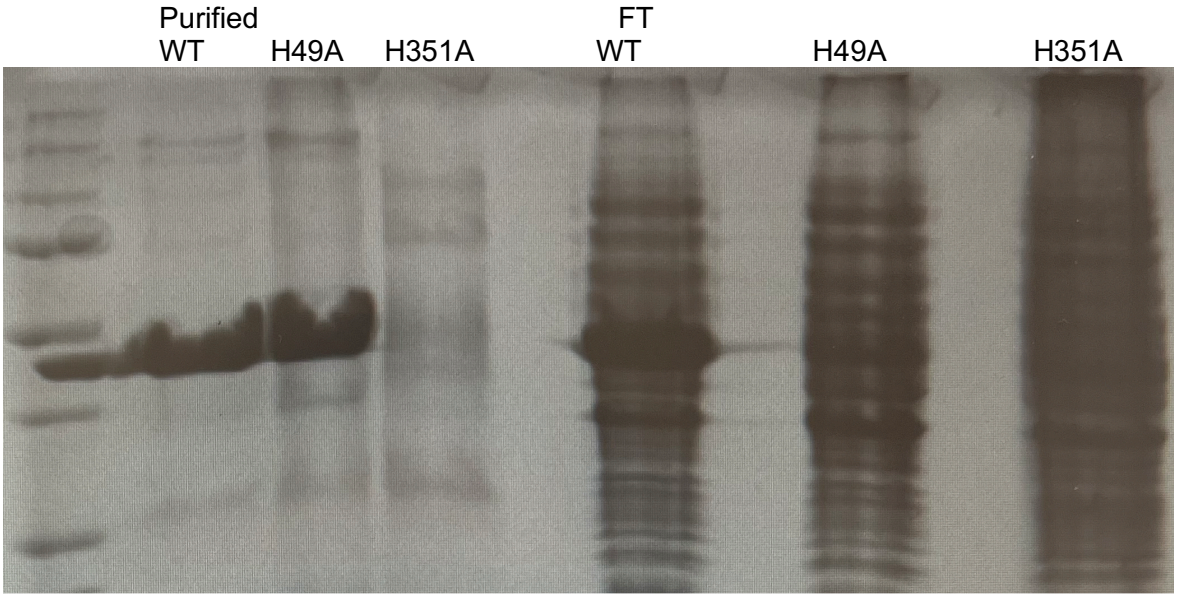

Fig 2A-2. SDS-PAGE for WT smCSE and histidine mutants. The purified fraction is shown at 1M imidazole elution, then the column flow through (FT).

H351A and H49A mutants exhibit different biomineralization than WT smCSE. Combination of H351A with precursors does not yield any biomineralization over an 18-hour period and no lagging biomineralization activity over 7 days. This suggests that H351A is crucial for biomineralization activity and supports the hypothesis that H351A coordinates with the metal precursor. The H49A mutant retains biomineralization activity, although it appears to be both delayed and potentially slowed, as shown in Fig 2A-3. By evaluating cadmium sulfide fluorescence with excitation 360 nm and emission of 520 nm, it is evident that peak nanoparticle production lags by approximately 14 hours. Interestingly, particle production (as measured by exc. 360 nm em. 520 nm) is detectable at 1 hour with WT smCSE and 9 hours for smCSE H49A. This suggests that particle production is delayed, but also slower as evidenced by the increased lag time seen with peak production.

A fluorescence spectral scan at 20 hours (exc. 360 nm) shows peak emission of smCSE H49A at 520 nm, while WT smCSE has a peak emission at ~600 nm. This is consistent with the time-course experiments

that illustrate slower biomineralization associated with smCSE H49A than WT smCSE and also consistent with previous work highlighting continued particle growth with time.[62,138]

The loss of activity associated with the H351A mutation supports Wang et al.'s assertion that tetramerization is necessary for biomineralization activity. However, Wang et al. highlight that the "extended loop region" (AA 1- 60) which contains H49 is the foundation for tetramerization rather than the corresponding H351. To further cloud the scenario, Wang et al.'s NSRm4 mutant P355, V356, R358 displayed little to no biomineralization as monitored by UV-Vis.[63] Taken together, these data may suggest that the N-terminal region of one protomer (including AA H351-R358) is critical for tetramerization and biomineralization activity, but that there is some flexibility associated with the corresponding C-terminal of the adjacent protomer (AA H49).

Hershey et. al report diminished biomineralization activity associated with mutation of the di-histidine motif in MamO, but some residual activity remained.[133] The authors report that this is likely due to the

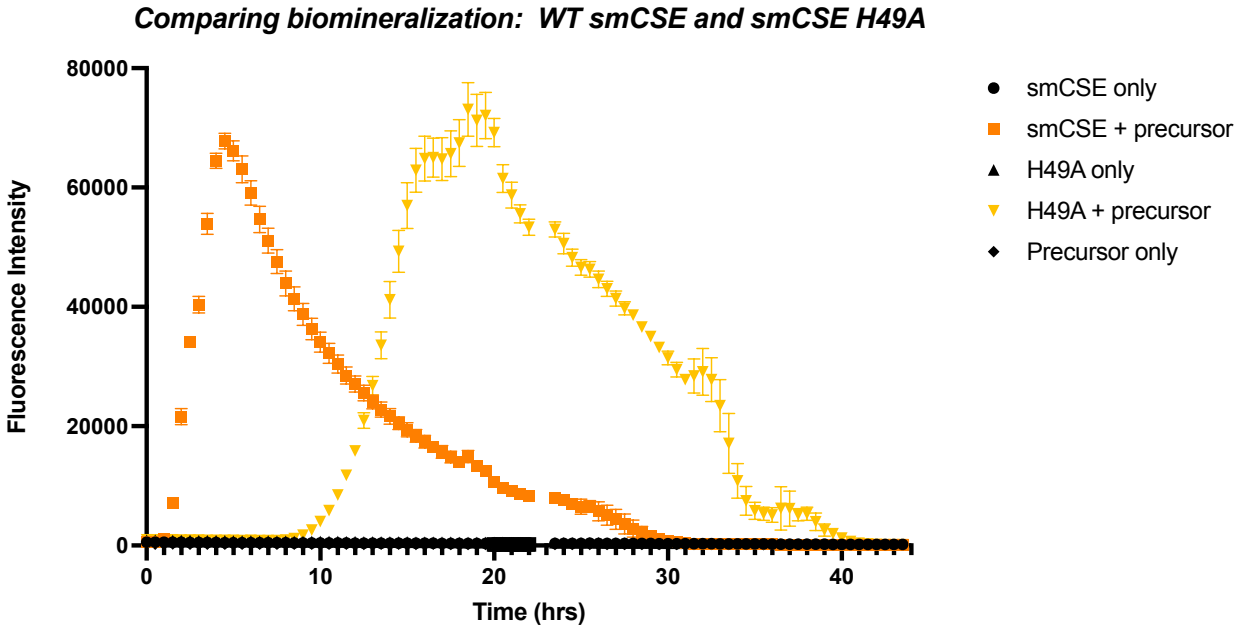

Figure 2A-3. Fluorescence over time shows cadmium sulfide quantum dot formation (exc. 360, em. 520 nm) of WT smCSE and mutant H49A.

ability of other residues or motifs to bind metal, implying a built-in redundancy that preserves protein function. For smCSE, the results with H49A support the possibility of an alternative binding site or mechanism of biomineralization, however the results with H351A do not. It is possible that H351A is the key for biomineralization with H49A providing additional support and redundancy.

Since production of H_2S is fundamental to smCSE biomineralization activity, H49A and H351A mutants were examined to determine if H_2S production remained intact. Intact H_2S production suggests that PLP binding and enzyme catalytic activity remains unchanged, and that any changes to biomineralization activity are due to enzyme interaction with the metal precursor. An H_2S generation assay shows that H49A and H351A retain H_2S production, as shown by the formation of dark pigment in Figure 2A-4. In the case of enzyme alone, no dark pigment is formed on filter paper soaked in a lead acetate solution. For enzyme with sulfur-containing L-cysteine, the filter paper soaked in lead acetate solution displays a dark color when reaction with H_2S occurs. For the WT and mutants, dark coloration results with the incubation of L-

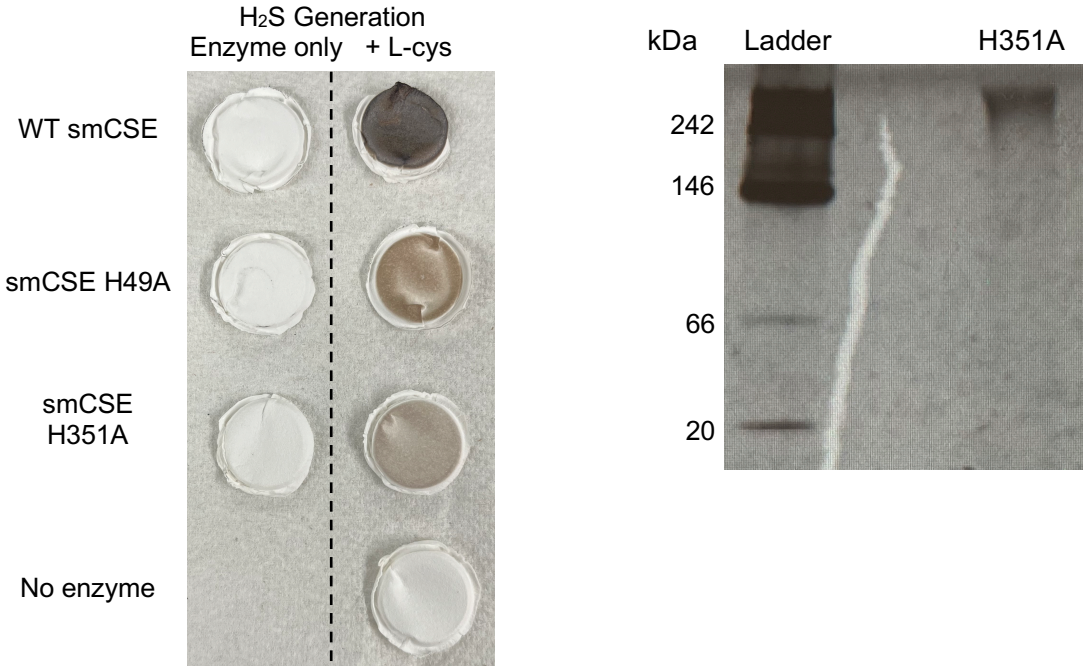

Fig. 2A-4. **A)** Hydrogen sulfide generation for WT smCSE, H49A, and H351A mutants. The "enzyme only" (negative control) and + L-cysteine conditions are shown as well as L-cysteine without added enzyme. **B)** Native PAGE for smCSE H351A. Band is above 242 kDa, anticipated tetramer molecular weight would be approximately 192 kDa.

cysteine. A no-enzyme control *(i.e.* L-cysteine in buffer solution) shows that the color change is not due to any auto-degradation of L-cysteine in solution. Consideration of this result together with the biomineralization results illustrates that changes in biomineralization activity are resulting from changes in enzyme interaction with metal precursor rather than any changes to catalytic activity. Further support for this premise is from native PAGE, showing tetramerization is retained in H351A (Fig. 2A-4).

Summary

The di-histidine motif has been implicated in metal coordination for Fe and Zn, with MamO and kallikrein respectively.[133,134] The crystal structure of smCSE (as performed by P. Mahanta, R. Acharya) shows Cd ion localization to H49 and H351. To probe the functional role of these histidine residues, we performed site-directed mutagenesis for each to create mutants H49A and H351A. H351A showed complete abolition of CdS QD production, while H49A showed delayed CdS QD production. H_2S generation of these mutants was examined to determine if the changes in QD production were due to changes in catalytic activity of the protein or changes in metal binding. In each case, H_2S generation remained intact. Furthermore, the oligomerization of H351A was evaluated via native PAGE, as previous reports show that tetramerization of the protein is necessary for activity.[63] Although resolution of this silver-stained native PAGE was low, it is clear that oligomerization of H351A is maintained. Altogether, these results show that changes in biomineralization production associated with H49A and H351A are due to changes in the metal cation binding mechanism, strongly supporting H49 and H351 as a metal-coordinating di-histidine motif.

Publication: *In preparation:* Vigil, T.N., Frost, A.J., Janiga, A.R., Mahanta, P., Acharya, R., Berger, B.W., "Structural basis for the CdS quantum dot (QDs) nanocrystals formation by cystathionine γ-lyase from Stenotrophomonas maltophilia strain (smCSE)" 2024.

Aim 2b

Hypothesis: smCSE has substrate flexibility to biomineralize REEs to sulfides, perhaps as a microbial survival mechanism to accommodate multiple challenges/threats. Since it has been established that smCSE will also mineralize Zn and Pb quantum dots,[62,63] it seems plausible that smCSE will interact with other metal salt substrates as well. Biomineralization activity with REEs will be instrumental in applying smCSE as a tool for REE extraction and recovery.

Approach: Previous work has reported smCSE biomineralization activity with Cd, Zn, and Pb to sulfides as well as selenides.[62,63,66,141] Since rare earth elements are of particular interest for many modern technologies, I will examine smCSE biomineralization of rare earth elements as a possible extraction tool. This can be evaluated both *in vivo* and *in vitro.* The main challenge will be confirming if a rare earth element sulfide is produced. Rare earth element sulfides are not well-characterized, with limited color descriptions and only few XRD spectra.[142,143] CdS quantum dot production exhibits fluorescent properties that serve as a visual signal to monitor biomineralization activity. Since rare earth element sulfides do not have any reported fluorescent properties, the limited colorimetric observational data will guide preliminary experiments, shown in table 2B-1.

Table 2B-1. Rare earth element sulfides and their colors.[142]

REE Sulfide	**Color**
b-La_2S_3	Light yellow
b-Ce_2S_3	Red
a-Nd_2S_3	Maroon
γ-Ce_2S_3	Red
γ-Nd_2S_3	Green

For our preliminary *in vitro* experiments I introduce rare earth element salts with well-established smCSE precursor L-cysteine. Visible precipitates are observed for color change, and further examined via UV-vis and XRD. I have done preliminary experiments with ceria ammonium nitrate (CAN), and further experiments will continue with lanthanum and neodymium salts. Ceria ammonium nitrate with L-cysteine and smCSE creates a red precipitate, consistent with Ce_2S_3 as made by Haibin et al.,[142] shown in Fig. 2B-1.

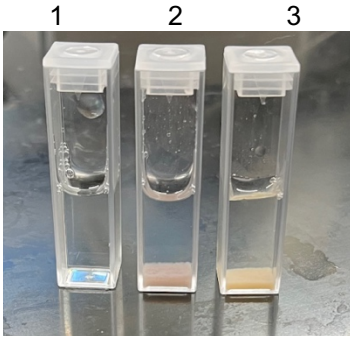

Figure 2B-1. smCSE biomineralization of CAN. Sample 1 is smCSE only, without precursors. Sample 2 is smCSE with CAN and L-cysteine. Sample 3 is CAN and L-cysteine.

Additional evidence supporting a reaction between smCSE and REE salts is the formation of a precipitate in the "smCSE + precursor" condition which is not matched by either the "smCSE only" or "precursor only" condition. With a surplus amount of L-cysteine in solution, the "precursor only" condition may form some precipitate, however, for this work 4 mM was found to be most appropriate. With higher L-cysteine concentrations (8, 16 mM), L-cysteine crystals precipitated alone and could be visualized via XRD. Previous works report a range of L-cysteine concentrations from 4 mM to 32 mM[62,63,138] in various ratios to cadmium precursor (1:8, 1:5, 1:4). With a 1:8 ratio of precursor metal to L-cysteine, REE sulfides were examined via XRD (Fig. 2B-2, 2B-3).

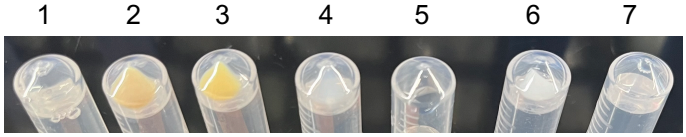

Figure 2B-2. Preliminary biomineralization with smCSE and REEs. Sample 1) smCSE only, 2) smCSE + ceria ammonium nitrate + L-cysteine, 3) ceria ammonium nitrate + L-cysteine, 4) smCSE + lanthanum (III) nitrate + L-cysteine, 5) lanthanum (III) nitrate + L-cysteine, 6) smCSE + neodymium (III) nitrate + L-cysteine, and 7) neodymium (III) nitrate + L-cysteine. Precipitates evident in samples 2, 3, 4, and 6.

Comparisons of XRD spectra for compounds made via biomineralizataion with smCSE are compared to XRD spectra for known REE sulfides (Fig. 2B-4). There are many known lanthanum sulfides, including LaS_2, La_3S_4, LaS, La_5S_7, and La_2S_3. Although each of these lanthanum sulfide compounds exist, the lanthanum cation only has a 3+ oxidation state suggesting that the most likely compound is La_2S_3. In spite of this, the XRD spectra from the lanthanum compound produced with smCSE seems to have a variety of peaks that may correspond with each. LaS_2 shows a triplet peak at approximately 23° which is similar to the sample. It is likely that the lanthanum sulfur compound produced is a mixture of LaS_2, La_3S_4, LaS, La_5S_7, and La_2S_3. Spectra matching with HighScore suggests that this compound is close to La_3CuSnS_7, $La_2Ti_4(SO_4)_{11}$, $LaK(SO_4)_2$, La_3CuGaS_7 which is consistent with identification of a lanthanum sulfide compound. Cu, Sn, Ti, and Ga are not present in the reaction solution which accounts for the incompleteness of matching with the spectra. K may be present in small amounts in the buffer or as residual from cell culture conditions, however, is not likely to be a major component.

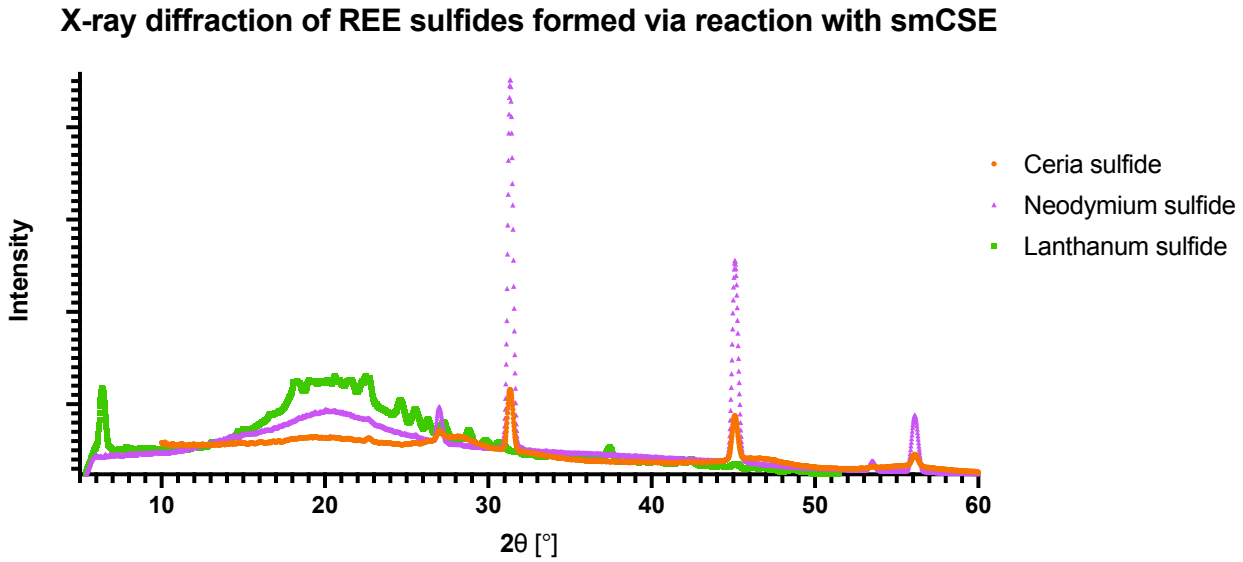

Figure 2B-3. X-ray diffraction spectra for REE sulfide compounds formed via reaction with smCSE.

Preliminary identification of ceria sample via XRD does not match known CeS ICSD spectra exactly, but seems to be slightly right shifted with a notable level of baseline noise. Interestingly, although XRD shows CeS rather than Ce_2S_3, the precipitate observed in these experiments was red or pink. Ceria has 2+, 3+, and 4+ oxidation states, while H_2S generated with smCSE sulfur has a 2- oxidation state. This may suggest that

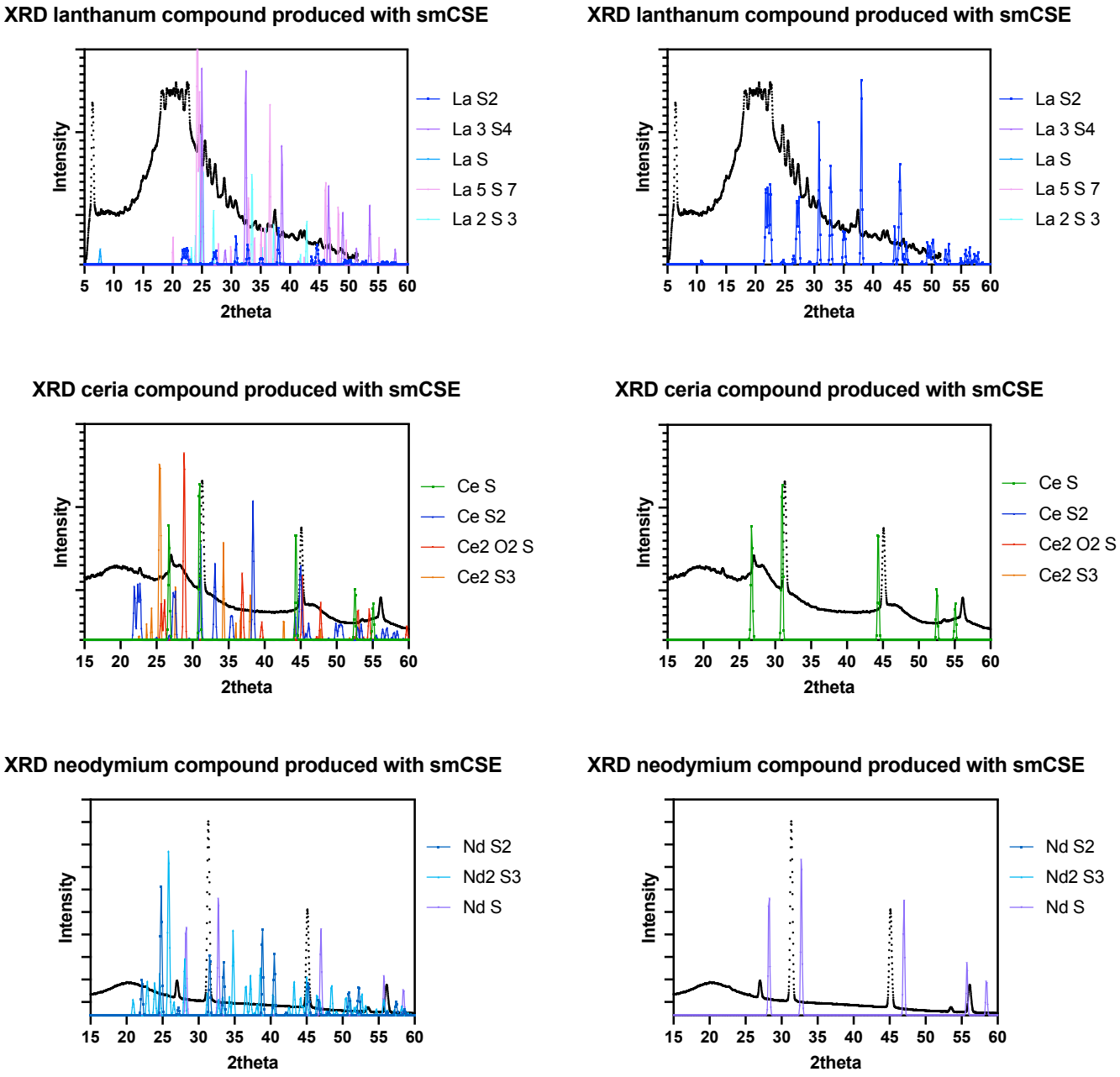

Figure 2B-4. XRD spectra comparing REE sulfide samples made via enzymatic biomineralization with smCSE and known REE sulfide compounds (left). The closest matches are shown on the right.

CeS_2 and Ce_2S_3 are the most likely compounds generated, however the spectra do not match. Spectra matching with HighScore suggests that this compound is close to $Ce_{0.5}Gd_{0.5}S$, which may further support a preliminary identification of CeS. CeS reportedly is a yellow solid. Once the precipitate is dried it transitions from the blush color to a yellow-orange. With greater amounts of precipitate product, a visual assessment of color would be more accurate than at present.

Neodymium has 2+, 3+, and 4+ oxidation states suggesting that NdS, NdS_2, and Nd_2S_3 are all possibilities for the compound generated via reaction of smCSE and neodymium (III) nitrate. XRD for the neodymium sample produced a spectra matching NdS. Notably, this is NdS rather than Nd_2S_3 which previous studies have recorded as green. This identification is consistent with the precipitate generated via biomineralization, which is seems to be white or colorless. Spectra matching with HighScore suggests that this compound is close to $LiNdS_2$ and $NaNdS_2$, which is consistent with identification as a neodymium sulfide compound.

Cadmium acetate, lead acetate, and zinc chloride are each precursor compounds for smCSE biomineralization to CdS, PbS, and ZnS quantum dots.[62,63,138] Each precursor species has the metal cation in a 2+ oxidation state, therefore the biomineralization product of NdS as produced with neodymium precursor makes sense as the neodymium cation can have 2+, 3+, and 4+ oxidation states. Cerium is most commonly in oxidation states of 3+ and 4+, but also has a 2+ oxidation state. The production of CeS as biomineralization product follows. Lanthanum exists in oxidation state 3+, with much lesser prevalence in 1+ and 2+ oxidation states, which may explain why smCSE biomineralization of lanthanum does not yield any clear lanthanum sulfide species, but apparently a mixture of several.

Cations with 2+ oxidation states are likely to be suitable substrates for biomineralization with smCSE. A comparison between smCSE biomineralization with cadmium acetate and L-cysteine and cadmium acetate, ceria ammonium nitrate, and L-cysteine shows no significant difference between production of CdS

quantum dot time-lapse curves (Fig. 2B-5). This suggests that smCSE biomineralizes cadmium acetate to cadmium sulfide at comparable rates regardless of the presence of another substrate. For rare earth element recovery, this result may indicate that smCSE will preferentially mineralize cadmium over cerium, therefore we can anticipate cadmium sulfide precipitation to bulk prior to cerium sulfide precipitation to bulk when both precursor cations are present in solution. One possible explanation is that cadmium acetate has cadmium cation in 2+ oxidation state, where-as ceria ammonium nitrate has cerium in the 4+ oxidation state, in which case reaction occurs more easily between H_2S and Cd^{2+}.

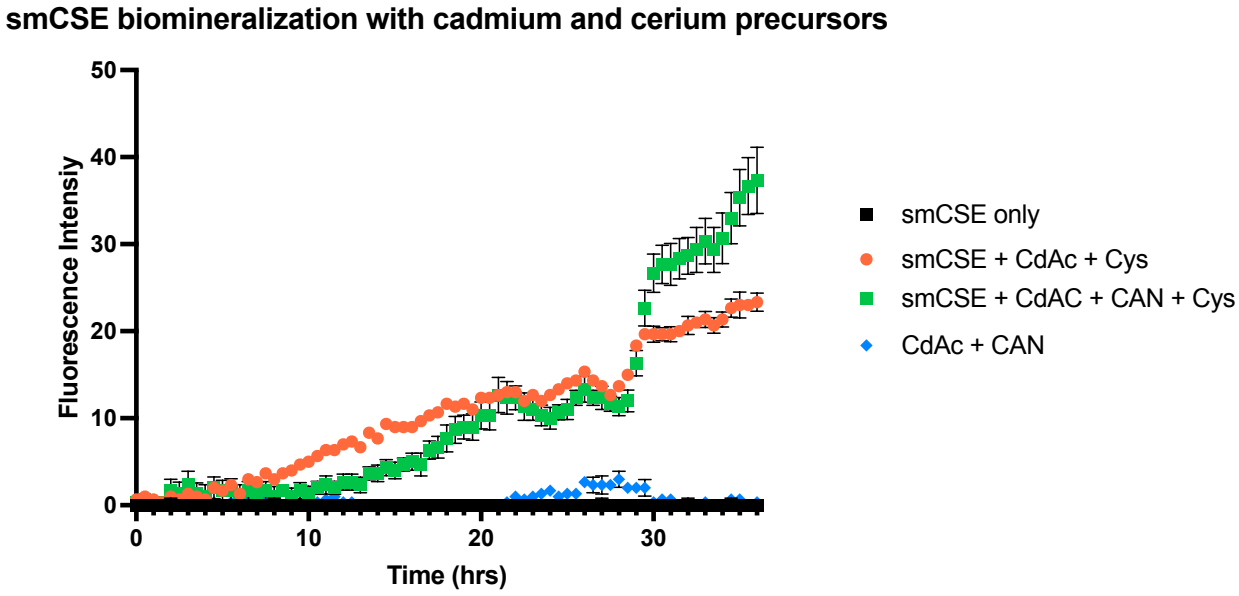

Figure 2B-5. smCSE biomineralization with cadmium and cerium precursors evaluated via fluorescence (exc 360 nm, em 520 nm) over 36 hours. Fluorescence is indicative of CdS quantum dot formation. CeS quantum dots do not fluoresce with this excitation and emission. Area under the curve is 376 and 373 for smCSE + CdAc + Cys and smCSE + CdAc + CAN + Cys respectively, illustrating no significant difference (two-tailed unpaired t-test, t=0.0061, df=144, p = 0.9951).

Summary

Understanding the smCSE metal binding motif (as in Aim 2a), with H49 and H351 supports substrate biomineralization with 2+ metal cations. Previous work showing smCSE biomineralization with Zn and Pb[62,63] strengthen the hypothesis that smCSE has substrate flexibility to biomineralize REEs to sulfides.

This hypothesis is supported by the work shown here, where-in smCSE is able to mineralize ceria, lanthanum, and neodymium precursors to sulfides as shown with XRD. The dominant sulfide species shown in XRD match CeS and NdS most closely, which shows that Ce and Nd in the 2+ oxidation state interact with the H_2S generated by smCSE. The XRD spectrum for the lanthanum product of smCSE biomineralization is more difficult to match, suggesting that there may be a variety of lanthanum sulfide compounds such as LaS_2, La_3S_4, LaS, La_5S_7, and La_2S_3. Finally, an evaluation of cadmium acetate and ceria ammonium nitrate biomineralization with smCSE suggests that smCSE preferentially biomineralizes cadmium acetate before ceria ammonium nitrate. A likely explanation is that in cadmium acetate, cadmium is in the 2+ oxidation state, whereas in ceria ammonium nitrate ceria is in the 4+ oxidation state, therefore via the di-histidine motif, cadmium 2+ coordinates in the binding region more readily. This possibility could be more thoroughly assessed via binding affinity experiments with isothermal titration calorimetry or microscale thermophoresis.

Aim 2c

Hypothesis: smCSE treatment in mining or e-waste streams will produce biological soil crusts via precipitation due to biomineralization, wherefrom valuable elements and minerals can be reclaimed.

Approach: Recent work by Kuang et al. explores algal-based biological soil crusts for acid mine drainage treatment.[144] Two major challenges for acid mine drainage treatment are the harsh acidic conditions and toxic contaminants.[144] Current treatment options often require harsh pH conditions and solvents, while also producing more toxic waste. A biological approach via biomineralization may be a greener and safer alternative. smCSE has already shown biomineralization activity with Cd, Zn, and Pb which are all found in relatively large amounts in acid mine drainage.[50,145] Additionally, the originating species *Stenotrophomonas maltophilia* displays a degree of tolerance to harsh pH conditions.[141] Using a biological soil crust approach, I can evaluate smCSE for the reclamation of REEs from acid mine drainage.

Biological soil crusts are made up of a biological agent such as bacteria, fungi, or algae, combined with abiotics such as clay. For our system, I can consider smCSE affixed to a surface, over which acid mine drainage will flow. Ideally, smCSE biomineralization will grow the biological soil crust with mineralized Cd, Zn, Pb, and REEs, forming a chunk which can later be collected. To investigate, I apply a dilute, mixture of cadmium acetate and L-cysteine over an IMAC column previously treated with smCSE, noting any color changes, fluorescence, or precipitate formation. Any of these could be indicative of biomineralization, with fluorescence being the most easily detectable. The proposed process is shown in Fig. 2C-1.

The same general process can be used for an e-waste slurry.

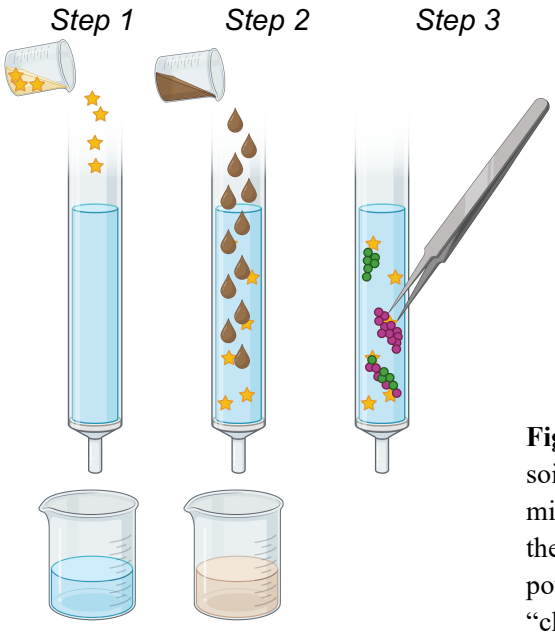

Figure 2C-1. Proposed column biological soil crust formation for smCSE and waste mixtures. In step 1, the protein is affixed to the column. In step 2, the waste mixture is poured over the column. In step 3, the REE "chunks" are visible and available for collection. Figure made with Biorender.

Results

Approximately 1 mg smCSE was added to an immobilized metal affinity chromatography column pre-treated with nickel chloride. Flow through was collected. To wash the column (and simulate flow) 50 mL 100 mM HEPES buffer was added to the column and flow through was collected. Next, 50 mL of 0.5 mM cadmium acetate and 4 mM L-cysteine hydrochloride were added to the column and flow through was collected. A UV check of the column did not show any fluorescence. An additional 50 mL HEPES buffer was added to the column and flow through was collected, followed by 50 mL 0.5 mM cadmium acetate and 4 mM L-cysteine hydrochloride. The column did not show any fluorescence. 50 mL additional HEPES buffer was added to the column then collected. The column did not show any fluorescence. At this point we have six 50 mL tubes of flow through which were also checked for fluorescence. No fluorescence was observed. Presumably the protein was bound to the column, but no biomineralization occurred with addition of the precursors due to short residence times.

Biomineralization with smCSE usually generates detectable levels of quantum dots (exc 360, em 520 nm) starting at the 5 hour mark. In this test, precursors were only co-incubated with smCSE for a few minutes maximum. Furthermore, the flow through tubes did not show any detectable fluorescence over a week-long period, indicating that smCSE did not leave the column as precursors flowed over. From this experiment, it seems necessary to increase the exposure of smCSE to precursors. If done over a column, this would mean increasing residence time. Another approach may be a prolonged incubation in solution, similar to the *in vitro* biomineralization experiments performed in test tubes.

To simulate batch-wise long-term incubation smCSE-soaked filter paper was added to a pool of precursor solution in a small petri dish with a non-smCSE filter paper control. Overnight incubation of these dishes did not show any evident reaction or detectable fluorescence. However, with prolonged incubation over 96 hours, fluorescence is evident in the smCSE + precursor case (Fig. 2C-2). Additional precursors were added to solution and fluorescence was sustained at 120 hours.

These results suggest that a batch-wise reactor system is more appropriate for applications of smCSE to critical mineral extraction than a flow reactor. Furthermore, it is notable that 96 hours were required to visualized detectable fluorescence in these experiments although other work shows smCSE biomineralization starting as quickly as 1 hour. Additionally, no bulk precipitation of CdS was observed here, further supporting the premise that the reaction is slowed. This may be due to the localization of smCSE to the filter paper support, although there is not any anchoring mechanism preventing smCSE from leaving the filter paper to float freely in solution. With longer incubation times accompanied by the addition of cadmium acetate and L-cysteine precursors, it is likely that bulk CdS precipitation will occur, however, over a 7-day incubation period bulk precipitation was not observed.

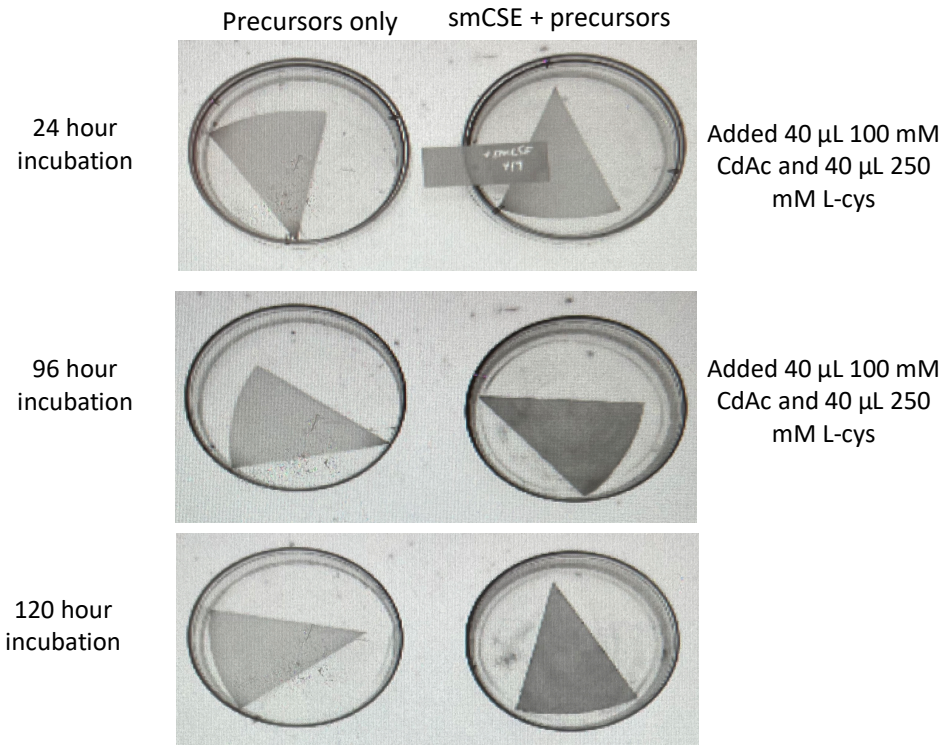

Figure 2C-2. Small batch reaction of smCSE, cadmium acetate, and L-cysteine as compared to cadmium acetate and L-cysteine (no enzyme) conditions over a time-course of several days. At 24 hours of incubation, there is no detectable difference in fluorescence between the precursor only condition and the smCSE + precursor condition. Additional precursors were added to each. After 96 hours, there is notable difference in fluorescence between the two cases (fluorescence manifests as darkness with this imager).

Summary

The formation of biological soil crusts via precipitation due to enzymatic biomineralization may be promising for the reclamation of critical minerals, including rare earth elements. Here I examine flow-type reaction conditions (analogous to an acid mine waste stream) with smCSE to induce precipitation of rare earth elements. The flow-type reaction does not have sufficient retention time of precursor colocalization with enzyme, illustrating no visible precipitation (i.e. biological soil crust formation). The alternate approach explored with a batch-type reactor system showed smCSE biomineralization of cadmium on solid porous substrate. Although there was no visible precipitation, biomineralization was exhibited via

fluorescence of CdS quantum dots. To support biological soil crust formation, longer reaction times and increased precursor concentrations should be examined.

Materials and Methods

Protein production and purification

pet28a(+) cystathionine gamma-lyase and mutants were transformed into *E. coli* BL21. Single colonies were picked for starter cultures in LB, grown at 37 °C shaking overnight. Cultures were centrifuged at 3,000 x g for 10 minutes and supernatant discarded. Cell pellet was inoculated in LB with kanamycin (minimum 50 mL) and grown to OD600 of 0.6-0.8. At OD600 > 0.6, isopropyl β-D-1-thiogalactopyranoside (IPTG) was added to a final concentration of 0.1 mM and flasks moved to 20 °C shaking incubator overnight. Cells were harvested via centrifugation at 3,000 x g for 10 minutes and supernatant discarded. Pellet was resuspended in sonication lysis buffer (5% v/v glycerol (99+%) , 36 mM tris HCl, 20 mM tris base, 100 mM NaCl, and 5 mM imidazole) at 5 mL buffer / 1 g pellet. Lysis was performed via sonication at 20% amplitude, for 20 minutes in 20 second on/off pulses. Lysate was centrifuged at 10,000 x g for minimum of 10 minutes, supernatant was collected and filtered with 0.4 μm syringe filter then purified via his-tag affinity chromatography. At this stage, the supernatant is generally transparent yellow in color. Purification fractions were collected and analyzed via 8% SDS PAGE.

Note: smCSE is insoluble in less than 100 mM imidazole. Dialysis cannot be performed into an imidazole-free solution. Precipitated smCSE can be resolubilized with dialysis into 500 mM imidazole. For the purposes of this work, protein concentrations were measured via A280 with an appropriate imidazole blank.

SDS-PAGE

8% SDS-PAGE with Blue Precision Plus Protein ladder (Biorad) was loaded with denatured lysates and purified samples, run at 110 V for 10 minutes, then 150 V for 1 hour. For staining, gel was transferred to fixing solution with Coomassie blue for at least 30 minutes (0.025% w/v brilliant blue, 7.5% v/v acetic acid, 50% v/v ethanol (95%), and 42.5% v/v DI H_2O), then de-stained (7.5% v/v acetic acid, 10% v/v

ethanol (95%), and 82.5% v/v DI H_2O) for 1 hour. Imaged with colorimetric transillumination on Amersham Imager 680.

Native PAGE

8% Native PAGE with Native Mark Unstained Protein Standard ladder (ThermoFisher) and protein samples (>50 mmol/L) was run at 110 V for 2 hours in 1.5x native PAGE buffer (192 mM glycine, 25 mM tris, pH 8.3). Gel was stained with FASTsilver (G Biosciences) or Coomassie staining solution. For biomineralization assay, gel was run normally then cut into three separate pieces and transferred to appropriate stains / buffers for 12 hours. The Coomassie blue stained gel was imaged with colorimetric transillumination. Buffer control and 2 mM CAN gels were imaged at 460 nm excitation to detect nanoceria. Fluorescence gels were imaged using an Amersham Imager 680 with semi-automatic exposure.

Silver Stain

FASTsilver kit from EMD Millipore. All steps performed on an orbital mixer. Gel was incubated in fixative I (30% ethanol, 10% acetic acid) for at least 30 minutes, then washed twice for 10 minutes each in fixative II (10% ethanol). Next, gel was washed three times for 10 minutes in DI H_2O. Following water discard, gel was soaked in sensitizing solution (5 mL silver, 65 µL sensitizer I, 45 mL DI H_2O) for 30 minutes. For 10-20 seconds, gel was rinsed in DI H_2O then soaked in developer (2.5 g developer powder, 32.5 µL sensitizer I, 32.5 µL sensitizer II, 45 mL DI H_2O) until bands are visible. 5 mL stopper solution (22% acetic acid) was added and gel was left to rock on orbital mixer for 10 minutes.

Site-directed mutagenesis

Site-directed mutagenesis for H49A and H351A mutants was performed with Monarch Q5 Site-Directed Mutagenesis kit (NEB) according to manufacturer's protocol followed by Q5 KLD reaction and transformation into *E. coli* DH5α. Transformations were performed via electroporation, quenched with 1 mL LB, then incubated at 37 °C shaking for at least 1 hour. Cultures were centrifuged at 3,000 x g for 2

minutes to precipitate cells, then cells were resuspended in 100 µL and plated on kanamycin. Plates were incubated at 37 °C overnight. Colony PCR was performed with T7 and T7term to amplify DNA insert. PCR products were purified via Monarch PCR and DNA Clean-up Kit (NEB), then sent to Eurofins Genomics for Sanger sequencing.

H49A F – 3' CAGCCCGGGTGAGGCCCAGGGCTTCGAG 5'

H49A R – 3' CTCGAAGCCCTGGGCCTCACCCGGGCTG 5'

Annealing temperature: 62° C, extension time 4 minutes

H351A F – 3' GCGGTGATGACGGCTGCGTCGATTCCG 5'

H35A R – 3' CGGAATCGACGCAGCCGTCATCACCGC 5'

Annealing temperature: 63° C, extension time 7 minutes (shorter extension time would also likely be adequate)

Biomineralization of cadmium sulfide

0.1 mg/mL smCSE, 0.5 mM CdAc, and 4 mM L-cysteine were combined in DI H_2O. Absorbance and fluorescence measurements were taken at intermediate intervals. Fluorescence was measured in with BioTek Synergy Neo2 plate-reader at excitation 360 nm and emission 520 nm. Time course of these experiments was varied from 18-36 hours and gain was adjusted from 100 to 50 as needed.

Biomineralization of rare earth elements

0.1 mg/mL smCSE, 0.5 mM ceria ammonium nitrate and 4 mM L-cysteine were combined in DI H_2O. Solutions were initially clear. After 24 hours incubation at room temperature, a blush-colored precipitate was evident in ceria samples. Experiments with lanthanum and neodymium were set up in the same manner.

Precipitates formed with lanthanum and neodymium experiments were white. A minimum of 10 mL total biomineralization experiments were combined and centrifuged to isolate sufficient samples for XRD.

H_2S generation assay

This assay was adapted from Bruna, N. *et al.* (2022).[146] Filter paper was soaked in 5% w/v lead acetate solution, then dried at 37 °C. The filter paper was then cut to fit inside the lid caps of tubes used for biomineralization assay experiments. Samples were prepared as 0.1 mg/mL protein and 4 mM L-cysteine in DI H_2O. Caps with filter paper were screwed onto samples tubes tightly and samples were allowed to react for a minimum of 24 hours.

X-ray diffraction

Samples were characterized with a Bruker ApexII Duo diffractometer with a Cu 1.54 angstrom source at room-temperature with expertise from Dr. Diane Dickey at the UVa XRD Core (instrument funding from NSF-MRI program (CHE-2018870)). Sample spectra were compared and matched to standards listed in the Inorganic Crystal Structure Database and HighScore Plus.

Extracting REEs via biocrust simulation on column

1 mg smCSE was added to an immobilized metal affinity chromatography column pre-treated with nickel chloride. Flow through was collected. Column was washed with 50 mL 100 mM HEPES buffer and flow through was collected. 50 mL of 0.5 mM cadmium acetate and 4 mM L-cysteine hydrochloride was added to the column and flow through was collected. Alternating HEPES buffer and cadmium acetate L-cysteine hydrochloride solutions were applied to the column for two additional rounds. Fluorescence on the column was checked with a UV flashlight periodically. Flow through for each fraction was collected and fluorescence was checked in subsequent days.

Extracting REEs via biocrust simulation in small batch long-term incubation

Filter paper was soaked with purified smCSE. (Water soaked filter paper was used for control). 3 mL of DI H_2O were added to a 60 mm diameter plastic dish and the protein-soaked filter paper was added. 40 µL 100 mM cadmium acetate and 40 µL 250 mM L-cysteine hydrochloride were added to each dish. Lids were placed on dishes and reaction incubation proceeded at room temperature overnight. Fluorescence was measured via imaging with blue excitation and automatic exposure on Amersham Imager 680.

Chapter 3: Identifying microbes and proteins compatible with the harsh conditions associated with rare earth elements

**Portions of this work are described in manuscript "Microbial mineralization with Lysinibacillus sphaericus for lithium nanoparticle extraction"*

Key Findings

- *Lysinibacillus sphaericus* shows PAH degradation
- *Lysinibacillus sphaericus* exhibits lithium biomineralization activity
- Particles mineralized by *L. sphaericus* are 2 nm LiOH
- LigFa is not promising for a biosensor via recombinant production in *E. coli*

Rare earth elements are in high demand for modern technology, however, are difficult to find and identify. In this work, I aim to learn more about the microbes and proteins native to REE conditions: ***3a)*** exploring microbes native to polycyclic aromatic hydrocarbon (PAH)-rich environments via culture from coal samples and evaluating growth with PAHs as carbon source and ***3b)*** probing for any biomineralization properties. While concurrently ***3c)*** modifying acidophilic protein LigFa to bind REEs rather than native substrate iron.

Aim 3a

Hypothesis: Although environmental pollutants are harmful to most life forms, microbes often evolve unique adaptations to address these challenges, as is often the case with microbes and environmental contaminants.[147–149] Therefore, I hypothesize that microbes native to PAH-rich environments (such as coal mines), will have unique PAH degradation abilities.

Approach: One obstacle in REE recovery is their entrapment in complex bitumen. Bitumen is a tarry substance made up of PAHs and other viscous hydrocarbon compounds. By isolating bacterial species from coal (a bituminous compound) I select for traits that enable survival and growth in these conditions. For this work, a coal sample from western Virginia was mixed with cell growth media, then incubated in 37 °C shaker overnight. This solution was then spread on LB agar plates and incubated and grown overnight. Colonies grown were sent for 16s RNA sequencing (Azenta Life Sciences), facilitating the identification of several species native to western Virginia coal, as seen in Table 3A-1.

Table 3A-1. Bacteria identified from western Virginia coal samples

Prevalence in sampling	*Species*	*Known characteristics*
20%	*Pseudomonas songnenensis*	Previously identified in alkaline, saline environments[149]
30%	*Bacillus aryabhattai*	Close proximity to plants, endophytic[150]
5%	*Bacillus velezensis*	Fresh water and saline environments, antimicrobial activity, potential as bio-fertilizer and bio-pesticide[151]
25%	*Lysinibacillus sphaericus*	Hydrocarbon degradation activity, endophytic, adsorption of toxic metals[152]

Each of the above species has been preliminarily identified in other works, with notable tolerance to saline and alkaline environments in *Pseudomonas songnensis* and to a lesser degree in *Bacillus velezensis*.[150–153] However, since *Bacillus velezensis* had relatively low prevalence (5%, Table 5), this species will not be evaluated in preliminary work. The limited information available for *Bacillus aryabhattai* notes association with plants,[151] which may or may not contribute positively to survival in the harsh conditions associated

with REEs. Most promisingly, *Lysinibacillus sphaericus* has been previously observed to have hydrocarbon degradation activity.[152]

Preliminary experiments with *P. songnenensis, B. aryabhattai,* and *L. sphaericus* in minimal salt media with PAHs and short chain hydrocarbons as the only available carbon source show growth of all three species. (PAH aqueous solubility is a challenge and there are different approaches in literature, including the *L. sphaericus* culture to solid PAHs.[154]) In this work, I dissolve PAH in heptane, then mix with *L. sphaericus* culture with the hypothesis that soluble PAH is more readily available for *L. sphaericus* consumption. In the short chain hydrocarbon (no PAH) condition, *L. sphaericus* seems to have significantly more growth than either *P. songnenensis, or B. aryabhattai* as seen in Fig. 14. One approach to quantifying total growth and the differences between species may be to integrate for the total area under the curve (AUC). Initial AUC calculations for the "Growth in hydrocarbon" condition give *L. sphaericus* a value of 11.2, then *P. songnenensis* and *B. aryabhattai* values of 4.50, 7.58, respectively.

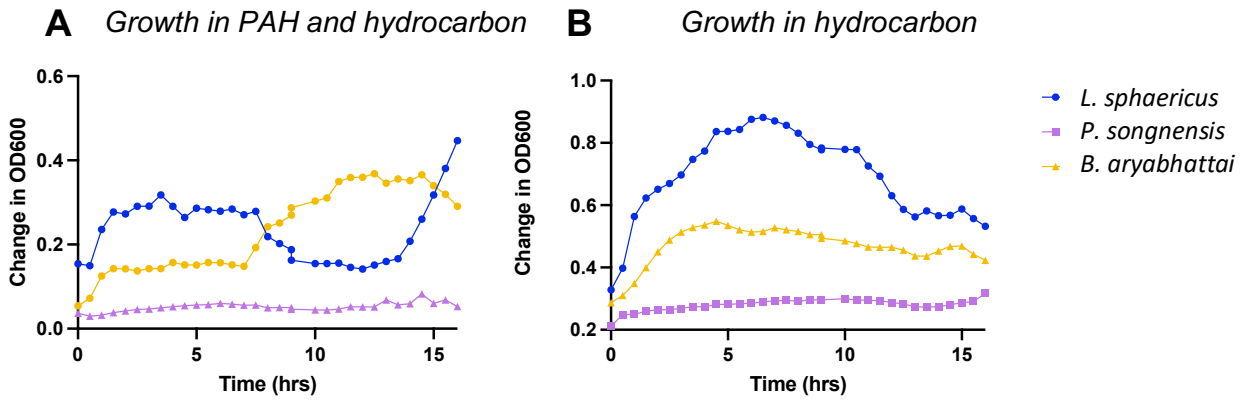

Figure 3A-1. Growth of *Lysinibacillus sphaericus*, *Pseudomonas songnensis*, and *Bacillus aryabhattai* over 16 hours. **A**) Each bacteria are grown in a hydrocarbon and PAH minimal media mixture, **B**) bacteria grown in hydrocarbon minimal media mixture.

With AUC growth curves in mind, *L. sphaericus* was chosen for further studies for PAH degradation. Growth conditions for *L. sphaericus* were adapted to 30° C shaking over 48-hour periods. Nonetheless,

PAHs continued to be most soluble in heptane, which presents a safety challenge when utilizing a Bunsen burner to maintain a sterile environment. Less flammable solvents were checked for PAH solubility, however heptane remained the only available solvent to readily solubilize PAHs. To mitigate safety concerns, PAHs in heptane were handled in a bio-safety cabinet to maintain sterility.

To highlight consumption of PAHs as sole carbon source, 100 µL of 0.1% w/v PAH was added to a final volume of 200 µL minimal media– therefore, final PAH concentration was 0.05% w/v. PAHs examined were naphthalene ($C_{10}H_8$) and anthracene ($C_{14}H_{10}$) dissolved in heptane. *L. sphaericus* showed growth with both naphthalene and anthracene as sole carbon sources, with an approximate increase of 0.5 in OD600 over a period of 18 hours. The compiled curve in figure 3A-2A shows growth of *L. sphaericus* from an OD600 of 0.5 to 1.0, however, other experiments show similar trends with *L. sphaericus* growth starting at 0.2, 0.4, or even 0.6. In each case, OD600 initially dips prior to rising again. These curves do not show the common sigmoidal exponential growth seen with *E. coli*, instead displaying behavior that is more biphasic.

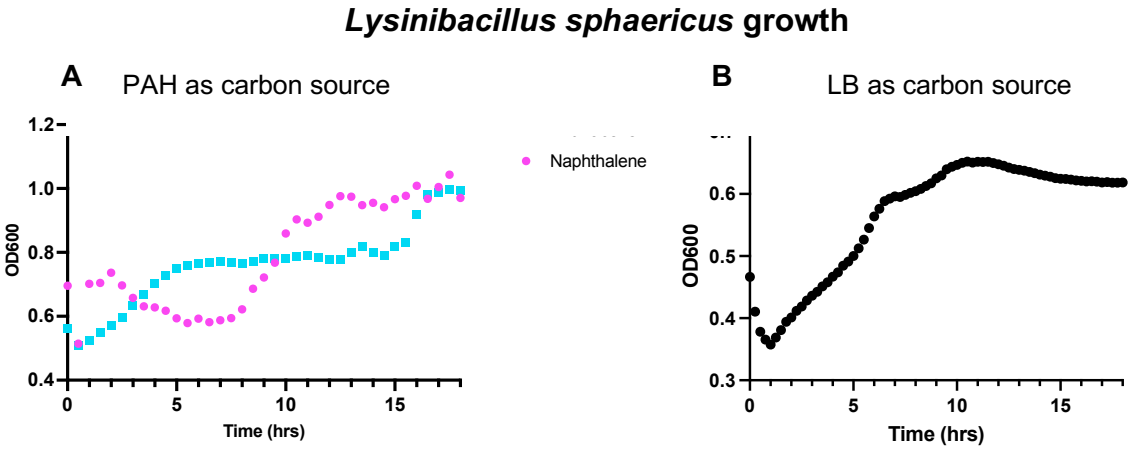

Figure 3A-2. *Lysinibacillus sphaericus* growth with A) polycyclic aromatic hydrocarbons as sole carbon source and B) LB as a carbon source over a period of 18 hours. For PAHs, blue shows growth with anthracene while pink represents growth with naphthalene.

Biphasic growth may suggest that *L. sphaericus* initially consume a preferred carbon source before transitioning to consuming PAHs. This behavior is commonly seen with *E. coli* when two carbon sources are present. In this work, however, *L. sphaericus* is in minimal media (no carbon source) and heptane dissolving the target PAH. Based on Figure 3A-1 it may be reasonable to extrapolate that the biphasic growth is due to a transition between heptane and PAH as carbon sources, as panel A, with both heptane and PAH as carbon sources shows growth, decrease, then growth, and panel B, where heptane is the sole carbon source shows growth then a decrease. In other words, the shape of the curve in panel B looks like the initial shape of the curve in panel A, but the curve changes in panel A due to the presence of PAH. Furthermore, an early consumption of heptane would ultimately result in precipitation of PAH, which has not been experimentally observed. Non-traditional bacterial growth curves are also consistent with cellular stress,[155–157] which is likely occurring here. This suggests that although *L. sphaericus* can grow with PAH as sole carbon source, it is not the preferred carbon source, which is especially evident with consideration to *L. sphaericus* growth with LB (Fig. 3A-2B). With LB as a carbon source, *L. sphaericus* growth follows a trajectory similar to classic exponential growth curves, with an exponential phase followed by a stationary phase.

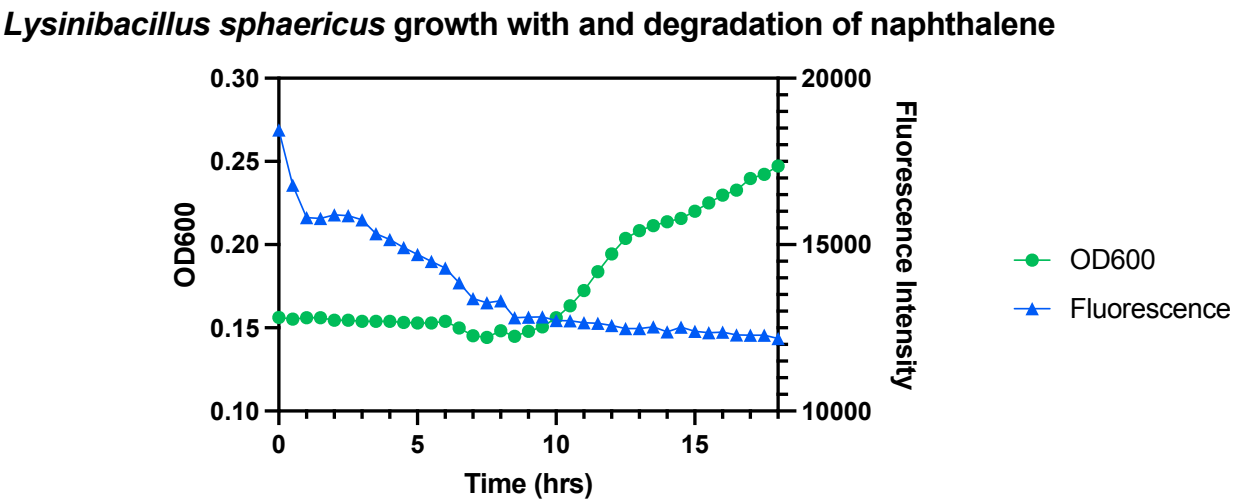

Figure 3A-3. *Lysinibacillus sphaericus* growth with and degradation of naphthalene. Time-course for *L. sphaericus* growth in minimal media with naphthalene (OD600, left y axis) compared to fluorescence intensity (arbitrary units, right y axis).

The degradation of naphthalene as monitored by fluorescence (exc. 350 nm, em. 450 nm) was compared with *L. sphaericus* growth (Fig. 3A-3). Notably, naphthalene undergoes significant fluorescence quenching in aqueous solution,[158] which provides some explanation to the relatively narrow range in change of fluorescence shown here. With that consideration, there is still notable decline in fluorescence intensity over the 18 hour time interval measured. A simple linear regression curve fit shows a slope of -263, or a decline in fluorescence of 263 fluorescence intensity units per hour. While this is an average value based on the entire curve, the decline between 0 and 9 hours is approximately 5,000 fluorescence intensity units (over the entire time course, the change is approximately 6,000 fluorescence units), which produces a local slope of -556 fluorescence intensity units per hour.

While naphthalene degradation occurs most from hours 0 to 9, the OD600 of the culture does not significantly change over the initial 9 hours. Simple linear regression curve fit of the whole data set gives a slope of 0.005 OD600 units per hour, from hours 0 to 9 however there is no change in slope, then from hours 9 to 18, the OD600 increases from 0.15 to 0.25. The relationship between fluorescence and OD600 shows that fluorescence decreases, i.e. naphthalene is degraded, from hours 0 to 9 while OD600 only

increases from hours 9 to 18. This illustrates that naphthalene degradation results in cell growth after a lag in time.

Preliminary experiments with powderized coal on LB agar plates were performed, but no *L. sphaericus* growth was observed. Similar experiments in liquid culture visually showed bacterial growth, however, analysis opportunities were limited by the presence of coal (i.e. measuring OD600 or other absorbance is impossible due to the overwhelming absorbance associated with coal dust).

Summary

Four species of bacteria were identified via 16s rRNA sequencing of bacteria grown in coal samples. These species were identified as *Pseudomonas songnenensis, Bacillus aryabhattai, Bacillus velezensis,* and *Lysinibacillus sphaericus.* The growth of each species in minimal media with PAH as carbon source showed that *L. sphaericus* seems to be capable of the degradation and consumption of PAHs for growth. Growth in minimal media with naphthalene or anthracene as PAHs showed biphasic growth curves. An analysis of naphthalene fluorescence during this growth period showed fluorescence loss alongside gain in OD600, further supporting the degradation and consumption of PAH for bacterial growth.

Future work

To further evaluate the possible role of *L. sphaericus* for bitumen degradation, *L. sphaericus* growth should be characterized in bituminous mixtures. Preliminary experiments with *L. sphaericus* and coal in minimal media present major challenges in measuring OD600 or separating cells and coal particles. To incrementally evaluate the possibility for bitumen degradation with *L. sphaericus,* polymer compounds such as PEG are being explored. Additional avenues of experimentation that should be pursued are 1) *L. sphaericus* growth times as it is possible that with longer growth times different degrees of PAH degradation will occur and 2) HPLC analysis of breakdown products.

Aim 3b

Hypothesis: Microbes native to PAH-rich environments, such as coal mines, are also likely exposed to metal precursor compounds, and accordingly may also have unique biomineralization adaptations that enable their survival. Previous work by Mangwani, et al. shows heavy metal tolerance accompanied PAH tolerance and degradation with *Stenotrophomonas acidominiphila*,[159] therefore it is reasonable to anticipate biomineralization may accompany PAH degradation.

Approach: The four bacteria species previously identified from western Virginia coal mine samples will be evaluated for biomineralization activity. Preliminary experiments will utilize cadmium salts, as cadmium is a situationally relevant metal that also displays fluorescent properties when mineralized from salt to oxide or sulfide. This will enable quick *in vivo* experiments in liquid culture, assuming that the metal precursor accesses the cell. In the case of *L. sphaericus*, which is reportedly able to adsorb toxic metals, it is likely cadmium will be taken up by the cell.

Further exploration with REEs can be conducted with similar methods to Paper, *et al.*'s work with REEs and cyanobacteria, which utilizes ICP-OES to measure the increase in REE concentration over time with the cyanobacteria.[160] This approach is limited due to the destructive nature of the technique and the analytical precision required to evaluate bio-accumulation of REE. However, if bio-accumulation is observed, then XRD will be used to determine if biomineralization has occurred. Additionally, the degree of bio-accumulation will be an important factor to note, in order to evaluate how well our species attract or interact with REEs. Very low levels of bio-accumulation, while interesting, are likely not impactful enough to contribute (even in a small portion) to meeting the world-wide demand for REEs.

Results: Each of the three coal friends evaluated showed some tolerance to ceria ammonium nitrate (CAN) on LB-agar plates. The concentrations of CAN here are greater than the critically toxic concentrations

observed with *E. coli* and silicatein (0.6 mM). Figure 3B-1. shows *L. sphaericus* growth in 10 and 100 mM conditions, while *P. songnensis* and *B. aryabhattai* each have substantial growth in each CAN concentration. Furthermore, there does not appear to be notable differences in the amount of growth per each CAN concentration for *P. songnensis* and *B. aryabhattai.* These results suggest that each of these species has some tolerance to CAN, and therefore may be a good candidate for biomineralization.

As a critical mineral, lithium was also used in subsequent screenings. In preliminary experiments, we examined the physical interaction between co-incubation of ceria, lanthanum, neodymium, and lithium salts in minimal salt media with *L. sphaericus, B. aryabhattai,* and *P. songnensis.* CAN, lanthanum nitrate, and neodymium nitrate each showed precipitation in the media alone. Therefore, precipitation with the co-

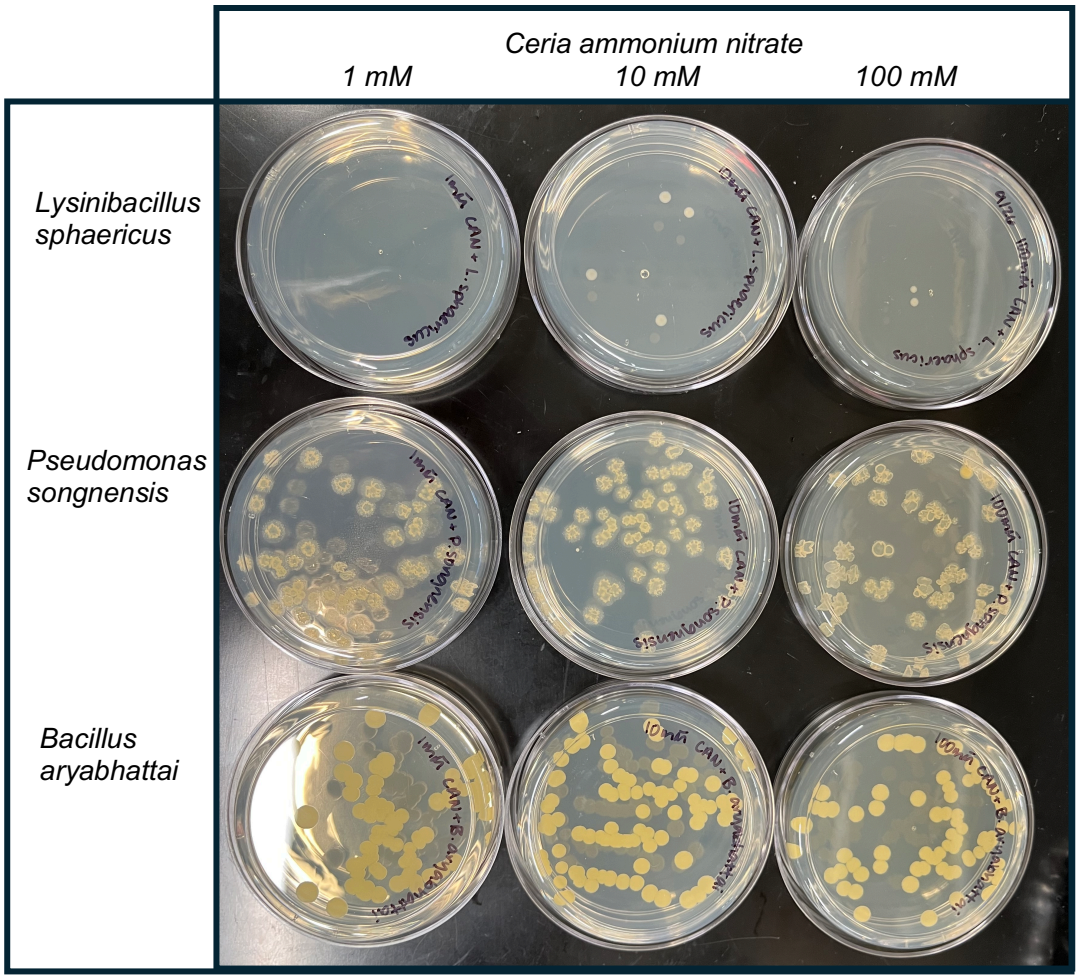

Figure 3B-1. Coal friends survival and tolerance to ceria ammonium nitrate.

incubation of *L. sphaericus, B. aryabhattai,* and *P. songnensis* could not be attributed to an interaction between the bacteria and salt. Lithium chloride, however, did not precipitate in media, and therefore precipitation upon co-incubation with *L. sphaericus* and *B. aryabhattai* is indicative of a physical interaction between the bacteria and salts, suggesting potential biomineralization activity. Further experiments with *B. aryabhattai* showed no significant precipitation, therefore *B. aryabhattai* was not examined further.

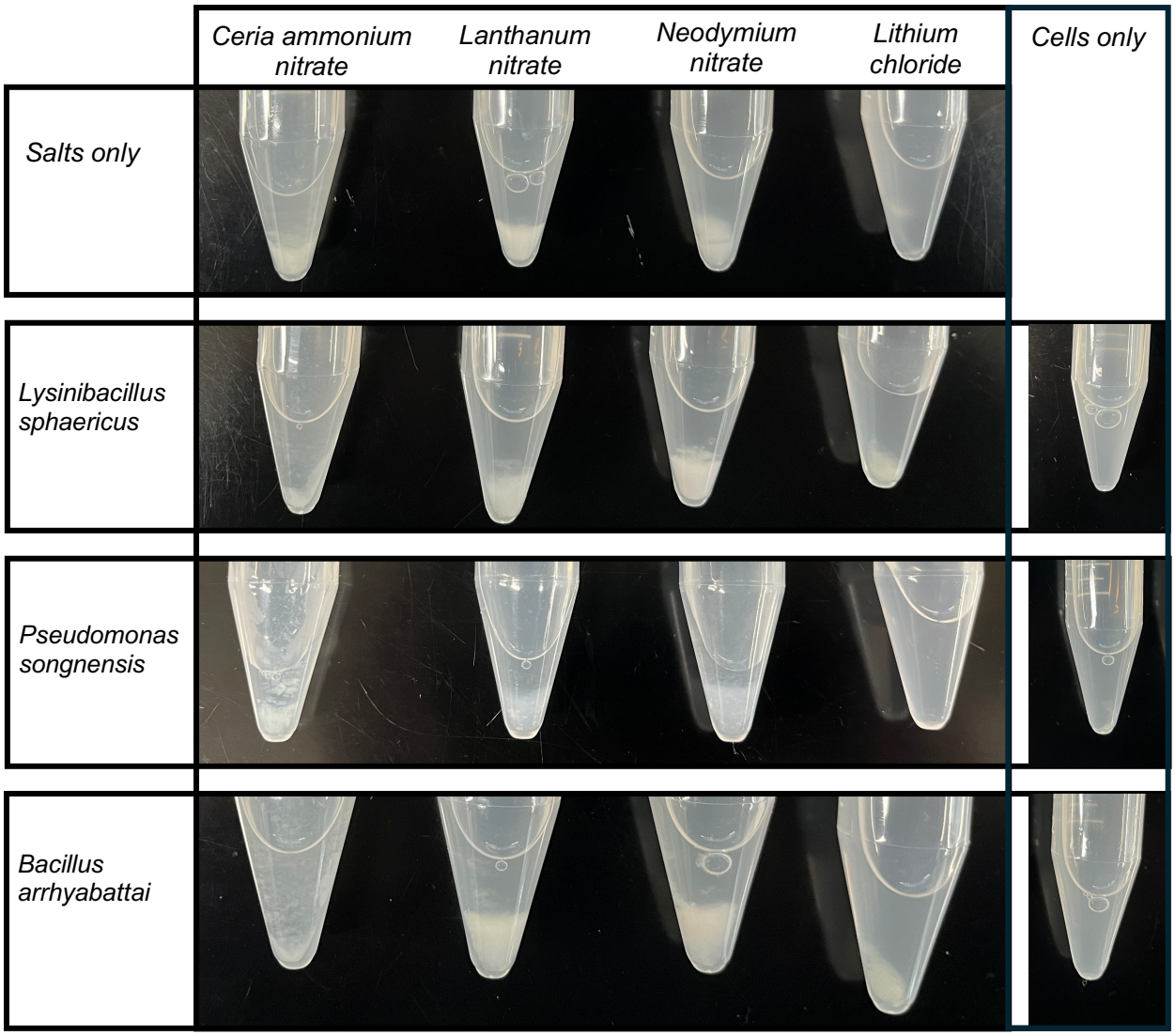

Figure 3B-2. Coal friends screening with ceria ammonium nitrate, lanthanum nitrate, neodymium nitrate, and lithium chloride in liquid culture.

Additional experiments co-incubating *L. sphaericus* with lithium salts showed repeated precipitation after 24-48 hours. To quantify the lithium precipitation, we utilized a fluorescent assay where-in the complexation of 2-(2-hydroxyphenyl)-benzoxazole (HPBO) with lithium results in quantifiable fluorescence.[161] Obare and Murphy report selective complexation of lithium with HPBO over sodium and potassium,[161] which is instrumental in this work to specifically quantify lithium extraction.

Here, we compared the lithium precipitation associated with *L. sphaericus* and lithium chloride salt in minimal salt media. In Figure 3B-3, lithium recovery with *L. sphaericus* is approximately 6x increased compared to the lithium in media condition. These results were statistically evaluated with an unpaired t-test, yielding a p value of 0.0011. Further, *L. sphaericus*, lithium chloride, and an equivalent amount of sodium chloride in minimal salt media was tested to evaluate possible specificity between *L. sphaericus* and lithium (Fig3B-3B). In this case, when combined with both lithium and sodium salts, *L. sphaericus* yields approximately 20x more lithium than sodium, indicating that *L. sphaericus* biomineralizes lithium specifically over sodium.

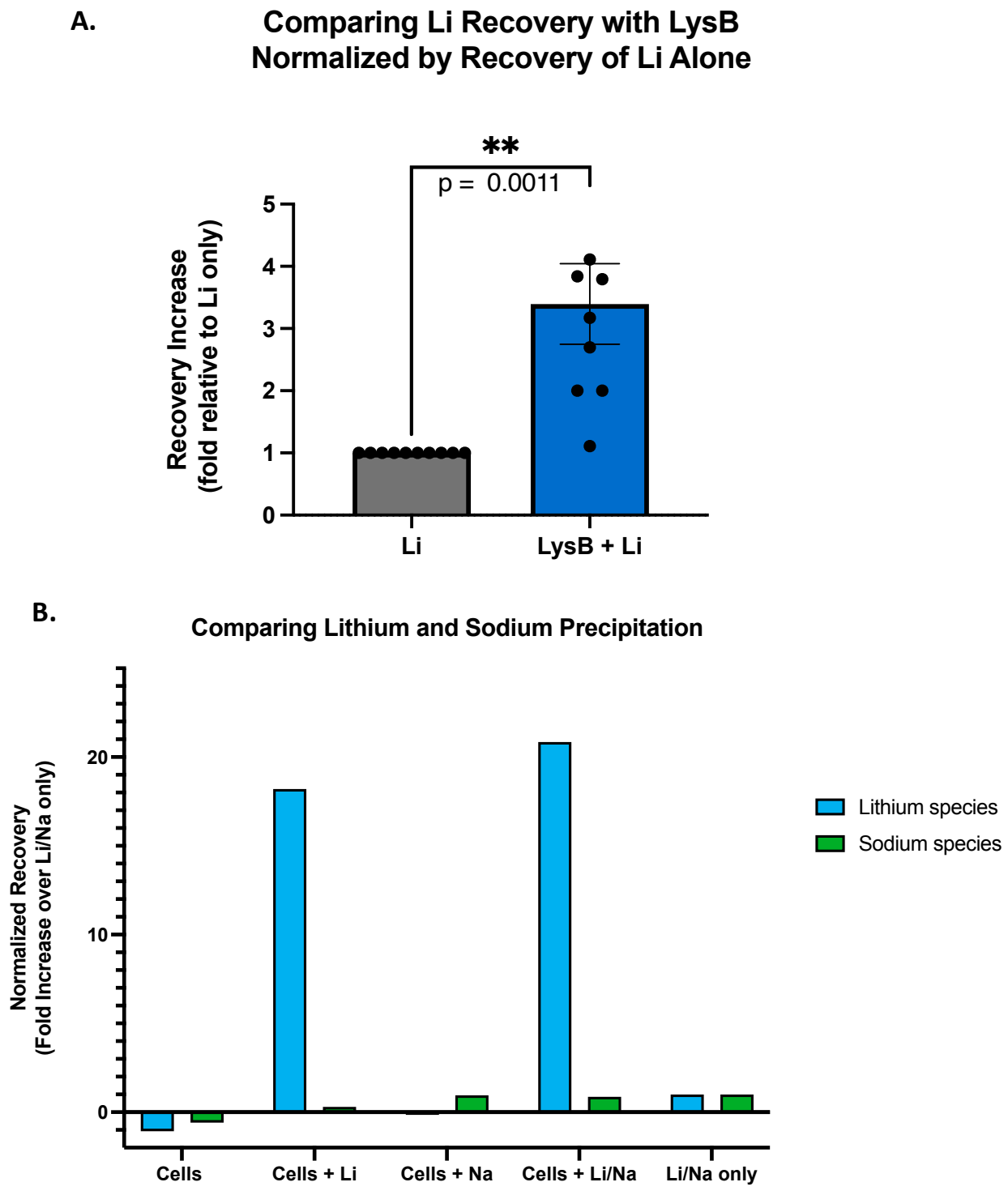

Figure 3B-3. **A)** Lithium recovery following incubation with *Lysinibacillus sphaericus* cells as measured by HPBO fluorescent assay. "Li" is the LiCl only condition, normalized to 1. *L. sphaericus* coincubated with LiCl is "LysB + Li". A two-tailed un-paired t-test df = 17 results in p = 0.0011. **B)** Comparing lithium and sodium precipitation by *L. sphaericus,* as measured by HPBO and CoroNa green fluorescent assays. HPBO for lithium species, and CoroNa green for sodium species. "LysB + Li" and "LysB + Li + Na" show that lithium species are precipitated with LysB significantly more than in the "Li + Na only" condition. Further, "LysB + Li + Na" shows that lithium species are in much greater abundance than sodium species.

To further characterize the lithium precipitated via *L. sphaericus,* FTIR and TEM were performed on precipitates. FTIR showed strong -OH peaks at 3400 cm^{-1} as well as additional peaks at 2250, 1650, 1440, 1050, and 900 cm^{-1} (Fig 3B-4). Database spectra for lithium hydroxide show a strong peak at 3600 cm^{-1}, broad peak at 2800 cm^{-1}, 2350 cm^{-1}, strong 1600 cm^{-1}, and 1000 cm^{-1}. With consideration to the relative impurity of particles generated with *L. sphaericus*, the observed 3400 cm^{-1} peak may correspond with reference peaks at 3600 cm^{-1}, broad peak at 2800 cm^{-1}, observed 1650 cm^{-1} with reference strong 1600 cm^{-1}, and observed 1050 cm^{-1} with reference 1000 cm^{-1}. These features are consistent with Li(OH). Notably, Li(OH) remained stable in acetonitrile as well as DI H_2O for a minimum period of weeks, suggesting that there may be biomolecules aiding in stability.

TEM characterization of LiOH NPs showed fairly monodisperse particles of 2.1 (+/- 0.4) nm diameter (Fig 3B-5). Fourier transform of particles reveals that they are highly crystalline. These monodisperse crystalline particles further suggest that there are biomolecules interacting on the surface of the particles to

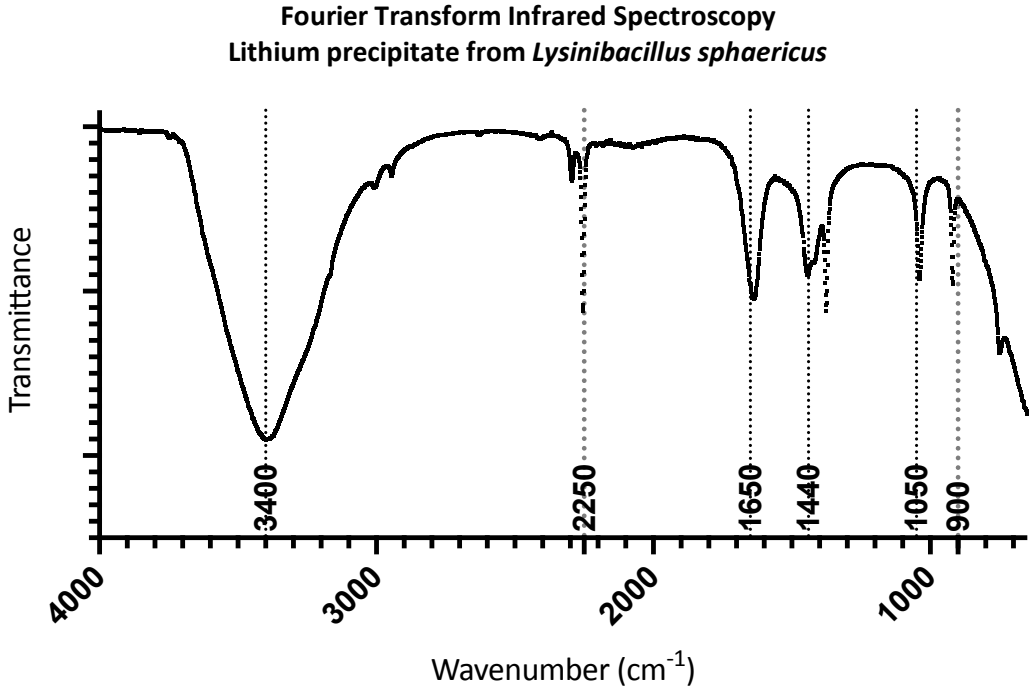

Figure 3B-4. Fourier transform infrared spectra for precipitated lithium. Notable peaks at 3400, 2250, 1650, 1440, 1050 and 900 cm^{-1}

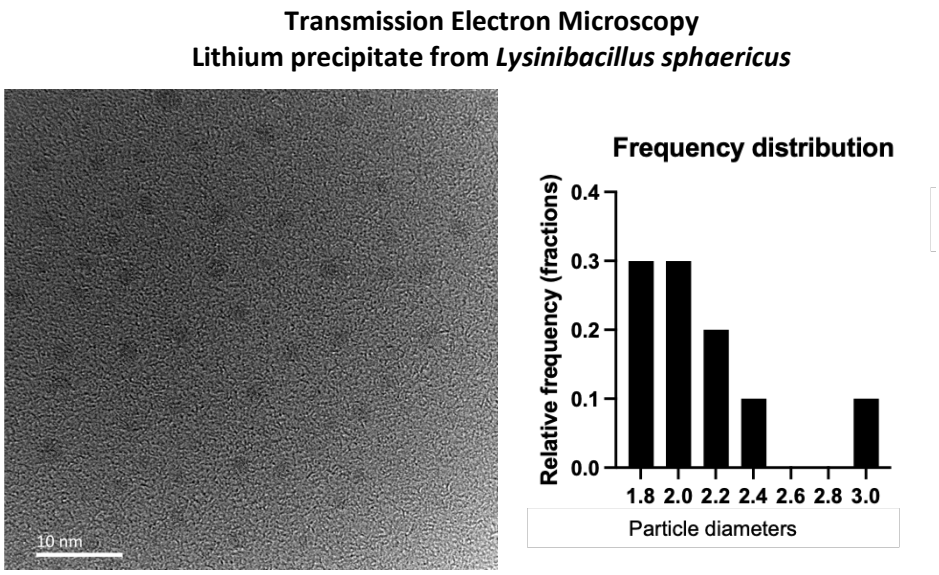

Figure 3B-5. Transmission electron microscopy imaging for lithium hydroxide nanoparticles. N=10. Avg diameter 2.1 +/- 0.4 nm.

stabilize them both chemically and physically. This is a relatively common occurrence with nanoparticles, where-in these biomolecules are known as capping ligands. Capping ligands impact the final physical form of particles.[4] Accordingly, we sought to identify the identity of the biomolecules.

With the discovery that *L. sphaericus* is able to convert lithium salts to relatively stable lithium hydroxide nanoparticles and to identify the biomolecules capping particles and potentially guiding biomineralization, LC/LC ESI mass spectrometry was used. SDS-PAGE facilitated the identification of approximate sizes of

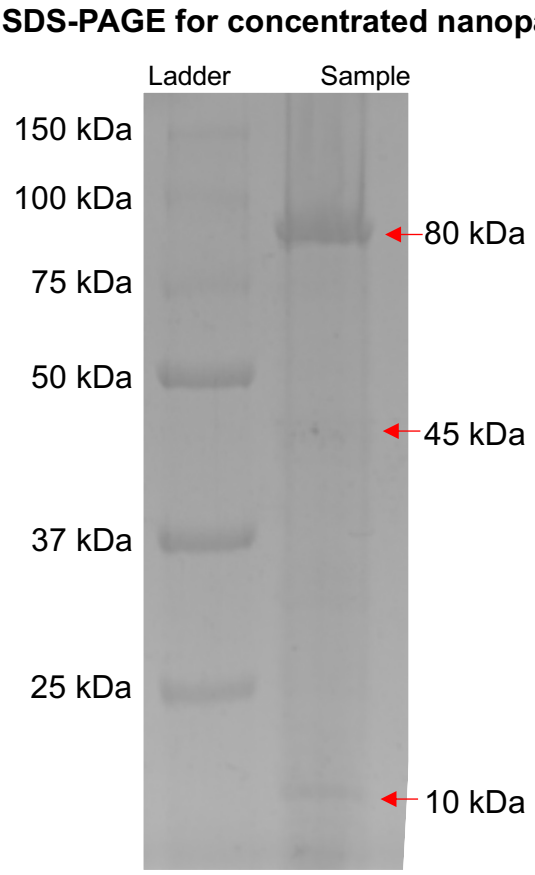

Figure 3B-6. SDS-PAGE for concentrated LiOH nanoparticles. 80, 45, and 10 kDa bands were taken for analysis via mass spectrometry.

biomolecules associated with the particles, showing major bands at approximately 80 kDa, 45 kDa, and 10 kDa (Fig 3B-6). With mass spectrometry, several biomolecules were identified, as shown in Table 3B-1.

Although the S-layer homology domain protein has an actual mass of 122 kDa, it was unsurprising that it is involved in *L. sphaericus* biomineralization. Several previous studies have shown metal affinity with the S-layer of *L. sphaericus,* suggesting that the negatively charged membrane interacts with positively charged metal ions.[162–166] One of these studies includes the biomineralization of gold nanoparticles with *B. sphaericus.*[162] The identification of S-layer homology domain protein is further supported by the apparent upregulation of S-layer proteins upon exposure of *L. sphaericus* with lithium (Supplemental Figure S.3B-5). Importantly, not every organism with an S-layer shows ready biomineralization.[165] The additional

bands shown in Fig 3B-6 at 45 and 10 kDa suggest the involvement of other protein biomolecules in this biomineralization process.

Table 3B-1. Biomolecules associated with LiOH nanoparticles as identified by ESI-LC-MS/MS

	Protein	Accession number (Swiss prot)	Percent coverage	Actual Mass (kDa)
80 kDa band	S layer homology domain containing protein	A0A7T2FPH4	36%	122
	Catalase OS= Lysinibacillus sp	A0A7T2FL42	28%	72
	Uncharacterised protein OS= Lysinibacillus sp	A0A2S0JR96	20%	12
	Aldehyde dehydrogenase family protein	A0A4U2YUK3	12%	31
	ATP synthase subunit alpha OS=Ureibacillus sinduriensis	A0A0A3H6SI	10%	55
	Glyceraldehyde 3 Phosphate dehydrogenase	A0A0A3IG21	12%	37
45 kDa band	Chaperonin GroEL OS=Lysinibacillus sp	A0A7T2Cq17	29%	57
	Peptide ABC transporter substrate binding protein	A0A7T2FPN4	17%	61
	Oligopeptide ABC transporter substrate binding protein	A0A7T2FPB5	18%	65
	Catalase OS= Lysinibacillus sp	A0A7T2FL42	11%	72
10 kDa band	Flagellin OS= Lysinibacillus odysseyi	A0A0A3IGC1	16%	29
	Flagellin OS = Lysinibacillus sp	A0A7T2FPL2	12%	29
	ZincABC transporter substrate binding protein	A0A7T2C5D6	7%	34
	HTH cro/C1-type domain containing protein	A0A806LIM6	9%	7.5

The proteins identified at 80 kDa were S-layer homology domain protein, catalase, an aldehyde dehydrogenase family protein, ATP-synthase subunit alpha, and glyceraldehyde-3-phosphate dehydrogenase. Aldehyde dehydrogenases, ATP-synthases, and glyceraldehyde-3-phosphaete dehydrogenases each have known interactions with metal ions, such as magnesium and iron, but also copper, cobalt, and lead.[167–169]

The proteins identified at 45 kDa were Chaperonin-GroEL, peptide ABC transporter substrate-binding protein, oligopeptide ABC transporter substrate-binding protein, and catalase. The presence of Chaperonin-GroEL peptide is interesting when considered in the context of silicatein and DnaK overexpression. Chaperonin-GroEL and DnaK are both chaperone proteins of the same family, and their co-occurrence in these separate biomineralization cases may suggest that chaperone proteins play a significant role in

biomineralization. Alternatively, it may suggest that chaperone proteins are able to enhance biomineralization, and therefore current biomineralization strategies could be improved with the addition of a chaperone. This premise is indicative that there are a multitude of proteins playing a role in biomineralization, such as with silicatein, silintaffins, and silaffins in the native marine sponge.[32,170] An interplay between multiple proteins and biomolecules may entail that single-enzyme biomineralization is not the most efficient way to produce the desired nanoparticles. Peptide and oligopeptide ABC transporter substrate-binding proteins show some roles in binding metal cations and metal detoxification.[171–173] Catalase (which was identified in both 80 and 45 kDa bands) has previously been implicated for upregulation in response to high metal stress conditions, and also requires bound iron for native activity.[174,175] With each of these proteins that natively binds metal cations, it is possible that here there is binding promiscuity with lithium, however that does not specifically account for the biomineralization to lithium hydroxide nanoparticles.

The proteins identified at 10 kDa were flagellin, Zinc ABC transporter substrate binding protein, and HTH/cro/C1 type domain containing protein. The presence of flagellin (an outer surface protein for the cellular chemotaxis) is consistent with the findings of the S-layer homology domain protein, as both are displayed on the outside of the cell. As implied by name, Zinc ABC transporter substrate binding protein normally binds zinc. As an ABC transporter, Zinc ABC transporter can be considered alongside peptide and oligopeptide ABC transporters as a metal cation binder and response for cellular metal detoxification.[171–173]

Probing the role of the S-layer protein in biomineralization

Crystalline S-layers are present in a variety of bacteria and archaea.[165,176] The S-layer can be separated from the cell and it's contents, creating what is known as a "ghost."[176] Figure 3B-7 shows an SDS-PAGE on ghosts with a band at the anticipated molecular weight for S-layer protein. To evaluate the role of the S-layer in LiOH nanoparticle production, we performed biomineralization assays with live *L. sphaericus* (positive control), UV-killed *L. sphaericus,* and *L. sphaericus* ghosts. If the S-layer entirely mediates biomineralization of LiOH nanoparticles, we would anticipate UV-killed *L. sphaericus* and *L. sphaericus* ghosts to produce equal amounts of LiOH nanoparticles as live *L. sphaericus.* If UV-killed and ghosts produce less LiOH nanoparticles, this suggests that the live cell (i.e. some metabolic process characteristic of the live cell) is necessary. For these experiments, the amount of *L. sphaericus,* UV-killed *L. sphaericus,* and ghosts was normalized by OD600 at the beginning of biomineralization experiment. This is not a perfect metric, as it is plausible that ghosts absorb differently at 600 nm than live *L. sphaericus*, but it seems to be the most practical method given the alternatives. One alternative is to measure total protein concentration in each solution via Bradford or BCA assay. While this alternative may seem appealing, we must consider that the live *L. sphaericus* condition will always have a higher concentration of total protein than a ghost condition because live *L. sphaericus* has the S-layer protein and the entire protein contents of the cell, while ghosts will only have the S-layer and associated proteins. Therefore, normalizing by total protein concentration in this way will effectively result in more ghosts than total S-layer in the live cell condition. Normalizing the relative amount of S-layer in each solution is further complicated by the probability that the cells in live *L. sphaericus* grow over the 48-hour biomineralization period. Therefore, even if normalized at the beginning of the experiment,

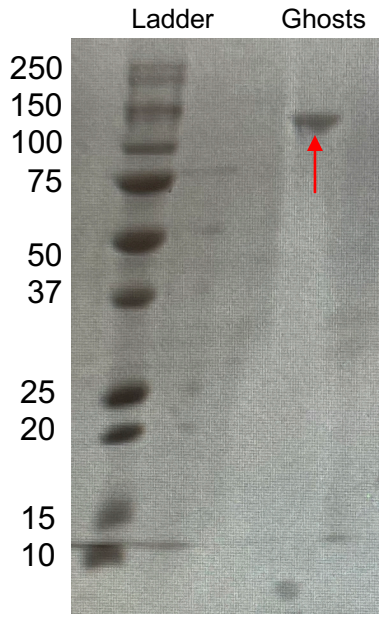

Figure 3B-7. SDS-PAGE gel for ghost extraction. MW of ghost proteins is anticipated at approximately 125 kDa. Band highlighted by red arrow is at approximately 125 kDa.

there will be a different amount of cells and S-layer protein at the end of the experiment. Accordingly, although normalizing via OD600 is not perfect, it is simple and sufficient for this preliminary work (Table 3B-2).

Table 3B-2. Normalizing *L. sphaericus* cells and ghosts via OD600 for biomineralization experiments.

	OD600	**OD600**	**OD600**
500 µL live *L. sphaericus*	0.042	0.007	0.027
50 µL live *L. sphaericus*	0.004	0.005	0.004
5 µL live *L. sphaericus*	0.003	0.004	0.002
No cells (LiCl only) condition	0.004	0.006	0.005
500 µL UV-killed *L. sphaericus*	0.035	0.005	0.021
50 µL UV-killed *L. sphaericus*	0.003	0.005	0.003
5 µL UV-killed *L. sphaericus*	0.005	0.010	0.003
20 µL Ghosts	0.005	0.008	0.004
10 µL Ghosts	0.003	0.006	0.005

Summary

With the rationale that microbes native to PAH-rich environments, such as coal mines, are also likely exposed to metal precursor compounds, this work identifies *L. sphaericus* from a western Virginia coal mine sample to evaluate biomineralization potential. Screening ceria ammonium nitrate, lanthanum (III) nitrate, and neodymium (III) nitrate did not reveal any notable interactions between *L. sphaericus* and these

salt species. Lithium chloride was also examined, as lithium is classified as a critical mineral worldwide.[177,178] When *L. sphaericus* is co-incubated with lithium chloride, an insoluble precipitate forms after 48 hours. Here I show that this precipitated lithium species is lithium hydroxide, that *L. sphaericus* preferentially biomineralizes lithium over sodium, and that this lithium hydroxide is in the form of discrete 2 nm particles. To further identify the individual proteins involved in this biomineralization process, ESI-LC-MS/MS was performed on LiOH nanoparticles, revealing 10 candidate proteins. One of these proteins was identified as S-layer homology domain containing protein, and as S-layers have been previously identified as potential metal ion interactors, we explored the role of S-layer ghosts for lithium hydroxide biomineralization. The precise proteins and mechanism of LiOH biomineralization with *L. sphaericus* is the focus of future work.

Future work

In order to determine if the whole cell, multiple proteins, or a single protein are necessary for lithium biomineralization and precipitation, each protein identified via mass spectrometry should be recombinantly expressed and evaluated individually (primers for amplification from genomic DNA are listed in Materials and Methods). Following individual evaluation of each, it may be beneficial to explore different combinations of the proteins. These experiments would be helpful in elucidating the mechanism of biomineralization, however may not be necessary for the direct application of *L. sphaericus* for lithium extraction. Preliminary experiments with high salt concentrations have been designed to evaluate the survival of *L. sphaericus* in a salt brine. This endeavor is complicated by the lack of reporting associated with salt brine compositions, as well as solubility challenges when mixing ultra-high concentrations of salts. To expedite this line of questioning, it would be advantageous to collect small samples from real lithium-extraction salt brines. This would allow for the evaluation of *L. sphaericus* to real-world salt concentrations as well as aiding in the understanding of what *L. sphaericus* applications within a salt brine might look like.

Aim 3c

Hypothesis: LigFa, an acidophilic protein from extremophile *Ferroplasma acidiphilium*, will bind rare earth elements (REEs) in place of natural substrate iron, while retaining optical activity.

Approach: A field use biosensor for REEs that could be deployed in acid mine drainage, e-waste, or other hostile environments would be most user-friendly. The low pHs characteristic of these circumstances present a challenge for the use of biologics, generally used at more neutral pHs.[179] To address this challenge first and foremost, and to design a biosensor that does not require extensive work-up of the sample prior to testing, I looked to acidophiles and associated proteins.[179] *Ferroplasma acidiphilium* is an acidophile with a purple DNA ligase (LigFa) generally found in environments of approximately pH 3. Iron is necessary for LigFa structure and function, with nearby tyrosine interactions resulting in the visible purple coloration.[69] Purple therefore serves as an optical indicator that iron is present with the protein. Acid tolerance and observable signal are both desirable properties for an REE biosensor.

Previous work with LigFa substituted iron for other elements (Cr(III), Al(III), W(IV)), observing limited colorimetric and functional changes.[69] Here, I will perform substitution of iron with REEs, monitoring changes in colorimetric properties. Importantly, previous work with LigFa required extremely high concentrations (100 mg/mL) to visually observe purple coloration.[69]

Results

In this work, LigFa was produced recombinantly in *E. coli* with IPTG induction, then purified by pH, dialysis, and lyophilization. The enzyme was resuspended in 10 mM citrate buffer (pH 3), then dialyzed in ferric nitroacetate (pH 3). Thus far, efforts to produce recombinant LigFa have yielded very low levels of protein, however sufficient amounts for detection with immunoblotting, as shown in Fig. 3C-1. Ferrer *et. al* do not specify any challenges with recombinant production of LigFa in *E. coli*, detailing a standard

procedure with LB growth media, IPTG-induction at OD600 of 0.6, and low temperature (20° C) overnight incubation.[69] With this protocol, we were able to produce recombinant LigFa and detect purple coloration via UV-Vis, as displayed in Fig. 3C-1. To increase protein expression, we varied media from LB to TB, induced at OD600 of 0.8, and varied temperature for induction. None of these changes resulted in significantly increased protein expression. Subsequent concentration of protein never exceeded 70 mg/mL for 1 mL.

Table 3C-1. LigFa concentrations for various samples. Sample volumes were approximately 1 mL.

Sample	Concentration (mg/mL)
7/14	7.6
7/26	60.6
7/27	62.5
8/2	5.7
8/12	2.7
8/15	10.3
8/18	4.5
8/22	1.2
8/24	2.0
9/8	6.2

Even with 70 mg/mL, no purple coloration was observed. Importantly, previous work with LigFa required extremely high concentrations (100 mg/mL) to visually observe purple coloration.[69] Although purple coloration could not be observed visually here, we were able to show absorbance at 564 nm via UV-vis (Fig. 3C-1, 3C-2).

For application of this protein as a biosensor ease of protein expression is fundamental. Furthermore, visible changes in coloration (with the eye) would be preferrable to changes in color that must be detected with instrumentation.

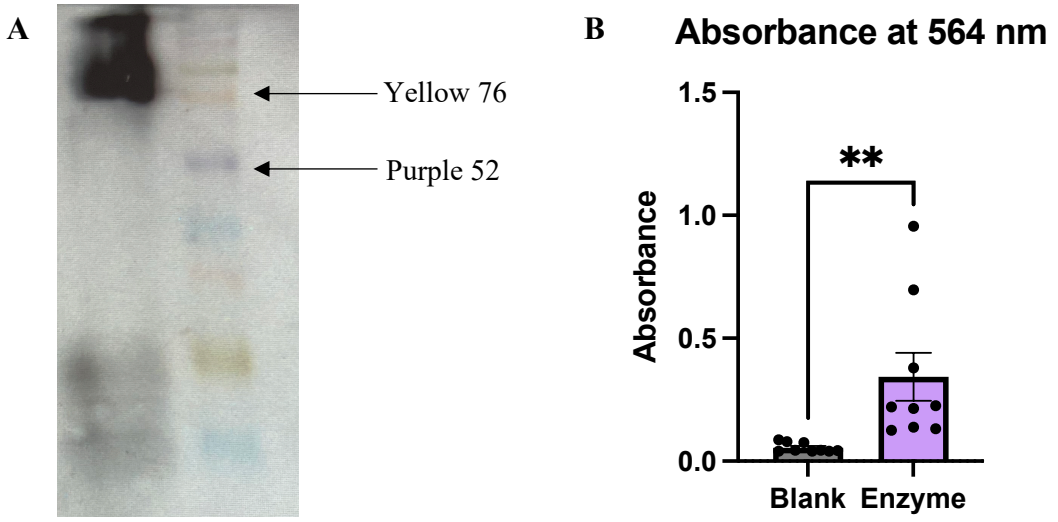

Figure 3C-1. A) Western blot for purified recombinant LigFa. The full-length protein has an anticipated MW of 77 kDa. Amersham rainbow ladder shows 76 kDa in yellow and 52 kDa in purple. **B)** Absorbance at 564 nm shows LigFa has significantly greater absorbance than a buffer-only blank as analyzed with a two-tailed unpaired t test, $t=2.976$, $df=18$, $p<0.01$.

There is limited literature available concerning *Ferroplasma acidiphilum* and genetic engineering, however another species, *Acidothiobacillus ferrooxidans,* which is also found in acid mine drainage has been of interest for genetic engineering. Early reports from the 1990s suggest that recombinant expression of an *A. ferrooxidans* gene for protein expression in *E. coli* is relatively straightforward, with optimization of different media, temperatures, and IPTG concentrations.[180] Other reports of recombinant protein production with proteins originally from *A. ferrooxidans* or *F. acidarmanus* detail difficulty producing target proteins in *E. coli*, often with poor final yields and solubility.[181,182] One possibility is that LigFa undergoes post-translational modifications in *F. acidiphilum* which are not reproduced in *E. coli.* Various extremophile bacteria (ranging from deep sea vents to acid mine drainage) are capable of post-translational modifications.[183,184] While *F. acidiphilum* and LigFa specifically have not been evaluated for post-translational modifications, this is one possibility that might explain the difficult recombinant production

in *E. coli*. If this is the case, it may be valuable to try recombinant production of LigFa in yeast or cyanobacteria, both of which are capable of post-translational modifications.

Another alternative is engineering *F. acidiphilum,* or more likely *A. ferrooxidans,* for greater production and possible secretion of LigFa. Work by Jung et al. 2023 genetically engineers *A. ferrooxidans* for the production of lanmodulin protein originally from *Methylorubrum extorquens*.[185] This successful example of recombinant protein production in *A. ferrooxidans* is promising for genetic engineering of this extremophile. Further, recent work by Kanao, et al. 2023 genetically engineer *A. ferrooxidans* tetrathionate hydrolase promoter for recombinant protein production.[186] Since *A. ferrooxidans* is also an acidophilic species (like *F. acidiphilum*), recombinant production of acidophilic LigFa may be possible with increased ease. This is especially likely if proper folding for LigFa is acid-dependent. Although Ferrer, *et al.* report that LigFa expression is not acid-dependent,[69] our work has not been able to reproduce results to support or refute this claim.

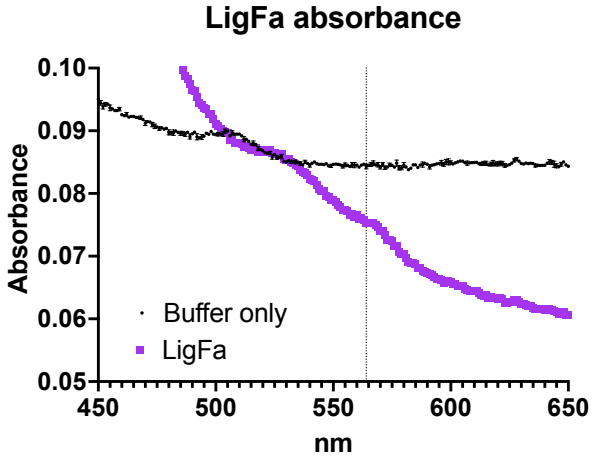

Figure 3C-2. Absorbance of LigFa compared to a buffer only solution. LigFa curve is comparable to what has been previously reported by Ferrer, et al.

Summary

LigFa is an exciting protein due to its reported purple coloration. However, as we have not been able to reproduce the results of Ferrer*, et al.* to consistently recombinantly produce LigFa in *E. coli*, it is not promising as a biosensor. If the protein expression challenges can be overcome, it may be valuable to pursue further.

Materials and Methods

16s rRNA sequencing was performed at Azenta with whole colony samples. Annotated results for *L. sphaericus* sample shown in Table 3M-1. Below.

Table 3M-1. Annotated results for *L. sphaericus* 16s rRNA sequencing from Azenta.

Each of the following identifications were made based on a 99% sequence similarity to 16s rRNA submitted. ggccaacctacccnnatagtttgggatanntccgggaaaccggggctaatnccganntantcttttgtntntcatganncaattctgaaagacgnnttcggctgtcgctataggatgggcccgcggcgcattagctagttggtgaggtaacggctcaccaaggcaacgatgcgtagccgacctgagagggtgatcggccacactgggactgagacacggcccagactcctacgggaggcagcagtagggaatcttccacaatgggcgaaagcctgatggagcaacgccgcgtgagtgaagaaggatttcggttcgtaaaactctgttgtaagggaagaacaagtacagtagtaactggctgtaccttgacggtaccttattagaaagccacggctaactacgtgccagcagccgcggtaatacgtaGGTGGCAAGCGTTGTCCGgAAttattgggcgtAaagcgcgcgcaggtggtttcttaagtctgatgtgaaagcccacggctcaaccgtggagggtcattggaaactgggagacttgagtgcagaagaggatagtggaattccaagtgtagcggtgaaatgcgtagagatttggaggaacaccagtggcgaaggcgactatctggtctgtaactgacactgaggcgcgaaagcgtggggagcaaacaggattagataccctggtagtccacgccgtaaacgatgagtgctaagtgttagggggtttccgcccccttagtgctgcagctaacgcattaaGcactccgcctggggagtacGGtcgcaaGaCTGaAACTCAAAggaattgacgggggcccgcacaagcggtggagcatgtggtttaattcgaagcaacgcgaagaaccttaccaggncttgacatcccgttgaccactgtagagatatggttttcccttcg		
Identification	**Strain**	**Notes**
L. sphaericus	NBRC 15095	NBRC 15095, DSM-28, ATCC-14577, and IAM13420 are all genetically identical[187,188]
L. sphaericus	DSM 28	NBRC 15095, DSM-28, ATCC-14577, and IAM13420 are all genetically identical[187,188]
L. mangiferihumi	M-GX18	Genome not sequenced. 16s rRNA is 98.5% identical to *L. sphaericus*[189]
L. sphaericus	ATCC 14577	NBRC 15095, DSM-28, ATCC-14577, and IAM13420 are all genetically identical[187,188]
L. sphaericus	IAM 13420	NBRC 15095, DSM-28, ATCC-14577, and IAM13420 are all genetically identical[187,188]

L. fusiformis	NBRC 15717	Although 16s rRNA sequences are similar to those of *L. sphaericus,* the genome is only approximately 50% identical.[190]
L. fusiformis	DSM 2898	Genetically identical to NBRC 15717 according to NBRC catalogue (https://www.nite.go.jp/nbrc/catalogue/NBRCCatalogueDetailServlet?ID=NBRC&CAT=15717)
L. parviboronicapiens	NBRC 103144	Synonymous with BAM 582 according to NBRC catalogue (https://www.nite.go.jp/nbrc/catalogue/NBRCCatalogueDetailServlet?ID=NBRC&CAT=00103144)
L. parviboronicapiens	BAM-582	Synonymous with NBRC 103144 according to NBRC catalogue (https://www.nite.go.jp/nbrc/catalogue/NBRCCatalogueDetailServlet?ID=NBRC&CAT=00103144)

Polycyclic aromatic hydrocarbon degradation screening

1.5% agar M9 minimal media plates were covered with 500 µL heptane containing 0.1% w/v anthracene, naphthalene, or phenanthrene. Solvent was allowed to evaporate. Saturated cell cultures were spread on plate, followed by incubation at 37 °C overnight.

Polycyclic aromatic hydrocarbon degradation

In a 96-well plate, 100 µL minimal salt media, 50 µL heptane with 0.1% w/v PAH, and 50 µL cells were added to each well. Cells were prepared by growing to saturation over two days, spun down at 3,000 x g, and resuspended in DI H_2O for a target OD600 of ~0.2 - 0.4. Plate was covered with a semi-permeable seal and incubated at 30 °C for a period of 18 hours, reading OD600 every 15 minutes.

Biomineralization screening plates

LB-agar media plates were treated with varying concentrations of ceria ammonium nitrate and let dry. Saturated cell cultures were applied to plate, followed by incubation at 37 °C overnight. Plates were checked for growth, then replaced in incubator for additional 24-hour incubation.

Biomineralization screening in liquid culture

DI H_2O and 1 mM precursor salt were mixed in a sterile 15 mL tube. Saturated starter culture was centrifuged, supernatant was discarded, and pellet was resuspended in DI H_2O. 500 µL cells were added to precursor salt solution. Mixture was incubated at 37 °C overnight shaking.

Minimal Salt Media (autoclave before use)

- 2g Na_2SO_4 / L
- 2.7g $NaH_2PO_4xH_2O$ / L
- 1 g $(NH_4)_2$) citrate / L

Fill to desired volume with DI H_2O

- Then 2 mL/L: 0.5 g $CaCl_2x2H_2O$, 0.18g $ZnSO_4$ x $7H_2O$, 0.1 g $MnSO_4$ x H_2O, 20.1 g Na_2-EDTA, 16.7 g $FeCl_3x6H_2O$, 0.16g $CuSO_4x5H_2O$, 0.18g $CoCl_2x6H_2O$.

HPBO lithium quantification assay

A 5 mL culture with *L. sphaericus* and 170 mM final concentration lithium chloride was incubated at 37° C shaking for 48 hrs. Culture was transferred to a 50 mL centrifuge tube and spun at 10,000 x g for 30 minutes. Supernatant was discarded and pellet was dried. Pellet was resuspended in 200 µL acetonitrile. A stock solution of 1 mM triethylamine and 4 mM 2-(2-hydroxyphenyl)-benzoxazole in acetonitrile was used to make a standard curve with LiCl content of 0.1 µmoles to 0 moles. 5 µL of sample was combined with 145 µL stock solution and fluorescence was read at 392 nm excitation and 428 nm emission.

CoroNa Geen sodium quantification assay

A 5 mL culture with *L. sphaericus* and 170 mM final concentration sodium chloride was incubated at 37° C shaking for 48 hrs. Culture was transferred to a 50 mL centrifuge tube and spun at 10,000 x g for 30 minutes. Supernatant was discarded and pellet was dried. Pellet was resuspended in 200 µL acetonitrile. A standard curve with high content of 0.1 µmoles NaCl was prepared in DI H_2O. Five µL of sample was combined with 145 µL stock solution and CoroNa Green dye (Thermofisher, C36675) was added to all wells at a final concentration of 0.013 µM. After 30 min incubation at room temperature, fluorescence was read at 492 nm excitation and 516 nm emission.

Fourier Transform Infrared Spectroscopy

As for HPBO, following *L. sphaericus* biomineralization with lithium chloride, culture was transferred to a 50 mL centrifuge tube and spun at 10,000 x g for 30 minutes. Supernatant was discarded and pellet was dried. Pellet was resuspended in 200 µL acetonitrile. A PerkinElmer FT-IR Spectrometer "Frontier" with Universal ATR Sampling Accessory (PerkinElmer) was blanked with acetonitrile followed by reading with sample. Spectrum was compared to those in SciFinder Spectral Database.

Transmission Electron Microscopy

Mineralized lithium was precipitated via centrifugation at 20,000 × g for 30 minutes. The supernatant was discarded and precipitates dried, then resuspended in 10 mM citrate buffer (pH 3.0). 100 µL samples were applied to TEM sample grid and let dry at room temperature. Samples were examined with FEI Titan 80-300 Transmission Electron Microscope. Image analysis and particle size measurement conducted with ImageJ. Utilization of the FEI Titan 80-300 Transmission Electron Microscope within UVa's Nanoscale Materials Characterization Facility was instrumental to this work. Dr. Grayson Johnson performed image acquisition and assistance with data analysis.

SDS-PAGE

A 50 mL culture with *L. sphaericus* and 170 mM final concentration lithium chloride was incubated at 37° C shaking for 48 hrs. Culture was transferred to a 50 mL centrifuge tube and spun at 10,000 xg for 30 minutes. Supernatant was discarded and pellet was dried. Pellet was gently resuspended in acetonitrile, diluted to 20% with DI H_2O then lyophilized for approximately 48 hrs. Lyophilization product was yellow powder. Lyophilization product was resuspended in 20 mL DI H_2O, then approximately 20 uL were loaded on a standard 8% resolving SDS PAGE gel. The gel was run at 110 V for 10 minutes then 150 V for 1 hr. The gel was removed and stored in a Ziploc bag with DI H_2O at 4°C.

Ghost separation

Ghost separation protocol adapted from Pfeifer, *et al.* (2022).[176] *L. sphaericus* starter culture was grown to saturation overnight at 37°C shaking. Cells were pelleted via centrifugation at 2,000 x g for 30 minutes. Supernatant was discarded, and cell pellet was resuspended in 1/5 original culture volume (i.e. if original culture was 5 mL, resuspension volume is 1 mL) buffer A (10 mM NaCl, 0.5% w/v sodium lauroylsarcosine). Incubated at 37 °C shaking for 1 hour. Added 1 mM PMSF, 10 µg/mL DNAse I. Centrifuged at 20,000 x g for 30 minutes. Discarded supernatant, resuspended in equal volume buffer B (10 mM NaCl, 0.5 mM $MgSO_4$, 0.5% w/v sodium dodecyl sulfate). Incubated at 40°C shaking for 1 hour.

Centrifuged at 20,000 x g for 30 minutes. Discarded supernatant, resuspended in equal volume buffer B. Repeated incubation and centrifugation with buffer B for a total of 3 times. After final centrifugation and discarded supernatant, rinsed pellet with DI H_2O. Resuspended in DI H_2O, measured A280. Extinction coefficient 177,600 M^{-1} cm^{-1}.[176] Ran on SDS-PAGE gel, anticipated molecular weight 122 kDa.[166]

Mass spectrometry

ESI-LC-MS/MS was performed at Virginia Commonwealth University Massey Cancer Center according to the following methods: "**Sample Preparation:** The protein bands were excised from the gel cut into equal size cubes (approximately 1mm) then transferred to an eppendorf tube. The gel pieces were washed with 80% acetonitrile (ACN) for 10 minutes, followed by a H_2O wash for 10 minutes. Gel pieces were then dehydrated with 50% ACN for 5 minutes, then vacuum centrifuged for 20 minutes. Samples were then rehydrated with 20 mM DTT and incubated for 1 hour at 56°C. Followed by 60 mM iodoacetimide for 45 minutes in the dark. The pieces were dehydrated with 50% ACN for 10 minutes, then vacuum centrifuged for 20 minutes. To rehydrate the gel cubes, samples were then incubated for 10 minutes in 20 µl of 12.5 ng/µl trypsin in 100 mM ammonium bicarbonate (AB). The gel pieces were then overlaid with 30 µl 100 mM AB and allowed to digest for 2 hours at 37°C. The digests were collected into fresh tubes for subsequent MS analysis. **LC-MS/MS:** All samples were analyzed using a Q Exactive HFX (Thermo) coupled to an Easy nLC 1200 (Thermo). **Data Analysis:** The LC-MS system consisted of a Thermo Electron Q-Exactive HF-X mass spectrometer with an Easyspray Ion source connected to an Acclaim PepMap 75µm x 2cm nanoviper C18 3µm x 100Å pre-column in series with an Acclaim PepMap RSLC 75µm x 15cm C18 2µm bead size (Thermo Scientific). Two µl of peptides were injected onto the column above. Peptides were eluted from the column with an 80%ACN 0.1% formic acid gradient at a flow rate of 0.3µl/min over 1 hour. The nano-spray ion source was operated at 1.9 kV. The digests were analyzed using the rapid switching capability of the instrument thus acquiring a full scan mass spectrum to determine peptide molecular weights followed by product spectra (15 High Energy C- trap Dissociation HCD spectra). This mode of analysis produces approximately 50,000 MS/MS spectra of ions ranging in abundance over several orders

of magnitude. Not all MS/MS spectra are derived from peptides. The data were analyzed by database searching using the Sequest HT search algorithm using a custom *Lysinibacillus* databases downloaded from Swiss Prot. The data was processed with Proteome Discoverer 3.0."

Primers for L. sphaericus genomic DNA amplification of target proteins

Chaperonin GroEL – 1635 bp, 35°C

5' TTACATCATGCCGCCCAT

5' TACCGTTTTCTGTAA

Flagellin – 849 bp, 46°C

5' ATGCTTGGTAAGTGGTCT

5' AAATCATAGCCCCTAAGGA

Zinc ABC transporter – 915 bp, 37°C

5' CTACTTTAATGCATCGAC

5' TACTTTGCAAAAAATCC

Peptide ABC transporter – 1656 bp, 33°C

5' TTATTTAGCGTCTAAATC

5' TACTTATTCTTGTTTTTC

Oligopeptide ABC transporter – 1728 bp, 36°C

5' ATGAAAAAGACAAAAACA

5' AATGAGTTGTTACACGGT

Catalase – 1518 bp, 39°C

5’ TTAGATGTTTGCTACTTG

5’ TACTGTTTGCGTTTACTA

S-layer domain – 4248 bp, 34°C

5’ ATGGATAAAACAAAAATC

5’ AATAACACAAGATCCAAC

Aldehyde dehydrogenase family protein – 1521 bp, 38°C

5’ TTAGAAGAAACCAAGTTT

5’ TACCAAATACGTAAAGGT

ATP-synthase subunit alpha – 1509 bp, 38°C

5’ ATGGGCATCAAGGCTGAA

5’ AATAAGACTAAATCGCTTT

Glyceraldehyde 3 phosphate dehydrogenase – 1023 bp, 36°C

5’ TTATGCGTTAACTGTTTC

5’ TACTGTCATAGTCAAC

Protein production and purification

pet28a(+) LigFa was transformed into *E. coli* BL21. Single colonies were picked for starter cultures in LB, grown at 37 °C shaking overnight. Cultures were centrifuged at 3,000 x g for 10 minutes and supernatant discarded. Cell pellet was inoculated in LB or TB with kanamycin (minimum 50 mL) and grown to OD600 of 0.6-0.8. At OD600 > 0.6, isopropyl β-D-1-thiogalactopyranoside (IPTG) was added to a final

concentration of 0.1 mM and flasks moved to 20 °C shaking incubator overnight. Cells were harvested via centrifugation at 3,000 x g for 10 minutes and supernatant discarded.

Pellet was resuspended in sonication lysis buffer (5% v/v glycerol (99+%), 36 mM tris HCl, 20 mM tris base, 100 mM NaCl, and 5 mM imidazole) at 5 mL buffer / 1 g pellet. Lysis was performed via sonication at 20% amplitude, for 20 minutes in 20 second on/off pulses. Lysate was centrifuged at 10,000 x g for minimum of 10 minutes, supernatant was collected and filtered with 0.4 μm syringe filter then purified via his-tag affinity chromatography. Purification fractions were collected and analyzed via 8% SDS PAGE.

For quicker protein purification, the pellet was resuspended in 10 mM citrate buffer (pH 3.0), then transferred to dialysis (MWCO 50 kDa) in 10 mM citrate buffer overnight. Dialysis sample then centrifuged at 10,000 xg for 5 min to separate insoluble precipitate. Supernatant was then concentrated with Centricon YM10 membrane spin columns (Sigma) at 14,000 xg for 20 minutes.

Dialysis into $Fe(NTA)_2$

0.1 M freshly prepared $Fe(NTA)_2$ was used for dialysis (MWCO 50 kDa) for 1 hour at RT. Dialysis packet was then transferred to extensive dialysis in 100 mM citrate buffer (pH 3.0).

100mM $Fe(NTA)_2$ – 0.04 M FeCl3, 0.08 M Nitrilotriacetic acid sodium salt – for 1 L 10.g FeCl3, 18.8g Nitrilotriacetic acid sodium salt

100 mM Citrate buffer (pH 3.0) – for 250 mL 4.35 g citric acid, 0.69 g trisodium citrate dihydrate

Protein concentration measured via A280.

Chapter 4: Silicatein Expression in Cyanobacteria

**This work was done in collaboration with USAFA researchers Dr. J. Jordan Steel and Ms. Melanie Grogger.*

Key Findings

- Designed and transformed CyanoGate silicatein construct into 3 cyanobacterial strains
- Growth of eGFP-sil pSyn6 in PCC 7942 showed GFP fluorescence
- Evaluated cyanobacterial tolerance to ceria ammonium nitrate as foundation for biomineralization assays
- Designed pAM1954-eGFP-silicatein plasmid for *Anabaena* PCC 7120

Background: Cyanobacteria, also known as blue-green algae, are an exciting prospect as a biotechnological tool because they perform photosynthesis.[73–75] Pairing photosynthesis with whatever the desired outcome is provides the added benefit of CO_2 consumption and O_2 production. Although cyanobacteria are often referred to generally, it can be important to distinguish the different characteristics associated with each strain. For example, *Synecococchus elongatus* PCC 7942 is an autotrophic strain that grows best at 38° C. In contrast, *Anabaena variabilis* PCC 7120 is an autotrophic, nitrogen-fixing strain that grows best at 30° C.[73] Therefore, for a study examining nitrogen-fixation, PCC 7120 should be chosen over PCC 7942.

Cyanobacteria differ from *E. coli* as a biotechnological tool primarily due to their longer doubling times and strain-specific growth conditions. However, an important distinction that should be considered in the case of silicatein is cyanobacteria's ability to perform post-translational modifications.[76] In marine sponges, silicatein undergoes phosphorylation at several sites.[191–193] *E. coli* are not able to perform post-translational modifications, and therefore *in vitro* recombinant protein production of silicatein in *E. coli* yields a protein

without phosphorylation. Introducing the silicatein gene in cyanobacteria for recombinant protein production enables the post-translational phosphorylations to take place, and may therefore yield a protein with added stability or increased activity. To date, there are not any studies which directly compare recombinant non-post-translationally modified silicatein with a post-translationally modified silicatein. An additional difference between the bio-engineering of cyanobacteria and *E. coli* is the option to incorporate genes directly into the genome, known as an *in cis* genetic transformation, or as a plasmid, which is known as an *in trans* genetic transformation.[73] *In cis* gene-editing entails integration directly into the chromosome, which suggests some degree of stability.[194] In addition, with integration into the chromosome there is not the need to maintain selective pressure indefinitely.[194] The major drawback to integration into the chromosome, however, is often low levels of gene expression, which can be problematic for recombinant protein expression. In contrast, *in trans* gene-editing requires the transformation and maintenance of a foreign plasmid within the cell. Maintaining the plasmid requires constant selective pressure, but enables more control of the desired gene expression.

Hypothesis: Silicatein expression in cyanobacteria will enable carbon-negative biomanufacturing of REEs.

Approach: This work utilizes three strains of cyanobacteria: *S. elongatus* UTEX 2973, *S. elongatus* PCC 7942, and *Anabaena* PCC 7120. UTEX 2973 is relatively fast-growing, known to have an equivalent biomass production rate of *S. cerevisae.*[77] PCC 7942 is a model cyanobacterium that has been previously used in many studies, and *Anabaena* PCC 7120 is nitrogen-fixing. Each of these cyanobacterial species have the potential to grow and thrive in austere environments such as space. In fact, recent work by Ramalho, et al. 2022 shows promising survival and growth of PCC 7120 with martian regolith as well as tolerance to toxic perchlorates.[79] Furthermore, Ramalho, et al. show the growth of *E. coli* from cyanobacterial lysates, suggesting that cyanobacteria may be able to support additional life in space.[79]

In order to efficiently express silicatein in these different strains, we utilized the CyanoGate modular cloning system to generalize plasmid vector and promoter.[195] With CyanoGate, we chose active promoter cpc560 which is light inducible and has been previously shown to successfully overexpress protein.[196] As a secondary approach, we also cloned silicatein into pAM1954-eGFP, which can be applied in PCC 7120 then easily screened for with eGFP fluorescence.

Results:

The CyanoGate modular cloning system is similar to Golden Gate or BioBrick cloning strategies. For successful expression in cyanobacteria, the up-flank, promoter, terminator, and down-flank parts must be considered carefully, in addition to linkers between up-flank and promoter then terminator and down-flank. The parts selected for this work are shown in Table 4-1.

Table 4-1. Selected CyanoGate parts

	Part number	Part
Initial plasmid	pCA0.002	From pSB4K5 backbone, kanamycin resistance, accepts initial constructs
Up-flank	pc0.024	Sequence upstream of cpc operon from pICH41295 backbone
Up-flank linker	pc0.117	From pICH41331 backbone
Promoter	pc0.005	P_{cpc560}
Terminator	pc0.078	T_{cpc_operon}
Down-flank linker	pc0.118	From pICH41331 backbone

Down-flank	pc0.025	Sequence downstream of cpc operon from pICH41276 backbone
Acceptor plasmid	pCAT.000	From pPMQAK1 backbone, ampicillin and kanamycin resistance

Each part is initially contained in an individual plasmid in *E. coli* DH5α. Glycerol stocks were streaked and let grow at 37° C overnight. Starter cultures were grown to saturation overnight and DNA was miniprepped. With mini-prepped DNA, a series of 4 reactions could be set up with Golden Gate cloning techniques.

CG1 – pCA0.002, pC0.024, pC0.117

CG2 – pcA.002, pC0.005, silicatein, pC0.078

CG3 – pCA0.002, pC0.118, pC0.025

CG4 – pCAT.000, CG1, CG2, CG3

Following each Golden Gate ligation, DNA was desalted then transformed into *E. coli* DH5α. For CG1, blue/white screening was used, however all colonies were blue so in further transformations blue/white screening was deemed unnecessary. Colony PCR was used to further confirm the presence of the desired ligation product (Fig 4-1) and successful transformants were mini-prepped.

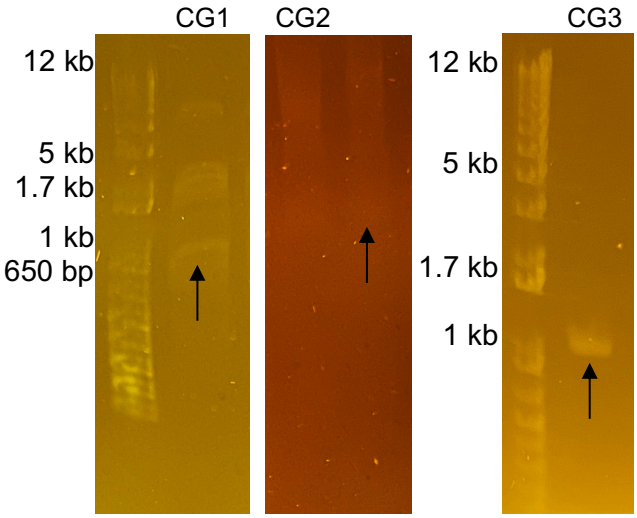

Figure 4-1. Colony PCR for CG1, CG2, and CG3. Anticipated size of inserts are CG2 767 bp, CG2 1300 bp, and CG3 1089 bp. Bands are indicated with black arrows.

CG1, CG2, and CG3 were all required for ligation into CG4, also known as CGF. After colony PCR confirmation of CGF, the miniprep was co-transformed into *E. coli* DH5α and HB101 with helper plasmid prL623. Helper plasmid prL623 is used to remove restriction sites of enzymes native to cyanobacteria that thwart transformation.

These transformants are also miniprepped, at which point the DNA can be transformed into cyanobacteria utilizing adapted protocols from Dr. Joe Scott and former 499 Cadet Kat Kowar. *Anabaena* and UTEX 2973 were always transformed via electroporation, while PCC 7942 was initially transformed by mixing magic and natural competence. Following transformation and quenching, cultures are left to recover at room temperature in the dark for at least 48 hours. They can then be spun down and transferred to a BG11 plate with a sterilized HATF filter. According to Dr. Scott's protocol, these plates were sealed with parafilm, then left to grow at room temperature with ambient light for 10 days. Vasudevan *et al.* let plates incubate at room temperature and ambient light for 2 days, then transfer them to a humidified incubator with light for the remaining growth period.

Colonies grown in incubator light were red and unable to be removed from filter paper when moving to 6-well plates. In this case, a small section of filter paper with the colony was transferred to the well. Colonies that had grown on agar rather than filter paper were transferred directly to wells.

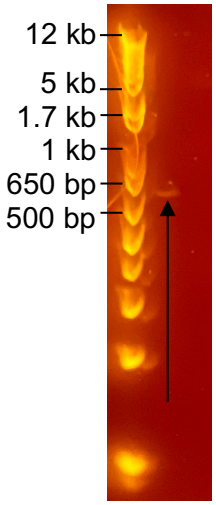

Figure 4-2. Colony PCR for pAM1954-eGFP-sil. Anticipated size of insert is 550 bp. Band is indicated with black arrow.

pAM1954-eGFP-silicatein was ultimately transformed according to the same techniques as above, although the cloning process was different. To clone silicatein into pAM1954-eGFP a XhoI restriction site was added to the N-terminal of eGFP via PCR. This PCR product was purified, then a HindIII and XhoI digested silicatein insert was ligated into pAM1954-eGFP-XhoI. Colony PCR with Sil F and Sil R primers was run to confirm the presence of silicatein in pAM1954-eGFP (Fig. 4-2). One colony was re-streaked for glycerol stocks and mini-preps. Following co-transformation into DH5α with prL623, pAM-sil was transformed into UTEX 2973, PCC 7942, and *Anabaena* PCC 7120.

At this point in time, we have CGF and pAM1954-eGFP-silicatein transformed into UTEX 2973, PCC 7942 and *Anabaena* PCC 7120 and growing under antibiotic selection conditions in 6-well plates (Fig 4-3). The CGF cultures do have noticeable amounts of green, however growth across all cultures is slow. This is likely due to the high concentration of antibiotic, however, the amount of antibiotic degradation under light should be considered in this scenario. Approximately 10 days after transfer to 6-well plates, antibiotic selection media was refreshed with the addition of 1-2 mL, depending on the degree of evaporation. These cultures should be refreshed again, antibiotic concentration should be checked and corrected, and the OD720 of these can be measured in reference to a media-only condition.

In addition to growth under antibiotic selection conditions, pAM-eGFP-sil can be screened for with GFP fluorescence. When cultures are sufficiently confluent that green is visually apparent, a small sample should be taken for fluorescence microscopy.

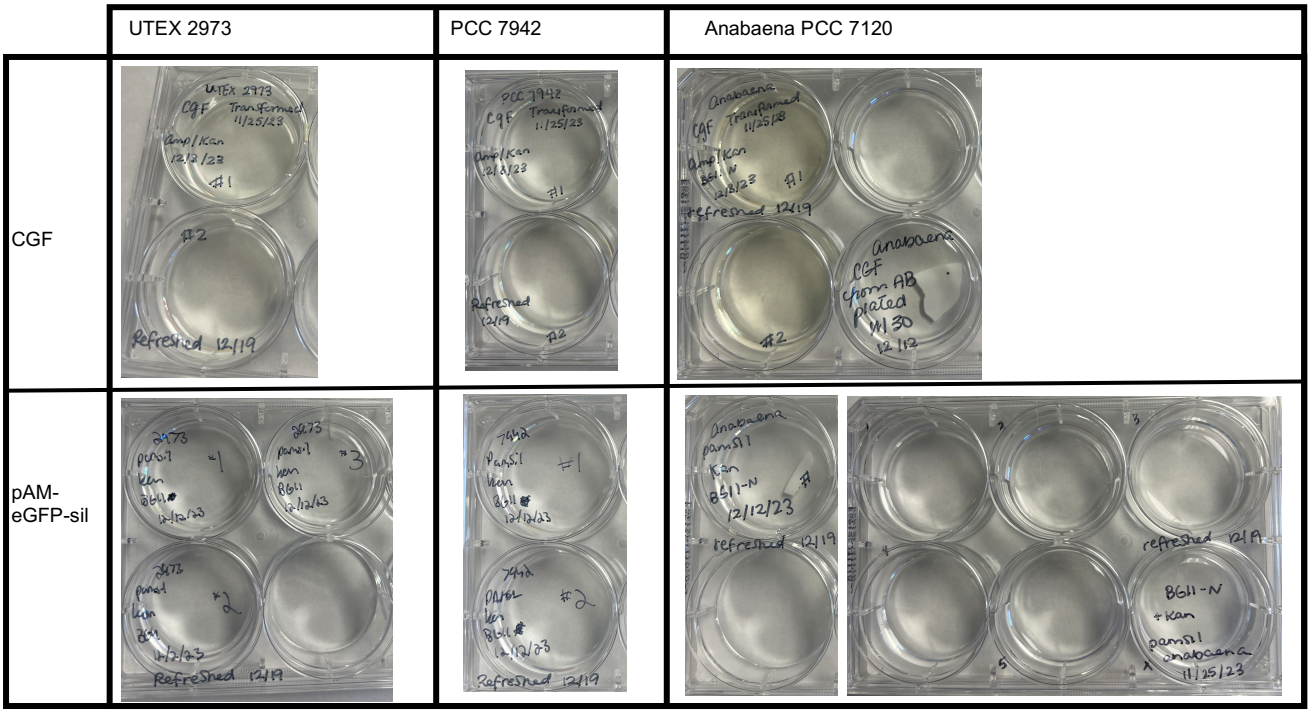

Figure 4-3. Growing cyanobacteria transformed with CGF or pAM-eGFP-sil in 6-well plates. Each strain of interest was transformed with each set of DNA. Growth can be visualized by green tinge of wells. In some cases, such as PCC 7942 with pAM-eGFP-sil, growth is not apparent and cannot be confirmed visually.

Preliminary fluorescence microscopy was performed with eGFP-sil pSyn6 in PCC 7942 cultures. eGFP-sil from our pet28-eGFP-sil construct (Aim 1) was transformed into the pSyn6 vector in Spring 2023 by 499 Cadet Margaret Warner. pSyn6 is has TEV site, 6xhis tag, and spectinomycin resistance gene and is designed to integrate in the chromosomal DNA via homologous recombination. The psbA promoter regulates the gene insert (in this case eGFP-sil) for constituitive expression. Under constituitive expression we can expect eGFP-sil to be continuously expressed without the addition of IPTG. Warner noted GFP fluorescence in some but not all PCC 7942 colonies after transformation. Here, colonies from Spring 2023 were inoculated in BG11 media with spectinomycin. Growth was extremely slow, although some green

could be visualized in culture tubes. Samples were taken for fluorescence microscopy with Keyence BZ-X810 Fluorescence Microscope (Fig. 4-4).

The cells in figure 4-4 appear circular, which is consistent with the expected morphology of PCC-7942. Some cells exhibit GFP fluorescence, suggesting that eGFP-sil is being produced, while others do not. As noted, these cultures did not grow robustly, so further characterization of eGFP-sil was not pursued. In a healthy robust culture, eGFP-silicatein fluorescence should accompany silicatein biomineralization activity. To confirm biomineralization activity is intact, silica or ceria precursors should be added to the solution.

To establish the appropriate amount of ceria precursor to add to cyanobacteria with silicatein for biomineralization, I examined the survival of cyanobacteria alone with ceria ammonium nitrate. Like many organisms, cyanobacteria require metals as cofactors for some metabolic functions. In fact, cyanobacteria in general require metal cofactors for more metabolic functions than most organisms, and metal availability can be a limiting factor for cyanobacterial survival in some environments.[197] Metal tolerance is highly variable across cyanobacterial strains, but in general tolerable concentrations are in the mg/L range.[198] As a preliminary screen, PCC 7942, UTEX 2973, and PCC 7120 were incubated with varying concentrations of ceria ammonium nitrate (high concentration 25 mM or 13.7 g/L). Following 24 hours of incubation in liquid culture, cells were plated and monitored for growth after 10 days in light. PCC 7942 and UTEX 2973 showed no growth even at low concentration of 0.31 mM or 170 mg/L.

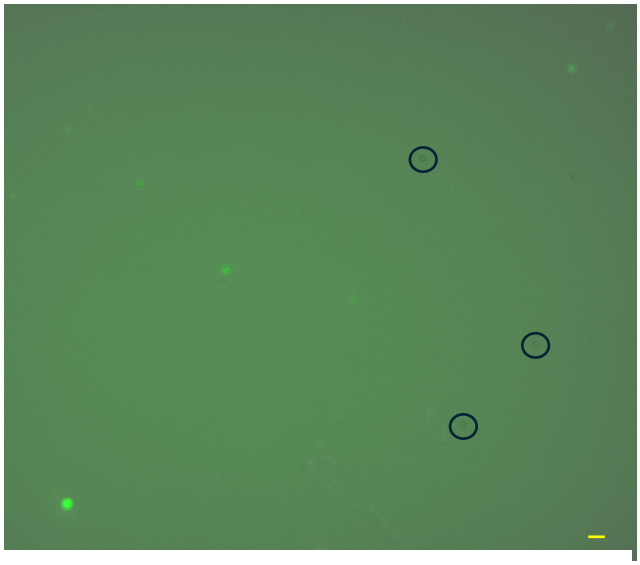

Figure 4-4. eGFP-sil pSyn6 PCC 7942 cells inoculated from Spring 2023 BG11 plates. Grown with spectinomycin. Fluorescence is evident with some cells, but not all (as circled in black). Scale bar (yellow) is 5 µm.

PCC 7120 did show tolerance to 0.31 mM CAN (Fig. 4-5). For PCC 7942 and UTEX 2973, lower concentrations of ceria ammonium nitrate should be tested. For PCC 7120, 0.31 mM CAN can be considered tolerable on a preliminary basis.

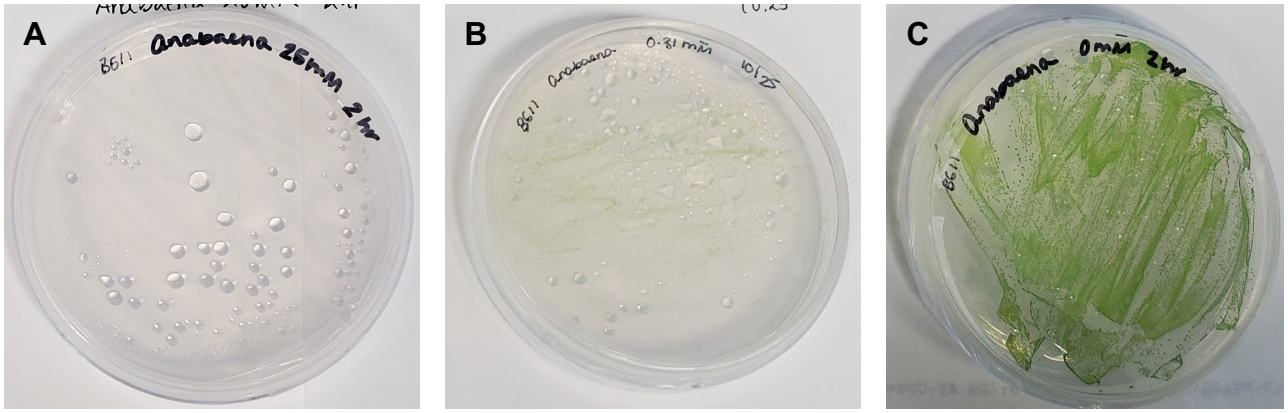

Figure 4-5. *Anabaena* PCC 7120 survival following incubation with ceria ammonium nitrate at various concentrations. A) ceria ammonium nitrate concentration 25 mM, B) 0.31 mM, C) 0 mM.

Summary

Silicatein expression in cyanobacteria is an exciting possibility as cyanobacteria are able to perform post-translational modifications, a variety of strains are adapted to many different environments, and the potential for pairing oxygen-generation via photosynthesis with biomineralization. This work produced the several plasmids with silicatein gene insert for expression in cyanobacteria. Due to the relatively short time-frame I was able to spend at USAFA, only preliminary expression has been observed. Continuing work at USAFA seeks to confirm the expression of silicatein in cyanobacteria with SDS-PAGE and biomineralization assays. The preliminary survival assays performed with cyanobacteria and ceria ammonium nitrate show that *Anabaena* PCC 7120 are not tolerant to 25 mM ceria ammonium nitrate, but that growth still occurs after exposure to 0.31 mM ceria ammonium nitrate. This provides the foundation for *in vivo* biomineralization assays with silicatein. Furthermore, introduction of silicatein into cyanobacteria may have possible applications in biocementation.

Materials and Methods

CyanoGate

Original CyanoGate glycerol stocks were moved from -80 °C freezer and streaked on LB spectinomycin plates then incubated at 37 °C overnight. Single colonies were selected and grown in 1 mL LB spectinomycin at 37 °C overnight, then mini-prepped with Monarch Plasmid Mini-prep kit (NEB). Concentrations of mini-preps were measured with Nanodrop 1000. Cloning was performed according to protocols from Vasudevan, *et al* (2019) and adapted from Patron Lab's "Type IIS-mediated Parallel DNA Assembly".[195,199] 20 femtomoles of acceptor plasmid was mixed with 40 femtomoles of DNA part plasmids. Sterile DI H_2O was added to a volume of 15 µL. Then 2 µL T4 DNA ligase buffer (NEB), 1 µL T4 DNA ligase (NEB), 1 µL 1 mg/mL bovine serum albumin, and 1 µL BsaI restriction enzyme were added and mixed gently via pipetting. Reactions were transferred to thermocycler for 26 cycles of 37 °C for 3 minutes and 16 °C for 4 minutes, followed by final incubation of 37 °C for 5 minutes then 80 °C for 5 minutes. 5 µL of each sample was desalted on nitrocellulose membrane and 4 µL of DNA was added to 20 µL *E. coli* DH5α for transformation.

E. coli DH5α transformation

DNA was incubated with 50 µL *E. coli* DH5α on ice for 5 minutes then transferred to pre-chilled electroporation cuvette. Electroporation cuvette was shocked at 1.8 kV and immediately quenched with LB. Quenched culture was incubated at 37 °C for at least 1 hour then plated on LB with antibiotics or blue/white screening plates (as available) and incubated at 37 °C overnight. Individual colonies were screened via colony PCR to confirm presence of insert. For CG1, CG2, and CG3 samples were then mini-prepped and recombined with CyanoGate protocol to make final CG4. CG4 was then transformed with helper plasmid pRL623 (demethylation) into *E. coli* DH5α or HB101. Following successful co-transformation with pRL623, samples were mini-prepped and then transformed into cyanobacteria.

Cyanobacteria transformations

Collected 1 mL of saturated culture, spun at 1,000 x g for 10 minutes to pellet cells. Discarded supernatant. *For natural competence* (PCC 7942), resuspended in 1 mL BG11, spun at 1,400 x g for 1 minutes. Discarded supernatant. Resuspended in 100 µL DI H_20. Added approximately 100 ng of DNA. Incubated in 34 °C water bath with dark lid for 1 hour and 30 minutes. Pre-warmed BG11 plates, treated with 10 µL antibiotic. Plated 100 µL transformation. Place plates (agar up) on illuminated shelf at 30 °C.

For electroporation (UTEX 2973, *Anabaena* PCC 7120), resuspend in 50 µL DI H_2O. Added 750 ng DNA to cells. Loaded in pre-chilled electroporation cuvette (0.1 cm gap), shocked at 1.2 kV, 50 µF, 250 ohm. Anticipated time constant was 10 milliseconds, observed 11.5 and 11.9 milliseconds, respectively. Quenched with 1 mL BG11. Plated on BG11 with sterile HATF filter. Incubated in low light conditions at 26 °C for 2 days. After 2 days, transferred filter to BG11 plate treated with antibiotics.

After 7-10 days, one colony was transferred to 3 mL BG11 with antibiotic in 6-well plate. Incubated at 26 °C with light.

NOTES: For antibiotics, 50 µg/mL is the standard for spectinomycin in *E. coli,* and 10 µg/mL for spectinomycin in cyanobacteria. Following this logic, we diluted standard antibiotics (prepped for *E. coli*) by 5. So for kanamycin, which is prepared at 50 mg/mL we diluted to a final in culture concentration of 10 mg/mL. Then we added 600 µL 50 mg/mL kanamycin to 2400 µL BG11 media for a total of 3 mL. The final antibiotic concentration for these 3 mL of culture was 10 mg/mL rather than the intended 10 µg/mL. This was a math error on my part.

Survival assay

Serial dilutions of CAN from 25 mM to 0 mM were performed in 150 µL in 96-well plate. 50 µL of saturated cyanobacterial cultures (UTEX 2973, PCC 7942, and *Anabaena* PCC 7120) were added to each

well. 96-well plate was incubated shaking at RT in light for 2 hours, then 2 µL from each sample was plated on BG11 plates. 96-well plate was returned to shaking incubator, then 2 µL from each sample was plated at 18 hours and again an additional 24 hours earlier. BG11 plates with cyanobacteria were incubated at 30 °C in light for 10 days and evaluated for growth.

Primers

024 F: 5’ ggaggacttggaagtttg 3’

117 R: 5’ agcgtgagatcgaggatg 3’

005 F: 5’ ggagcacctgtagagaag 3’

078 R: 5’ agcgagacaaaaagagaa 3’

118 F: 5’ tggagtcggtcacatgtg 3’

025 R: 5’ agcggaccgtttgaaaac 3’

pAM-XhoI F: 5’ gtagcacgctcgagcttgagatccttttttctgcgcg 3’

pAM-XhoI R: 5’ gcgagctactcgagaagatcctttgatcttttctacggggtctg 3’

Chapter 5: Biocementation with silicatein

**This work was done in collaboration with USAFA researchers Dr. J. Jordan Steel, Ms. Melanie Grogger, Capt. Victoria Morrison, 2Lt. Nikolas Schwendeman, and others. Manuscript "Surface-displayed silicatein-alpha enzyme in bioengineered E. coli enables biocementation and silica mineralization"*

Key Findings

- INP-silicatein fusion results in silicatein surface display.
- Surface-displayed silicatein retains biomineralization activity, as shown with silica and ceria.
- Biosilicification is a promising alternative to microbially induced calcite precipitation, producing bricks with comparable unconfined compressive strength.
- Biocementation with Martian regolith simulant as substrate reflects trends seen in biocementation with fine-grain sand.

Hypothesis: Silicatein will polymerize silica present in soil, sand, and regolith. This polymerization will increase particle size and effectively solidify loose particles.

Approach:

Biocementation via microbially induced calcite precipitation (MICP) has been explored with a variety of microbial species that breakdown urea to ammonia, thus inducing ambient calcium precipitation.[99] The breakdown of ammonia is known as ureolysis, which is an aerobic process. *Sporosarcina pasteurii* is a commonly used microbe for ureolysis and biocementation. Ma, *et. al* 2020 compared microbially induced calcite precipitation between *S. pasteurii, B. subtilis,* and *E. coli,* showing that *S. pasteurii* remain intact under biocementation conditions, while *B. subtilis* and *E. coli* display cell lysis.[99,200–202] Furthermore, the structure of precipitates was greater than those made by *B. subtilis* and *E. coli* forming large aggregates of calcium carbonate.[200] This work utilized 2 mL *S. pasteurii* saturated culture in each experiment. One

drawback of microbially induced calcite precipitation with *S. pasteurii* is the requirement to add large amounts of calcium to the reaction. In the case of Ma, et al. 11% w/v $CaCl_2$ was added per 2 mL bacterial culture,[200] with others reporting up to 28% w/v added $CaCl_2$.[90,92,203,204] A potential benefit of targeting silica for biocementation rather than calcium is the sheer abundance of silica naturally occurring in sand and regolith (approximately 30%).[95,100] This may entail that it is not necessary to add components other than silicatein for this biocementation. Fewer additional reactants is attractive for applications in austere environments, such as space, to which additional reaction components would need to be transported. Utilizing the available resources in space, or other austere environments, is known as *in situ* resource utilization. Since silica has a natural abundance of approximately 30% in regolith,[100] it would not be necessary to add additional silica for biocementation with silicatein. Accordingly, transportation requirements would only be for *E. coli* INP-silicatein maintenance, expression, and growth.

To easily produce and access silicatein, we created an INP-silicatein fusion for surface display on *E. coli.* Ice nucleation protein (INP) from *Pseudomonas* has been widely used to surface display proteins of various sizes. INP has an N domain and C domain, with repeating spacer domains in between.[205] The spacer domains in native *Pseudomonas* function as sites for ice nucleation, with the N-domain being hydrophobic and the C-domain being hydrophilic.[205] Previous studies show that only the N-domain is necessary for surface display in *E. coli* but that spacer domains can be added to distance the display cargo from the cell.[205] Here, we utilized the INP N-domain to create an INP-silicatein fusion protein to surface display silicatein on *E. coli.* Surface display allows for the *in vivo* use of silicatein's enzyme activity, which will require fewer post-production processing steps than cellular protein expression and purification. With INP-sil, *E. coli* can be applied directly to biocementation experiments and processes. Furthermore, the available silica will in sand or regolith suggests that only *E. coli* INP-silicatein will be necessary to add for biocementation.

Results

INP-silicatein was recombinantly expressed in *E. coli* BL21. Purification via his-tag Ni-affinity chromatography shows the dimerized protein at approximately ~100 kDa (Figure 5-1). SDS-PAGE highlights the presence of protein, however, for applications INP-silicatein will be used *in vivo* unpurified on *E. coli*. Western blot results also confirm the production of INP-silicatein, with bands at approximately 50 and 100 kDa. Experiments showed that inclusion of a serine protease inhibitor such as PMSF during sonication is highly beneficial for gel electrophoresis, as silicatein will undergo significant proteolysis otherwise. This may be due in part to silicatein sequence similarity with protease Cathepsin L – presumably the overlap in catalytic triad residues which facilitate proteolysis for Cathepsin L may have similar activity in silicatein. Therefore, silicatein may face protease activity from other silicatein molecules present in solution. As our work shows that the catalytic triad is not the sole mechanism of biomineralization activity (Aim 1), it is reasonable to presume that treatment with a protease inhibitor will not negatively impact biomineralization activity in a significant way.[206]

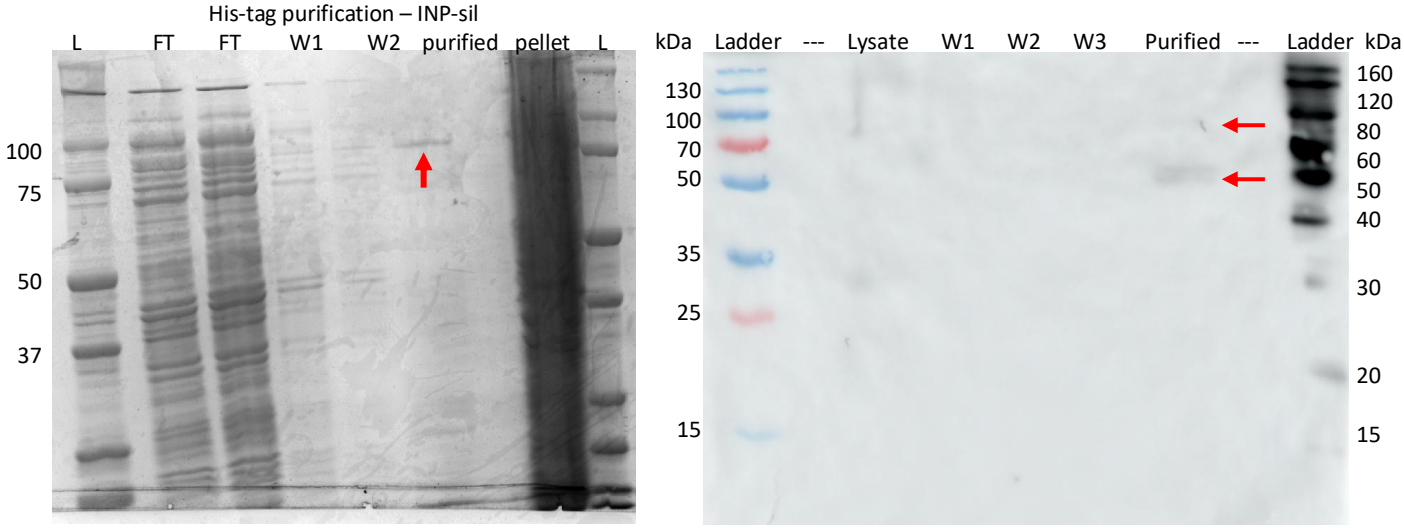

Figure 5-1. His-tag purification for recombinant INP-silicatein. SDS-PAGE (left) with band in the purified fraction at approximately 100 kDa. Western blot (right) with bands in the purified fraction at approximately 50 and 100 kDa.

For *in vivo* biomineralization with INP-silicatein, the precursor sodium orthosilicate was used, as reported previously by Muller, et. al.[207] In preliminary experiments, *E. coli* with INP-silicatein were combined with silica precursor, then incubated at room temperature shaking overnight. The cells were removed via

centrifugation and the supernatant – presumably containing any biomineralized product – was collected. The supernatant was then ultra-centrifuged to precipitate out biomineralized nanoparticles. (This is consistent with isolation of biomineralization product that we perform with nanoceria in Aim 1). *E. coli* with INP-silicatein was compared to WT BL21 *E. coli* and a no-cells condition. The WT BL21 *E. coli* serve as a baseline for potential silica precipitation due to interactions with the cell itself. The no-cells condition is a control targeting autohydrolysis of precursor. A visual comparison of precipitates generated following 24-hour incubation shows much greater silica precipitation with INP-silicatein than WT BL21 and the no-cells condition. This result therefore suggests that INP-silicatein is displaying biomineralization activity. Preliminary analysis of precipitates with ImageJ shows INP-silicatein precipitate has an area of approximately 13,000 pixels (13,166) while the precipitate from WT BL21 has an area of 8,600 pixels (8,641). Comparison with an unpaired t-test shows that the difference is statistically significant with $p<0.01$ ($p=0.0055$). Additional *in vivo* biomineralization experiments including *E. coli* expressing TF-silicatein have followed. The identity of this precipitate as silica is further supported via analysis with the silicomolybdate assay. The silicomolybdate assay has been previously used by Povarova, Dakhili, Sparkes et al. to quantify silica oxide produced by silicatein.[34,37,47,208] Here the silicomolybdate assay shows that *E.*

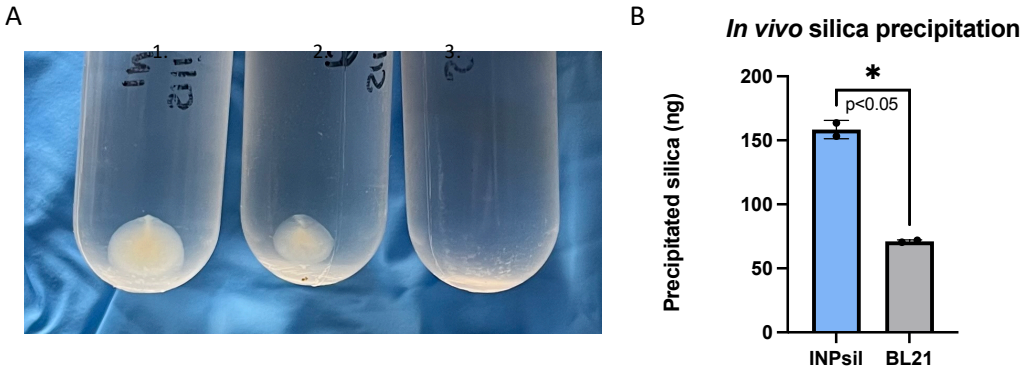

Fig. 5-2. *In vivo* biomineralization with INP-silicatein-a. Silica mineralization can be visualized as precipitate after sample ultra-centrifugation. 1) Precipitate from *E. coli* INP-silicatein-a and sodium orthosilicate after 24 hour incubation, 2) precipitate from WT BL21 *E. coli* and sodium orthosilicate after 24 hour incubation, 3) precipitate from sodium orthosilicate alone after 24 hour incubation. B) Comparison of precipitated silica (ng) as quantified via silicomolybdate assay. Two-tailed unpaired t-test $t=16.93$, $df=2$, $p<0.05$.

coli INP-silicatein produces significantly greater precipitate than BL21 cells alone (Fig. 5-2, two-tailed unpaired t-test $p<0.05$).

To further illustrate surface display of INP-silicatein, immunocytochemistry for silicatein was performed (Fig. 5-3). *E. coli* INP-silicatein and *E. coli* BL21 were each treated with an anti-silicatein goat antibody, which was then followed by anti-goat AlexaFluor 488. Microscopy shows DAPI staining of the nucleic acids within the cells in both INP-silicatein and BL21 cases. For INP-silicatein, however, we are also able to detect and visualize green fluorescence decorating the exterior of the cell – effectively a green outline around each blue DAPI stain, which does not occur with the BL21 cells. In this way, we are showing surface display of INP-silicatein on *E. coli.*

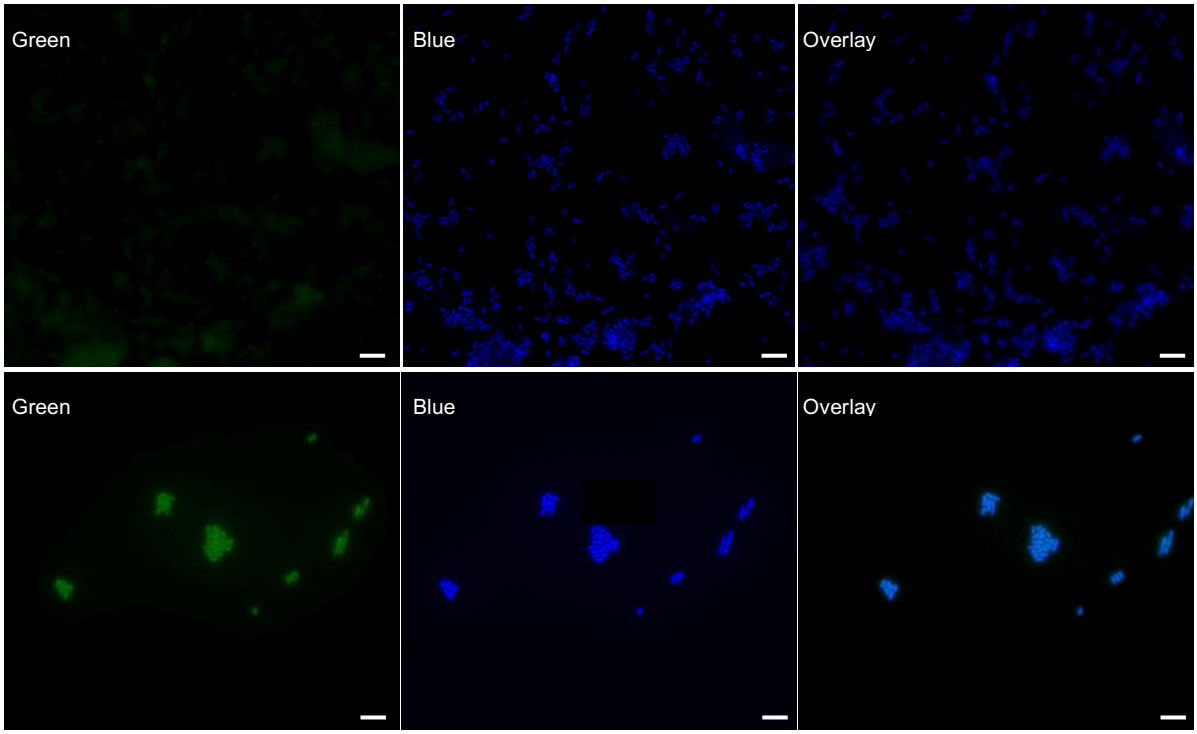

Fig. 5-3. Immunocytochemistry of WT BL21 *E. coli* and *E. coli* INP-silicatein. Green fluorescence shows AlexaFluor 488 conjugated to anti-silicatein. Blue fluorescence shows DAPI staining of nucleic acids, highlighting the interior of bacterial cells. Overlay shows co-localization of INP-silicatein on the exterior of DAPI-stained cells for *E. coli* INP-silicatein, but not on WT BL21 *E. coli.*

The *in vivo* biomineralization assays show that silica biomineralization is occurring with *E. coli* INP-silicatein. To evaluate this biomineralization in the context of biocementation, *E. coli* INP-silicatein was used to make bricks. The 2022 USAFA iGEM team established a biocementation protocol with *S. pasteurii* and coarse grain sand. Here, we adapted this protocol for three microbial cases: 1) *S. pasteurii,* 2) *S. pasteurii* + *E. coli* INP-silicatein, and 3) *E. coli* INP-silicatein using fine grain sand. *S. pasteurii* bricks serve as the baseline, as *S. pasteurii* is frequently used in microbially induced calcite precipitation and there is significant literature discussing *S. pasteurii* MICP bricks. Five complete sets of bricks were made, with several additional *S. pasteurii* bricks to serve as a baseline for comparison with 2022 iGEM results. Bricks were tested for maximum load (kPa) in an unconfined compression test, revealing maximum load tolerated before breaking, utilizing a compaction tool from USAFA Civil Engineering. As drying or curation time impacts brick strength, these bricks were crushed at 21 (+/-2) days after synthesis.

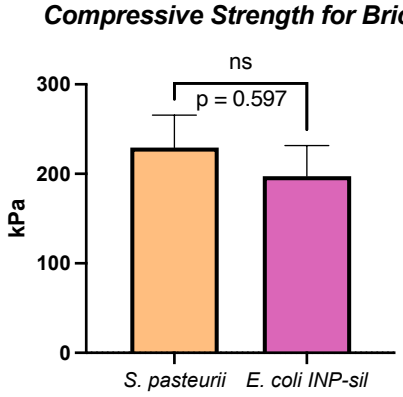

Fig. 5-4. Unconfined compressive strengths for *S. pasteurii* and *E. coli* INP-silicatein-a bricks. *S. pasteurii* bricks show an average tolerance to 229 kPa (S.E.M. 36 kPa). *E. coli* INP-silicatein-a bricks show an average tolerance of 197 kPa (S.E.M. 34 kPa). A two-tailed unpaired t-test shows no significant difference between the two t=0.5407, df=14, p=0.597.

On average, *S. pasteurii* bricks could tolerate a maximum load of 229 kPa, which is strikingly less than values documented by 2022 iGEM at approximately 1,379 kPa. One possible explanation is in the particle

size of sand used. 2022 iGEM used coarse grain yellow sand, where-as here, in order to more closely approximate regolith, fine grain sand was used.

An additional possibility is that the amount of *S. pasteurii* cultures of 2022 iGEM had greater OD600s than cultures here, and therefore more cells to perform biocementation. Most studies do not report OD600 of *S. pasteurii* applied, and there does not appear to be a standard across studies. There is one report, however, that highlights increasing biocementation as a result of increased OD600,[90] with various reports that claims optimal OD600 of 0.2-4.[91,200,202,209,210]

Notably, there was no significant difference in the unconfined compressive strength of bricks made with *S. pasteurii* and bricks made with *E. coli* INP-silicatein. This suggests that biosilicification with surface-displayed silicatein produces comparable biocementation (in terms of unconfined compressive strength) as traditional ureolytic MICP.

Table 5-1. Unconfined compressive strengths for bricks made with fine-grain sand.

Bricks made on date:	***S. pasteurii***	***S. pasteurii* + INP-sil**	**INP-sil**
	Load (PSI)		
Nov 11	47		
Nov 11	38		
Nov 29	19*		
Nov 30	15.6	4	10
Dec 1	17.3*		
Dec 1	41	0.5	34
Dec 4	18.2	15.3	28.9
Dec 5	56.1	10.8	-----

Dec 5	43.3*		
Dec 6	59.2	12.1	31.3
Dec 11			

Regolith bricks

To further evaluate the possibility of applications for *in situ* resource utilization on Mars, bricks made with *S. pasteurii* and *E. coli* INP-silicatein and martian regolith simulant were examined. The entire brick making process was the same as previous except that martian regolith simulant was used instead of sand. Martian regolith reportedly has ultra-fine particle sizes with this martian regolith simulant reportedly having a median particle size of 63 um and a range of 0.04-1000 um. Silica oxide was present at approximately 44%.[100] Due to the small particle size and silica oxide composition, martian regolith simulant has a health advisory score of 1 (range 0-4), The Biology Department Safety Officer at USAFA did not support the use of martian regolith simulant citing health concerns, and therefore martian regolith simulant bricks were made off-site then shipped to USAFA for unconfined compression testing. It is important to note that cross country shipping may introduce significant impacts to brick form and strength.

Three sets of *S. pasteurii* and *E. coli* INP-silicatein bricks were made, however, one *S. pasteurii* brick and one *E. coli* INP-silicatein brick were broken upon arrival at USAFA. Therefore, two bricks of each type were crushed after 21 days of curing. As with the previous comparison of *S. pasteurii* and *E. coli* INP-silicatein bricks, there was no significant difference in the unconfined compressive strength (unpaired t-test, p=0.2098). Although there is no significant difference between the two types of bricks at present, there may be the beginning of a trend here suggesting that *E. coli* INP-silicatein bricks are stronger than traditional MICP *S. pasteurii* bricks with martian regolith simulant.

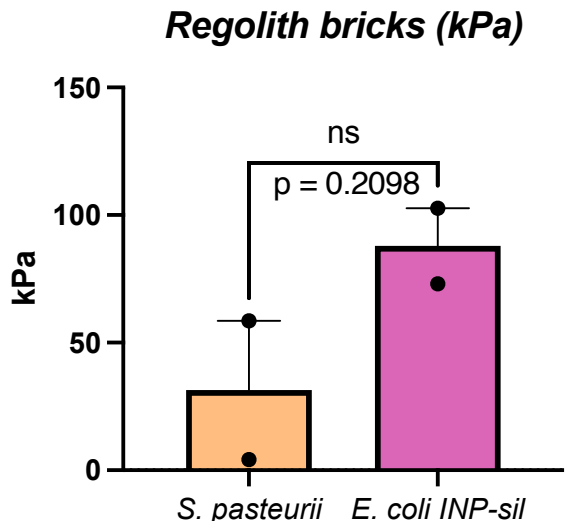

Fig. 5-5. Unconfined compressive strengths for *S. pasteurii* and *E. coli* INP-silicatein-a martian regolith simulant bricks. *S. pasteurii* bricks show an average tolerance to 31.4 kPa (S.E.M. 27.2 kPa). *E. coli* INP-silicatein-a bricks show an average tolerance of 87.9 kPa (S.E.M. 14.8 kPa). A two-tailed unpaired t-test shows no significant difference between the two t=1.824, df=2, p=0.2098.

It may also be relevant to note that with the decreased particle size of martian regolith simulant, a lesser compressive load (kPa) was tolerated than the fine sand brick counterparts. This supports our hypothesis that particle size prior to biocementation treatments plays a significant role in brick strength. Thus far iGEM 2022 bricks made with coarse sand (largest particle size) were strongest, with fine sand bricks (smaller particle size, but larger than regolith) then martian regolith (finest particle size) bricks following.

Current work at USAFA is further examining the relationship between initial particle size and final strength of biocementation product.

Biomineralization with ceria ammonium nitrate

To further confirm INP-silicatein biomineralization activity, the *E. coli* INP-silicatein was co-incubated with ceria ammonium nitrate for *in vivo* biomineralization. Figure 5-6 shows biomineralized ceria precipitated from *in vivo* biomineralization with INP-silicatein in tube 1 as a rust-colored precipitate. Tube 2 shows no precipitate, which is consistent with our expectation for non-biomineralized ceria ammonium nitrate. These results are consistent with early *in vitro* biomineralization assays with eGFP-silicatein. One challenge with *in vivo* biomineralization going forward may be standardizing the amount of protein per reaction – OD600 of cells will likely be the metric, however, at this time we cannot quantify the amount of INP-silicatein expression per cell.

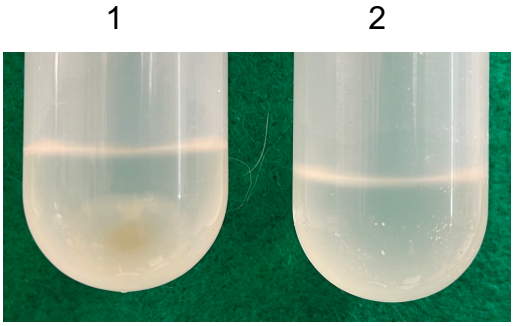

Figure 5-6. INP-silicatein biomineralization with ceria ammonium nitrate. 1) Supernatant from INP-silicatein with ceria ultracentrifuged at 50,000 x g, showing rust-colored precipitate. 2) Supernatant from ceria ammonium nitrate only condition, ultracentrifuged at 50,000 x g, showing no precipitate.

Summary

This work shows surface-displayed silicatein biomineralizes sodium orthosilicate to silica and ceric ammonium nitrate to nanoceria. INP-silicatein was confirmed as surface-displayed through confocal microscopy with DAPI and silicatein-specific staining. Further, INP-silicatein *E. coli* was applied to fine-grain sand and regolith for biocementation. Bricks made with INP-silicatein *E. coli* showed comparable unconfined compressive strength to bricks made via traditional biocementation with microbially induced calcite precipitation. This makes INP-silicatein a promising alternative to MICP, since biocementation via biosilicification does not produce ammonium or carbonate as polluting by-products. INP-silicatein *E. coli* biocementation strategies are also exciting for *in situ* resource utilization on Mars. Since Martian regolith has significant silica content, biosilicification would not require added substrate other than the INP-silicatein *E. coli,* which is a notable improvement to the amount of calcium that would be necessary via MICP. Bricks made with Martian regolith also showed no significant difference in unconfined compressive strength between INP-silicatein *E. coli* and MICP's *S. pasteurii.* In fact, there are beginnings of a trend to suggest that INP-silicatein bricks may have increased unconfined compressive strength over MICP bricks.

Materials and Methods

Molecular biology

Standard molecular biology procedures were used for DNA maintenance and cloning using *E. coli* DH5α. For INP-silicatein work, the GeneJET PCR Purification Kit (ThermoFisher), QIAquick Gel Extraction Kit (Qiagen), and Monarch Plasmid Mini-prep Kit (NEB) were used according to manufacturer's instructions. To construct pet28a(+) INP-silicatein, the pet28a(+) TF-silicatein plasmid was used as a backbone. First, backbone plasmid was digested with BamHI and HindIII to remove the TF DNA insert, followed by agarose gel electrophoresis and gel extraction of desired band. The INP-N gene fragment was PCRed out of pet28a(+) INP-OspA plasmid (Twist Bioscience) and confirmed with agarose gel electrophoresis. Following PCR clean-up, the INP gene fragment was ligated into pet28a(+) BamHI/HindIII silicatein according to NEB T4 ligation protocol. Ligation product was desalted with nitrocellulose membrane, then 2-5 μL were used for transformation into DH5α via electroporation. Transformed cells were quenched with LB, let recover at 37° C shaking for 1 hour, then centrifuged at 3,000 x g. Supernatant was discarded, pellet was resuspended in approximately 100 μL LB, then plated on LB-agar plates with kanamycin. After overnight incubation at 37° C, colonies were selected for colony PCR to confirm the presence of INP-silicatein gene.

Frequently used primers

INP F: 5' ATGAATATCGACAAAGCGTTG 3'

INP R: 5' CTTAAGGGTACCCTCGACCTC 3'

Sil R: 5' cccaccCTCGAGTTGATTGTATTTGTT 3'

Protein production and purification

pet28a(+) INP-silicatein, was transformed into *E. coli* BL21 (DE3). Single colonies were picked for starter cultures in LB, grown at 37° C shaking overnight. Cultures were centrifuged at 3,000 x g for 10 minutes

and supernatant discarded. Cell pellet was inoculated in TB with kanamycin (minimum 50 mL) and grown to OD600 of 0.6-0.8. At OD600 > 0.6, isopropyl β-D-1-thiogalactopyranoside (IPTG) was added to a final concentration of 0.1 mM and flasks moved to 20° C shaking incubator overnight. Cells were harvested via centrifugation at 3,000 x g for 10 minutes and supernatant discarded. Pellet was resuspended in sonication lysis buffer (5% v/v glycerol (99+%), 36 mM tris HCl, 20 mM tris base, 100 mM NaCl, and 5 mM imidazole) at 5 mL buffer / 1 g pellet. Lysis was performed via sonication at 20% amplitude, for 20 minutes in 20 second on/off pulses. Lysate was centrifuged at 10,000 x g for minimum of 10 minutes, supernatant was collected and filtered with 0.4 μm syringe filter then purified via his-tag affinity chromatography. Purification fractions were collected and analyzed via 8% SDS PAGE.

SDS-PAGE

8% SDS-PAGE were loaded with lysates and purified samples, run at 110 V for 10 minutes, then 150 V for 1 hr. For staining, gel was transferred to fixing solution with Coomassie blue for at least 30 minutes (0.025% w/v brilliant blue, 7.5% v/v acetic acid, 50% v/v ethanol (95%), and 42.5% v/v DI H_2O), then destained (7.5% v/v acetic acid, 10% v/v ethanol (95%), and 82.5% v/v DI H_2O) for 1 hour. Imaged with colorimetric transillumination on Amersham Imager 680.

In vivo biomineralization

5 mL of saturated induced INP-silicatein in *E. coli* cultures was spun down at 3,000 x g for 10 minutes. The supernatant was discarded. Cell pellet was resuspended in 25 mL of sterile, DI H_2O with aeration beads in a 125 mL flask. A final concentration of 2 mM sodium orthosilicate was added. This *in vivo* biomineralization mixture was left to proceed overnight shaking at room temperature. A WT BL21 *E. coli* and silica only control were included.

After 24 hours, cells were removed from solution via centrifugation at 1,000 x g for 10 minutes. The supernatant was ultracentrifuged in 5 mL increments at 50,000 x g for 45 minutes to precipitate silica biomineralization products.

Silicomolybdate assay

Silica recovery was measured with the silicomolybdate assay adapted from Povarova, *et al.* 2018 with extinction coefficient as derived by Coradin, *et al.* 2004.[136]

Immunocytochemistry (adapted from Lazzara Lab protocol)

Cells were grown and induced as for protein production and *in vivo* biomineralization. Following overnight induction, 1 mL of culture was centrifuged at 3,000 x g for 2 min to isolate the cells. Supernatant was discarded and pellet was resuspended in 1 mL TBS, then spun at 3,000 x g for 2 minutes again. One additional wash with TBS was performed. Cell pellet was then resuspended in 1 mL ice cold methanol and incubated on ice for a maximum of 10 minutes. With gentle mixing via pipette, 100 μL was dropped onto a glass microscope slide and allowed to dry via evaporation. Once dry, 125 μL of 1/1,000 anti-silicatein goat antibody (antibodies.com) was added. Slides were transferred to a humidified chamber and incubated at 4 °C overnight.

After overnight incubation, slides were gently washed with DI H_2O and dried with a slide warmer. 125 μL of 1/10,000 anti-goat AlexaFluor 488 antibody (Invitrogen) was added and slide in humidified chamber was incubated at 37° C for 1 hr. Slides were gently washed with DI H_2O and dried with a slide warmer. One drop of Anti-fade Gold Pro-long mounting media with DAPI (Invitrogen) was added, followed by a cover slip. Slides were examined with a Keyence BZ-X810 Fluorescence Microscope.

S. pasteurii growth

A 1.5 mL glycerol stock of *S. pasteurii* from 2022 was revived via cell separation and inoculation in Brain Heart Infusion Urea media (37% w/v BHI, 20% w/v urea). This culture was incubated overnight at room temperature shaking.

Bricks

Fine sand (Sandtastik) was placed in a 3 in x 1.5 in (height x diameter) cylindrical mold. Cell cultures (40 mL, average OD600 4.3 and 2.3 for INP-sil and *S. pasteurii* respectively) and biocementation solution (80 mL, 20% w/v urea, 10% w/v ammonium chloride, 49% w/v calcium chloride dihydrate) were alternately applied and left to fully percolate through sand for three total treatments of each. Bricks incubated at RT for at least 24 hours prior to removal from mold. Following removal from mold, bricks were left to cure for at least 21 days prior to crushing.

For regolith bricks, martian regolith simulant MRS-1 from Exolith Labs was used in place of fine sand.

Cylindrical mold

3 in x 1.5 in (height x diameter) cylindrical molds were 3D printed using Stratasys' Rigur™ (RGD450) filament. Two designs, one classic cylinder (shown below) and one "swiss cheese" cylinder were made printed, and used. SolidWorks software was used to design the molds and create a CAD file, then printing was done with Stratasys Object30 V5 Pro 3D Printer. The "swiss cheese" cylinder has holes for air flow which we hypothesize will allow the brick to dry faster and more thoroughly.

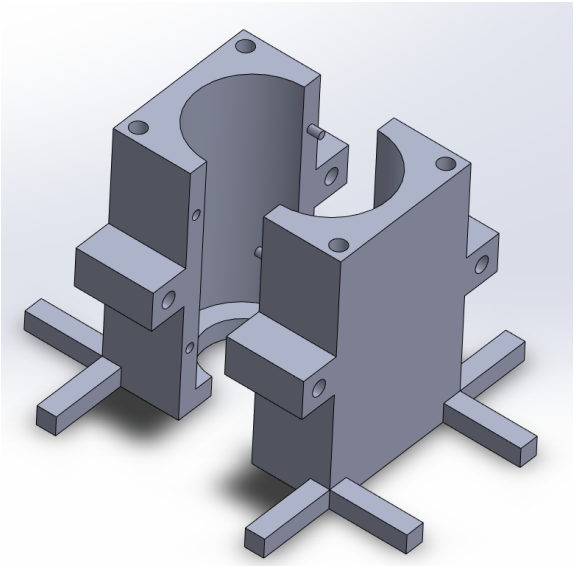

Figure 5-7. Cylindrical 3D-printed mold for biocementation bricks.

Conclusions

Enzymatic biomineralization, like many protein-mediated processes, is unique for each enzyme.

In the case of silicatein, this work shows that silicatein biomineralization activity is not impacted by fusion partner and that the leading catalytic triad hypothesis is not true for biomineralization with ceria. To further investigate the mechanism of biomineralization, we performed directed evolution with survival-based selection. The directed evolution library revealed enhanced biomineralization activity resulting from induced genetic mosaicism. In particular, the revelation that truncated silicatein mutants retain biomineralization activity was in stark contrast with understanding across the field. Furthermore, these results showed that silicatein tolerates a multitude of sequence changes yet retains biomineralization activity, suggesting that silicatein biomineralization activity cannot be attributed to a single mechanism, but likely results from an interplay of multiple processes. As intrinsic disorder is a hallmark of some biomineralization proteins (*i.e.* calcite and PFMG1), several regions of potential intrinsic disorder within silicatein were investigated, however did not result in any significant changes in biomineralization activity. Overall, the precise mechanism of silicatein biomineralization remains unknown.

The biomineralization mechanism of smCSE is better understood – with previous work illustrating that catalytic H_2S production is critical for CdS production. Based on crystal structures generated by Mahanta, Acharya, and Berger this work investigates the metal coordination di-histidine motif: H49 and H351. Site-directed mutagenesis reveals that H351 is crucial for smCSE quantum dot production, but that there are no major changes in H_2S production or oligomerization associated with H351A. With consideration for rare earth element extraction applications, we show that smCSe can mineralize ceria ammonium nitrate, lanthanum nitrate, and neodymium nitrate to sulfides. Further, smCSE reaction time is a key consideration for rare earth element extraction – with WT smCSE, an *in vitro* reaction time greater than 24 hours will precipitate bulk minerals – a comparison between CdS and CeS production show that CdS production is not interrupted with the addition of ceria ammonium nitrate, indicating that CdS biomineralization occurs

preferentially to CeS biomineralization. Experiments with smCSE in different reactor simulating systems reveal that a flow-based reactor system is unlikely to facilitate REE extraction due to low residence times, but a batch reactor simulation yields promising results.

Whole-cell biomineralization with *Lysinibacillus sphaericus*, a microbe identified from a western Virginia coal mine sample, is promising for bituminous degradation and lithium extraction. *L. sphaericus* shows polycyclic aromatic hydrocarbon degradation with naphthalene and anthracene. As PAHs are prevalent in bitumen, this is promising as an approach to "free up" minerals of interest. When co-incubated with precursor salt, *L. sphaericus* produced 2 nm LiOH nanoparticles. The discrete size and relative stability of LiOH particles suggests that there are biomolecules acting as capping agents. Via ESI-LC-MS/MS, 10 candidate proteins have been identified as involved in this biomineralization process. Further exploration will narrow down the specific role of each protein and determine if a single-enzyme biomineralization process is feasible. As is, *L. sphaericus* displays PAH degradation and biomineralization, which is promising for bioremediation of pollutants as well as critical mineral extraction.

Acidophilic purple protein LigFa was evaluated as a potential biosensor for REEs. Although one previous report shows recombinant production of LigFa in *E. coli*, we were unable to reproduce these results. An acidophile is promising for applications in acid mine drainage, however, ease of recombinant production is fundamental.

While acidophilic purple protein LigFa was disappointing, cyanobacteria may provide tolerance to the same extreme conditions. There are hundreds of cyanobacterial strains uniquely adapted to a variety of environmental conditions. Although still a bacteria, cyanobacteria care and growth are vastly different from *E. coli* and the cyanobacterial expertise and infrastructure from the Life Sciences Research Center at the U.S. Air Force Academy was invaluable. As part of this work, we designed and transformed a CyanoGate silicatein construct into 3 cyanobacterial strains – PCC 7942, UTEX 2973, and PCC 7120. Each

strain was also evaluated for toxicity to ceria ammonium nitrate as a foundation to evaluate biomineralization with silicatein. Interestingly, cyanobacteria may be an appropriate expression chassis for silicatein in earthly austere environments (such as acid mine drainage), but also in outer space.

A major roadblock for colonizing space is the cost to transport building materials. One alternative to traditional building materials may be biocementation – which would only require the transport of microbe and select substrates. Microbially induced calcite precipitation with *S. pasteurii* is the current gold-standard for biocementation, however, we experimented with surface-displayed silicatein on *E. coli* for biocementation via biosilicification. We show that INP-silicatein fusion results in silicatein surface display and that surface-displayed silicatein retains biomineralization activity, as shown with silica and ceria. To compare biosilicification with MICP, we made bricks with fine-grain sand using both techniques. With both biosilicification and MICP, bricks showed comparable unconfined compressive strength. Additional experimentation with Martian regolith simulant as substrate reflects trends seen in biocementation with fine-grain sand.

Overall, this work investigates biomineralization, rare earth element extraction approaches, pollutant bioremediation, and biocementation – addressing a variety of geological challenges with synthetic biology.

List of Publications

- *In preparation:* **Vigil, T.N.,** Jacob, S.G., Johnson, G.C., Spangler, L.C., Berger, B.W. "Microbial mineralization with Lysinibacillus sphaericus for lithium nanoparticle extraction" 2024.
- *In preparation:* **Vigil, T.N.,** Frost, A.J., Janiga, A.R., Mahanta, P., Acharya, R., Berger, B.W., "Structural basis for the CdS quantum dot (QDs) nanocrystals formation by cystathionine γ-lyase from Stenotrophomonas maltophilia strain (smCSE)" 2024.
- *Submitted, In Review:* **Vigil, T.N.,** Schwendeman, N.K. Grogger, M.L.M., Morrison, V.L., Warner, M.C., Bone, N.B., Vance, M.T., Morris, D.C., McElmurry, K., Berger, B.W., Steel, J.J. "Surface-displayed silicatein-alpha enzyme in bioengineered E. coli enables biocementation and silica mineralization" 2024.
- *Submitted, In Review:* **Vigil, T.N.,** Rowson, M.J.C., Frost, A.J., Janiga, A.R., Berger, B.W. "Directed evolution of silicatein reveals biomineralization synergism between protein sequences" 2024.
- **Vigil, T.N.** Felton, S.M., Fahy, W.E., Kinkeade, M.A., Visek, A.M., Janiga, A.R., Jacob, S.G. and Berger, B.W. "Biosurfactants as templates to inspire new environmental and health applications" Front. Syn. Bio. 2024.
- **Vigil, T.N.** Spangler, L.C. "Understanding biomineralization mechanisms to produce size-controlled, tailored nanocrystals for optoelectronic and catalytic applications: A review" ACS Appl. Nano Mater. 2024.
- **Vigil, T.N**., Rowson, M.J.C., Frost, A.J., Berger, B.W. "Understanding the relationships between solubility, stability, and activity of silicatein" Mater. Adv. 2023, 4, 662-668.
- Mann, M.M., **Vigil, T.N.,** Felton, S.M., Fahy, W.E., Kinkeade, M.A., Kartseva, V.K., Rowson, M.J.C., Frost, A.J. and Berger, B.W. Proteins in synthetic biology with agricultural and environmental applications. SynBio, 2022, 1(1), pp.77

Teaching and Mentorship Experience

Teaching assistant for Chemical Engineering Thermodynamics Jan – May 2023

University of Virginia

Professor: Bryan W. Berger

iGEM instructor Sept – Dec 2023

United States Air Force Academy

Professor: J. Jordan Steel

Guest lecture for Microbial Diversity Fall 2023

United States Air Force Academy

Professor: J. Jordan Steel

Guest lecture for Biochemical Engineering Spring 2024

University of Virginia

Professor: Bryan W. Berger

Research mentor for M.J. Rowson (UVa BME) Jan 2022 – May 2023

Dean's Undergraduate Summer Research

Poster presentation at BMES (Fall 2022)

Now pursuing PhD at Cornell University

Research mentor for Abigail Frost (UVa ChE) Jan 2022 – May 2024

Dean's Undergraduate Summer Research

Poster presentation at ACS (Spring 2024)

Research mentor for Madison Stampley (UVa Advanced Materials Synthesis REU) Summer 2022

Now pursuing PhD at University of Virginia

Research mentor for Abigail Janiga (UVa ChE) May 2023 – May 2024

Research mentor for Sarah Jacob (UVa Advanced Materials Synthesis REU) Summer 2023

Research mentor for Abigail Cook (USAFA Biology Department) Nov – Dec 2023

Appendix A: Lyme-AID

Lyme disease is a tick-borne disease caused by *Borrelia burgdorferi*. If a patient is bitten by a tick carrying *B. burgdorferi*, there is a small window for antibiotic treatment. Often, antibiotics are administered too late, and the patient will have Lyme disease for the remainder of their life. Early detection is key for treatment to be effective.[211] Further background and motivation can be found on the 2023 USAFA iGEM wiki, which is publicly available at https://2023.igem.wiki/usafa/.

The 2023 USAFA iGEM designed a colorimetric biosensor patch for the detection of Lyme disease. Via protein engineering, two proteins native to ticks and *B. burgdorferi*, Salp12 and OspA,[212,213] respectively could be applied to a tick bite via a microneedle patch. Salp12 is a tick salivary protein that has previously been shown to act as a chemoattractant for *B. burgdorferi)*.[212] OspA, or outer surface protein A, conjugated to DNA-aptamer-gold nanoparticles could function as a colorimetric sensor.

We engineered Salp12 and OspA for recombinant expression in *E. coli.* Plasmids were ordered from Twist Biosciences and transformed into DH5a and BL21 *E. coli.* Challenges with recombinant expression led us to screen transformed colonies via PCR, which revealed that the gene insert was only present in approximately 20% of colonies (Fig. A-A 1).

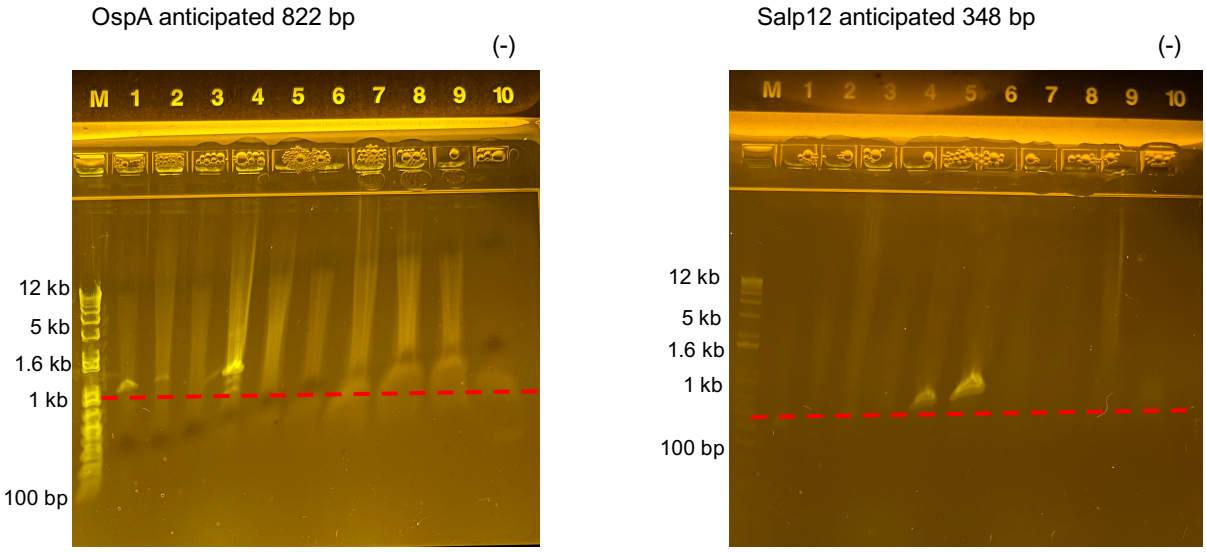

Figure A-A 1. Agarose screening gels for colony PCR with pet28-OspA and pet28-Salp12. OspA anticipated at 822 bp, Salp12 anticipated at 348 bp. Samples directly from PCR, therefore "streaky" appearance anticipated with salts. The negative control is shown in lane 10 for each, denoted (-).

After confirming the gene insert, we pursued recombinant expression in *E. coli* BL21. USAFA iGEM had been growing 1 mL starter cultures in LB at 37 °C shaking overnight, then diluting to 5 mL, growing for 2-3 hours at 37 °C shaking, then adding 1 mM IPTG for 5 hour induction. After a 5 hour induction at 37 °C shaking, the cells were pelleted via centrifugation and the cell pellet was frozen at -20 °C overnight. Distinctive recombinant protein bands were not visualized with SDS-PAGE.

To begin troubleshooting, we first scaled up cultures to 5 mL for starter cultures and 50 mL for inductions, adding glass beads to the induction flask for aeration. We also began to measure OD600 for timed induction at OD600 of 0.6 with 0.1 mM IPTG. Starter cultures and growth to OD600 of 0.6 was done at 37 °C shaking, but after addition of IPTG we let induction proceed at room temperature shaking overnight. The following day, cells were pelleted via centrifugation and the pellet was frozen at – 20 °C, then lysates were examined via SDS-PAGE. No distinctive recombinant protein bands were seen on the SDS-PAGE.

In the next trial, cells were grown and induced as previously described. After overnight induction, cells were pelleted via centrifugation, then the pellet was resuspended in sonication lysis buffer at 5 mL / 1 g cell pellet (5% v/v glycerol (99+%), 36 mM tris-HCl, 20 mM tris base, 100 mM NaCl, 5 mM imidazole) and sonicated at 20% amplitude in 20 second on/off pulses for 10 minutes. The cell lysate was clarified via centrifugation at 10,000 x g for 10 minutes. Supernatant was then taken for SDS-PAGE. SDS-PAGE did not show distinct bands of recombinant protein. We hypothesized that recombinant protein expression was low, and that bands would be easier to visualize in a purified sample. INP-OspA was purified via immobilized metal affinity chromatography with Ni-NTA his tag affinity column (NEB). SDS-PAGE revealed a band at approximately 60 kDa in the purified fraction (Fig. A-A 2).

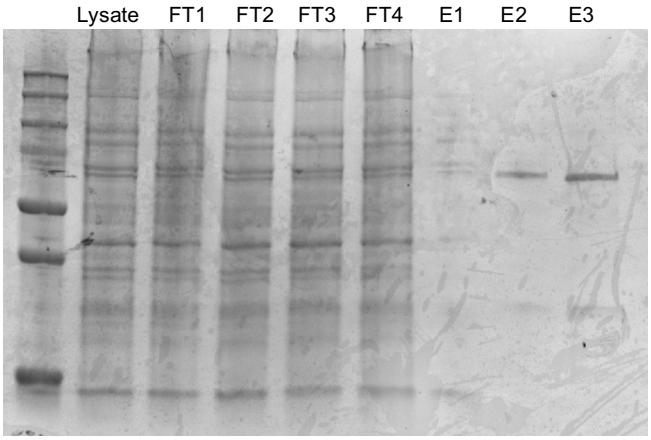

Figure A-A 2. SDS-PAGE for INP-OspA purification. Lysate, flow through 1, flow through 2, flow through 3, flow through 4, elution 1, elution 2, and elution 3. Purifed bands evident in elutions 2 and 3 at approximately 60 kDa, with breakdown product at approximately 30 kDa.

OspA was expressed as a fusion to INP for surface-display on *E. coli*. To confirm surface expression of INP-OspA, we performed immunocytochemistry with an anti-OspA antibody. I made a cartoonized diagram of the immunocytochemistry process to aid in teaching the iGEM team about the goals and steps of this experiment, as well as show anticipated results as shown in Figure A-A 3.

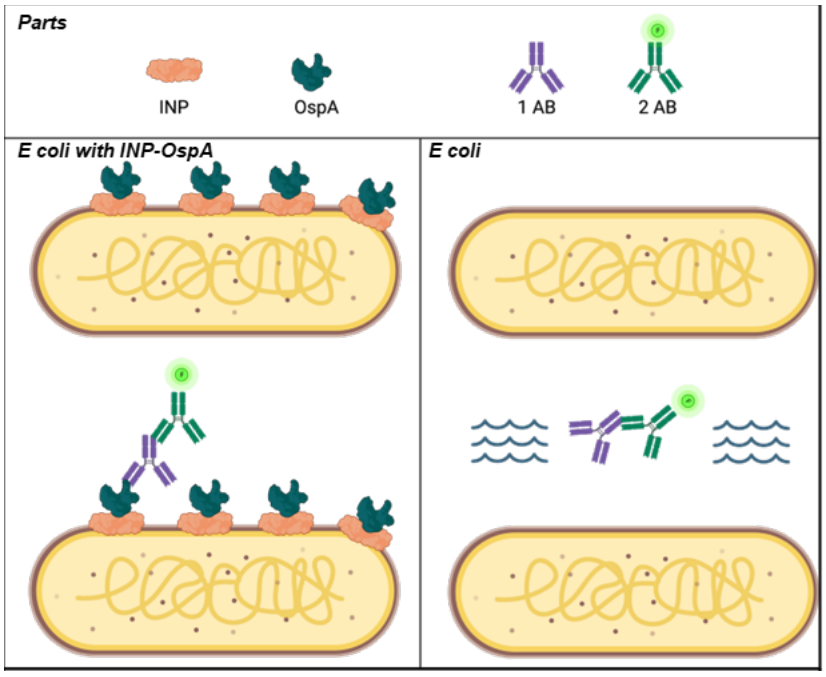

Figure A-A 3. Visualizing surface-display with immunocytochemistry. INP, OspA, primary and secondary antibodies (1AB and 2AB) are shown at the top. In the case of *E. coli* with INP-OspA (left) INP-OspA is displayed to the surface of the cell. The primary antibody binds OspA, then the secondary antibody with fluorophore binds the primary antibody. In the case of *E. coli* alone (right), no INP-OspA is surface displayed, the primary antibody does not have an antigen to bind, and the primary and secondary antibodies are washed away. Figure made with BioRender.

Immunocytochemistry and fluorescence microscopy showed that INP-OspA *E. coli* has surface-displayed OspA. The primary antibody was specific to OspA and the secondary antibody had fluorophore AlexFluor 488, which fluoresces green. Our wild-type BL21 *E. coli* control did not exhibit green fluorescence, confirming that OspA was not surface-displayed on the wild-type and that the antibodies did not non-specifically bind to the wild-type. Figure A-A 4 shows *E. coli* INP-OspA on the left, with wild-type *E. coli* on the right. The scale bar is 100 µm, so individual cells cannot be visualized, however the overall expression of INP-OspA is further confirmed.

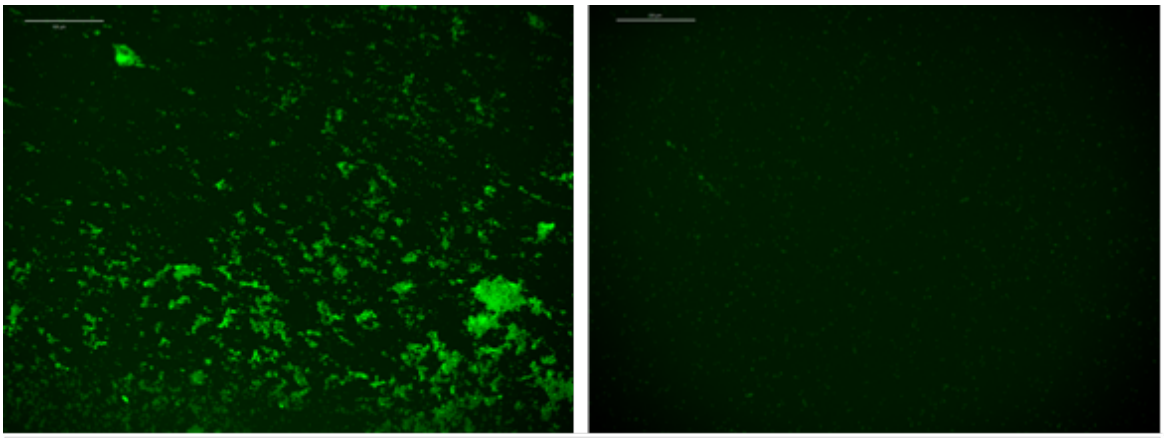

Figure A-A 4. Fluorescence microscopy for immunocytochemistry of *E. coli* INP-OspA (left) and wild-type *E. coli* (right). Scale bar is 100 µm. Green fluorescence is evident in *E. coli* INP-OspA, indicating OspA is surface-displayed. See Figure A-A 3 for a cartoonized schematic.

These results were presented at the 2023 iGEM competition, illustrating that OspA could be surface-displayed via INP. The next steps include pairing OspA with DNA-aptamer-gold nanoparticle constructs to build the sensor portion of the microneedle patch, as well as recombinantly expressing Salp12 to chemoattract *B. burgdorferi* back to the patch. Preliminary results suggest Salp12 expression, however these should be confirmed via Western blot (Fig. A-A 5).

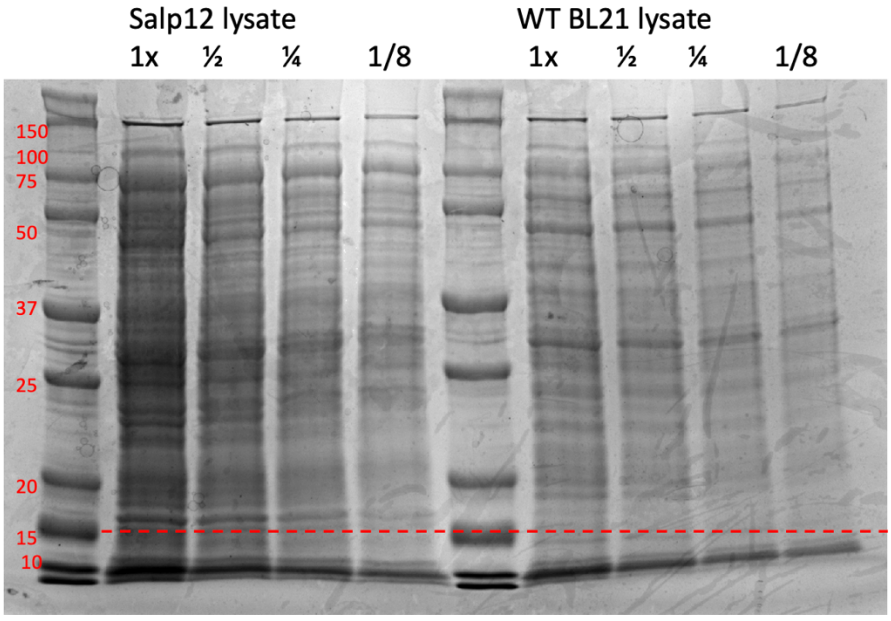

Figure A-A 5. SDS-PAGE for Salp12 lysates as compared to wild-type BL21 lysates.

Figure A-A 6. USAFA iGEM team 2023 at iGEM jamboree in Paris, France.

Appendix B: Supplemental Figures

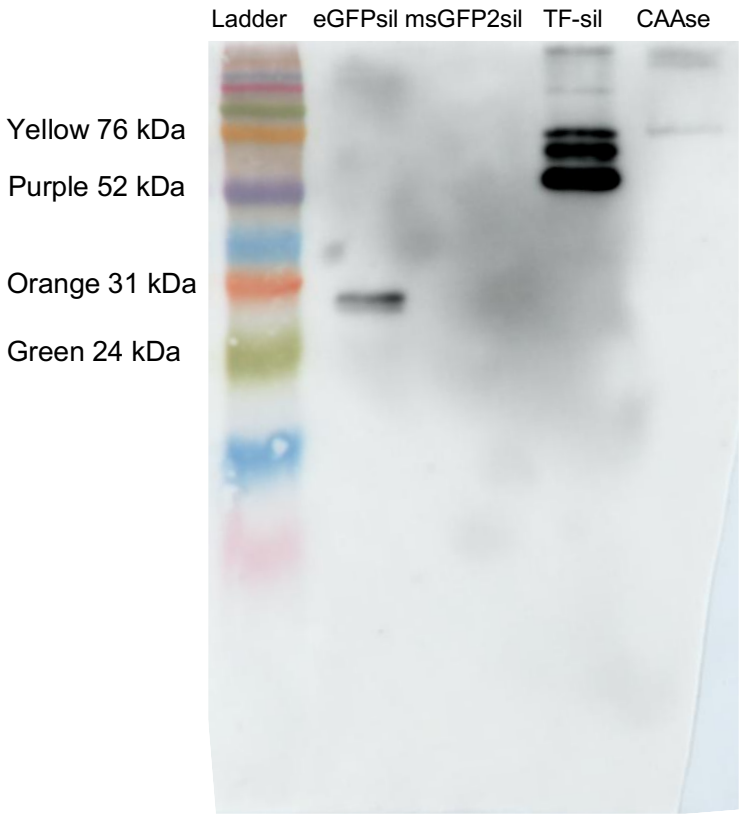

Supplemental Figure S.1A-1. Western blot of eGFP-sil, msGFP2-sil, and TF-sil along with CAAse positive control. Detection of his-tag reveals that smaller bands in TF-sil and eGFP-sil are consistent with protein degradation products. Anticipated MWs are 52, 50, 75 kDa respectively for eGFP-sil, msGFP2sil, and TF-sil.

Supplemental Table S.1B-1. Preliminary silicatein mutant identifications, with wild type sequence as reference. Mutations are highlighted in yellow, X refers to an undetermined amino acid.

	Wild Type
	GASYAFSAMGALEGANALAKGNAVSLSEQNIIDCSIPYGN HGCHGGNMYDAFLYVIANEGVDQDSAYPFVGKQSSCNY NSKYKGTSMSGMVSIKSGSESDLQAAVSNVGPVSVAIDGA NSAFRFYYSGVYDSSRCSSSSLNHAMVVTGYGSYNGKKY WLAKNSWGTNWGNSGYVMMARNKYNQLE
Fusion protein	**Mutant (yellow highlights change from WT)**
eGFP	GASYAFSAMGALEGANALAKGNAVSLSEQNIIDCSIPYGN HGCHGGNMYDAFLYVIANEGVDQDSAYPFVGKQSSCNY NSKYKGTSMSGMVSIKSGSESDF*
eGFP	GASYAFSAMGALEGANALAKGNAVSLSEQNIIDCSIPYGN HGCHGGNMYDAFLYVIANEGVDQDSAYPFVGKQSSCNY NSKYKGTSMSGMVSIKSGSESDLQAAVSNVGPVSVAIDGA NSAFRFYYSGVYVSSRRSSRFLNRYTIPPS*
Trigger Factor	GESYAFSAMGALEGANALAKGNAVSVSEQNIIDCSIPYGN HGCHGGNMYDAFLYVIANEGVDQDSAYPLVGKQSSCNY XSKYKGTSMSGMVSIKSGSESDLQAAVSNVVPVSVAIDGA NSAFRFYYSGEYASSRCSSSSXNHAMVVTGYGSYNGKKY WLAKNSWGTNWGNSGYVMMARNKYNQLE
Trigger Factor	GESYAFYAMGAVEGANALAKGNAVSVSEQNIIDCCILYXNH GCHDGNMYDAFVYVIANEGVDQDSAYPLVGKQSSCNYTYK YKGTIMSGIXSINSGSESDLQAAVSNXGPVSVPIHGANSSFRFY YSGEXXSSRCSSSSMNHAMVVTGYGSXNGKKYWQSKNXWG QNWGNSGYVTTARNKYNLL

Supplemental Table S1.B-2. Sequences for TF-silicatein mutant 2.6 with wild type sequence as reference. Mutations are highlighted in yellow, X refers to an undetermined amino acid. Consensus shown is 80%.

	Wild Type GASYAFSAMGALEGANALAKGNAVSLSEQNIIDCSIPYGN HGCHGGNMYDAFLYVIANEGVDQDSAYPFVGKQSSCNY NSKYKGTSMSGMVSIKSGSESDLQAAVSNVGPVSVAIDGA NSAFRFYYSGVYDSSRCSSSSLNHAMVVTGYGSYNGKKY WLAKNSWGTNWGNSGYVMMARNKYNQLE
Sample ID	**Sequence (yellow highlights are differences from WT)**
2126841 TU6	LASKAFSAMGALEGANALAKGNAVSLSEQNIIDCSIPYGN HGCHGGNMYDAFLYVIANEGVDQDSAYPFVGKQSSCNY NSKYKGTSMSGMVSIKSGSESDLQAAVSNVGPVSVAIDGA NSAFRFYYSGVYDSSRCSSSSLNHAMVVTGYGSYNGEKY WLAKNSWGTNWGE*
2138869 TU3	GASYAFSAMGALEGANALDKGNAVSLSEQNIIDCSIPYGN HGCHGGNMYDAFLYVIANEGVDQDSAYPFVGKQSSCNY NSKYKGTSMSGMVSIKSGSESDLQAAVSNVGPVSVAIDGG NFGFCFYY*
2138869 TU6	GASYAFSAMGALEGANALAKGNAVSLSEQNIIDCSIPYGN HGCHGGNMYDAFLYVIANEGVDQDSAYPFVGKQSSCNY NSKYKGTSMSGMVSIKSGSESDLQAAVSNVGPVSVAIDGA NSAFRFYYSGVYDSSRCSSSSLNHAMVVTGYGSYNGKKCWLV*
2138869 TU8	GASYAFSAMGALEGANALAKGNAVSLSEQNIIDCSIPYGN HGCHGGNMYDAFLYVIANEGVDQDSAYPFVGKQSSCNY NSKYKGTSMSGMVSIKSGSESDLQAAVSNVGPVSVAIDGA NSAFRFYYSGVYDSSRCSSSSLNHAMVVTGYGSYNGKKY WLAKNSWGTNWGNSGYVMMARNXYNQLEHHHH
2138869 TU9	GASYAFSAMGALEGANALAKGNAVSLSEQNIIDCSIPYGN HGCHGGNMYDAFLYVIANEGVDQDSAYPFVGKQSSCNY

	NSKYKGTSMSGMVSIKSGSESDLQAAVSNVGPVSVAIDGA NSAFRFYYSGVYDSSRCSSSSLNHAMVVTGYGSYNGKKY WLAKNSWGKKQDNNE*
2142324 TU1	GASYAFSAMGALEGANALAKGNAVSLSEQNIIDCSIPYGN HGCHGGNMYDAFLYVIANEGVDQDSAYPFVGKQSSCNY NSKYKGTSMSGMVSIKSGSESDLQAAVSNVGPVSVAIDGA NSAFRFYYSGVYDSSRCSSSSLNHAMVVTGYGSYTGKKN*
2142324 TU4	GASYAFSAMGALEGANALAKGNAVSLSEQNIIDCSIPYGN HGCHGGNMYDAFLYVIANEGVDQDSAYPFVGKQSSCNY NSKYKGTSMSGMVSIKSGSESDLQAAVSNVGPVSVAIDGA NSAFRFYYSGVYDSSRCSSSSLNHAMVVTGYGYLQRATTIAESGIXXLRW WYRRGPIPSGTFSRKKRTFSKS*
2142324 TU10	GASYAFSAMGALEGANALAKGNAVSLSEQNIIDCSIPYGN HGCHGGNMYDAFLYVIANEGVDQDSAYPFVGKQSSCNY NSKYKGTSMSGMVSIKSGSESDLQAAVSNVGPVSVAIDGA NSAFRFYYSGVYDSSHCSSRSXTQTMIDTQXKSNT*
2142226 TU1 **read with Sil F primer	MQPWCHGGXMYDAFLYVIANEGVDQDSAYPFVGKQSSCNY NSKYKGTSMSGMVSIKSGSESDLQAAVSNVGPVSVAIDGA NSAFRFYYSGVYDSSRCSSSSLNHAMVVTGYGSYNGKKY WLAKNSWGTNWGNSGYVMMARNKYNQLEHHHHHH*
CONSENSUS 2.6	GASYAFSAMGALEGANALAKGNAVSLSEQNIIDCSIPYGN HGCHGGNMYDAFLYVIANEGVDQDSAYPFVGKQSSCNY NSKYKGTSMSGMVSIKSGSESDLQAAVSNVGPVSVAIDGA NSAFRFYYSGVYDSSRCSSSSLNHAMVVTGYGSYNGKKX WLXXXXXXXXXX-XX----------

Supplemental Table S1B-3. Sequences for TF-silicatein mutant 2.7 with wild type sequence as reference. Mutations are highlighted in yellow, X refers to an undetermined amino acid. Consensus shown is 80%.

	Wild Type GASYAFSAMGALEGANALAKGNAVSLSEQNIIDCSIPYGN HGCHGGNMYDAFLYVIANEGVDQDSAYPFVGKQSSCNY NSKYKGTSMSGMVSIKSGSESDLQAAVSNVGPVSVAIDGA NSAFRFYYSGVYDSSRCSSSSLNHAMVVTGYGSYNGKKY WLAKNSWGTNWGNSGYVMMARNKYNQLE
Sample ID	**Sequence (yellow highlights are differences from WT)**
2119647 TU7	GESYAFSAMGALEGANALAKGNAVSVSEQNIIDCSIPYGN HGCHGGNMYDAFLYVIANEGVDQDSAYPLVGKQSSCNY XSKYKGTSMSGMVSIKSGSESDLQAAVSNVVPVSVAIDGA NSAFRFYYSGEYASSRCSSSSXNHAMVVTGYGSYNGKKY WLAKNSWGTNWGNSGYVMMARNKYNQLEHHHHH---
2121209 TU7	GSSEAFSAMGALEGANALAKGNAVSLSEQSIIDCSIPYGN HGCHGGNMYDAFLYVIANEGVDQDSAYPFVGKQSSCNY NSKYKGTSMSRYG*
2126841 TU7	FASYAFSAMGALEGANALAKGNAVSLSEQNIIDCSIPYGN HGCHGGNMYDAFLYVIANEGVDQDSAYPFVGKQSSCNY NSKYKGTSMSGMVSIKSGSESDLQAAVSNVGPVSVAIDGA NSAFRFYYSGVYDSSRCSSSSLNHADGGYRLWFLQRRKDTGWLKIRGVR KLEATSGYVMNXRVTNTDQTXAPPPPPT*
2131323 TU2	VCEYAFSAMGALEGANALAKGNAVSLSEQNIIDCSIPYGN HGCHGGNMYDAFLVVIANEGVDQDSAYPFVGKQSSCNY NSKYKGTSMSGMVSIKSGSESDLQAAVSNVGPVSVAIDGA NSAFRFYYSGVYDSSRCSSSYLNHAMVVTGYGSYNGKKY WLGKNLVGYELGQ*
2142324 TU2	GASYAFSPMGALEGATALAQANAVSLSDHNIIDCSIPYGT HGCHGGNMSDAFLYVIANEGVDPDSAYPFVGKQSSCNY

	NSKYKGTSMSGMVSIKSGSESDLQAAVYNVGPVSVAIDGEK*
CONSENSUS 2.7	GXSYAFSAMGALEGANALAKGNAVSLSEQNIIDCSIPYGN HGCHGGNMYDAFLYVIANEGVDQDSAYPFVGKQSSCNY NSKYKGTSMSGMVSIKSGSESDLQAAVSNVGPVSVAIDGA NSAFRFYYSGXYXSSRCSSSXXNHAXXXXXXXXXXGXXXWXXXXXXX XXXX----------XXXXXXXXXXXXXXXX-XXXXXXX—

Supplemental Table S.1B-4. Sequences for TF-silicatein mutant 2.8 with wild type sequence as reference. Mutations are highlighted in yellow, X refers to an undetermined amino acid. Consensus shown is 80%

	Wild Type GASYAFSAMGALEGANALAKGNAVSLSEQNIIDCSIPYGN HGCHGGNMYDAFLYVIANEGVDQDSAYPFVGKQSSCNY NSKYKGTSMSGMVSIKSGSESDLQAAVSNVGPVSVAIDGA NSAFRFYYSGVYDSSRCSSSSLNHAMVVTGYGSYNGKKY WLAKNSWGTNWGNSGYVMMARNKYNQLE
Sample ID	**Sequence (yellow highlights are differences from WT)**
2119647 TU8	GESYAFYAMGAVEGANALAKGNAVSVSEQNIIDCCILYXN HGCHDGNMYDAFVYVIANEGVDQDSAYPLVGKQSSCNY TYKYKGTIMSGIXSINSGSESDLQAAVSNXGPVSVPIHGA NSSFRFYYSGEXXSSRCSSSSMNHAMVVTGYGSXNGKKY WQSKNXWGQNWGNSGYVTTARNKYNLLEHHPHHL*
2126841 TU8	CASYAFSAMGALEGANALAKGNAVSLSEQNIIDCSIPYGN HGCHGGNMYDAFLYVIANEGVDQDSAYPFVGKQSSCNY NSKYKGTSMSGMVSIKSGSESDLQAAVSNVGPVSVAIDGA NSAFRFYYSGVYDSSRCSSSSLNHAMVVTGYGSYNGEKY WLAKNSWGTNWGE*
2131323 TU3	CASYAFSAMGALEGANALAKGNAVSLSEQNIIDCSIPYGN HGCHGGNMYDAFLYVIANEGVDQDSAYPFVGKQSSCNY NSKYKGTSMSGMVSIKSGSESDLQAAVSNVGPVSVAIDGA NSAFRFYYSGVYDSSRCSSSSLNHAMVVTGYGSYNGKKY WLAKNSWGTNWGNSGYVMMARNKYNQLEHHHHHH*
2138869 TU7	GASYAFSAMGALEGANALAKGNAVSLSEQNIIDCSIPYGN HGCHGGNMYDAFLYVIANEGVDQDSAYPFVGKQSSCNY NSKYKGTSMSGMVSIKSGSESDLQAAVSNVGPVSVAIDGA NSAFRFYYSGVYDSSRCSSSSLNHAMVVTGYGYLQRAKNAGWYKNDAX XNRGPXRSR*

2138869 TU10	GASYAFSAMGALEGANALAKGNAVSLSEQNIIDCSIPYGN HGCHGGNMYDAFLYVIANEGVDQDSAYPFVGKQSSCNY NSKYKGTSMSGMVSIKSGSESDLQAAVSNVGPVSVAIDGA NSAFRFYYSGVYDSSRCSSSSLNHAMVVTGYGSYNGKKY WLAKNSWGTKRGISG*
2142226 TU3 *sil F primer	VGGXXXDAFLYVIANEGVDQDRAYPVVGKQSSCNY XSKYKGARXAGMVSIKSGSESDLRXAVSNVXPXGXXVDGA NSAFRFYYSGVYDSSRCSSSSLNHAMVVTGYGSYNGKKY WLAKNSWGTNWGNSGYVMMARNKYNQLEHHHHHH*
2.8 CONSENSUS	GASYAFSAMGALEGANALAKGNAVSLSEQNIIDCSIPYGN HGCHGGNMYDAFLYVIANEGVDQDSAYPFVGKQSSCNY NSKYKGTSMSGMVSIKSGSESDLQAAVSNVGPVSVAIDGA NSAFRFYYSGVYDSSRCSSSSLNHAMVVTGYGSYNGKK-- YWLAKNSWGTNWGNSGYVXXARNKYNXLEXXXXXX---------

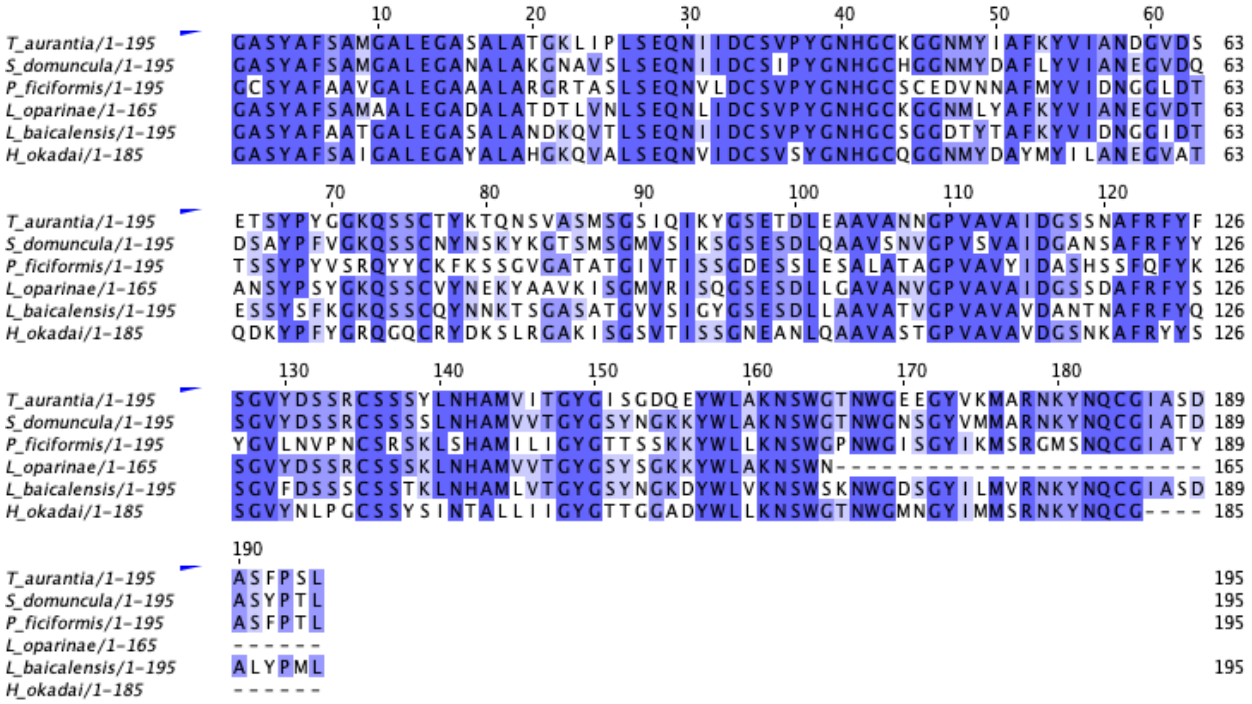

Supplemental Figure S.2B-1. Sequence alignment for silicatein-alpha from *T. aurantia, S. domuncula, P. ficiformis, L. oparinae, L. baicalensis,* and *H. okadai.* Shades of blue represent identity with *T. aurantia.*

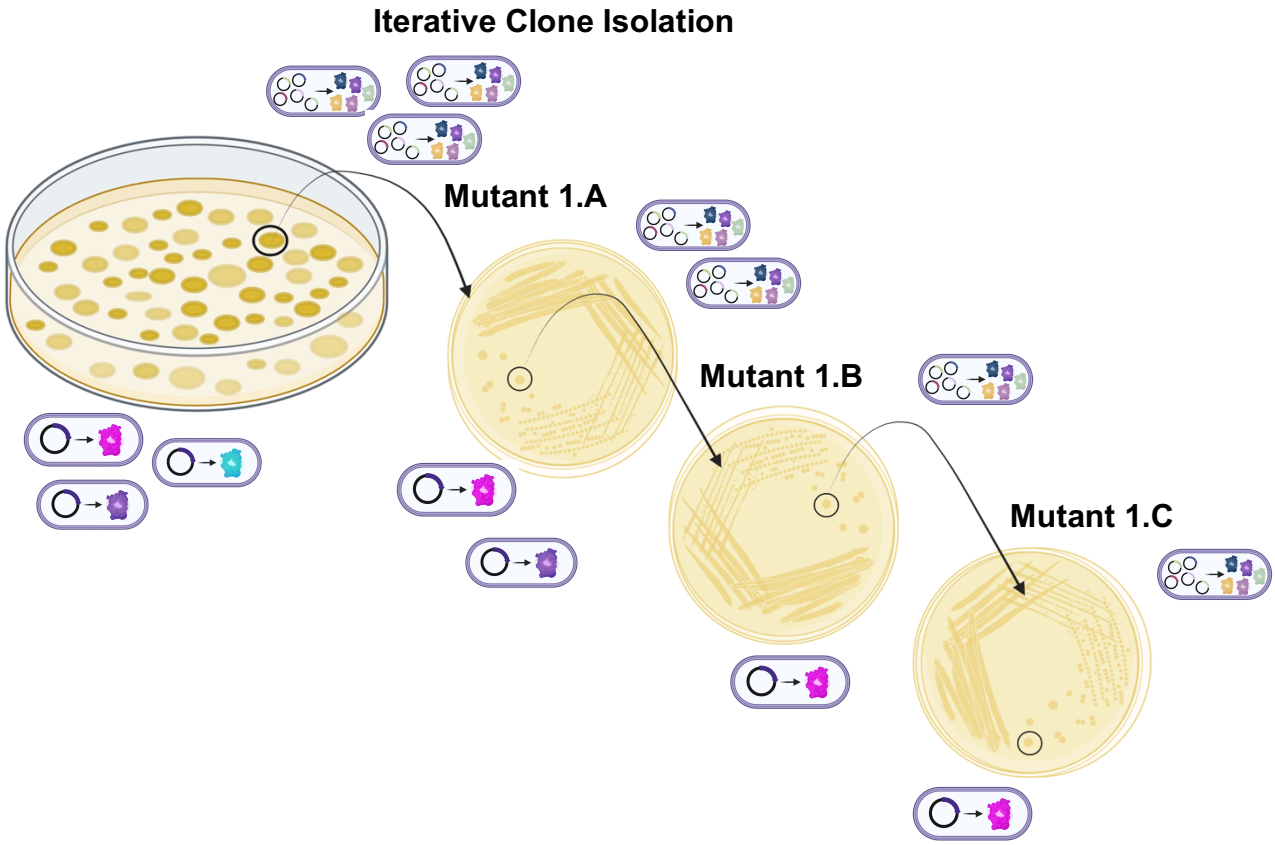

Supplemental Figure S1B-6. Iterative clone isolation from a library colony. For multiple plasmids in the same cell, sequencing will show different sequences for mutant 1A, 1B, 1C, etc. as shown in the cells above plates. For colonies that contain cells with different plasmids, iterative clone isolation will eventually reveal a single repeated sequence as shown with the cells below plates.

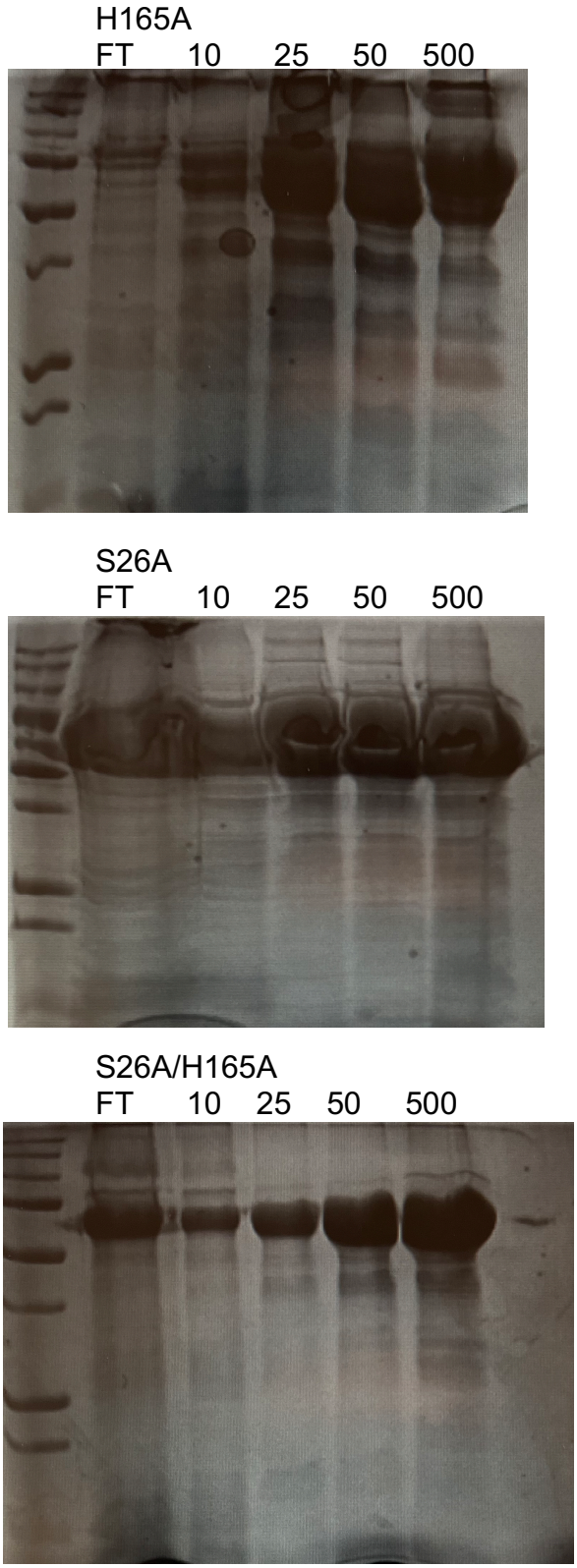

Supplemental Figure S.1B-7. SDS-PABE for TF-sil H165A, S26A, and S26A/H165A mutant purifications.

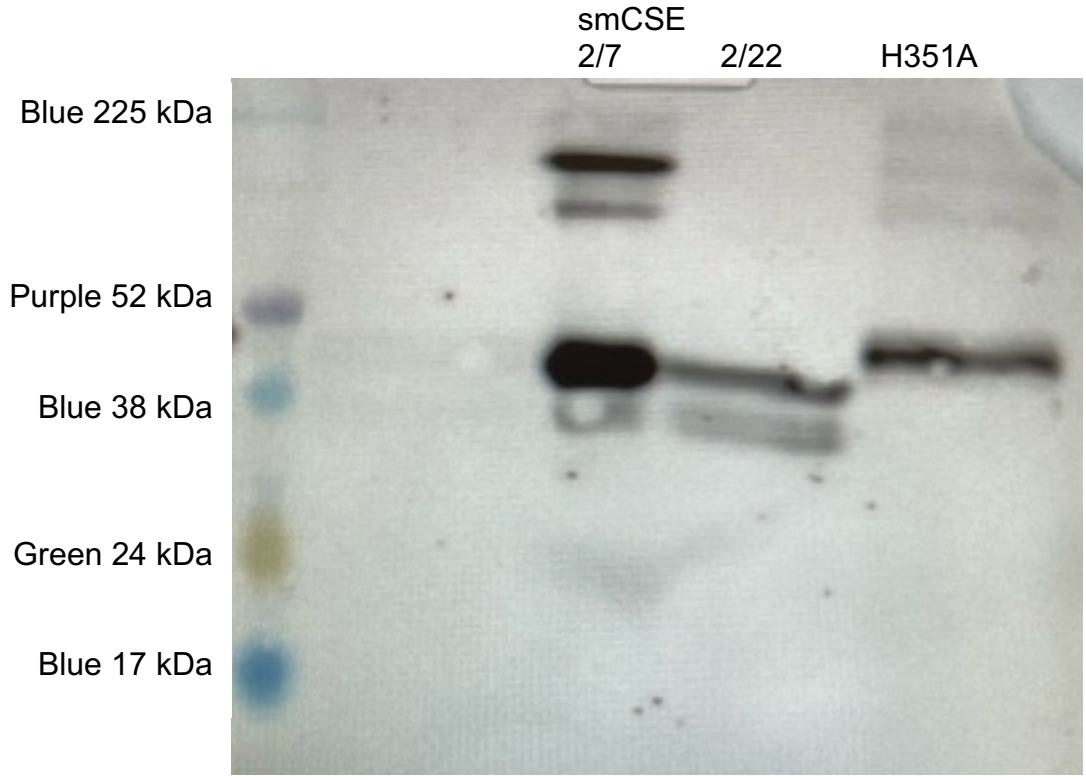

Supplemental Figure S.2A-1. Western blot for smCSE purified on 2/7, smCSE purified on 2/22, and smCSE H351A. Anticipated MW is 48 kDa – each sample shows a band between 38 and 52 kDa. smCSE also forms a tetramer, which can be visualized with the bands just below 225 kDa.

Comparing Lithium Biomineralization with Lysinibacillus sphaericus and Bacillus aryabhattai

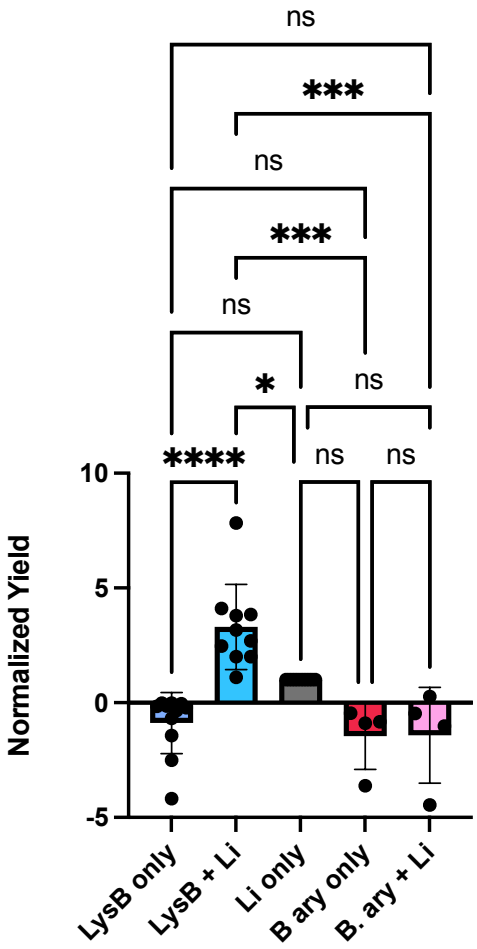

Supplemental Figure S.3B-1. Comparing *Lysinibacillus sphaericus* and *Bacillus arryabhattai* lithium precipitation via HPBO fluorescent assay. Moles recovered were determined via standard curve and associated equation, then yields were normalized to the lithium only condition. Normalized yield for "Li only" is 1.

LiCl BioRad (SciFinder Spectral Database)

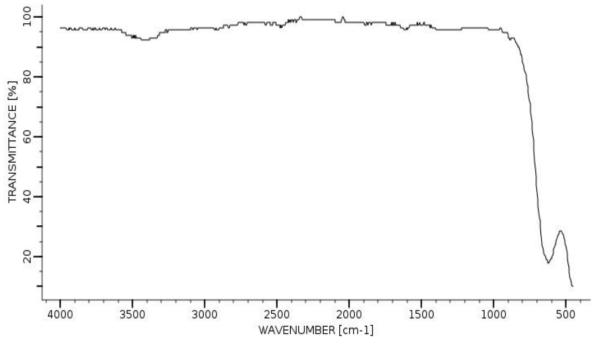

LiOH BioRad (SciFinder Spectral Database)

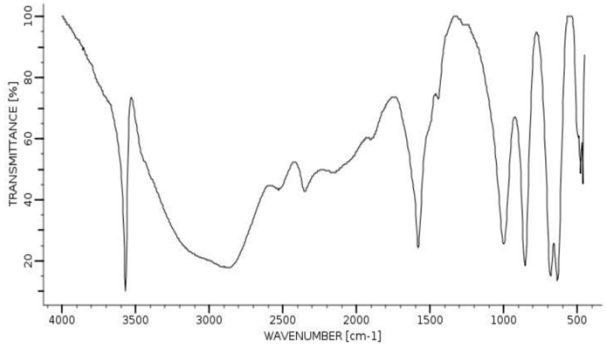

NaOH BioRad (SciFinder Spectral Database)

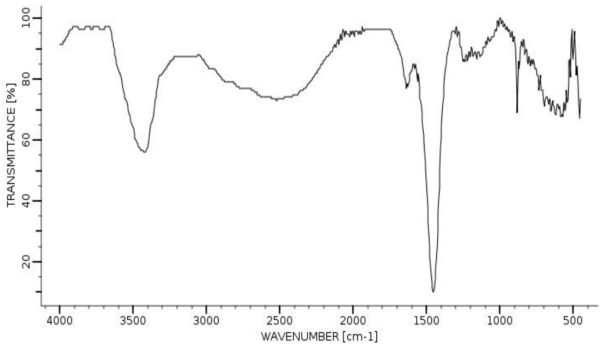

$LiCH_2O_3$ BioRad (SciFinder Spectral Database)

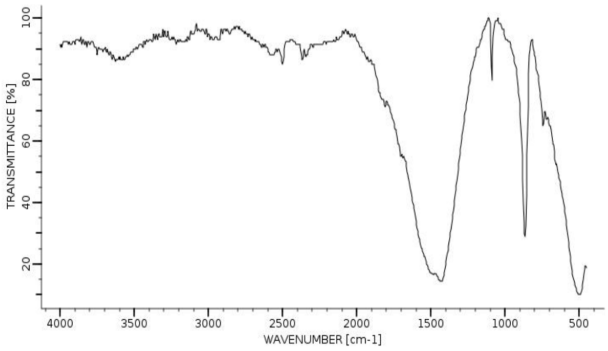

$NaCH_2O_3$ BioRad (SciFinder Spectral Database)

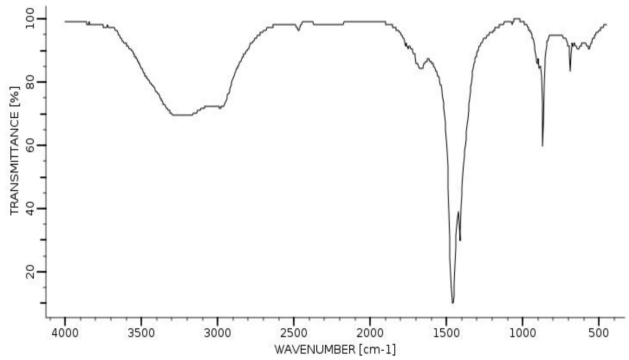

Supplemental Figure S.3B-2. Reference FTIR spectra for LiCl, LiOH, $LiCH_2O_3$, NaOH, $NaCH_2O_3$.

Main Graphics, Analyze View:

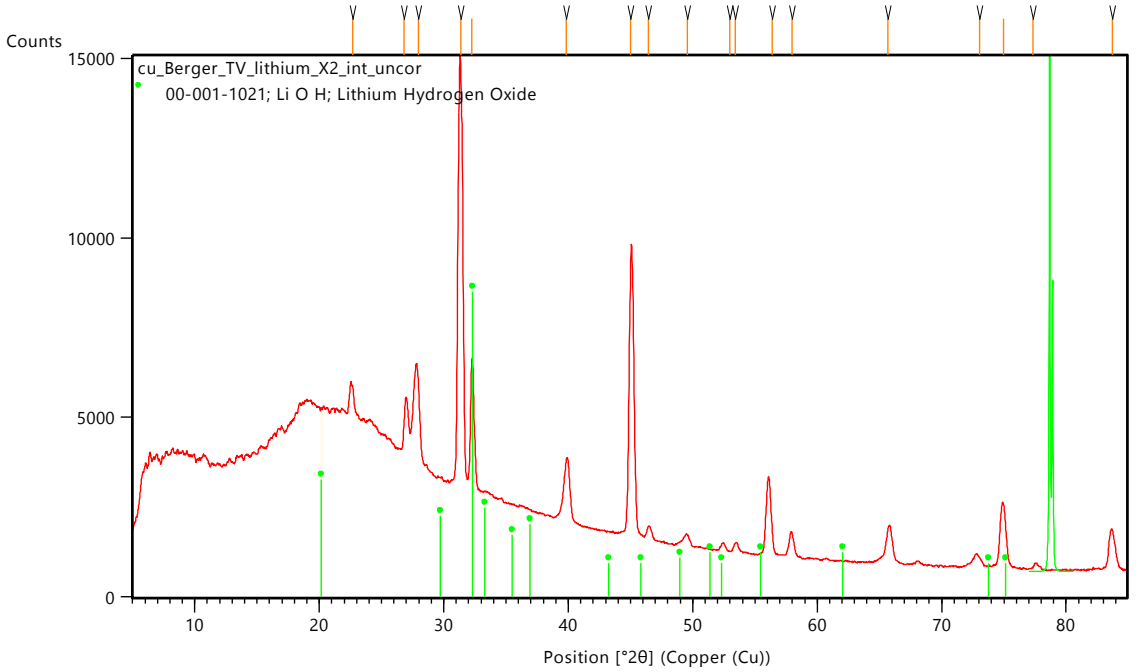

Peak List:

Pos. [°2θ]	Height [cts]	FWHM Left [°2θ]	d-spacing [Å]	Rel. Int. [%]
22.6690	5219.10	0.0900	3.91937	37.28
26.8069	4586.15	0.0900	3.32302	32.76
27.9892	5931.17	0.0900	3.18529	42.36
31.3882	14001.30	0.0900	2.84767	100.00
32.2749	5693.81	0.0900	2.77143	40.67
39.8118	2964.21	0.0900	2.26241	21.17
44.9842	9016.81	0.0900	2.01356	64.40
46.4621	1104.91	0.0900	1.95289	7.89
49.5655	1025.79	0.0900	1.83764	7.33
52.9645	669.76	0.0900	1.72744	4.78
53.4079	788.44	0.0900	1.71414	5.63
56.3635	2449.94	0.0900	1.63106	17.50
57.9891	1025.79	0.0900	1.58914	7.33
65.6739	1104.91	0.0900	1.42056	7.89
73.0630	590.64	0.0900	1.29404	4.22
74.9842	1856.54	0.0900	1.26558	13.26
77.3487	155.49	0.0900	1.23269	1.11
83.7034	1065.35	0.0900	1.15452	7.61

Pattern List:

Visible	Ref.Code	Score	Compound Name	Displ.[°2θ]	Scale Fac.	Chem. Formula
*	00-001-1021	42	Lithium Hydrogen Oxide	-0.223	0.494	Li O H

Supplemental Figure S.3B-3. XRD report for *L. sphaericus* synthesized LiOH particles. Note: FWHM refers to the green assigned peaks, and should not be used to calculate particle size.

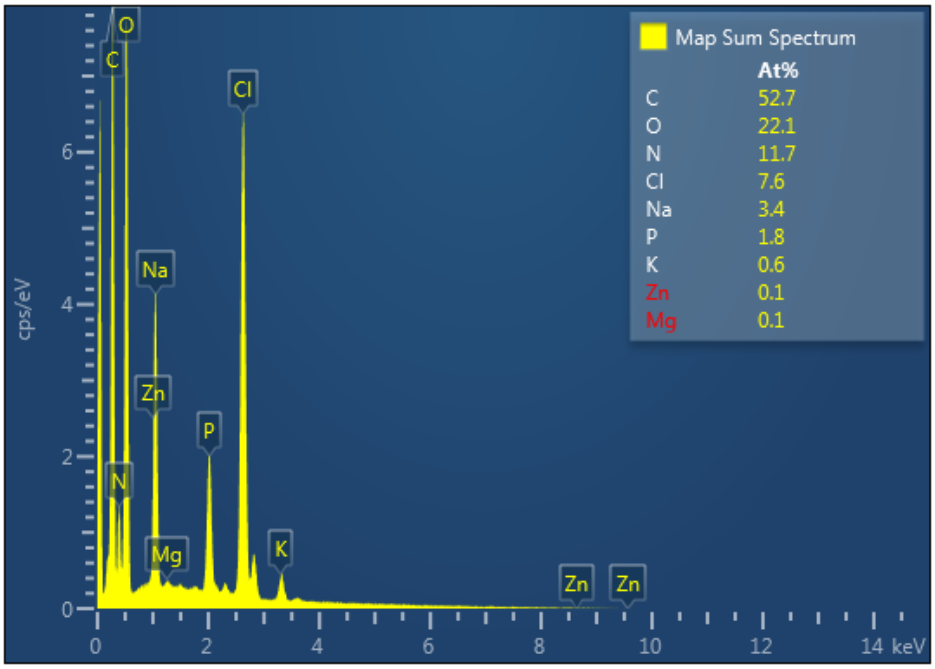

Supplemental Figure S.3B-4. EDS composition report for *L. sphaericus* synthesized LiOH particles. Note: lithium does not have an electron signature detectable by EDS.

Lysinibacillus sphaericus soluble and insoluble lysates after co-incubation with lithium chloride

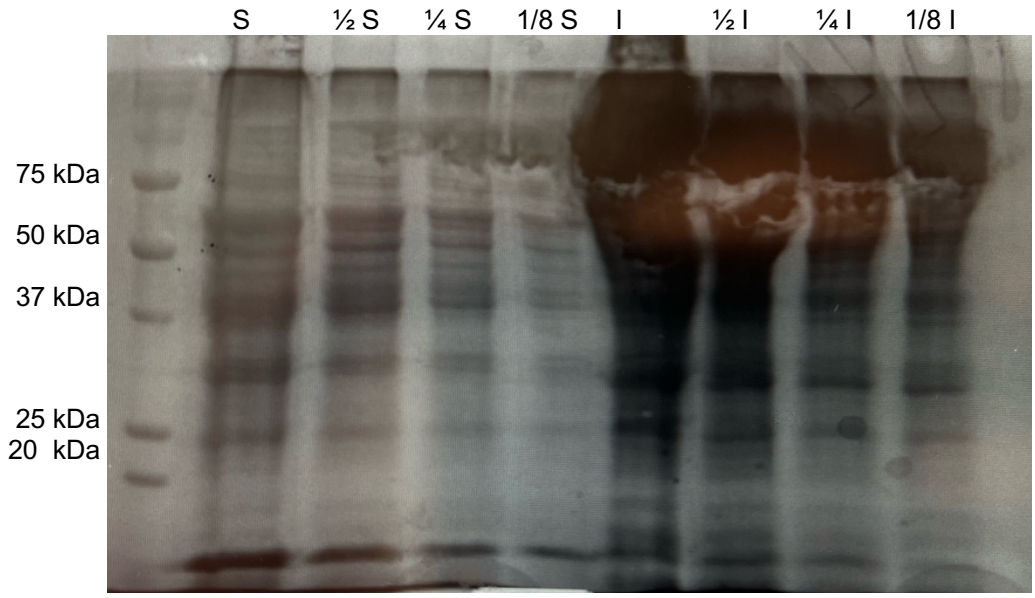

Supplemental Figure S.3B-5. SDS-PAGE for soluble and insoluble fractions of *L. sphaericus* cell lysate after co-incubation with lithium chloride. S denotes soluble lysate. I denotes insoluble lysate. Over-expression at 125 kDa is consistent with S-layer protein.

References

(1) Chavali, M. S.; Nikolova, M. P. Metal Oxide Nanoparticles and Their Applications in Nanotechnology. *SN Applied Sciences* **2019**, *1* (6), 607. https://doi.org/10.1007/s42452-019-0592-3.

(2) Mann, M. M.; Vigil, T. N.; Felton, S. M.; Fahy, W. E.; Kinkeade, M. A.; Kartseva, V. K.; Rowson, M.-J. C.; Frost, A. J.; Berger, B. W. Proteins in Synthetic Biology with Agricultural and Environmental Applications. *SynBio* **2022**, *1* (1), 77–88. https://doi.org/10.3390/synbio1010006.

(3) Espina, G.; Muñoz-Ibacache, S. A.; Cáceres-Moreno, P.; Amenabar, M. J.; Blamey, J. M. From the Discovery of Extremozymes to an Enzymatic Product: Roadmap Based on Their Applications. *Frontiers in Bioengineering and Biotechnology* **2022**, *9*, 752281. https://doi.org/10.3389/fbioe.2021.752281.

(4) Vigil, T. N.; Spangler, L. C. Understanding Biomineralization Mechanisms to Produce Size-Controlled, Tailored Nanocrystals for Optoelectronic and Catalytic Applications: A Review. *ACS Appl. Nano Mater.* **2024**, acsanm.3c04277. https://doi.org/10.1021/acsanm.3c04277.

(5) Nudelman, F.; Sommerdijk, N. A. J. M. Biomineralization as an Inspiration for Materials Chemistry. *Angewandte Chemie International Edition* **2012**, *51* (27), 6582–6596. https://doi.org/10.1002/anie.201106715.

(6) Mann, S. *Biomineralization: Principles and Concepts in Bioinorganic Materials Chemistry*; Oxford University Press, 2001.

(7) Di Costanzo, L. F. Atomic Details of Biomineralization Proteins Inspiring Protein Design and Reengineering for Functional Biominerals. *Chemistry* **2022**, *4*, 827–847.

(8) Gilbert, P.U.P.A., Bergmann, K.D., Boekelheide, N., Tambutte, S., Mass, T., Marin, F., Adkins, J.F., Erez, J., Gilbert, B., Knutson, V., Cantine, M., Hernandez, J.O., Knoll, A. H. Biomineralization: Integrating Mechanism and Evolutionary History. *Science Advances* **2022**, *8*, eabl9653.

(9) Tafforeau, P.; Bentaleb, I.; Jaeger, J.-J.; Martin, C. Nature of Laminations and Mineralization in Rhinoceros Enamel Using Histology and X-Ray Synchrotron Microtomography: Potential Implications for Palaeoenvironmental Isotopic Studies. *Palaeogeography, Palaeoclimatology, Palaeoecology* **2007**, *246* (2–4), 206–227. https://doi.org/10.1016/j.palaeo.2006.10.001.

(10) Chen, M.; Hu, N.; Zhou, C.; Lin, X.; Xie, H.; He, Q. The Hierarchical Structure and Mechanical Performance of a Natural Nanocomposite Material: The Turtle Shell. *Colloids and Surfaces A: Physicochemical and Engineering Aspects* **2017**, *520*, 97–104. https://doi.org/10.1016/j.colsurfa.2017.01.063.

(11) Wang, Z.; Pascual-Anaya, J.; Zadissa, A.; Li, W.; Niimura, Y.; Huang, Z.; Li, C.; White, S.; Xiong, Z.; Fang, D.; Wang, B.; Ming, Y.; Chen, Y.; Zheng, Y.; Kuraku, S.; Pignatelli, M.; Herrero, J.; Beal, K.; Nozawa, M.; Li, Q.; Wang, J.; Zhang, H.; Yu, L.; Shigenobu, S.; Wang, J.; Liu, J.; Flicek, P.; Searle, S.; Wang, J.; Kuratani, S.; Yin, Y.; Aken, B.; Zhang, G.; Irie, N. The Draft Genomes of Soft-Shell Turtle and Green Sea Turtle Yield Insights into the Development and Evolution of the Turtle-Specific Body Plan. *Nat Genet* **2013**, *45* (6), 701–706. https://doi.org/10.1038/ng.2615.

(12) Frankel, R. B.; Bazylinski, D. A. Biologically Induced Mineralization by Bacteria. *Reviews in Mineralogy and Geochemistry* **2003**, *54* (1), 95–114. https://doi.org/10.2113/0540095.

(13) LaMer, V. K.; Dinegar, R. H. Theory, Production and Mechanism of Formation of Monodispersed Hydrosols. *J. Am. Chem. Soc.* **1950**, *72* (11), 4847–4854. https://doi.org/10.1021/ja01167a001.

(14) Dobberschutz, S., Nielsen, M.R., Sand, K.K., Civioc, R., Bovet, N., Stipp, S.L.S., Andersson, M. P. The Mechanisms of Crystal Growth Inhibition by Organic and Inorganic Inhibitors. *Nature Communications* **2018**, *9*, 1578.

(15) Anderssson, M.P., Dobberschutz, S., Sand, K.K., Tobler, D.J., De Yoreo, J.J., Stipp, S. L. S. A Microkinetic Model of Calcite Step Growth. *Angewandte Chemie - International Edition* **2016**, *55*, 11086–11090.

(16) Prabhu, N. , Howe, J. M. The Structure of Kinks at Dislocation Interphase Boundaries and Their Role in Boundary Migration - II. Kinetic Analyses Including Kink Motion. *Acta metall. mater.* **1990**, *38* (6), 889–896.
(17) Christen, T. Nucleation of Kinks at Grain Boundaries. *Europhysics Letters* **1995**, *31* (3), 181–186.
(18) Hamm, L.M., Giuffre, A.J., Han, N., Tao, J., Wang, D., De Yoreo, J.J., Dove, P. M. Reconciling Disparate Views of Template-Directed Nucleation through Measurement of Calcite Nucleation Kinetics and Binding Energies. *PNAS* **2014**, *111* (4), 1304–1309.
(19) Gebauer, D.; Cölfen, H. Prenucleation Clusters and Non-Classical Nucleation. *Nano Today* **2011**, *6* (6), 564–584. https://doi.org/10.1016/j.nantod.2011.10.005.
(20) Ehrlich, H., Deutzmann, R., Brunner, E., Cappellini, E., Koon, H., Solazzo, C., Yang, Y., Ashford, D., Thomas-Oates, J., Lubeck, M., Baessmann, C., Langrock, T., Hoffmann, R., Worheide, G., Reitner, J., Simon, P., Tsurkan, M., Ereskovsky, A.V., Kurek, D., M. J. Mineralization of the Metre-Long Biosilica Structures of Glass Sponges Is Templated on Hydroxylated Collagen. *Nature Chemistry* **2010**, *2*, 1084–1088.
(21) Goerlich, S.; Samuel, A. J.; Best, R. J.; Seidel, R.; Vacelet, J.; Leonarski, F. K.; Tomizaki, T.; Rellinghaus, B.; Pohl, D.; Zlotnikov, I. Natural Hybrid Silica/Protein Superstructure at Atomic Resolution. *Proceedings of the National Academy of Sciences of the United States of America* **2020**, *117*, 31088–31093.
(22) Zúñiga-Estrada, M. A.; Zúñiga-Estrada, E. A.; Cuéllar-Cruz, M. Silica-Carbonate Biomorphs of Alkaline Earth Metals: Relationship with Minerals since the Precambrian Era. *Progress in Crystal Growth and Characterization of Materials* **2023**, *69* (1), 100594. https://doi.org/10.1016/j.pcrysgrow.2023.100594.
(23) Kellermeier, M.; Cölfen, H.; García-Ruiz, J. M. Silica Biomorphs: Complex Biomimetic Hybrid Materials from "Sand and Chalk." *Eur J Inorg Chem* **2012**, *2012* (32), 5123–5144. https://doi.org/10.1002/ejic.201201029.
(24) Brutchey, R. L.; Morse, D. E. Silicatein and the Translation of Its Molecular Mechanism of Biosilicification into Low Temperature Nanomaterial Synthesis. *Chemical Reviews* **2008**, *108* (11), 4915–4934. https://doi.org/10.1021/cr078256b.
(25) Sinatra, L., Pan, J., Bakr, O. M. Methods of Synthesizing Monodisperse Colloidal Quantum Dots. *Material Matters* **2017**, *12* (1), 3–7.
(26) Nyoka, M.; Choonara, Y. E.; Kumar, P.; Kondiah, P. P. D.; Pillay, V. Synthesis of Cerium Oxide Nanoparticles Using Various Methods: Implications for Biomedical Applications. *Nanomaterials* **2020**. https://doi.org/10.3390/nano10020242.
(27) Shimizu, K.; Cha, J.; Stucky, G. D.; Morse, D. E. Silicatein α: Cathepsin L-like Protein in Sponge Biosilica. *Proceedings of the National Academy of Sciences of the United States of America* **1998**, *95* (11), 6234–6238. https://doi.org/10.1073/pnas.95.11.6234.
(28) Curran, C. D.; Lu, L.; Jia, Y.; Kiely, C. J.; Berger, B. W.; McIntosh, S. Direct Single-Enzyme Biomineralization of Catalytically Active Ceria and Ceria-Zirconia Nanocrystals. *ACS Nano* **2017**, *11* (3), 3337–3346. https://doi.org/10.1021/acsnano.7b00696.
(29) Roberts, E.J., Karadagh, L.R., Wang, L., Malmstadt, N., Brutchey, R. L. Continuous Flow Methods of Fabricating Catalytically Active Metal Nanoparticles. *ACS Applied Material Interfaces* **2019**, *11*, 27479–27502.
(30) Ayling, A. L. Growth and Regneration Rates in Thinly Encrusting Demospongiae from Temperate Waters. *Biol. Bull.* **1983**, *165*, 343–352.
(31) Schlobmacher, U., Wiens, M., Schroder, H.C., Wang, X., Jochum, K.P., Muller, W. E. G. Silintaphin-1 - Interaction with Silicatein during Structure-Guided Bio-Silica Formation. *The Febs Journal* **2011**, *278* (7), 1145–1155.
(32) Lechner, C.C., Becker, C. F. W. Silaffins in Silica Biomineralization and Biomimetic Silica Precipitation. *Marine Drugs* **2015**, *13* (8), 5297–5333. https://doi.org/10.3390/md13085297.
(33) Cha, J. N.; Shimizu, K.; Zhou, Y.; Christiansen, S. C.; Chmelka, B. F.; Stucky, G. D.; Morse, D. E. Silicatein Filaments and Subunits from a Marine Sponge Direct the Polymerization of Silica and

Silicones in Vitro. *Proceedings of the National Academy of Sciences of the United States of America* **1999**, *96* (2), 361–365. https://doi.org/10.1073/pnas.96.2.361.
(34) Povarova, N. V.; Barinov, N. A.; Baranov, M. S.; Markina, N. M.; Varizhuk, A. M.; Pozmogova, G. E.; Klinov, D. V.; Kozhemyako, V. B.; Lukyanov, K. A. Efficient Silica Synthesis from Tetra(Glycerol)Orthosilicate with Cathepsin- and Silicatein-like Proteins. *Scientific Reports* **2018**, *8* (1), 1–9. https://doi.org/10.1038/s41598-018-34965-9.
(35) Fairhead, M., Johnson, K.A., Kowatz, T., McMahon, S.A., Carter, L.G., Oke, M., Liu, H., Naismith, J.H., van der Walle, C. F. Crystal Structure and Silica Condensing Activities of Silicatein A-Cathepsin L Chimeras. *Chemical Communications* **2008**, No. 15, 1765–1767.
(36) Ki, M.-R.; Jang, E.-K.; Pack, S. P. Hypothetical Cathepsin-like Protein from Nematostella Vectensis and Its Silicatein-like Cathepsin Mutant for Biosilica Production. *Process Biochemistry* **2014**, *49* (1), 95–101. https://doi.org/10.1016/j.procbio.2013.10.010.
(37) Dakhili, S.Y.T., Caslin, S.A., Faponle, A.S., Quayle, P., de Visser, S.P., Wong, L. S. Recombinant Silicateins as Model Biocatalysts in Organosiloxane Chemistry. *PNAS* **2017**, *114* (27), E5285–E5291.
(38) Meredith M. Murr, D. E. M. Fractal Intermediates in the Self-Assembly of Silicatein Filaments. *PNAS* **2005**, *102* (33), 11657–11662.
(39) Schroder, H.C., Wang, X., Manfrin, A., Yu, S. Grebenjuk, V.A., Korzhev, M., Wiens, M., Schlossmacher, U., Muuler, W. E. G. Acquisition of Structure-Guiding and Structure-Forming Properties during Maturation from the pro-Silicatein to the Silicatein Form. *Journal of Biological Chemistry* **2012**, *287* (26), 22196–22205.
(40) Nishi, M., Kobayashi, H., Amano, T., Sakate, Y., Bito, T., Arima, J., Shimizu, K. Identification of the Domains Involved in Promotion of Silica Formation in Glassin, a Protein Occluded in Hexactinellid Sponge Biosilica, for Development of a Tag for Purification and Immobilization of Recombinant Proteins. *Marine Biotechnology* **2020**, *22*, 739–747.
(41) Meszaros, B., Simon, I., Dosztanyi, Z. Prediction of Protein Binding Regions in Disordered Proteins. *PLOS Computational Biology* **2009**, *5* (5), e1000376.
(42) Shimizu, K.; Amano, T.; Bari, M. R.; Weaver, J. C.; Arima, J.; Mori, N. Glassin, a Histidine-Rich Protein from the Siliceous Skeletal System of the Marine Sponge Euplectella, Directs Silica Polycondensation. *Proceedings of the National Academy of Sciences of the United States of America* **2015**, *112* (37), 11449–11454. https://doi.org/10.1073/pnas.1506968112.
(43) Bawazer, L. A.; Izumi, M.; Kolodin, D.; Neilson, J. R.; Schwenzer, B.; Morse, D. E. Evolutionary Selection of Enzymatically Synthesized Semiconductors from Biomimetic Mineralization Vesicles. *Proceedings of the National Academy of Sciences of the United States of America* **2012**. https://doi.org/10.1073/pnas.1116958109.
(44) Shkryl, Y. N.; Semiletova, I. V.; Nepomnyaschiy, A. V.; Kovalchuk, S. N.; Veremeichik, G. N.; Avramenko, T. V.; Bulgakov, V. P.; Shchipunov, Y. A.; Voznesenskiy, S. S.; Kozhemyako, V. B. Biomimetic Synthesis of Nanosized Silica Structures on a Substrate with Silicatein. *Russian Journal of Bioorganic Chemistry* **2018**, *44* (4), 465–467. https://doi.org/10.1134/S1068162018040180.
(45) Waldo, G.S., Standish, B.M., Berendzen, J., Terwilliger, T. C. Rapid Protein-Folding Assay Using Green Fluorescent Protein. *Nature Biotechnology* **1999**, *17*, 891–895.
(46) Terpe, K. Overview of Tag Protein Fusions: From Molecular and Biochemical Fundamentals to Commercial Systems. *Applied Microbiology and Biotechnology* **2003**, *60* (5), 523–533. https://doi.org/10.1007/s00253-002-1158-6.
(47) Sparkes, E. I.; Kettles, R. A.; Egedeuzu, C. S.; Stephenson, N. L.; Caslin, S. A.; Dakhili, S. Y. T.; Wong, L. S. Improved Production and Biophysical Analysis of Recombinant Silicatein-α. *Biomolecules* **2020**, *10* (9), 1–17. https://doi.org/10.3390/biom10091209.
(48) Oguri, H., Nakashima, K., Godigamuwa, K., Okamoto, J., Takeda, Y., Okazaki, F., Sakono, M., Kawasaki, S. Solubilization and Aggregation Control of Silica-Polymerizing Enzyme Fused with a Removable Soluble Protein. *Journal of Bioscience and Bioengineering* **2021**, *133* (3), 222–228.

(49) Van Gosen. B.S., Verplanck, P.L., Long, K.R., Gambogi, J., Seal, R. R. II. *The Rare-Earth Elements – Vital to Modern Technologies and Life Styles*.
(50) Survey, U. S. G. *Rare Earths - Mineral Commodity Summaries*; 2022; pp 1–2.
(51) Wang, Z-Y., Fan, H-R., Zhou, L., Yang, K-F., She, H.-D. Carbonatite-Related REE Deposits: An Overview. *Minerals* **2020**, *10* (11), 965.
(52) Barmettler, F.; Castelberg, C.; Fabbri, C.; Brandl, H. Microbial Mobilization of Rare Earth Elements (REE) from Mineral Solids—A Mini Review. *AIMS Microbiology* **2016**, *2* (2), 190–204. https://doi.org/10.3934/microbiol.2016.2.190.
(53) Jha, M.K., Kumari, A., Panda, R., Kumar, J.R., Yoo, K., Lee, J. Y. Review on Hydrometallurgical Recovery of Rare Earth Metals. *Hydrometallurgy* **2016**, *165* (1), 2–26.
(54) Han, P., Teo, W.Z., Yew, W. S. Biologically Engineered Microbes for Bioremediation of Electronic Waste: Wayposts, Challenges, and Future Directions. *Engineering Biology* **2022**, *6*, 23–34.
(55) Debbarma, P.; Zaidi, M. G. H.; Kumar, S.; Raghuwanshi, S.; Yadav, A.; Shouche, Y.; Goel, R. Selection of Potential Bacterial Strains to Develop Bacterial Consortia for the Remediation of E-Waste and Its in Situ Implications. *Waste Management* **2018**, *79*, 526–536. https://doi.org/10.1016/j.wasman.2018.08.026.
(56) Yang, Z., Lu, L. Berard, V.F., He, Q., Kiely, C.J., Berger, B.W., McIntosh, S. Biomanufacturing of CdS Quantum Dots. *Green Chemistry* **2015**, *17*, 3775–3782.
(57) Carrasco, V., Amarelle, V., Lagos-Moraga, S., Quezada, C.P., Espinoza-Gonzalez, R., Faccio, R., Fabiano, E., Perez-Donoso, J. M. Production of Cadmium Sulfide Quantum Dots by the Lithobiontic Antarctic Strain Pedobacter Sp. UYP1 and Their Application as Photosensitizer in Solar Cells. *Microbial Cell Factories* **2021**, *20* (1), 41.
(58) Xu, S.Z., Luo, X.S., Xing, Y.H., Liu, S., Huang, Q.Y., Chen, W. L. Complete Genome Sequence of Raoultella Sp. Strain X13, a Promising Cell Factory for the Synthesis of CdS Quantum Dots. *3 Biotech* **2019**, *9* (4), 120.
(59) Gallardo-Benavente, C., Carrion, O., Todd, J.D., Pieretti, J.C., Seabra, A.B., Duran, N., Rubilar, O., Perez-Donoso, J.M., Quiroz, A. Biosynthesis of CdS Quantum Dots Mediated by Volatile Sulfure Compounds Released by Antarctic Pseudomonas Fragi. *Frontiers in Microbiology* **2019**, *10*, 1866.
(60) Marusak, K.E., Feng, Y., Eben, C.F., Payne, S.T., Cao, Y., You, L., Zauscher, S. Cadmium Sulfphide Quantum Dots with Tunable Electronic Properties by Bacterial Precipitation. *RSC Advances* **2016**, *6* (80), 76158–76166.
(61) Ulloa, G., Collao, B., Araneda, M., Escobar, B., Alvarez, S., Bravo, D., Perez-Donoso, J. M. Use of Acidophilic Bacteria of the Genus Acidithiobacillus to Biosynthesize CdS Fluorescent Nanoparticles (Quantum Dots) with High Tolerance to Acidic pH. *Enzyme and Microbial Technology* **2016**, *95*, 217–224.
(62) Dunleavy, R.; Lu, L.; Kiely, C. J.; McIntosh, S.; Berger, B. W. Single-Enzyme Biomineralization of Cadmium Sulfide Nanocrystals with Controlled Optical Properties. *Proceedings of the National Academy of Sciences of the United States of America* **2016**, *113* (19), 5275–5280. https://doi.org/10.1073/pnas.1523633113.
(63) Wang, Y., Chen, H., Huang, Z., Yang, M., Yu, H., Peng, M., Yang, Z., Chen, S. Structural Characterization of Cystathioninee Gamma-Lyase smCSE Enables Aqueous Metal Quantum Dot Biosynthesis. *International Journal of Biological Macromolecules* **2021**, *174*, 42–51.
(64) Yang, Z., Lu, L., Kiely, CJ., Berger, B.W., McIntosh, S. Single Enzyme Direct Biomineralization of CdSe and CdSe-CdS Core-Shell Quantum Dots. *ACS Applied Material Interfaces* **2017**, *9* (15), 13430–13439.
(65) Lambertini, E., Penolazzi, L., Angelozzi, M., Grassie, F., Gambari, L., Lisignoli, G., De Bonis, P., Cavallo, M., Piva, R. The Expression of Cystathionine Gamma Lyase Is Regulated by Estrogen Receptor Alpha in Human Osteoblasts. *Oncotarget* **2017**, *8* (60), 101686–101696.
(66) Ozdemir, N.K., Cline, J.P., Kiely, C.J., McIntosh, S., Snyder, M. A. Scalable Biomineralization of CdS Quantum Dots by Immobilized Cystathionine Gamma-Lyase. *ACS Sustainable Chem Eng* **2020**, *8* (40), 15189–15198.

(67) Al-Mebayedh, H.; Niu, A.; Lin, C. Petroleum Hydrocarbon Composition of Oily Sludge and Contaminated Soils in a Decommissioned Oilfield Waste Pit under Desert Conditions. *Applied Sciences* **2022**, *12* (3), 1355. https://doi.org/10.3390/app12031355.
(68) Goddard, B., Butler, R., Pudasainee, D., Khan, M. Analyzing the Rare Earth Elements and Trace Metals in Tailings. *Alberta Academic Review* **2019**, *2* (2), 17–18.
(69) Ferrer, M., Golyshina, O.V., Beloqui, A., Golyshin, P. N. A Purple Acidophilic Di-Ferric DNA Ligase from Ferroplasma. *PNAS* **2008**, *105* (26), 8878–8883.
(70) Featherston, E.R., Issertell, E.J., Cotruvo, J. A. J. Probing Lanmodulin's Lanthanide Recognition via Sensitized Luminescence Yields a Platform for Quantification of Terbium in Acid Mine Drainage. *J Am Chem Soc* **2021**, *143* (35), 14287–14299.
(71) Cotruvo, J.A., Featherston, E.R., Mattocks, J.A., Ho, J.V., Laremore, T. N. Lanmodulin: A Highly Selective Lanthanide-Binding Protein from a Lanthanide-Utilizing Bacterium. *J Am Chem Soc* **2018**, *140* (44), 15056–15061.
(72) Hatanaka, T.; Matsugami, A.; Nonaka, T.; Takagi, H.; Hayashi, F.; Tani, T.; Ishida, N. Rationally Designed Mineralization for Selective Recovery of the Rare Earth Elements. *Nature Communications* **2017**, *8* (1), 15670. https://doi.org/10.1038/ncomms15670.
(73) Berla, B. M.; Saha, R.; Immethun, C. M.; Maranas, C. D.; Moon, T. S.; Pakrasi, H. B. Synthetic Biology of Cyanobacteria: Unique Challenges and Opportunities. *Front. Microbiol.* **2013**, *4*. https://doi.org/10.3389/fmicb.2013.00246.
(74) Żymańczyk-Duda, E.; Samson, S. O.; Brzezińska-Rodak, M.; Klimek-Ochab, M. Versatile Applications of Cyanobacteria in Biotechnology. *Microorganisms* **2022**, *10* (12), 2318. https://doi.org/10.3390/microorganisms10122318.
(75) López-Hernández, J.-F.; Kean-Meng, T.; Asencio-Alcudia, G.-G.; Asyraf-Kassim, M.; Alvarez-González, C.-A.; Márquez-Rocha, F.-J. Sustainable Microalgae and Cyanobacteria Biotechnology. *Applied Sciences* **2022**, *12* (14), 6887. https://doi.org/10.3390/app12146887.
(76) Sound, J. K.; Bellamy-Carter, J.; Leney, A. C. The Increasing Role of Structural Proteomics in Cyanobacteria. *Essays in Biochemistry* **2023**, *67* (2), 269–282. https://doi.org/10.1042/EBC20220095.
(77) Yu, J.; Liberton, M.; Cliften, P. F.; Head, R. D.; Jacobs, J. M.; Smith, R. D.; Koppenaal, D. W.; Brand, J. J.; Pakrasi, H. B. Synechococcus Elongatus UTEX 2973, a Fast Growing Cyanobacterial Chassis for Biosynthesis Using Light and CO2. *Sci Rep* **2015**, *5* (1), 8132. https://doi.org/10.1038/srep08132.
(78) Mapstone, L. J.; Leite, M. N.; Purton, S.; Crawford, I. A.; Dartnell, L. Cyanobacteria and Microalgae in Supporting Human Habitation on Mars. *Biotechnology Advances* **2022**, *59*, 107946. https://doi.org/10.1016/j.biotechadv.2022.107946.
(79) Ramalho, T. P.; Chopin, G.; Pérez-Carrascal, O. M.; Tromas, N.; Verseux, C. Selection of *Anabaena* Sp. PCC 7938 as a Cyanobacterium Model for Biological ISRU on Mars. *Appl Environ Microbiol* **2022**, *88* (15), e00594-22. https://doi.org/10.1128/aem.00594-22.
(80) Verseux, C.; Heinicke, C.; Ramalho, T. P.; Determann, J.; Duckhorn, M.; Smagin, M.; Avila, M. A Low-Pressure, N2/CO2 Atmosphere Is Suitable for Cyanobacterium-Based Life-Support Systems on Mars. *Front. Microbiol.* **2021**, *12*, 611798. https://doi.org/10.3389/fmicb.2021.611798.
(81) Cycil, L. M.; Hausrath, E. M.; Ming, D. W.; Adcock, C. T.; Raymond, J.; Remias, D.; Ruemmele, W. P. Investigating the Growth of Algae Under Low Atmospheric Pressures for Potential Food and Oxygen Production on Mars. *Front. Microbiol.* **2021**, *12*, 733244. https://doi.org/10.3389/fmicb.2021.733244.
(82) De Belie, N. Microorganisms versus Stony Materials: A Love–Hate Relationship. *Mater Struct* **2010**, *43* (9), 1191–1202. https://doi.org/10.1617/s11527-010-9654-0.
(83) Iqbal, D. M.; Wong, L. S.; Kong, S. Y. Bio-Cementation in Construction Materials: A Review. *Materials* **2021**, *14* (9), 2175. https://doi.org/10.3390/ma14092175.
(84) Nasser, A. A.; Sorour, N. M.; Saafan, M. A.; Abbas, R. N. Microbially-Induced-Calcite-Precipitation (MICP): A Biotechnological Approach to Enhance the Durability of Concrete Using

Bacillus Pasteurii and Bacillus Sphaericus. *Heliyon* **2022**, *8* (7), e09879. https://doi.org/10.1016/j.heliyon.2022.e09879.
(85) Anbu, P.; Kang, C.-H.; Shin, Y.-J.; So, J.-S. Formations of Calcium Carbonate Minerals by Bacteria and Its Multiple Applications. *SpringerPlus* **2016**, *5* (1), 250. https://doi.org/10.1186/s40064-016-1869-2.
(86) Dhami, N. K.; Reddy, M. S.; Mukherjee, A. Application of Calcifying Bacteria for Remediation of Stones and Cultural Heritages. *Front. Microbiol.* **2014**, *5*. https://doi.org/10.3389/fmicb.2014.00304.
(87) Portugal, C. R. M. E.; Fonyo, C.; Machado, C. C.; Meganck, R.; Jarvis, T. Microbiologically Induced Calcite Precipitation Biocementation, Green Alternative for Roads – Is This the Breakthrough? A Critical Review. *Journal of Cleaner Production* **2020**, *262*, 121372. https://doi.org/10.1016/j.jclepro.2020.121372.
(88) Su, F.; Yang, Y.; Qi, Y.; Zhang, H. Combining Microbially Induced Calcite Precipitation (MICP) with Zeolite: A New Technique to Reduce Ammonia Emission and Enhance Soil Treatment Ability of MICP Technology. *Journal of Environmental Chemical Engineering* **2022**, *10* (3), 107770. https://doi.org/10.1016/j.jece.2022.107770.
(89) Gao, J.; Liu, L.; Ma, N.; Yang, J.; Dong, Z.; Zhang, J.; Zhang, J.; Cai, M. Effect of Ammonia Stress on Carbon Metabolism in Tolerant Aquatic Plant—Myriophyllum Aquaticum. *Environmental Pollution* **2020**, *263*, 114412. https://doi.org/10.1016/j.envpol.2020.114412.
(90) Zhao, Q.; Li, L.; Li, C.; Li, M.; Amini, F.; Zhang, H. Factors Affecting Improvement of Engineering Properties of MICP-Treated Soil Catalyzed by Bacteria and Urease. *J. Mater. Civ. Eng.* **2014**, *26* (12), 04014094. https://doi.org/10.1061/(ASCE)MT.1943-5533.0001013.
(91) Erdmann, N.; De Payrebrune, K. M.; Ulber, R.; Strieth, D. Optimizing Compressive Strength of Sand Treated with MICP Using Response Surface Methodology. *SN Appl. Sci.* **2022**, *4* (10), 282. https://doi.org/10.1007/s42452-022-05169-8.
(92) Bhaduri, S.; Debnath, N.; Mitra, S.; Liu, Y.; Kumar, A. Microbiologically Induced Calcite Precipitation Mediated by Sporosarcina Pasteurii. *JoVE* **2016**, No. 110, 53253. https://doi.org/10.3791/53253.
(93) Ghasemi, P.; Montoya, B. M. Field Application of the Microbially Induced Calcium Carbonate Precipitation on a Coastal Sandy Slope. In *Geo-Congress 2020*; American Society of Civil Engineers: Minneapolis, Minnesota, 2020; pp 141–149. https://doi.org/10.1061/9780784482834.016.
(94) Churchman, G. J.; Lowe, D. J. Alteration, Formation, and Occurence of Minerals in Soils. In *Handbook of Soil Sciences*; Taylor & Francis: Boca Raton, FL, 2012; Vol. 1 Properties and Processes, p 20.1-20.72.
(95) Krupenikov, I. A.; Boincean, B. P.; Dent, D. Soil Mineralogy and Elemental Composition. In *The Black Earth*; Springer Netherlands: Dordrecht, 2011; pp 27–32. https://doi.org/10.1007/978-94-007-0159-5_4.
(96) Shacklette, H. T.; Boerngen, J. G. *Element Concentrations in Soil and Other Surficial Materials of the Conterminous United States*; U.S. Geological Survey Professional Paper 1270; United States Department of the Interior: Washington, 1984.
(97) Jones, H. W. The Recent Large Reduction in Space Launch Cost; NASA: Albuquerque, NM, 2018; pp 1–10.
(98) Space Communications and Navigations Classroom Worksheet. Money Mass-Ematics: Ratios and Percentages with Laser Communication.
(99) Zuo, H.; Ni, S.; Xu, M. An Assumption of in Situ Resource Utilization for "Bio-Bricks" in Space Exploration. *Front. Mater.* **2023**, *10*, 1155643. https://doi.org/10.3389/fmats.2023.1155643.
(100) Exolith Lab. LHS-1 Lunar Highlands Simulant Fact Sheet, 2023.
(101) Yoshikuni, Y., Dietrich, J.A., Nowroozi, F.F., Babbitt, P.C., Keasling, J. D. Redesigning Enzymes Based on Adaptive Evolution for Optimal Function in Synthetic Metabolic Pathways. *Chem Biol* **2008**, *15* (6), 607–618.

(102) Leonard, E., Ajikumar, P.K., Thayer, K., Xiao, W., Mo, J.D., Tidor, B., Stephanopoulos, G., Prather, K. L. J. Combining Metabolic and Protein Engineering of a Terpenoid Biosynthetic Pathway for Overproduction and Selectivity Control. *Proceedings of the National Academy of Sciences of the United States of America2* **10AD**, *107* (31), 13654–13659.
(103) Christensen, S., Ramisch, S., Andre, I. DnaK Response to Expression of Protein Mutants Is Dependent on Translation Rate and Stability. *Communications Biology* **2022**, *5*, 597.
(104) Martinez-Alonso, M., Vera, A., Villaverde, A. Role of the Chaperone DnaK in Protein Solubility and Conformational Quality in Inclusion Body-Forming Escherichia Coli Cells. *FEMS Microbiology Letters* **2007**, *273* (2), 187–195.
(105) Pettinger, N. W.; Williams, R. E. A.; Chen, J.; Kohler, B. Crystallization Kinetics of Cerium Oxide Nanoparticles Formed by Spontaneous, Room-Temperature Hydrolysis of Cerium(<scp>iv</Scp>) Ammonium Nitrate in Light and Heavy Water. *Physical Chemistry Chemical Physics* **2017**, *19* (5), 3523–3531. https://doi.org/10.1039/C6CP08227K.
(106) Zaccolo, M., Williams, D.M., Brown, D.M., Gherardi, E. An Approach to Random Mutagenesis of DNA Using Mixtures of Triphosphate Derivatives of Nucleoside Analogues. *J. Mol. Biol* **1996**, *255*, 589–603.
(107) Studier, F.W., Moffatt, B. A. Use of Bacteriophage T7 RNA Polymerse to Direct Selective High-Level Expression of Cloned Genes. *Journal of Molecular Biology* **1986**, *189* (1), 113–130.
(108) Peng, L., Hongyu, X., Xi, L., Chaocan, Z., Yi, L. Study on the Toxic Mechanism of La3+ to Escherichia Coli. *Biological Trace Element Research* **2006**, *114*, 293–299.
(109) Thill, A.; Zeyons, O.; Spalla, O.; Chauvat, F.; Rose, J.; Auffan, M.; Flank, A. M. Cytotoxicity of CeO2 Nanoparticles for Escherichia Coli. Physico-Chemical Insight of the Cytotoxicity Mechanism. *Environmental Science & Technology* **2006**, *40* (19), 6151–6156. https://doi.org/10.1021/es060999b.
(110) Ferla, M. P. Mutanalyst, an Online Tool for Assessing the Mutational Spectrum of epPCR Libraries with Poor Sampling. *BMC Bioinformatics* **2016**, *17* (1), 152. https://doi.org/10.1186/s12859-016-0996-7.
(111) Goldsmith, M., Kiss, C., Bradbury, A.R.M., Tawfik, D. S. Avoiding and Controlling Double Transformation Artifacts. *Protein Engineering, Design, and Selection* **2007**, *20* (7), 315–318.
(112) Tomoiaga, D., Bubnell, J., Herndon, L., Feinstein, P. High Rates of Plasmid Cotransformation in E Coli Overturn the Clonality Myth and Reveal Colony Development. *Scientific Reports* **2022**, *12*, 11515.
(113) Schweinsberg, M.; Weiss, L. C.; Striewski, S.; Tollrian, R.; Lampert, K. P. More than One Genotype: How Common Is Intracolonial Genetic Variability in Scleractinian Corals? *Molecular Ecology* **2015**, *24* (11), 2673–2685. https://doi.org/10.1111/mec.13200.
(114) Rinkevich, B. Coral Chimerism as an Evolutionary Rescue Mechanism to Mitigate Global Climate Change Impacts. *Glob Change Biol* **2019**, *25* (4), 1198–1206. https://doi.org/10.1111/gcb.14576.
(115) Bitter, M. C.; Kapsenberg, L.; Gattuso, J.-P.; Pfister, C. A. Standing Genetic Variation Fuels Rapid Adaptation to Ocean Acidification. *Nat Commun* **2019**, *10* (1), 5821. https://doi.org/10.1038/s41467-019-13767-1.
(116) Zhou, Y.; Shimizu, K.; Cha, J. N.; Stucky, G. D.; Morse, D. E. Efficient Catalysis of Polysiloxane Synthesis by Silicateinα Requires Specific Hydroxy and Imidazole Functionalities. *Angewandte Chemie International Edition* **1999**, *15* (38(6)), 779–782. https://doi.org/10.1002/(sici)1521-3773(19990315)38:6<779::aid-anie779>3.0.co;2-#.
(117) Tarczewska, A., Bielak, K., Zoglowek, A., Soltys K., Dobryszycki, P., Ozyhar, A., Rozycka, M. The Role of Intrinsically Disordered Proteins in Liquid-Liquid Phase Separation during Calcium Carbonate Biomineralization. *Biomolecules* **2022**, *12*, 1266.
(118) Buljan, M., Lang, B., Weatheritt, R.J., Daughdrill, G.W., Dunker, A.K., Fuxreiter, M., Gough, J., Gsponer, J., Jones, D.T., Kim, P.M., Kriwacki, R.W., Oldefield, C.J., Pappu, R.V., Tompa, P., Uversky, V.N., Wright, P.E., Babu, M. M. Classification of Intrinsically Disordered Regions and Proteins. *Chemical Reviews* **2014**, *114*, 6589–6631.

(119) Evans, J. S. Aragonite-Associated Biomineralization Proteins Are Disordered and Contain Interactive Motifs. *Bioinformatics* **2012**, *28* (24), 3182–3185.
(120) Perovic, I., Mandal, T., Evans, J. S. A Pearl Protein Self-Assembles to Form Protein Complexes That Amplify Mineralization. *Biochemistry* **2013**, *52*, 5696–5702.
(121) Mukhopadhyay, S. The Dynamism of Intrinsically Disordered Proteins: Binding-Induced Folding, Amyloid Formation, and Phase Separation. *J Phys Chem B* **2020**.
(122) Romero, P.; Obradovic, Z.; Li, X.; Garner, E. C.; Brown, C. J.; Dunker, A. K. Sequence Complexity of Disordered Protein. *Proteins* **2001**, *42* (1), 38–48. https://doi.org/10.1002/1097-0134(20010101)42:1<38::AID-PROT50>3.0.CO;2-3.
(123) Stankovic, I.M., Niu, S., Hall, M.B., Zaric, S. D. Role of Aromatic Amino Acids in Amyloid Self-Assembly. *International Journal of Biological Macromolecules2* **20AD**, *156*, 949–959.
(124) L. Keresztes, E. Szogi, B. Varga, V. Farkas, A. Perczel, V. G. The Budapest Amyloid Predictor and Its Applications. *Biomolecules* **2021**, *11* (4), 500.
(125) Ishida, T., Kinoshita, K. PrDOS: Prediction of Disordered Protein Regions from Amino Acid Sequence. *Nucleic Acids Research* **2007**, *35*, W460–W464.
(126) Jones, D. T. Protein Secondary Structure Prediction Based on Position-Specific Scoring Matricies. *J. Mol. Biol.* **1999**, *292*, 195–202.
(127) Mittag, E. W. M. and T. Relationship of Sequence and Phase Separation in Protein Low-Complexity Regions. *Biochemistry* **2018**.
(128) Shen, Y.; Maupetit, J.; Derreumaux, P.; Tufféry, P. Improved PEP-FOLD Approach for Peptide and Miniprotein Structure Prediction. *J. Chem. Theory Comput.* **2014**, *10* (10), 4745–4758. https://doi.org/10.1021/ct500592m.
(129) Rey, J.; Murail, S.; de Vries, S.; Derreumaux, P.; Tuffery, P. PEP-FOLD4: A pH-Dependent Force Field for Peptide Structure Prediction in Aqueous Solution. *Nucleic Acids Research* **2023**, *51* (W1), W432–W437. https://doi.org/10.1093/nar/gkad376.
(130) Mier, P.; Paladin, L.; Tamana, S.; Petrosian, S.; Hajdu-Soltész, B.; Urbanek, A.; Gruca, A.; Plewczynski, D.; Grynberg, M.; Bernadó, P.; Gáspári, Z.; Ouzounis, C. A.; Promponas, V. J.; Kajava, A. V.; Hancock, J. M.; Tosatto, S. C. E.; Dosztanyi, Z.; Andrade-Navarro, M. A. Disentangling the Complexity of Low Complexity Proteins. *Briefings in Bioinformatics* **2020**, *21* (2), 458–472. https://doi.org/10.1093/bib/bbz007.
(131) Gonçalves-Kulik, M.; Mier, P.; Kastano, K.; Cortés, J.; Bernadó, P.; Schmid, F.; Andrade-Navarro, M. A. Low Complexity Induces Structure in Protein Regions Predicted as Intrinsically Disordered. *Biomolecules* **2022**, *12* (8), 1098. https://doi.org/10.3390/biom12081098.
(132) Lee, B.; Jaberi-Lashkari, N.; Calo, E. A Unified View of Low Complexity Regions (LCRs) across Species. *eLife* **2022**, *11*, e77058. https://doi.org/10.7554/eLife.77058.
(133) Hershey, D.M., Ren, X., Melnyk, R.A., Browne, P.J., Ozyamak, E., Jones, S.R., Chang, M.C.Y., Hurley, J.H., Komeili, A. . MamO Is a Repurposed Serine Protease That Promotes Magnetite Biomineralization through Direct Transition Metal Binding in Magnetotactic Bacteria. *PLOS Biology* **2016**.
(134) Goettig, P., Magdolen, V., Brandstetter, H. Natural and Synthetic Inhibitors of Kallikrein-Related Peptidases (KLKs). *Biochimie* **2010**, *92* (11), 1546–1567.
(135) Chao, G.; Lau, W. L.; Hackel, B. J.; Sazinsky, S. L.; Lippow, S. M.; Wittrup, K. D. Isolating and Engineering Human Antibodies Using Yeast Surface Display. *Nature Protocols* **2006**, *1* (2), 755–768. https://doi.org/10.1038/nprot.2006.94.
(136) Coradin, T.; Eglin, D.; Livage, J. The Silicomolybdic Acid Spectrophotometric Method and Its Application to Silicate/Biopolymer Interaction Studies. *Spectroscopy* **2004**, *18*, 567–576.
(137) Hogendoorn, C.; Roszczenko-Jasińska, P.; Martinez-Gomez, N. C.; de Graaff, J.; Grassl, P.; Pol, A.; Op den Camp, H. J. M.; Daumann, L. J. Facile Arsenazo III-Based Assay for Monitoring Rare Earth Element Depletion from Cultivation Media for Methanotrophic and Methylotrophic Bacteria. *Applied and Environmental Microbiology* **2018**, *84* (8). https://doi.org/10.1128/AEM.02887-17.

(138) Spangler, L. Single Enzyme Biomineralization of Semiconductor Nanocrystals. PhD, Lehigh University, Bethlehem Pennsylvania, 2018.
(139) Lu, Y.; O'Dowd, B. F.; Orrego, H.; Israel, Y. Cloning and Nucleotide Sequence of Human Liver cDNA Encoding for Cystathionine γ-Lyase. *Biochemical and Biophysical Research Communications* **1992**, *189* (2), 749–758. https://doi.org/10.1016/0006-291X(92)92265-Y.
(140) Sun, Q., Collins, R., Huang, S., Holmberg-Schivone, L., Anand, G.S., Tan, C.H., van-den-Berg, S., Deng, L.W., Moore, P.K., Karlberg, T., Sivaraman, J. Structural Basis for the Inhibition Mechanism of Human Cystathionine Gamma-Lyase, an Enzyme Responsible for the Production of H2S. *The Journal of Biological Chemistry* **2009**, *284* (5), 3076–3085.
(141) Pages, D.; Rose, J.; Conrod, S.; Cuine, S.; Carrier, P.; Heulin, T.; Achouak, W. Heavy Metal Tolerance in Stenotrophomonas Maltophilia. *PLoS ONE* **2008**, *3* (2). https://doi.org/10.1371/journal.pone.0001539.
(142) Haibin, Y., Jianhui, Z., Ruijin, Y., Qiang, S. Synthesis of Rare Earth Sulfides and Their UV-Vis Absorption Spectra. *Journal of Rare Earths* **2009**, *27* (2), 308–311.
(143) Schleid, T., Lauxmann, P., Graf, C., Bartsch, C., Doert, T. Rare Earth Metal Disulfides - Syntheses and Crystal Structures of a-CeS2, a-NdS2, b-LaS2, b-CeS2, and b-PrS2. *Z. Naturforsch.* **2009**, *64b*, 189–196.
(144) Kuang, X., Peng, L., Chen, S., Peng, C., Song, H. Immobilization of Metal(Loid)s from Acid Mine Drainage by Biological Soil Crusts through Biomineralization. *Journal of Hazardous Materials* **2022**, 130314.
(145) Gadd, G. M. Metals, Minerals and Microbes: Geomicrobiology and Bioremediation. *Microbiology* **2010**, *156* (3), 609–643. https://doi.org/10.1099/mic.0.037143-0.
(146) Bruna, N.; Galliani, E.; Oyarzún, P.; Bravo, D.; Fuentes, F.; Pérez-Donoso, J. M. Biomineralization of Lithium Nanoparticles by Li-Resistant Pseudomonas Rodhesiae Isolated from the Atacama Salt Flat. *Biol Res* **2022**, *55* (1), 12. https://doi.org/10.1186/s40659-022-00382-6.
(147) Arshadi, M., Mousavi, S. M. Multi-Objective Optimization of Heavy Metals Bioleaching from Discarded Mobile Phone PCBs: Simultaneous Cu and Ni Recovery Using Acidithiobacillus Ferroxidans. *Separation and Purification Technology* **2015**, *147*, 210–219.
(148) Sun, W.; Xiao, E.; Xiao, T.; Krumins, V.; Wang, Q.; Häggblom, M.; Dong, Y.; Tang, S.; Hu, M.; Li, B.; Xia, B.; Liu, W. Response of Soil Microbial Communities to Elevated Antimony and Arsenic Contamination Indicates the Relationship between the Innate Microbiota and Contaminant Fractions. *Environmental Science & Technology* **2017**, *51* (16), 9165–9175. https://doi.org/10.1021/acs.est.7b00294.
(149) Liu, M.; Chen, S.; Wang, S.; Hu, C.; Liu, B. High-Quality Draft Genome Sequence of Pseudomonas Songnenensis L103, a Denitrifier Isolated from a 100-Meter-Deep Aquifer in a Heavily Nitrogen-Fertilized Agricultural Area. *Microbiology Resource Announcements* **2019**, *8* (36). https://doi.org/10.1128/MRA.00373-19.
(150) Xu, H., Portieles, R., Du, L., Gao, X., Borras-Hidalgo, O. Endophytic Bacterium Bacillus Aryabhattai Induces Novel Transcriptomic Changes to Stimulate Plant Growth. *PLoS ONE* **2022**, *17* (8), e0272500.
(151) Rabbee, M.F., Ali, M.S., Choi, J., Hwang, B.S., Jeong, S.C., Baek, K. Bacillus Velezensis: A Valuable Member of Bioactive Molecules within Plant Microbiomes. *Molecules* **2019**, *24*, 1046.
(152) Zhu, X.; Ni, X.; Waigi, M.; Liu, J.; Sun, K.; Gao, Y. Biodegradation of Mixed PAHs by PAH-Degrading Endophytic Bacteria. *International Journal of Environmental Research and Public Health* **2016**, *13* (8), 805. https://doi.org/10.3390/ijerph13080805.
(153) Hernandez-Santana, A., Gomez-Garzon, C., Dussan, J. Lysinibacillus Sphaericus. *Trends in Microbiology* **2022**, *30* (7), 705–706.
(154) Hernández-Santana, A.; Dussán, J. *Lysinibacillus Sphaericus* Proved to Have Potential for the Remediation of Petroleum Hydrocarbons. *Soil and Sediment Contamination: An International Journal* **2018**, *27* (6), 538–549. https://doi.org/10.1080/15320383.2018.1490888.

(155) Tonner, P. D.; Darnell, C. L.; Engelhardt, B. E.; Schmid, A. K. Detecting Differential Growth of Microbial Populations with Gaussian Process Regression. *Genome Res.* **2017**, *27* (2), 320–333. https://doi.org/10.1101/gr.210286.116.
(156) Cesar, S.; Anjur-Dietrich, M.; Yu, B.; Li, E.; Rojas, E.; Neff, N.; Cooper, T. F.; Huang, K. C. Bacterial Evolution in High-Osmolarity Environments. *mBio* **2020**, *11* (4), e01191-20. https://doi.org/10.1128/mBio.01191-20.
(157) Fasnacht, M.; Polacek, N. Oxidative Stress in Bacteria and the Central Dogma of Molecular Biology. *Front. Mol. Biosci.* **2021**, *8*, 671037. https://doi.org/10.3389/fmolb.2021.671037.
(158) Meidinger, R.; St. Germain, R. W.; Dohotariu, V.; Gillispie, G. D. *Fluorescence of Aromatic Hydrocarbons in Aqueous Solution*; Field Screening Methods for Hazardous Wastes and Toxic Chemicals; Technical Report 33; SERDP: Arlington, VA, 1993; pp 395–403.
(159) Mangwani, N.; Shukla, S. K.; Kumari, S.; Rao, T. S.; Das, S. Characterization of Stenotrophomonas Acidaminiphila NCW-702 Biofilm for Implication in the Degradation of Polycyclic Aromatic Hydrocarbons. *Journal of Applied Microbiology* **2014**, *117*, 1012–1024.
(160) Paper, M. , Koch, M., Jung, P., Lakatos, M., Nilges, T., Bruck, T. B. Rare Earths Stick to Rare Cyanobacteria: Future Potential for Bioremediation and Recovery of Rare Earth Elements. *Frontiers in Bioengineering and Biotechnology* **2023**.
(161) Obare, S. O.; Murphy, C. J. Selective Blue Emission from an HPBO–Li+ Complex in Alkaline Media. *New J. Chem.* **2001**, *25* (12), 1600–1604. https://doi.org/10.1039/b103562m.
(162) Merroun, M.; Rossberg, A.; Hennig, C.; Scheinost, A. C.; Selenska-Pobell, S. Spectroscopic Characterization of Gold Nanoparticles Formed by Cells and S-Layer Protein of Bacillus Sphaericus JG-A12. *Materials Science and Engineering: C* **2007**, *27* (1), 188–192. https://doi.org/10.1016/j.msec.2006.05.001.
(163) Chandramohan, A.; Duprat, E.; Remusat, L.; Zirah, S.; Lombard, C.; Kish, A. Novel Mechanism for Surface Layer Shedding and Regenerating in Bacteria Exposed to Metal-Contaminated Conditions. *Front. Microbiol.* **2019**, *9*, 3210. https://doi.org/10.3389/fmicb.2018.03210.
(164) Mesnage, S.; Tosi-Couture, E.; Gounon, P.; Mock, M.; Fouet, A. The Capsule and S-Layer: Two Independent and Yet Compatible Macromolecular Structures in *Bacillus Anthracis*. *J Bacteriol* **1998**, *180* (1), 52–58. https://doi.org/10.1128/JB.180.1.52-58.1998.
(165) Fagan, R. P.; Fairweather, N. F. Biogenesis and Functions of Bacterial S-Layers. *Nat Rev Microbiol* **2014**, *12* (3), 211–222. https://doi.org/10.1038/nrmicro3213.
(166) Velásquez, L.; Dussan, J. Biosorption and Bioaccumulation of Heavy Metals on Dead and Living Biomass of Bacillus Sphaericus. *Journal of Hazardous Materials* **2009**, *167* (1–3), 713–716. https://doi.org/10.1016/j.jhazmat.2009.01.044.
(167) Mukherjee, A.; Yadav, R.; Marmeisse, R.; Fraissinet-Tachet, L.; Reddy, M. S. Heavy Metal Hypertolerant Eukaryotic Aldehyde Dehydrogenase Isolated from Metal Contaminated Soil by Metatranscriptomics Approach. *Biochimie* **2019**, *160*, 183–192. https://doi.org/10.1016/j.biochi.2019.03.010.
(168) Frasch, W. D. The Participation of Metals in the Mechanism of the F1-ATPase. *Biochimica et Biophysica Acta (BBA) - Bioenergetics* **2000**, *1458* (2–3), 310–325. https://doi.org/10.1016/S0005-2728(00)00083-9.
(169) Wai, I.; Chong, K.; Ho, W. S. Influence of Heavy Metals on Glyceraldehyde-3-phosphate Dehydrogenase Interactions in *Chironomus Riparius* Larvae. *Enviro Toxic and Chemistry* **2013**, *32* (8), 1882–1887. https://doi.org/10.1002/etc.2265.
(170) Wiens, M.; Schröder, H.-C.; Wang, X.; Link, T.; Steindorf, D.; Müller, W. E. G. Isolation of the Silicatein-α Interactor Silintaphin-2 by a Novel Solid-Phase Pull-Down Assay. *Biochemistry* **2011**, *50* (12), 1981–1990. https://doi.org/10.1021/bi101429x.
(171) Procko, E.; O'Mara, M. L.; Bennett, W. F. D.; Tieleman, D. P.; Gaudet, R. The Mechanism of ABC Transporters: General Lessons from Structural and Functional Studies of an Antigenic Peptide Transporter. *FASEB j.* **2009**, *23* (5), 1287–1302. https://doi.org/10.1096/fj.08-121855.

(172) Janulczyk, R.; Pallon, J.; Björck, L. Identification and Characterization of a *Streptococcus Pyogenes* ABC Transporter with Multiple Specificity for Metal Cations. *Molecular Microbiology* **1999**, *34* (3), 596–606. https://doi.org/10.1046/j.1365-2958.1999.01626.x.
(173) Lee, J. Y.; Yang, J. G.; Zhitnitsky, D.; Lewinson, O.; Rees, D. C. Structural Basis for Heavy Metal Detoxification by an Atm1-Type ABC Exporter. *Science* **2014**, *343* (6175), 1133–1136. https://doi.org/10.1126/science.1246489.
(174) Banerjee, G.; Pandey, S.; Ray, A. K.; Kumar, R. Bioremediation of Heavy Metals by a Novel Bacterial Strain Enterobacter Cloacae and Its Antioxidant Enzyme Activity, Flocculant Production, and Protein Expression in Presence of Lead, Cadmium, and Nickel. *Water Air Soil Pollut* **2015**, *226* (4), 91. https://doi.org/10.1007/s11270-015-2359-9.
(175) Chelikani, P.; Fita, I.; Loewen, P. C. Diversity of Structures and Properties among Catalases. *Cellular and Molecular Life Sciences (CMLS)* **2004**, *61* (2), 192–208. https://doi.org/10.1007/s00018-003-3206-5.
(176) Pfeifer, K.; Ehmoser, E.-K.; Rittmann, S. K.-M. R.; Schleper, C.; Pum, D.; Sleytr, U. B.; Schuster, B. Isolation and Characterization of Cell Envelope Fragments Comprising Archaeal S-Layer Proteins. *Nanomaterials* **2022**, *12* (14), 2502. https://doi.org/10.3390/nano12142502.
(177) Vera, M. L.; Torres, W. R.; Galli, C. I.; Chagnes, A.; Flexer, V. Environmental Impact of Direct Lithium Extraction from Brines. *Nat Rev Earth Environ* **2023**, *4* (3), 149–165. https://doi.org/10.1038/s43017-022-00387-5.
(178) *The Role of Critical Minerals in Clean Energy Transitions*; World Energy Outlook Special Report; International Energy Agency, 2022. https://iea.blob.core.windows.net/assets/ffd2a83b-8c30-4e9d-980a-52b6d9a86fdc/TheRoleofCriticalMineralsinCleanEnergyTransitions.pdf.
(179) Ilyas, S.; Kim, M. S.; Lee, J. C.; Jabeen, A.; Bhatti, H. N. Bio-Reclamation of Strategic and Energy Critical Metals from Secondary Resources. *Metals* **2017**, *7* (6), 1–17. https://doi.org/10.3390/met7060207.
(180) Zeng, J.; Zhang, Y.; Liu, Y.; Zhang, X.; Xia, L.; Liu, J.; Qiu, G. Expression, Purification and Characterization of a Cysteine Desulfurase, IscS, from Acidithiobacillus Ferrooxidans. *Biotechnol Lett* **2007**, *29* (12), 1983–1990. https://doi.org/10.1007/s10529-007-9491-6.
(181) Leng, F.; Li, Y.; Luo, W.; Wei, Q.; Jing, Y.; Wang, X.; Yang, M.; Wang, Y. Cloning, Expression, and Bioinformatics Analysis of Heavy Metal Resistance Gene Afe_1862 from Acidithiobacillus Ferrooxidans L1 in Escherichia Coli. *Biol Trace Elem Res* **2019**, *189* (1), 291–300. https://doi.org/10.1007/s12011-018-1462-3.
(182) Jackson, B. R.; Noble, C.; Lavesa-Curto, M.; Bond, P. L.; Bowater, R. P. Characterization of an ATP-Dependent DNA Ligase from the Acidophilic Archaeon "Ferroplasma Acidarmanus" Fer1. *Extremophiles* **2007**, *11* (2), 315–327. https://doi.org/10.1007/s00792-006-0041-2.
(183) Zhang, W.; Sun, J.; Cao, H.; Tian, R.; Cai, L.; Ding, W.; Qian, P.-Y. Post-Translational Modifications Are Enriched within Protein Functional Groups Important to Bacterial Adaptation within a Deep-Sea Hydrothermal Vent Environment. *Microbiome* **2016**, *4* (1), 49. https://doi.org/10.1186/s40168-016-0194-x.
(184) Li, Z.; Wang, Y.; Yao, Q.; Justice, N. B.; Ahn, T.-H.; Xu, D.; Hettich, R. L.; Banfield, J. F.; Pan, C. Diverse and Divergent Protein Post-Translational Modifications in Two Growth Stages of a Natural Microbial Community. *Nat Commun* **2014**, *5* (1), 4405. https://doi.org/10.1038/ncomms5405.
(185) Jung, H.; Su, Z.; Inaba, Y.; West, A. C.; Banta, S. Genetic Modification of *Acidithiobacillus Ferrooxidans* for Rare-Earth Element Recovery under Acidic Conditions. *Environ. Sci. Technol.* **2023**, *57* (48), 19902–19911. https://doi.org/10.1021/acs.est.3c05772.
(186) Kanao, T.; Kunihisa, T.; Ohgimoto, S.; Ito, M.; Murakami, C.; Nakayama, H.; Tamura, T.; Kamimura, K. Recombinant Expression Using the Tetrathionate Hydrolase Promoter in Acidithiobacillus Ferrooxidans. *Journal of Bioscience and Bioengineering* **2023**, *135* (3), 176–181. https://doi.org/10.1016/j.jbiosc.2022.12.005.

(187) Jeong, H.; Jeong, D.-E.; Sim, Y. M.; Park, S.-H.; Choi, S.-K. Genome Sequence of Lysinibacillus Sphaericus Strain KCTC 3346 ^{T}. *Genome Announc* **2013**, *1* (4), e00625-13. https://doi.org/10.1128/genomeA.00625-13.
(188) Nakamura, L. K. Phylogeny of Bacillus Sphaericus-like Organisms. *International Journal of Systematic and Evolutionary Microbiology* **2000**, *50* (5), 1715–1722. https://doi.org/10.1099/00207713-50-5-1715.
(189) Yang, L.-L.; Huang, Y.; Liu, J.; Ma, L.; Mo, M.-H.; Li, W.-J.; Yang, F.-X. Lysinibacillus Mangiferahumi Sp. Nov., a New Bacterium Producing Nematicidal Volatiles. *Antonie van Leeuwenhoek* **2012**, *102* (1), 53–59. https://doi.org/10.1007/s10482-012-9712-4.
(190) Xu, K.; Yuan, Z.; Rayner, S.; Hu, X. Genome Comparison Provides Molecular Insights into the Phylogeny of the Reassigned New Genus Lysinibacillus. *BMC Genomics* **2015**, *16* (1), 140. https://doi.org/10.1186/s12864-015-1359-x.
(191) Wang, X.; Schloßmacher, U.; Wiens, M.; Batel, R.; Schröder, H. C.; Müller, W. E. G. Silicateins, Silicatein Interactors and Cellular Interplay in Sponge Skeletogenesis: Formation of Glass Fiber-like Spicules. *The FEBS Journal* **2012**, *279* (10), 1721–1736. https://doi.org/10.1111/j.1742-4658.2012.08533.x.
(192) Müller, W. E. G.; Boreiko, A.; Wang, X.; Belikov, S. I.; Wiens, M.; Grebenjuk, V. A.; Schloβmacher, U.; Schröder, H. C. Silicateins, the Major Biosilica Forming Enzymes Present in Demosponges: Protein Analysis and Phylogenetic Relationship. *Gene* **2007**, *395* (1–2), 62–71. https://doi.org/10.1016/j.gene.2007.02.014.
(193) Armirotti, A.; Damonte, G.; Pozzolini, M.; Mussino, F.; Cerrano, C.; Salis, A.; Benatti, U.; Giovine, M. Primary Structure and Post-Translational Modifications of Silicatein Beta from the Marine Sponge *Petrosia Ficiformis* (Poiret, 1789). *J. Proteome Res.* **2009**, *8* (8), 3995–4004. https://doi.org/10.1021/pr900342y.
(194) Hudson, P. *Cyanobacteria Biotechnology*; Advanced biotechnology; Wiley-VCH: Weinheim, 2021.
(195) Vasudevan, R.; Gale, G. A. R.; Schiavon, A. A.; Puzorjov, A.; Malin, J.; Gillespie, M. D.; Vavitsas, K.; Zulkower, V.; Wang, B.; Howe, C. J.; Lea-Smith, D. J.; McCormick, A. J. CyanoGate: A Modular Cloning Suite for Engineering Cyanobacteria Based on the Plant MoClo Syntax. *Plant Physiol.* **2019**, *180* (1), 39–55. https://doi.org/10.1104/pp.18.01401.
(196) Zhou, J.; Zhang, H.; Meng, H.; Zhu, Y.; Bao, G.; Zhang, Y.; Li, Y.; Ma, Y. Discovery of a Super-Strong Promoter Enables Efficient Production of Heterologous Proteins in Cyanobacteria. *Sci Rep* **2014**, *4* (1), 4500. https://doi.org/10.1038/srep04500.
(197) Huertas, M.; López-Maury, L.; Giner-Lamia, J.; Sánchez-Riego, A.; Florencio, F. Metals in Cyanobacteria: Analysis of the Copper, Nickel, Cobalt and Arsenic Homeostasis Mechanisms. *Life* **2014**, *4* (4), 865–886. https://doi.org/10.3390/life4040865.
(198) Kalita, N.; Baruah, P. P. Cyanobacteria as a Potent Platform for Heavy Metals Biosorption: Uptake, Responses and Removal Mechanisms. *Journal of Hazardous Materials Advances* **2023**, *11*, 100349. https://doi.org/10.1016/j.hazadv.2023.100349.
(199) Patron, N. J. DNA Assembly for Plant Biology. *CP Plant Biology* **2016**, *1* (4), 604–616. https://doi.org/10.1002/cppb.20038.
(200) Ma, L.; Pang, A.-P.; Luo, Y.; Lu, X.; Lin, F. Beneficial Factors for Biomineralization by Ureolytic Bacterium Sporosarcina Pasteurii. *Microb Cell Fact* **2020**, *19* (1), 12. https://doi.org/10.1186/s12934-020-1281-z.
(201) Yu, X.; Chu, J.; Yang, Y.; Qian, C. Reduction of Ammonia Production in the Biocementation Process for Sand Using a New Biocement. *Journal of Cleaner Production* **2021**, *286*, 124928. https://doi.org/10.1016/j.jclepro.2020.124928.
(202) Carter, M. S.; Tuttle, M. J.; Mancini, J. A.; Martineau, R.; Hung, C.-S.; Gupta, M. K. Microbially Induced Calcium Carbonate Precipitation by *Sporosarcina Pasteurii* : A Case Study in Optimizing Biological $CaCO_3$ Precipitation. *Appl Environ Microbiol* **2023**, *89* (8), e01794-22. https://doi.org/10.1128/aem.01794-22.

(203) Dong, Y.; Gao, Z.; Wang, D.; Di, J.; Guo, X.; Yang, Z.; Li, Y.; Wang, Y.; Wang, Y. Optimization of Growth Conditions and Biological Cementation Effect of Sporosarcina Pasteurii. *Construction and Building Materials* **2023**, *395*, 132288. https://doi.org/10.1016/j.conbuildmat.2023.132288.
(204) Ghosh, T.; Bhaduri, S.; Montemagno, C.; Kumar, A. Sporosarcina Pasteurii Can Form Nanoscale Calcium Carbonate Crystals on Cell Surface. *PLoS ONE* **2019**, *14* (1), e0210339. https://doi.org/10.1371/journal.pone.0210339.
(205) Van Bloois, E.; Winter, R. T.; Kolmar, H.; Fraaije, M. W. Decorating Microbes: Surface Display of Proteins on Escherichia Coli. *Trends in Biotechnology* **2011**, *29* (2), 79–86. https://doi.org/10.1016/j.tibtech.2010.11.003.
(206) Smith, S. M.; Gottesman, M. M. Activity and Deletion Analysis of Recombinant Human Cathepsin L Expressed in Escherichia Coli. *Journal of Biological Chemistry* **1989**, *264* (34), 20487–20495. https://doi.org/10.1016/S0021-9258(19)47088-9.
(207) Muller, W.; Engel, S.; Wang, X.; Wolf, S.; Tremel, W.; Thakur, N.; Krasko, A.; Divekar, M.; Schroder, H. Bioencapsulation of Living Bacteria (Escherichia Coli) with Poly(Silicate) after Transformation with Silicatein-α Gene. *Biomaterials* **2008**, *29* (7), 771–779. https://doi.org/10.1016/j.biomaterials.2007.10.038.
(208) Povarova, N. V.; Markina, N. M.; Baranov, N. S.; Barinov, N. A.; Klinov, D. V.; Kozhemyako, V. B.; Lukyanov, K. A. A Water-Soluble Precursor for Efficient Silica Polymerization by Silicateins. *Biochemical and Biophysical Research Communications* **2018**, *495* (2), 2066–2070.
(209) Heveran, C. M.; Liang, L.; Nagarajan, A.; Hubler, M. H.; Gill, R.; Cameron, J. C.; Cook, S. M.; Srubar, W. V. Engineered Ureolytic Microorganisms Can Tailor the Morphology and Nanomechanical Properties of Microbial-Precipitated Calcium Carbonate. *Sci Rep* **2019**, *9* (1), 14721. https://doi.org/10.1038/s41598-019-51133-9.
(210) Spencer, C. A.; Sass, H.; Van Paassen, L. Increased Microbially Induced Calcium Carbonate Precipitation (MICP) Efficiency in Multiple Treatment Sand Biocementation Processes by Augmentation of Cementation Medium with Ammonium Chloride. *Geotechnics* **2023**, *3* (4), 1047–1068. https://doi.org/10.3390/geotechnics3040057.
(211) Rogerson, A. G.; Lloyd, V. K. Lyme Disease Patient Outcomes and Experiences; A Retrospective Cohort Study. *Healthcare* **2020**, *8* (3), 322. https://doi.org/10.3390/healthcare8030322.
(212) Murfin, K. E.; Kleinbard, R.; Aydin, M.; Salazar, S. A.; Fikrig, E. Borrelia Burgdorferi Chemotaxis toward Tick Protein Salp12 Contributes to Acquisition. *Ticks and Tick-borne Diseases* **2019**, *10* (5), 1124–1134. https://doi.org/10.1016/j.ttbdis.2019.06.002.
(213) Tabb, J. S.; Rapoport, E.; Han, I.; Lombardi, J.; Green, O. An Antigen-Targeting Assay for Lyme Disease: Combining Aptamers and SERS to Detect the OspA Protein. *Nanomedicine: Nanotechnology, Biology and Medicine* **2022**, *41*, 102528. https://doi.org/10.1016/j.nano.2022.102528.